

**Advanced analysis techniques
for x-ray reflectivities:
Theory and application**

Dissertation
zur Erlangung des Doktorgrades
der Mathematisch–Naturwissenschaftlichen Fakultät
der Universität Dortmund

vorgelegt von
Klaus Martin Zimmermann

Karlsruhe

2005

Referent:
Co-referent:
Tag der mündlichen Prüfung:
Freigegeben zum Druck: Dortmund, den

Prof. Dr. M. Tolan
Dekan

Contents

1	Introduction	1
2	Theory of x-ray reflectivity	4
2.1	Basics	4
2.2	Dynamical scattering-theory	5
2.2.1	Scattering from sharp interfaces	5
2.2.2	Scattering from rough interfaces	7
2.3	Kinematical approximation	9
2.3.1	Derivation from quantum mechanics	9
2.3.2	Derivation from the Parratt formalism	11
2.4	The Patterson function	15
2.5	The phase problem	16
3	Analytical properties of the reflection coefficient	18
3.1	The Hilbert phase	18
3.1.1	The Kramers-Kronig relations	18
3.1.2	Derivation of the Hilbert Phase	19
3.1.3	Computation of the Hilbert phase	20
3.2	Zeros of the complex reflection coefficient	27
3.2.1	Zeroless reflection coefficients	28
3.2.2	Equivalence of the phase problem and the unknown zeros .	32
3.2.3	Locating Zeros	38
3.2.4	Flipping zeros	43
4	Analysis of reflectivities	47
4.1	Direct analysis methods	47
4.1.1	Model-dependent direct analysis	47
4.1.2	Model-independent methods	48
4.2	Inverse methods in the framework of dynamical scattering theory	50
4.2.1	Phaseless inverse scattering	52
4.2.2	Including pre-knowledge	54
4.3	Inverse methods in the framework of kinematical scattering theory	55
4.3.1	The Box-refinement technique	55

4.3.2	Inversion methods proposed by Sanyal et al.	57
4.4	Previously obtained results	59
4.4.1	The inversion scheme	59
4.4.2	Numerical examples	60
4.4.3	Determination of alternative density profiles	61
4.5	Experimental solution of the phase problem	62
5	Experimental influences	64
5.1	Measuring x-ray reflectivities	64
5.2	Experimental setup: The BRUKER AXS D8 diffractometer	66
5.3	Influence of the experimental setup on the measurement	67
5.3.1	The resolution function	68
5.3.2	Influence of the finite sample size	68
5.3.3	The true specular reflectivity	70
5.3.4	Convolution vs. Deconvolution	73
6	The new inversion algorithm	76
6.1	The linear inverse problem	77
6.1.1	The Discrete Prolate Spheroidal Sequences	78
6.1.2	Application of DPSS to the phase-reconstruction problem in x-ray reflectivity	82
6.1.3	Eigendensities for the piecewise-constant density profile . .	86
6.1.4	Analytical expression for $\partial R(q_z)/\partial \rho_n$	90
6.1.5	Stabilization of the inversion step	91
6.2	Smoothness	94
6.3	Representation of the profile by a polygon	95
6.3.1	Modified Fresnel coefficients for the linear-graded interface	96
6.3.2	Eigendensities for the linear-graded density profile	98
6.4	Profile representation by second order B-splines	102
6.4.1	Modified Fresnel coefficient for the second order B-spline profile	103
6.4.2	Derivation of the partial derivatives $\partial R(q_z)/\partial b_j$	110
6.4.3	Eigendensities for the second order B-spline profile	111
6.5	Connection between the different types of profile representation .	117
6.6	Computation of the Hilbert-phase of a B-spline profile	121
6.6.1	The Hilbert-phase of a B-spline profile	121
6.6.2	Computation of the Hilbert-profile for B-spline profiles . .	126
6.6.3	Computation of the <i>conjugate</i> profile ρ_{H^*}	131
7	Application of inverse iteration schemes to experimental data	136
7.1	Single Carbon layer on a Silicon substrate	137
7.2	Structural investigation of Ti-C samples	141
7.2.1	Sample pl366	141

7.2.2	Sample pl367	143
7.2.3	Comparison of the obtained profiles	148
7.3	Structural investigation of Ni–C samples	148
7.4	The SiGe standard-sample from BRUKER AXS	154
7.5	Summary and concluding remarks	158
8	Summary and Outlook	160
A		163
A.1	Sufficient condition for zero-free UHP for layer-stack with gaussian interfaces	163
A.2	Partial derivatives $\partial R(q)/\partial b_m$ for the second-order B-spline profile within the WSA	167
A.3	Modification of the proposed algorithm	168
	References	169

Chapter 1

Introduction

More than 45 years have passed since Richard Feynman gave his famous talk "There's Plenty of Room at the Bottom" on 29. December 1959 at the annual meeting of the American Physical Society that laid the inspirational bases for today's nanotechnology. Enormous progress was made in the fields of material research and thin-film technology over the last decades: Microelectronics is part of our daily life, spintronics is in research and quantum computing the next logical step. All the processes for the preparation of high quality surfaces and interfaces require also characterization techniques on atomic length scales. With the ongoing reduction of the film thicknesses, the influence of the interfaces and the surfaces increases and properties of the materials can change radically. The understanding of the physics of surfaces and interfaces is therefore of fundamental interest for explaining the material properties. X-ray scattering is a powerful non-destructive method for structure-analysis; X-ray reflectometry can probe the variation of the electron density with Ångstrom resolution. This makes it highly sensitive to surfaces and interfaces. It fits exactly the requirement of state-of-the-art nano samples.

However, X-ray scattering experiments lack from the fact, that only the amplitude of the scattered X-rays can be measured in the experiment, whereas the determination of the scattering profile also requires knowledge of the phase. In other words: No direct picture of the surface or interface can be created like with other methods, i.e. scanning electron microscopy (SEM) or transmission electron microscopy (TEM). The lack of phase-information is known as the *phase-problem* and is the main reason for ambiguities in the analysis of x-ray reflectivity data. Large efforts have been spent in to the experimental solution of this phase problem with limited applicability: Neutron-scattering is sensitive to magnetic structures and uses the reference layer method [90][91][92]. Anomalous x-ray scattering is restricted to certain sample systems only [11][125]. The frequently used fitting of a calculated profile to the measurement data, requires a theoretical description of the sample in a model, that is often hard to find and even ambiguous; no constraints can be imposed to overcome this phase-problem.

For these reasons a different approach will be followed in this thesis - the so-called inverse methods or model independent description. A large variety of these analysis-schemes have been proposed in the literature [20][36][107][123][176]. The common goal is to - at least partly - overcome the phase-problem, by using a-priori information about the sample structure.

From the analyticity of the reflection coefficient follows that its phase can be separated in two terms: The first term is the Hilbert phase, which is fully determined by the reflectivity alone. The second term is a function of the complex zeros of the reflection coefficient that are located in the upper half complex plane (UHP)¹. Thus, the analysis of x-ray reflectivity can be split in three major tasks: 1) Recovery of the Hilbert profile. 2) Locating the zeros of the reflection coefficient. 3) Decide which zeros should be located in the UHP. Whereas the first two tasks require a limited computational effort and can be solved in a reasonable time, the third task is a severe problem. The number of combinations for N zeros is 2^N so that required computational time exceeds the life-time of a human being - even for N of moderate size.

The scope of this thesis is to widen the application field of the inverse methods, by overcoming known constraints to the sample structures and developing new techniques to decrease the required numerical effort. The resulting new algorithm is finally used to evaluate samples, not analyzable with standard fitting methods.

This thesis is structured as follows:

- Chapter 2 gives an introduction into the theory of x-ray reflectivity. The treatment in terms of classical optics and in the kinematical approximation is reviewed.
- The phase problem and the analytical properties of the reflection coefficient are subject of Chapter 3. The Hilbert-phase is reviewed and formulas for its calculation are discussed. The important question under what conditions this phase uniquely determines the density profile is discussed. Existing procedures for locating the zeros of the reflection coefficient are reviewed and new methods will be proposed. The influence of zeros in the UHP on the profile is discussed.
- An overview on already existing analysis-techniques for x-ray reflectivities is given in Chapter 4. Inversion methods in the framework of quantum scattering theory, iterative inversion schemes based on the kinematical approximation as well as model-independent fitting techniques are revised and discussed.

¹Criteria for zeroless reflection coefficients have been derived for some classes of profiles. But a general answer to this problem is unlikely to be found.

- Chapter 5 addresses the x-ray reflectivity experiment. The influence of the experimental setup on the measured data is revised and the required corrections for the extraction of the true specular reflectivity are described. The x-ray diffractometer used for the experiments in this thesis is briefly presented.
- Based on the previous chapters, a new iterative inversion algorithm will be proposed in Chapter 6. Different types of bases for the expansion of the profile are proposed. These bases will be used for the approximation of the eigenfunctions of the linear inverse problem. Other topics are the calculation of Hilbert-phase and of the corresponding Hilbert-profile as well as the locating of the zeros.
- In Chapter 7, examples for the application of iterative inversion schemes to experimental x-ray reflectivity data are presented: Long-time irradiation of samples with x-rays under ambient condition causes small changes in the sample structure. Series of reflectivities are measured and analyzed. The obtained density profiles will be discussed and emphasize the importance of model-independent analysis techniques.
- Chapter 8 summarizes this thesis and closes with an outlook.

Chapter 2

Theory of x-ray reflectivity

2.1 Basics

An electromagnetic plane wave described by its electric field $\mathbf{E}(\mathbf{r}) = \mathbf{E}_0 \exp(i\mathbf{k}\cdot\mathbf{r})$, which penetrates into a medium characterized by an index of refraction $n(\mathbf{r})$, propagates according to the Helmholtz equation.

$$\Delta_{\mathbf{r}}\mathbf{E}(\mathbf{r}) + k^2 n(\mathbf{r})^2 \mathbf{E}(\mathbf{r}) = 0 \quad , \quad (2.1)$$

where $k = 2\pi/\lambda$ is the modulus of the wavevector \mathbf{k}_i and λ denotes the x-ray wavelength. Treating the N atoms per unitcell as harmonic oscillators with resonance frequencies ω_j , the index of refraction is given by

$$n(\mathbf{r}) = 1 + N \frac{e^2}{\varepsilon_0 m} \sum_{j=1}^N \frac{f_j(\omega)}{\omega_j^2 - \omega^2 - 2i\omega\eta_j} \quad , \quad (2.2)$$

where ω is the frequency of the incoming wave, e is the charge and m the mass, respectively, of the electron. The η_j is the damping factor and the f_j is the forced oscillation strength of atom j . The formfactor f_j is a complex number, $f_j = f_j^0 + f_j'(E) + i f_j''(E)$, with the dispersion and absorption corrections $f_j'(E)$ and $f_j''(E)$ dependent on the radiation energy E . Since for x-rays $\omega > \omega_j$, the index of refraction can be rewritten as

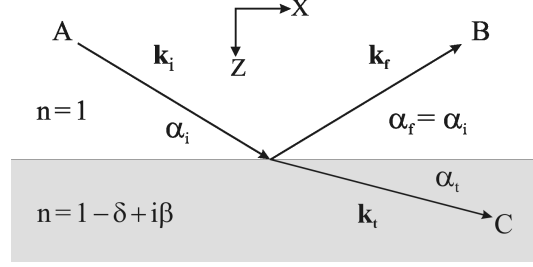
$$n(\mathbf{r}) = 1 - \delta(\mathbf{r}) + i\beta(\mathbf{r}) \quad , \quad (2.3)$$

with the dispersion and absorption terms

$$\delta(\mathbf{r}) = \frac{\lambda^2}{2\pi} \varrho(\mathbf{r}) \sum_{j=1}^N \frac{f_j^0 + f_j'(E)}{Z} \quad (2.4)$$

$$\beta(\mathbf{r}) = \frac{\lambda^2}{2\pi} \varrho(\mathbf{r}) \sum_{j=1}^N \frac{f_j''(E)}{Z} = \frac{\lambda}{4\pi} \mu(\mathbf{r}) \quad . \quad (2.5)$$

Figure 2.1: A plane electromagnetic wave with wavevector \mathbf{k}_i hits the surface at a grazing angle α_i . The wave splits into a reflected ($\alpha_i = \alpha_f$) and a refracted wave at the angle α_t according to Snell's law from classical optics.



$\varrho(\mathbf{r}) = r_e \rho(\mathbf{r})$ is the scattering length density (SLD). $r_e = e^2/4\pi\epsilon_0 mc^2 = 2.814 \times 10^{-1} \text{\AA}$ is the classical electron radius, $\rho(\mathbf{r})$ denotes the electron density and $Z = \sum_j Z_j$ is the total number of electrons in the unitcell. Neglecting $f_j'(E)$ and approximating $f_j^0(E)$ by $f_j^0(E) \approx Z_j$, Eq. (2.2) may be rewritten as

$$n(\mathbf{r}) = 1 - \frac{\lambda^2}{2\pi} \rho(\mathbf{r}) + i \frac{\lambda}{4\pi} \mu(\mathbf{r}) \quad , \quad (2.6)$$

where $\mu(\mathbf{r})$ is the linear absorption coefficient. The dispersion δ is a positive number of the order 10^{-6} for x-rays. The absorption β is typically one or two orders of magnitude smaller. Both, dispersion and absorption, are proportional to the electron density $\varrho(\mathbf{r})$.

2.2 Dynamical scattering-theory

2.2.1 Scattering from sharp interfaces

When an electromagnetic plane wave $\mathbf{E}_i(\mathbf{r}) = \mathbf{E}_0 \exp(i\mathbf{k}_i \cdot \mathbf{r})$ hits the sharp surface of a medium with the index of refraction n at grazing angle α_i , it splits into a reflected and a transmitted wave as shown in Fig. 2.1. The vectors of their electric fields $\mathbf{E}_r(\mathbf{r})$ and $\mathbf{E}_t(\mathbf{r})$ are given by

$$\mathbf{E}_r(\mathbf{r}) = r_{s,p} \mathbf{E}_i(\mathbf{r}) \exp(i\mathbf{q} \cdot \mathbf{r}) \quad \text{and} \quad \mathbf{E}_t(\mathbf{r}) = t_{s,p} \mathbf{E}_i(\mathbf{r}) \exp[i(\mathbf{k}_t - \mathbf{k}_i) \cdot \mathbf{r}] \quad (2.7)$$

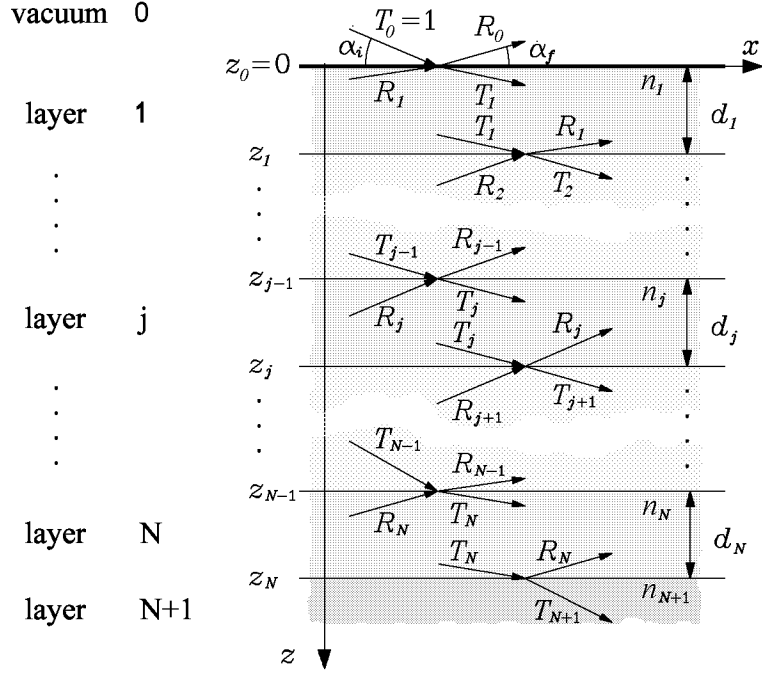
with the reflection coefficient $r_{s,p}$ and the transmission coefficient $t_{s,p}$. $\mathbf{q} = \mathbf{k}_f - \mathbf{k}_i$ is the wavevector transfer. For the case of s- and p-polarization, $r_{s,p}$ and $t_{s,p}$ are given by the so-called Fresnel formulas from classical optics [24],

$$r_s = \frac{k_{i,z} - k_{t,z}}{k_{i,z} + k_{t,z}} \quad , \quad r_p = \frac{n^2 k_{i,z} - k_{t,z}}{n^2 k_{i,z} + k_{t,z}} \quad , \quad (2.8)$$

$$t_s = \frac{2k_{i,z}}{k_{i,z} + k_{t,z}} \quad , \quad t_p = \frac{2k_{i,z}}{n^2 k_{i,z} + k_{t,z}} \quad , \quad (2.9)$$

where $k_{i,z} = k \sin \alpha_i$ and $k_{t,z} = k \sin \alpha_t = k \sqrt{n^2 - \cos^2 \alpha_i}$ are the z -components of the wavevectors of the incoming and the transmitted waves. Since $n \approx 1$ for

Figure 2.2: Sketch of a system consisting of $N + 1$ layers of with N sharp interfaces located at z_j . The amplitude of the impinging wave is unity, $T_0 = 1$, The amplitude of the wave reflected from the surface at $z = 0$ is R_0 . No reflection, $R_{N+1} = 0$, arises from the substrate, that extends from z_N to ∞ .



x-rays, both cases are effectively identical and only the formulas for s-polarization are used in the following. Because n is smaller than unity for x-rays, there exists a *critical angle* $\alpha_c \approx \sqrt{2\delta}$ below which the real part of $k_{t,z}$ vanishes and total external reflection ($r \approx 1$) occurs. The intensity of the reflected radiation, the so-called Fresnel reflectivity, $r_F = |r|^2$ is given by ¹

$$r_F(q_z) = \left| \frac{q_z^2 - \sqrt{q_z^2 - q_c^2}}{q_z^2 + \sqrt{q_z^2 - q_c^2}} \right|^2 \approx \left(\frac{q_c}{2q_z} \right)^4 \quad \text{for } q_z \gg q_c, \quad (2.10)$$

where $q_z = 2k \sin \alpha_i$ is the z -component of the wavevector transfer \mathbf{q} and $q_c = 2k \sin \alpha_c$ is the critical wavevector transfer that is related to the SLD by $q_c = \sqrt{16\pi\rho}$.

The formalism for the description of the scattering at a single sharp interface has been extended to systems consisting of an arbitrary number of homogeneous layers with sharp interfaces. Fig. 2.2 shows such a system. *Abelès* [5] connected the transmission and reflection coefficients of two consecutive layers via matrices. *Parratt* [105] developed a recursive formalism that provides equivalent results. The ratio $X_j = R_j/T_j$ of the amplitudes of the transmitted and reflected waves

¹Note that in this work $r(q_z) = |R(q_z)|^2$ denotes the reflectivity and the Fresnel reflection $r_{j,j+1}$ from the interface between the layers j and $j + 1$ inside the sample. Furthermore $r_F(q_z)$ denotes the Fresnel reflectivity.

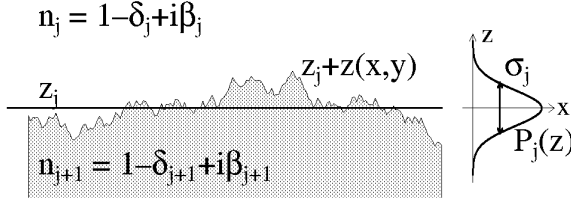


Figure 2.3: Rough interface with mean z -coordinate z_j and fluctuations $z(x, y)$. The probability to find the sharp interface at $z_j + z$ is given by the distribution $P_j(z)$ with variance σ_j (taken from [155]).

at the lower interface of layer j is given by the recursion formula

$$X_j = \frac{R_j}{T_j} = \exp(2ik_{z,j}z_j) \frac{r_{j,j+1} + X_{j+1} \exp(-2ik_{z,j+1}z_j)}{1 + r_{j,j+1}X_{j+1} \exp(-2ik_{z,j+1}z_j)}, \quad (2.11)$$

with the Fresnel reflection coefficient

$$r_{j,j+1} = \frac{k_{z,j} - k_{z,j+1}}{k_{z,j} + k_{z,j+1}}. \quad (2.12)$$

$k_{z,j} = k^2 \sqrt{n_j^2 - \cos^2 \alpha_i}$ denotes the z -component of the wave vector inside the layer j with the index of refraction n_j . Since there is no reflection from the substrate, the recursion starts with $R_{N+1} = X_{N+1} = 0$. With the normalization $T_0 = 1$ the intensity reflected in the specular direction ($\alpha_i = \alpha_f$), in the following denoted by r , is given by

$$r = |X_0|^2 = |R_0|^2. \quad (2.13)$$

With the knowledge of R_0 and $T_0 = 1$ the amplitudes R_j and T_j are given by the recursive relationships

$$R_{j+1} = \frac{1}{t_{j+1,j}} \left\{ T_j r_{j,j+1} \exp[-i(k_{z,j+1} + k_{z,j})z_j] + R_j \exp[-i(k_{z,j+1} - k_{z,j})z_j] \right\} \quad (2.14)$$

$$T_{j+1} = \frac{1}{t_{j+1,j}} \left\{ T_j \exp[i(k_{z,j+1} - k_{z,j})z_j] + R_j r_{j,j+1} \exp[i(k_{z,j+1} + k_{z,j})z_j] \right\}, \quad (2.15)$$

with the Fresnel transmission coefficient $t_{j+1,j} = 1 - r_{j,j+1}$.

2.2.2 Scattering from rough interfaces

The model described above only deals with sharp interfaces. Since real interfaces and surfaces are always rough, some extensions of the formalism are necessary to include roughness.

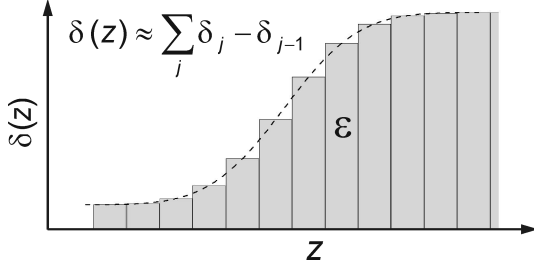


Figure 2.4: A continuous density profile is approximated by an ensemble of very thin layers of thickness ε with constant electron density δ_j and sharp interfaces. The reflectivity can be calculated using the *Parratt* algorithm.

In Figure 2.3 a rough interface with density fluctuations around z_j is shown. In the specular direction, the wavevector transfer $\mathbf{q} = \mathbf{k}_f - \mathbf{k}_i$ has only a z -component so that the sample structure laterally averaged over (x, y) is probed, i.e.

$$n_j(z) = \iint n_j(x, y, z) dy dx \quad . \quad (2.16)$$

The sharp interface located at z_j is then replaced by an ensemble of interfaces whose position is given by a probability distribution function $P_j(z)$ with variance σ_j (see Fig. 2.3). The index of refraction around the interface between two media with the respective indices of refraction n_j and n_{j+1} is given by

$$n_j(z) = n_j w_j(z) + n_{j+1} [1 - w_j(z)] \quad (2.17)$$

where

$$w_j(z) = \int_{-\infty}^z P_j(\zeta - z_j) d\zeta \quad (2.18)$$

is the fraction of material j at the position z . For a Gaussian probability distribution,

$$P_j(z) = \frac{1}{\sqrt{2\pi}\sigma_j} \exp\left(-\frac{z^2}{2\sigma_j^2}\right) \quad , \quad (2.19)$$

so-called *modified* Fresnel coefficients,

$$\tilde{r}_{j,j+1} = r_{j,j+1} \exp(-2k_{z,j}k_{z,j+1}\sigma_j^2) \quad (2.20)$$

$$\tilde{t}_{j,j+1} = t_{j,j+1} \exp\left[-(k_{z,j} - k_{z,j+1})^2\sigma_j^2/2\right] \quad , \quad (2.21)$$

can be derived, which replace the Fresnel coefficients $r_{j,j+1}$ and $t_{j,j+1}$ for a sharp interface in the Parratt algorithm. At large angles of incidence, $\alpha_i \gg \alpha_c$, Eq. (2.20) simplifies to $\tilde{r}_{j,j+1} = r_{j,j+1} \exp(-q_z^2\sigma_j^2/2)$, where the exponential term is known as Debye-Waller factor. A comprehensive overview about scattering from rough interfaces is given in [155] and Refs. in there.

An alternative approach is to slice the continuous profile $n(z)$ into very thin layers of thickness ε with a constant index of refraction $n_j = n(\varepsilon j)$ and sharp interfaces (see Fig. 2.4). ε has to be small enough to correctly represent rapid density changes, i.e. $\varepsilon \ll \sigma$. In addition, ε must be smaller than π/q_{max} , where

q_{max} is the maximum value of q_z for which the reflectivity is requested. The reflectivity can then be calculated with the Parratt algorithm using the Fresnel coefficient $r_{j-1,j}$ for a sharp interface. This approach is more general because it does not depend on the form of the density profile, whereas the derivation of the modified Fresnel coefficients requires some probability distribution function for which the modified Fresnel coefficients have to be calculated analytically. The increased number N of slabs for the description of the profile results in an increase of the computational time ($\mathcal{O}(N^2)$ operations), but does not cause problems nowadays.

Since this work deals with arbitrary density profiles all reflectivities are calculated within dynamical theory by the slicing technique, if not mentioned otherwise.

2.3 Kinematical approximation

2.3.1 Derivation from quantum mechanics

In quantum theory the scattering process can be described by the time-independent Schrödinger equation

$$(\Delta_{\mathbf{r}} + k^2) \psi(\mathbf{r}) = V(\mathbf{r})\psi(\mathbf{r}) \quad , \quad (2.22)$$

A comparison with the Helmholtz equation, see Eq. (2.1), imposes to connect the scattering potential $V(\mathbf{r})$ to the index of refraction via $V(\mathbf{r}) = k^2(1 - n(\mathbf{r})^2)$. With Green's function $G(\mathbf{r} - \mathbf{r}')$ as solution of the equation

$$(\Delta_{\mathbf{r}} + k^2) G(\mathbf{r} - \mathbf{r}') = \delta(\mathbf{r} - \mathbf{r}') \quad (2.23)$$

and the solution $\psi_0(\mathbf{r}) = \exp(i\mathbf{k} \cdot \mathbf{r})$ of the associated homogeneous differential equation

$$(\Delta_{\mathbf{r}} + k^2) \psi_0(\mathbf{r}) = 0 \quad , \quad (2.24)$$

the solution of Eq. (2.22) satisfies the integral equation

$$\psi(\mathbf{r}) = \psi_0(\mathbf{r}) + \int G(\mathbf{r} - \mathbf{r}')V(\mathbf{r}')\psi(\mathbf{r}') d^3\mathbf{r}' \quad . \quad (2.25)$$

For the physically meaningful solution of Eq. (2.23), an outgoing spherical wave, the Green's function has the form

$$G(\mathbf{r} - \mathbf{r}') = -\frac{1}{4\pi} \frac{\exp(ik|\mathbf{r} - \mathbf{r}'|)}{|\mathbf{r} - \mathbf{r}'|} \quad . \quad (2.26)$$

Identifying ψ_0 with the incoming plane wave $\psi_i = \exp(i\mathbf{k} \cdot \mathbf{r})$, Eq. (2.25) becomes

$$\psi(\mathbf{r}) = \psi_i(\mathbf{r}) - \frac{1}{4\pi} \int V(\mathbf{r}') \frac{\exp(ik|\mathbf{r} - \mathbf{r}'|)}{|\mathbf{r} - \mathbf{r}'|} \psi(\mathbf{r}') d^3\mathbf{r}' \quad , \quad (2.27)$$

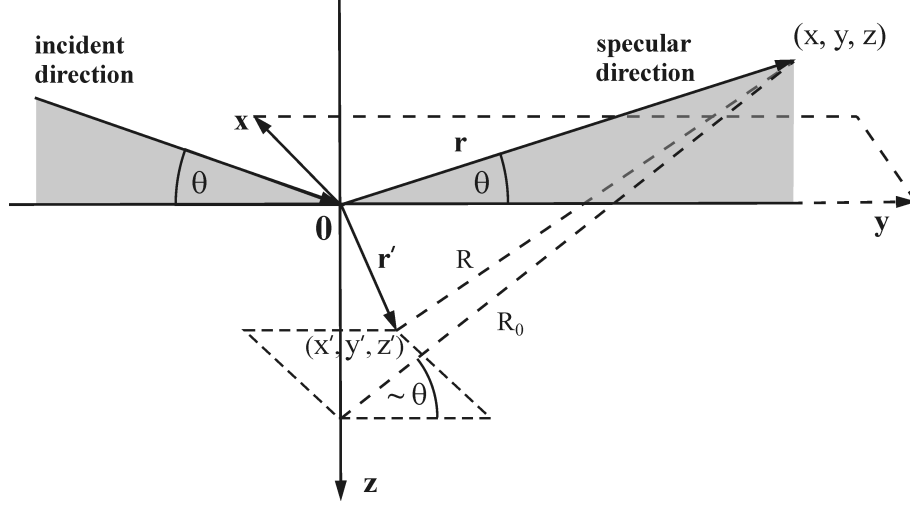


Figure 2.5: Geometry showing the field point \mathbf{r} relative to the source point \mathbf{r}' . The stratification coincides with the xy -plane and the scatter wave direction makes the same angle θ with the xy -plane as the incident wave [171].

where the second term describes the scattered wave

$$\psi_s(\mathbf{r}) = -\frac{1}{4\pi} \int \frac{\exp(ikR)}{R} V(\mathbf{r}') \psi(\mathbf{r}') d^3\mathbf{r}' . \quad (2.28)$$

$R = |\mathbf{r} - \mathbf{r}'|$ is the distance from the source point \mathbf{r}' to the field point \mathbf{r} as shown in Fig. 2.5. Inserting $\psi(\mathbf{r}) = \psi_i(\mathbf{r}) + \psi_s(\mathbf{r})$ into Eq. (2.28) leads to

$$\begin{aligned} \psi_s(\mathbf{r}) = & -\frac{1}{4\pi} \int \frac{\exp(ikR)}{R} V(\mathbf{r}') \psi_i(\mathbf{r}') d^3\mathbf{r}' \\ & -\frac{1}{4\pi} \int \frac{\exp(ikR)}{R} V(\mathbf{r}') \psi_s(\mathbf{r}') d^3\mathbf{r}' \end{aligned} \quad (2.29)$$

The first term is the first order Born approximation and is due to direct illumination of $V(\mathbf{R})$ by the incident wave $\psi_i(\mathbf{r}')$. The second term is the multiple scattering effect because the source term $V(\mathbf{r}')\psi_s(\mathbf{r}')$ is due to the illumination of the scatterer by the scattered wave $\psi_s(\mathbf{r})$, which itself arises from $V(\mathbf{r}')$. Neglecting multiple scattering effects, inserting $\psi_i(\mathbf{r}) = \exp(i\mathbf{k} \cdot \mathbf{r})$ and assuming a stratified medium, i.e. $V(\mathbf{r}') = V(z')$, the above equation becomes

$$\psi_s(\mathbf{r}) = -\frac{1}{4\pi} \int \frac{\exp(ikR)}{R} V(z') \exp(i\mathbf{k} \cdot \mathbf{r}') d^3\mathbf{r}' . \quad (2.30)$$

In the specular direction, outgoing scattered wave vector and incident wave vector make the angle θ with the xy -plane and the scattering plane coincides with the yz -plane (see Fig. 2.5). In the far field the distance R can be approximated as

$$R \approx R_0 - y' \cos \theta + \frac{x'^2 + y'^2 \sin^2 \theta}{2R_0} \quad (2.31)$$

and $R_0 \approx r + z' \sin \theta$. Replacing R by R_0 in the denominator of Eq. (2.30) and by Eq. (2.31) in the numerator, integrating with respect to x' and y' over $(-\infty, \infty)$, one obtains

$$\psi_s(\mathbf{r}) = -\frac{i}{q_z} \exp(i\mathbf{k}\mathbf{r}) \int V(z') \exp(iq_z z') dz' \quad (2.32)$$

where $q_z = 2k \sin \theta$. The reflection coefficient $R(q_z)$ of the surface is equal to the amplitude of the scattered wave $\psi_s(\mathbf{r})$. Thus, in the first order Born approximation the reflectance is proportional to the Fourier transform of the scattering potential with respect to the vertical position z

$$R(q_z) = -\frac{i}{q_z} \int V(z) \exp(iq_z z) dz = \frac{1}{q_z^2} \int \frac{dV(z)}{dz} \exp(iq_z z) dz \quad . \quad (2.33)$$

For x-rays, the complex scattering potential $V(z)$ is given by

$$V(z) = k^2[1 - n^2(z)] \approx 2k^2[\delta(z) - i\beta(z)] \quad . \quad (2.34)$$

If absorption is neglected, $\beta(z) = 0$, $V(z)$ becomes real and can be approximated by $4\pi\rho(z)$. The reflectivity $r(q_z) = |R(q_z)|^2$ is given by

$$r(q_z) = |R(q_z)|^2 = \frac{16\pi^2}{q_z^4} \left| \int \frac{d\rho(z)}{dz} \exp(iq_z z) dz \right|^2 \quad . \quad (2.35)$$

The kinematical approximation can also be derived from the dynamical scattering theory which will be done in the next section.

2.3.2 Derivation from the Parratt formalism

To derive the kinematical approximation from the dynamical theory, we rewrite Parratt's recursion formula, see Eq. (2.11), in a slightly different way:

$$R_j = \frac{r_{j,j+1} + R_{j+1} \exp(-iq_{z,j+1}\Delta z_{j+1})}{1 + r_{j,j+1}R_{j+1} \exp(-iq_{z,j+1}\Delta z_{j+1})} \quad (2.36)$$

$q_{z,j} = 2k_{z,j}$ is the wave vector transfer in the layer j (see Fig. 2.2). The second term in the denominator can be neglected compared to unity and Eq. (2.36) can be approximated with high accuracy by

$$R_j \approx r_{j,j+1} + R_{j+1} \exp(-iq_{z,j+1}\Delta z_{j+1}) \quad . \quad (2.37)$$

The recursion in Eq. (2.37) can be carried out and one obtains for the reflectance at the surface

$$R_0 \approx \sum_{j=1}^{N+1} r_{j,j+1} \exp\left(i \sum_{l=1}^{j-1} q_{z,l} \Delta z_l\right) \quad . \quad (2.38)$$

The Fresnel reflectance at the interface j is given by

$$r_{j,j+1} = \frac{q_{z,j} - q_{z,j+1}}{q_{z,j} + q_{z,j+1}} = \frac{16\pi(\rho_{j+1} - \rho_j)}{(q_{z,j} + q_{z,j+1})^2} \quad (2.39)$$

Inserting Eq. (2.39) in Eq. (2.38) one obtains in the continuous limit, $N \rightarrow \infty$ and $\Delta z_l \rightarrow 0$,

$$R_0 \approx 4\pi \int_{-\infty}^{+\infty} \frac{1}{q_z(z)^2} \frac{d\rho(z)}{dz} \exp\left(i \int_{-\infty}^z q_z(\zeta) d\zeta\right) dz \quad . \quad (2.40)$$

Far away from the region of total external reflection, i.e. $q_z \gg q_c$, the wave vector inside the sample can be approximated by that of the vacuum, $q_z(z) \approx q_z$, and one obtains the reflectance of the entire sample

$$R(q_z) = \frac{4\pi}{q_z^2} \int_{-\infty}^{+\infty} \frac{d\rho(z)}{dz} \exp(iq_z z) dz \quad , \quad (2.41)$$

which is identical to Eq. (2.33) derived from quantum theory.

In the kinematical approximation, the density profile and the reflectance are connected by the Fourier transform, which is a linear transformation. In dynamical theory, their relationship is highly nonlinear and can be described by a Riccati differential equation [171]. The kinematical approximation in the form of Eq. (2.31) is obtained by neglecting multiple scattering and approximating the wave vector inside the sample $k_z(z)$ by that of the vacuum $k_{z,0}$. Each of these omissions corresponds to a source of nonlinearity. The omission of the multiple-scattering term only becomes important, whenever the reflectance is of the order of unity. If, for example, $|R| = 0.5$ then $|R|^2 = 0.25$ and multi-scattering cannot be neglected. But if $|R| = 0.1$, then $|R|^2 = 0.01$ can be neglected compared to unity. This is already the case for wave vector transfers very close to region of total external reflection, i.e. $q_z \approx 1.2 q_c$. The second omission, the assumption of a constant wave vector inside the sample, has a much stronger impact on the quality of the kinematical approximation. The phase-speed of the electromagnetic wave inside the sample is determined by $q_z(z)$ in the exponential term in Eq. (2.40). It depends in a nonlinear fashion on the electron density $\rho(z)$. Thus, by assuming a constant wave speed inside the sample, wavelets reflected from different positions do not overlap with correct phases anymore. In addition, the neglect of the non-linear dependency of the Fresnel reflectance on the electron density results in incorrect amplitudes of the wavelets. The effect of the latter two omissions is important, whenever $(q_c/q_z)^2$ cannot be neglected against unity. To improve the approximation, the wavevector in the exponent may be approximated by a wavevector $\bar{q}_z \approx \int q_z(z) dz$ averaged over the sample. Another improvement is to replace the factor $1/q_{z,0}^2$ by some Fresnel reflectance. If one chooses that of the (usually known) substrate, the reflectivity becomes the widely used form, see

e.g. Refs. [65][109],

$$r(q_z) = r_F(q_z) |F(q_z)|^2 \quad , \quad (2.42)$$

with the complex structure factor

$$F(q_z) = \frac{1}{\varrho_\infty} \int_{-\infty}^{+\infty} \frac{d\varrho(z)}{dz} \exp(iq'_z z) dz \quad . \quad (2.43)$$

where $q'_z = \sqrt{q_z^2 - \bar{q}_z^2}$ and ϱ_∞ is the electron density of the substrate. If the electron density ϱ_{film} at the surface region of the sample differs significantly from that of the substrate, it is, however, more appropriate to choose rather the Fresnel reflectivity of the film instead of that of the substrate and the normalization factor in Eq. (2.43) has to be replaced by $1/\varrho_{film}$ [65].

A density profile consisting of N layers of density ϱ_n and interfaces located at z_n with gaussian roughness σ_n can be expressed as²

$$\varrho(z) = \sum_{n=0}^N \Delta\varrho_n \operatorname{erf}\left(-\frac{z - z_n}{\sqrt{2}\sigma_n}\right) \quad , \quad (2.44)$$

where $\Delta\varrho_n = \varrho_{n-1} - \varrho_n$ and $\operatorname{erf}(z) = \int_0^z \exp(-\zeta^2) d\zeta$. Inserting the derivative with respect to z into Eq. (2.43) yields the structure factor,

$$F(q_z) = \sum_{n=0}^N \frac{\Delta\varrho_n}{\varrho_\infty} \exp(iq_z z_n) \exp(-q_z^2 \sigma_n^2 / 2) \quad , \quad (2.45)$$

with $\varrho_\infty = \sum_n \Delta\varrho_n$. For a single interface, i.e. $N = 0$, Eq. (2.45) reduces to $F(q_z) = \exp(-q_z^2 \sigma^2 / 2)$ and hence $r(q_z) = r_F(q_z) \exp(-q_z^2 \sigma^2)$, which is identical to the result from dynamical theory.

Figure 2.6 shows the density profile $\varrho(z)$ of a substrate with two layers of thickness 150 Å and 90 Å, respectively, on top. The substrate is extended to $+\infty$ and its interface has a roughness of 3 Å. The layer upon has a smaller electron density and the topmost layer has a larger electron density. The roughnesses of their interfaces are 8 Å and 5 Å, respectively. Fig. 2.7 depicts the corresponding reflectivity calculated with the Parratt formalism and within the kinematical approximation. The open circles represent the exact reflectivity calculated with the Parratt formalism. The thin curve is the reflectivity calculated in the kinematical approximation using the free wavevector transfer q_z to approximate the phase-speed inside the sample, i.e. $q' = q_z$ in Eq. (2.43). Around the region of total external reflection, $q_z \approx q_c$, the failure of the kinematical approximation is obvious. The thick curve represents the reflectivity calculated from Eq. (2.43), but

²Here we assume non-overlapping interfaces, i.e. $\exists z \in [z_n, z_{n+1}] | P_n(z) < \epsilon \wedge P_{n+1}(z) < \epsilon \forall n = 0..N - 1$, where $P_n(z)$ denotes the probability distribution of the n th interface. For a detailed discussion of density profiles with over-lapping interfaces see Refs. [155] and [127].

Figure 2.6: Density profile of a substrate with two layers on top. The thicknesses of the layers are 150 Å and 90 Å, respectively. The dashed vertical lines indicate the mean position of the interfaces. The reflectivities calculated with the Parratt formalism and within the kinematical approximation are shown in Figure 2.7.

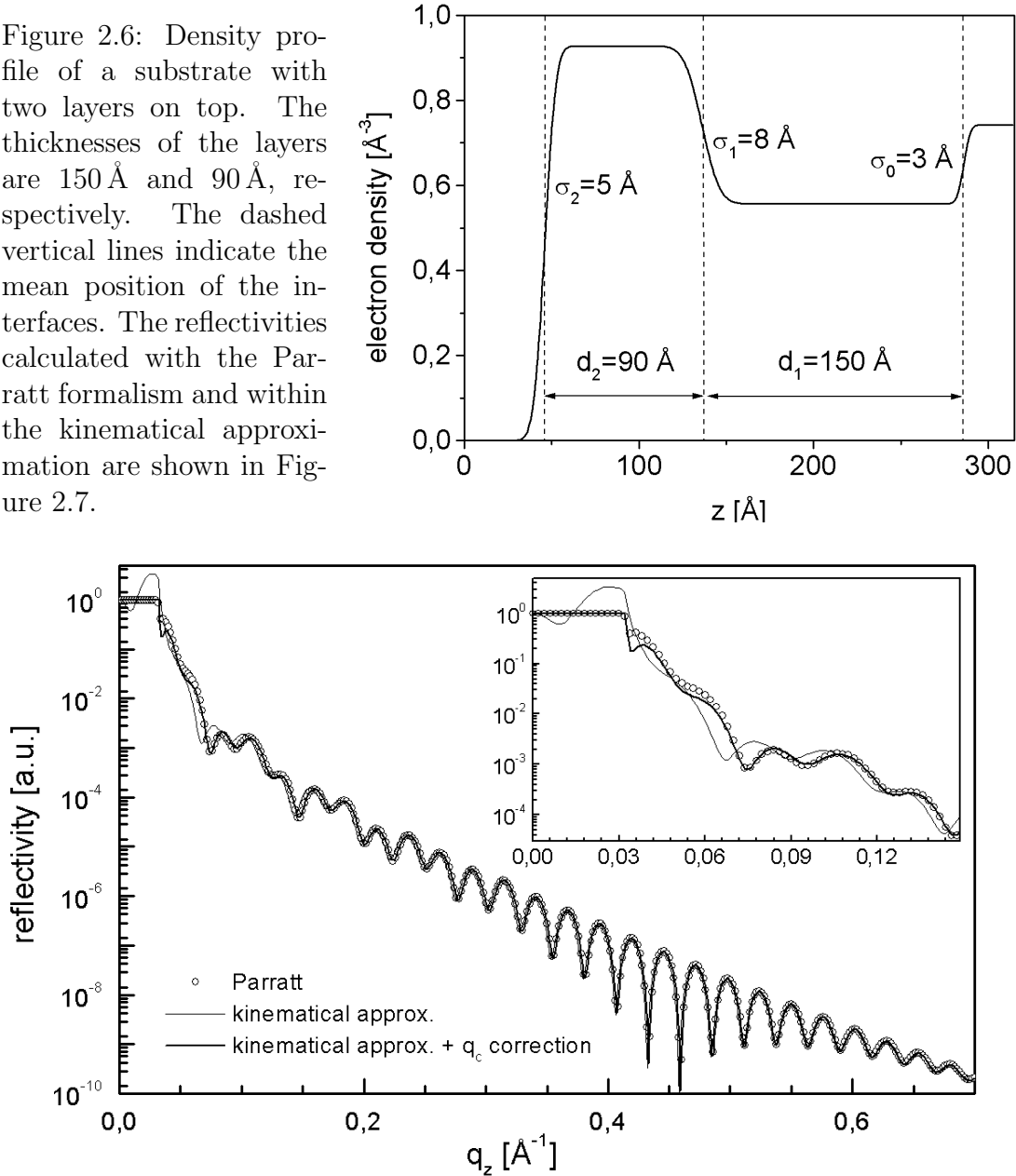


Figure 2.7: Reflectivities of the density profile shown in Fig. 2.6: The open circles represent the exact reflectivity calculated with the Parratt formalism. The two solid lines are the reflectivities calculated in the kinematical approximation from Eq. (2.43) with (thick line) and without (thin line) q -correction. Both curves differ from the true reflectivity in the region of total external reflection (see inset) and are almost indistinguishable at higher q_z -values. The q -correction leads to an improvement of the approximation and the reflectivity agrees well for $q_z \gtrsim 3q_c$.

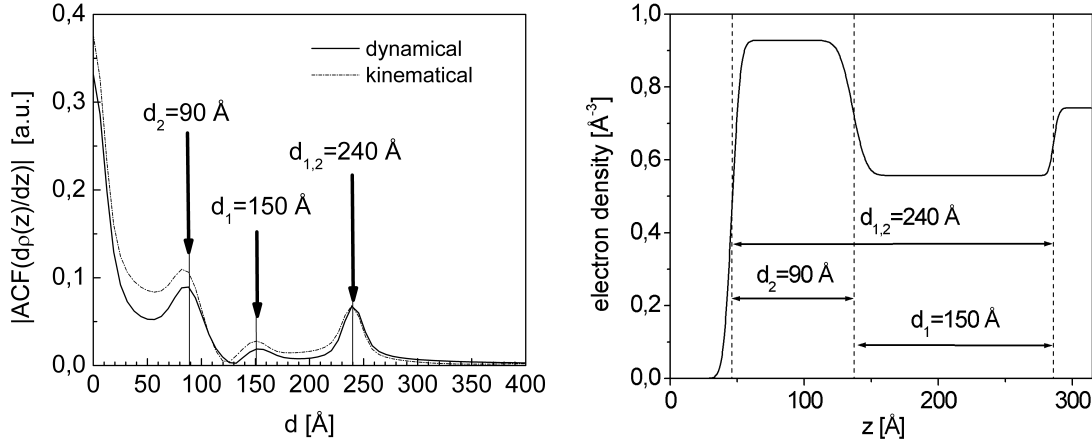


Figure 2.8: Patterson functions of the reflectivities from Fig. 2.7: The thick solid line represents the Patterson function of the exact reflectivity (open circles in Fig. 2.7), the dashed line is the Patterson function obtained from the reflectivity calculated from the density profile within the q -corrected kinematical approximation (solid line in Fig. 2.7). The peaks in the Patterson function correspond to distances between regions of density variations, i.e. the interfaces between the layers (right panel).

with a correction of the exponential term, $q'_z = \sqrt{q_z^2 - q_{c,\infty}^2}$. This leads to a much better agreement with the exact reflectivity at low q_z -values. For $q_z \lesssim (2-3)q_c$ the approximation fails. At high q_z -values, where $(q_c/q_z) \ll 1$, the kinematical approximation coincides almost with the exact reflectivity.

2.4 The Patterson function

From x-ray crystallography it is known that the Fourier transform of the modulus squared of the structure factor $|F(\mathbf{q})|$ is proportional to the autocorrelation function of the density distribution in 3D-space [106]. For x-ray reflectivities the one-dimensional *Patterson* function $P^{1D}(d)$ is obtained from the normalized reflectivity $r(q_z)/r_F(q_z) = |F(q_z)|^2$,

$$\begin{aligned} P^{1D}(d) &= \int_{-\infty}^{+\infty} \frac{r(q_z)}{r_F(q_z)} \exp(-iq_z d) dq_z \\ &= \int_{-\infty}^{+\infty} |F(q_z)|^2 \exp(-iq_z d) dq_z \end{aligned} \quad (2.46)$$

$$= \frac{1}{\rho_\infty^2} \int_{-\infty}^{+\infty} \frac{d\rho(\zeta)}{d\zeta} \frac{d\rho(\zeta+d)}{d\zeta} d\zeta \quad , \quad (2.47)$$

where the equality of Eqs. (2.46) and (2.47) follows from the Wiener-Khinchin Theorem and the symmetry of the structure factor, $F(-q) = F(q)^*$. To account

for the non-linearity effects discussed in previous section it is preferable to use

$$P^{1D}(d) = \int_{-\infty}^{+\infty} \frac{r(q')}{r_F(q')} \exp(-iq_z d) dq_z \quad , \quad (2.48)$$

with the corrected wave vector transfer $q' = \sqrt{q_z^2 + q_c^2}$. Since the corrected kinematical approximation fails for small values of q_z , the Patterson function calculated from Eq. (2.49) is disturbed by long periodical oscillations and one considers the modulus $|P^{1D}(d)|$ [25][26] instead, i.e. the power spectral density.

For the N -layer system defined by Eq. (2.44) the Patterson function is given by [25][26]

$$P^{1D}(d) = \sum_k \sum_l \frac{\Delta \varrho_k \Delta \varrho_l}{\sigma_{k,l}} \exp \left[\frac{-(d - d_{k,l})^2}{\sigma_{k,l}^2} \right] \quad , \quad (2.49)$$

with $d_{k,l} = z_k - z_l$ and $\sigma_{k,l} = \sqrt{\sigma_k^2 + \sigma_l^2}$. If only the modulus $|P^{1D}(d)|$ is considered, the sign of $\Delta \varrho_k \Delta \varrho_l$ gets lost. Figure 2.8 shows the Patterson functions calculated from the reflectivities in Fig. 2.7. The solid line represents that of the kinematical approximation (cf. Eq. (2.43)). The thin line is obtained from the exact reflectivity. The positions of the three Gaussian peaks correspond to distances of the interfaces in the density profile (right panel). By inspecting the width and height of the peaks one may extract further information about the density profile, but the sample structure itself cannot be obtained.

The Patterson function is intensively used in the analysis of reflectivities from soft-matter films, see e.g. Refs. [133][146][164][169], where the kinematical approximation is sufficiently accurate. It also became a powerful analysis method for low density-contrast systems [128]. Recently, a modified version of the Patterson function was proposed [63] in order to determine the interfacial distances more precisely. Furthermore, the use of window functions and wavelets may be used to gain additional information on the layer-stacking as proposed in Refs. [114][138][139][141].

2.5 The phase problem

The measurable quantity in x-ray scattering experiments is the magnitude of the reflection coefficient $r(q_z) = R^*(q_z)R(q_z)$. An unambiguous determination of the density profile from a single measurement is only possible if the complex reflection coefficient $R(q_z)$, i.e. its modulus $|R(q_z)| = \sqrt{r(q_z)}$ and its phase are known.

This is illustrated in Figure 2.9, where the two different density profiles (right panel) result in almost identical reflectivities (left panel). The small difference at low q_z -values (see circle) is due to dynamical scattering effects. Within the kinematical approximation, the modulus of the respective structure factors are identical.

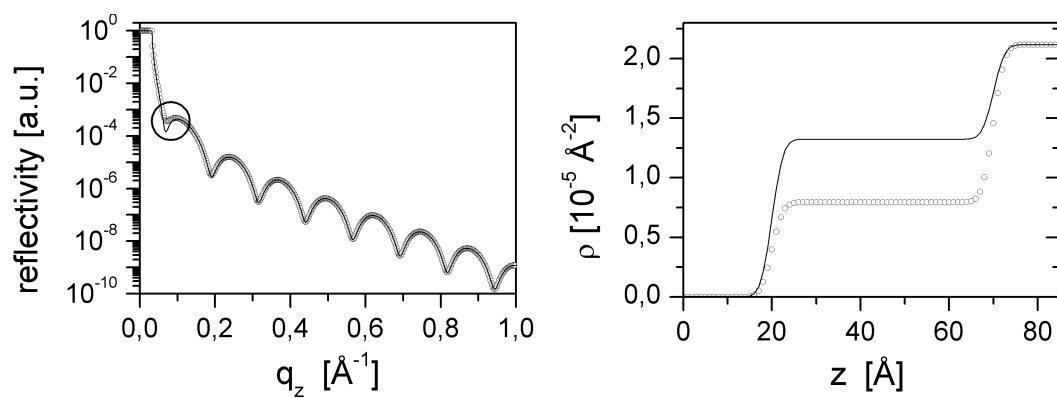


Figure 2.9: Left panel: Reflectivities of the density profiles shown in the right panel. They differ at small q_z -values (see circle) but coincide at large q_z -values. In kinematical approximation, both reflectivities are identical.

Chapter 3

Analytical properties of the reflection coefficient

In this chapter the analytical properties of the complex reflection coefficient $R(q)$ are reviewed. These properties impose, that $R(q)$ is completely known up to the sign of the imaginary parts of its zeros in the complex plane. Furthermore, when the density profile fulfills certain criteria, then the phase of $R(q)$ is equal to the so-called *Hilbert phase* which is completely determined by reflectivity. These criteria will be discussed and formula for the calculation of the Hilbert phase will be derived. Illustrative examples will be given.

In the following, the reflection coefficient $R(q)$ is regarded as a function of the complex wavevector transfer $q = q_z + i\kappa$.

3.1 The Hilbert phase

3.1.1 The Kramers-Kronig relations

If a complex function $\gamma(q) = \alpha(q) + i\beta(q)$ is analytical, the Cauchy-Riemann equations $\partial\alpha/\partial q_z = \partial\beta/\partial\kappa$ and $\partial\alpha/\partial\kappa = -\partial\beta/\partial q_z$ hold and in the upper half complex plane (UHP) the Cauchy Principal Value theorem,

$$\oint_C \frac{\gamma(\zeta)}{q - \zeta} d\zeta = 0 \quad , \quad (3.1)$$

is valid. If furthermore $\lim_{|q| \rightarrow \infty} \gamma(q) = 0$, then $\alpha(q)$ and $\beta(q)$ are not independent from each other but connected by the Kramers-Kronig relations,

$$\alpha(q) = -\frac{1}{\pi} \text{P.V.} \int_{-\infty}^{+\infty} \frac{\beta(\zeta)}{q - \zeta} d\zeta \quad \beta(q) = \frac{1}{\pi} \text{P.V.} \int_{-\infty}^{+\infty} \frac{\alpha(\zeta)}{q - \zeta} d\zeta \quad , \quad (3.2)$$

for $q \in \mathbb{R}$. P.V. denotes the principle value of the respective integral. Thus, if $\alpha(q)$ is known on the entire real q -axis, $\beta(q)$ may be obtained from Eq. (3.2) and

vice versa.

The analyticity of the reflection coefficient $R(q)$ follows from the Titchmarsh theorem [28][101][154] which states that a function is analytic in the UHP if its Fourier transform is zero on some domain on the real axis. If one chooses the origin of the z -axis in real space such that $V(z) \equiv 0$ for $z < 0$, then in kinematical theory the analyticity of the structure factor $F(q)$ follows immediately from the fact that $d\rho(z)/dz$ vanishes for $z < 0$. In dynamical scattering theory, the reflection coefficient $R(q)$ is analytic in the UHP since the impulse response function $g(t) = \int R(q) \exp(iqt) dq$ vanishes for $t < 0$, see e.g. [73][122].

3.1.2 Derivation of the Hilbert Phase

If $R(q)$ is analytic in the UHP, then $\ln R(q)$ is also analytic except where $R(q) = 0$. From

$$\ln R(q) = \frac{1}{2} \ln r(q) + i\phi(q) \quad , \quad (3.3)$$

we see, that the reflectivity $r(q)$ and the phase ϕ appear separately in the real part and imaginary part of $\ln R(q)$, respectively. However, Eqs. (3.2) do not apply for $\ln r(q)$ since $r(q) \rightarrow 0$ for $r(q) \rightarrow \infty$, and thus $\ln r(q) \rightarrow -\infty$. Instead, one considers the quantity $[\ln R(q) - \ln R(0)]/q$ for which a once-subtracted dispersion relation, see e.g. [28][73][148][156],

$$\phi(q_z) = \phi(0) - \frac{q_z}{2\pi} \text{P.V.} \int_{-\infty}^{+\infty} \frac{\ln r(q')}{q'(q' - q_z)} dq' \quad , \quad (3.4)$$

can be derived. If the reflection coefficient $R(q)$ has zeros in the UHP, one can still calculate the integral (3.4) along the real q -axis and obtains the so-called *Hilbert phase*,

$$\phi_H(q_z) = \phi(0) - \frac{q_z}{2\pi} \text{P.V.} \int_{-\infty}^{+\infty} \frac{\ln r(q')}{q'(q' - q_z)} dq' \quad , \quad (3.5)$$

which is not identical with the phase $\phi(q)$ of $R(q)$, but differs from it by the contribution of the zeros. By adding the identity

$$\frac{q}{2\pi} \text{P.V.} \int_{-\infty}^{+\infty} \frac{\ln r(q')}{q'(q' - q)} dq' = 0 \quad (3.6)$$

to the right hand-side of Eq. (3.5) and assuming real potentials, which implies $r(-q) = r(q)$, the Hilbert phase becomes

$$\phi_H(q_z) = \phi(0) - \frac{q_z}{\pi} \int_0^{+\infty} \frac{\ln r(q') - \ln r(q_z)}{q'^2 - q_z^2} dq' \quad (3.7)$$

and can be calculated from the reflectivity $r(q_z)$, which is known only for $q_z > 0$. If $r(q)$ is differentiable at some $q \in \mathbb{R}$, the singularity of the integrand in Eq. (3.7) at $q' = q_z$ is removable with the limiting value

$$\lim_{q' \rightarrow q_z} \frac{\ln r(q') - \ln r(q_z)}{q'^2 - q_z^2} = \frac{1}{2q_z} \frac{r'(q_z)}{r(q_z)} . \quad (3.8)$$

In the kinematical approximation the same arguments hold for the complex structure factor $F(q_z)$. Noting that $\phi(0)$ is equal to zero¹, since $F(0) = 1$, the Hilbert phase is given by [37]:

$$\phi_H(q_z) = -\frac{2q_z}{\pi} \int_0^{+\infty} \frac{\ln |F(q')| - \ln |F(q_z)|}{q'^2 - q_z^2} dq' . \quad (3.9)$$

For the rest of the chapter we restrict ourselves, if not mentioned explicitly, to the kinematical theory, which we will use later on. The reflection coefficient $R(q)$ has the same analytic properties as the structure factor $F(q)$, since $R(q) = R_F(q)F(q)$ and the Fresnel coefficient $R_F(q)$ is an analytic function with no zeros in the UHP. Finally it should be mentioned that the same results may be obtained for the reflection coefficient $R(q)$ within the dynamical scattering theory.

3.1.3 Computation of the Hilbert phase

For real potentials the calculation of the Hilbert phase $\phi_H(q_z)$ requires the knowledge of $r(q_z)$ on the entire left q_z -axis. In reality $r(q_z)$ can only be measured over a finite interval $0 < q_z < q_{max}$. This is due to diffuse scattering and the limited dynamical range of the experimental setup. Thus, Eq. (3.9) has to be rewritten as

$$\phi_H(q_z) = -\frac{q_z}{\pi} \int_0^{q_{max}} \frac{\ln r(q') - \ln r(q_z)}{q'^2 - q_z^2} dq' + \Delta\Phi_H(q_z, q_{max}) , \quad (3.10)$$

where the first term can be calculated from a measured reflectivity $r(q_z)$ and $\Delta\Phi_H(q_z, q_{max})$ is the not available contribution of $r(q_z)$ with $q_z > q_{max}$ to the Hilbert phase $\phi_H(q_z)$.

If the N -th derivative of the potential $V(z)$ has a discontinuity at $z = 0$, i.e. $V(0) = V'(0) = \dots = V^{(N-1)}(0) = 0$ and $V_N = \lim_{z \rightarrow +0} V^{(N)}(z)$, the asymptotic behavior is given by [74][122]:

$$r(q_z) \rightarrow \frac{V_N}{16q_z^{2N+4}} \quad \text{for } q_z \rightarrow +\infty , \quad (3.11)$$

which reduces to $r(q_z) \rightarrow V(0)/q_z^4$ for an ideal surface, i.e. $N = 0$. Assuming an asymptotic behavior given by Eq. (3.11) with $N = 0$, it was proposed [115][117]

¹In dynamical theory we have $R(0) = -1$ and hence $\phi(0) = -\pi$.

to compute the Hilbert phase of the reflectivity $r(q_z)$ given on $[0, q_{max}]$ via

$$\begin{aligned}
\phi_H(q_z) &= -\pi - \frac{q_z}{\pi} \int_0^{q_z+\epsilon} \frac{\ln r(q') - r(q_z)}{q'^2 - q_z^2} dq' - \frac{q_z}{\pi} \int_{q_z+\epsilon}^{q_{max}} \frac{\ln r(q')}{q'^2 - q_z^2} dq' \\
&+ \frac{1}{2\pi} \ln r(q_z) \ln \frac{2q_z + \epsilon}{\epsilon} - \frac{1}{\pi} \ln \frac{V_0}{4} \ln \frac{q_{max} + q}{q_{max} - q} \\
&+ \frac{4q_z}{\pi q_{max}} \left[\ln q_{max} \left(1 + \frac{q_z^2}{3q_{max}^2} \right) + \left(1 + \frac{q_z^2}{9q_{max}^2} \right) \right] , \quad (3.12)
\end{aligned}$$

where ϵ is some small positive number. The last term stems from a series expansion of the integral $\int \ln(q')/(q'^2 - q_z^2) dq'$. V_0 is not equal to $V(0)$ in Eq. (3.11) but it is estimated from the last data of the reflectivity $r(q_{max})$ instead to avoid a singularity at q_{max} .

If we calculate ϕ_H within the kinematical approximation, the extrapolation $r(q_z) \rightarrow 1/q_z^4$ does not lead to an improvement since $\ln |r(q_z)/r_F(q_z)| \rightarrow 0$. A first improvement of Eq. (3.12) can be achieved by replacing $r(q_z)$ by $r_F(q_z)f(q_z)$,

$$\begin{aligned}
\phi_H(q_z) &= -\pi - \frac{q_z}{\pi} \int_0^{q_{max}} \frac{\ln |r_F(q_z)f(q_z)| - \ln |r_F(q_z)f(q_z)|}{q'^2 - q_z^2} dq' \\
&= \phi_F(q_z) - \frac{q_z}{\pi} \int_0^{q_{max}} \frac{\ln |f(q')/f(q_z)|}{q'^2 - q_z^2} dq' \quad (3.13)
\end{aligned}$$

Since $\phi_F(q_z) = \arg\{R_F(q_z)\}$ is known exactly, the last two terms of Eq. (3.12) are replaced by the correct result. Nevertheless, Eq. (3.13) and Eq. (3.12) do obviously not apply to real samples with rough interfaces (see Section 2.2.2). For a surface with roughness σ of Gaussian type, the asymptotic behavior is given by $r(q_z) = r_F(q_z) \exp(-q_z^2 \sigma^2)$ which is not equal to Eq. (3.11). For a density profile consisting of N layers with interfaces located at z_n and Gaussian roughness σ_n and density contrasts $\Delta \varrho_n = \varrho_n - \varrho_{n-1}$, the structure factor is given by Eq. (2.45) :

$$F(q_z) = \sum_{n=0}^N \frac{\Delta \varrho_n}{\varrho_\infty} \exp(iq_z \bar{z}_n) \exp(-q_z^2 \sigma_n^2 / 2) \quad . \quad (3.14)$$

If there exist an interface such that $\sigma_j < \sigma_n$ for $j \neq n$, then the asymptotic behavior of $|F(q_z)|$ is given by

$$|F(q_z)| = C \exp(-q_z^2 \sigma_j^2 / 2) \quad \text{for } q_z \rightarrow +\infty \quad , \quad (3.15)$$

with the constant $C \in \mathbb{R}^+$. If $|F(q_z)|$ is known up q_{max} and we assume the above asymptotic behavior, we get:

$$\begin{aligned} \phi_H(q_z) = & - \frac{2q_z}{\pi} \int_0^{q_{max}} \frac{\ln |F(q')| - \ln |F(q_z)|}{q'^2 - q_z^2} dq' \\ & + 2q_z \frac{\ln |F(q_z)| - \ln C}{\pi} \int_{q_{max}}^{\infty} \frac{1}{q'^2 - q_z^2} dq' \\ & + \frac{\sigma_j^2}{\pi} q_z \int_{q_{max}}^{\infty} \frac{q'^2}{q'^2 - q_z^2} dq' \quad , \end{aligned} \quad (3.16)$$

where the last integral diverges since the integrand approaches unity with increasing q' . This can be explained in different ways: First, we have a violation of the causality condition since the probability distribution $P(z) \propto \text{erf}(z/\sqrt{2}\sigma)$ is not vanishing on a half-line². Consequently, the profile has no compact support and be made causal by a translation of the origin. Second, the Kramers-Kronig relations (see Eq. (3.2)) are not valid any more, because $\ln |F(q)|/|q|$ does not vanish for $|q| \rightarrow \infty$. A detailed mathematical discussion of the logarithmic dispersion relation in case of functions having non-causal Fourier transforms is given in Refs. [28] and [156]. However, if one considers the above integral for finite limits of integration a and b , one finds

$$q_z \int_a^b \frac{q'^2}{q'^2 - q_z^2} dq' = q_z(b - a) + \frac{q_z^2}{2} \left[\ln \left(\frac{a + q_z}{a - q_z} \right) + \ln \left(\frac{b - q_z}{b + q_z} \right) \right] \quad . \quad (3.17)$$

The divergence of the integral is caused by the linear term $q_z b$, which can be eliminated by redefining the origin of the sample system. The limit $b \rightarrow \infty$ is problematic and actually requires to calculate the Hilbert phase in a slightly different manner. However, here we drop $q_z b$, since the spatial extent of real samples is always limited. In practice, the causality can always be enforced by simply cutting the sample when the density at the surface reaches a certain lower limit ϵ , even if the interface distribution functions have no compact support. Insertion into Eq. (3.16) with $b = +\infty$ yields

$$\begin{aligned} \phi_H(q_z) = & - \frac{2q_z}{\pi} \int_0^{q_{max}} \frac{\ln |F(q')| - \ln |F(q_z)|}{q'^2 - q_z^2} dq' - \frac{\sigma_j^2 q_{max}}{\pi} q_z \\ & + \frac{1}{\pi} \left[\ln |F(q_z)| - \ln C + \frac{\sigma_j^2 q_z^2}{2} \right] \ln \frac{q_{max} + q_z}{q_{max} - q_z} \quad . \end{aligned} \quad (3.18)$$

The last term of the above equation needs to be discussed in further detail: Obviously the last logarithmic term has a singularity at $q_z = q_{max}$. Since the first two terms do not diverge at q_{max} , the whole last term must be bounded. This means that the sum has to approach zero for $q_z \rightarrow q_{max}$. Unfortunately, the first

²For $\sigma \rightarrow 0$ one has $\text{erf}(z/\sqrt{2}\sigma) \rightarrow z/|z|$ and the system becomes causal again.

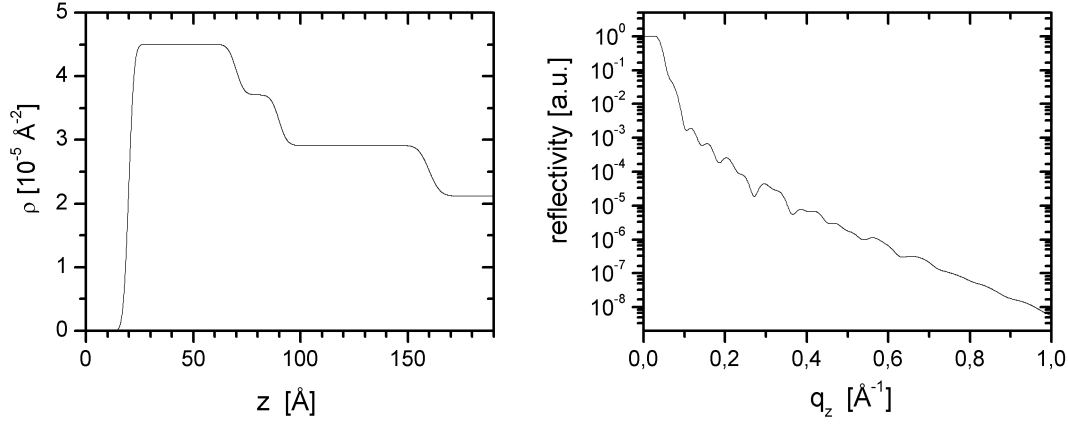


Figure 3.1: Density profile (left side) and the corresponding reflectivity (right side). The roughness of the surface is 2\AA , that of the internal interfaces 4\AA . At higher q_z values the scattering from the surface dominates the reflectivity.

term has two unknowns, C and σ . Let us assume that we are not able to estimate C since it is related to the density contrast of the (unknown) sample structure. If we can estimate σ from the reflectivity, we obtain $C = |F(q_{max})| \exp[\sigma^2 q_{max}^2/2]$ and Eq. (3.18) becomes,

$$\begin{aligned} \phi_H(q_z) = & - \frac{2q_z}{\pi} \int_0^{q_{max}} \frac{\ln |F(q')| - \ln |F(q_z)|}{q'^2 - q_z^2} dq' - \frac{\sigma_j^2}{\pi} q_z q_{max} \quad (3.19) \\ & + \frac{1}{\pi} \left[\ln \frac{|F(q_z)|}{|F(q_{max})|} + \frac{\sigma_j^2}{2} (q_z^2 - q_{max}^2) \right] \ln \frac{q_{max} + q_z}{q_{max} - q_z} . \end{aligned}$$

where the last term vanishes at q_{max} . Inspecting the above equation, we see that σ enters in quadratic form. Hence, the estimation of σ has to be done as precisely as possible and an underestimation of σ will lead to smaller errors than an overestimation.

Figure 3.1 shows a density profile and the corresponding reflectivity. The roughness of all interior interfaces is larger than that of the surface ($\sigma = 2\text{\AA}$). Thus, the asymptotic behavior of the reflectivity is given by the Fresnel reflectivity of the surface and may be estimated by fitting a straight line to $\ln[r(q_z)q_z^4]$ plotted against q_z^2 . Then the slope of the line at large q_z -values is equal to $-\sigma^2$. For the present example above the procedure yields $\sigma \approx 1.98\text{\AA}$, which is close to the exact value. This is shown in the right panel of Figure 3.2. The left panel of 3.2 depicts the Hilbert phase calculated within the different approximations and the exact phase (full line) of the reflection coefficient. An additional phase-shift $\Delta\phi = q_z\Delta z$ was added to the calculated phases to achieve a good agreement in the low q_z -region. For clarity the uppermost and the lowermost phases are shifted by $\pi/2$ and $-\pi/2$, respectively. For the topmost Hilbert phase (open triangles) no extrapolation was used, which corresponds to calculating of the first integral

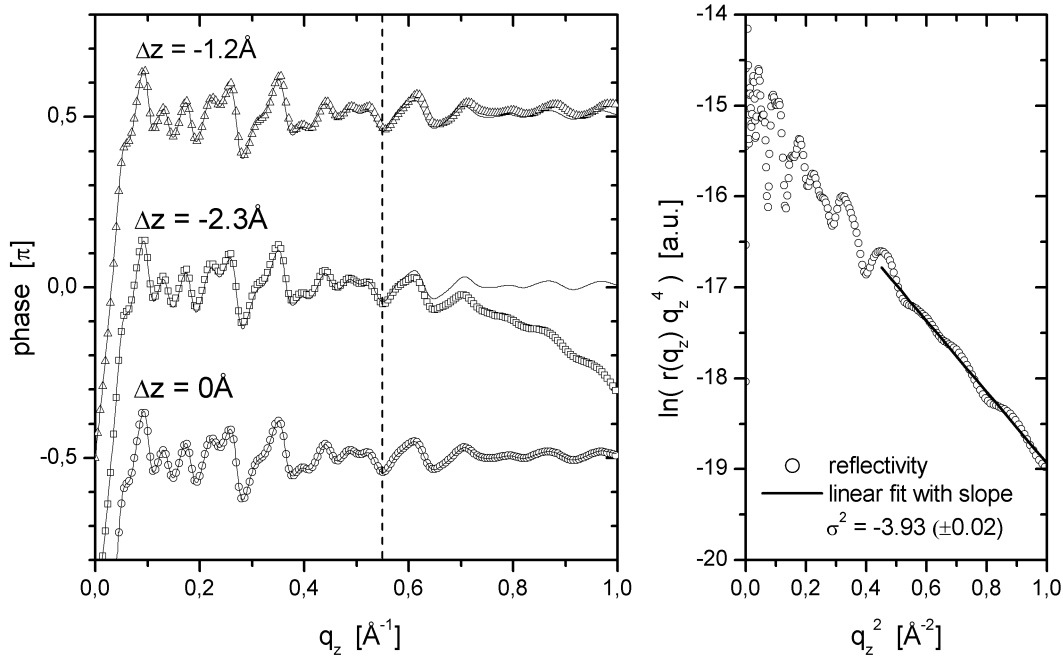


Figure 3.2: The left panel shows Hilbert phases calculated from the reflectivity presented in Fig. 3.1 assuming different asymptotic behavior for $q_z \rightarrow \infty$. The curves are shifted by $\pi/2$ for clarity. The thin line is the exact Hilbert phase. An almost perfect agreement with the exact phase is obtained by extrapolation of the reflectivity with $r(q_z) = r_F(q_z) \exp(-\sigma^2 q_z^2)$ (open circles). The value for σ was obtained by fitting a straight line to $\ln[r(q_z)q_z^4]$ plotted against q_z^2 as shown in the right panel. The Δz values give the offset $\Delta z q_z$ that was used to obtain a good agreement with the exact phase at low q_z values.

of Eq. (3.19). Compared to the exact phase, the *overall* agreement is pretty good. However, differences appear already for $q_z < 0.3 \text{ \AA}^{-1}$ and with increasing q_z the frequency of the phase oscillations decreases. The second Hilbert phase (open squares) is obtained from Eq. (3.19) with $\sigma = 0 \text{ \AA}$, which in principle corresponds to Eq. (3.12). The phase is almost identical to the exact phase up to $q_z \approx 0.5 \text{ \AA}^{-1}$, but deviates from the exact phase with increasing q_z . Finally, the lowest Hilbert phase (open circles) is calculated using Eq. (3.19) with $\sigma \approx 2 \text{ \AA}$, as obtained from the reflectivity. Both phases are virtually identical over the whole q_z -region. Additionally, no phase-shift is required compared to the exact phase, which means that the origin is set to the mean position of the surface. If we are not able to estimate σ , we have to set $\ln C - \sigma^2 q_z^2/2 = \ln |F(q_{max})|$ and the second term has to be dropped, too. In this case the phase can be calculated using the above equation with $\sigma = 0$.

Figure 3.3 shows a density profile almost identical to that in Figure 3.1. The only difference is that all interfaces have an identical roughness of $\sigma = 2 \text{ \AA}$. Con-

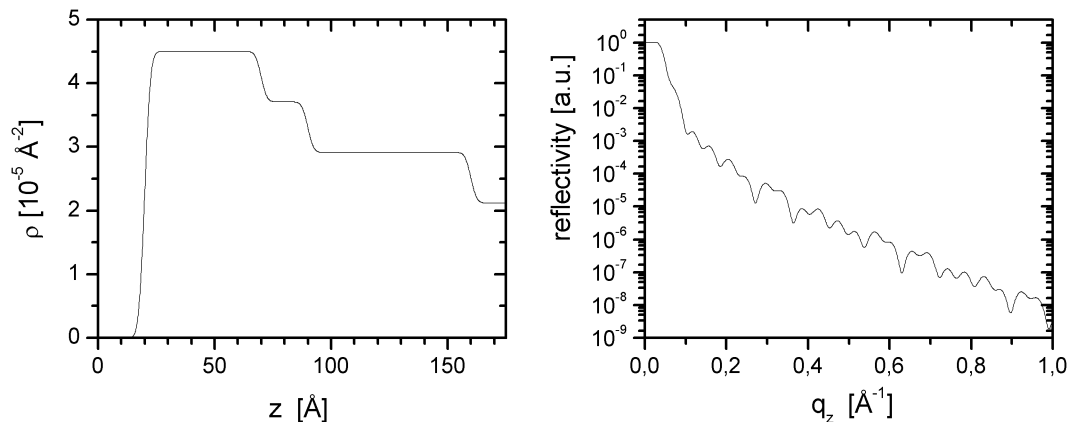


Figure 3.3: Density profile (left side) and the corresponding reflectivity (right side). In comparison to the profile shown in Fig. 3.1, the surface and the interior interfaces have the same roughness of 2\AA . Hence, all interfaces contribute to the reflectivity over the whole q_z range.

sequently, the corresponding reflectivity (right panel of Fig. 3.3) has strong oscillations over the whole q_z -range and an estimation of the asymptotic behavior is not possible. Figure 3.4 depicts the Hilbert phases calculated using the different approximations and, since σ is unknown, for different values of σ . Again, the exact phase is shown as a full line. The curves are shifted by π for clarity and a phase-shift was added to the calculated phases so that they match the exact phase in the low q_z region. The lowest phase (filled triangles) is calculated using no extrapolation at all. As in the previous example, the *overall* agreement with the exact phase is pretty good and the deviation close to q_{max} becomes significant. The other five Hilbert phases (open symbols) are obtained from Eq. (3.19) using the σ values and the linear phase shifts $q_z\Delta z$ specified in the figure. The phase calculated for $\sigma = 2\text{\AA}$ (crosses) agrees perfectly with the exact phase up to $\approx 0.9\text{\AA}$ and differs very little at higher q_z -values. The other phases (open symbols) also agree very well except for the bending away at higher q_z -values due to the terms in Eq. (3.19) containing σ . To give an impression on how precisely one may estimate σ without any detailed analysis, e.g. the fitting procedure described above, Figure 3.5 depicts the reflectivity together with a series of reflectivities from a single rough interface³ (dotted lines). From the brief inspection by eye, one obtains $\sigma \approx 1\text{\AA} - 3\text{\AA}$. A comparison of the corresponding phases shows that the Hilbert phase can be calculated precisely only up to some fraction of q_{max} as indicated by the vertical line in Figure 3.4.

In practice, it may be difficult to estimate the roughness of the sharpest interface whenever strong oscillations are present in the high q_z -region of the reflectivity-

³The critical wave-vector transfer q_c of the Fresnel reflectivity was roughly estimated from $r(q_c) = 0.5$.

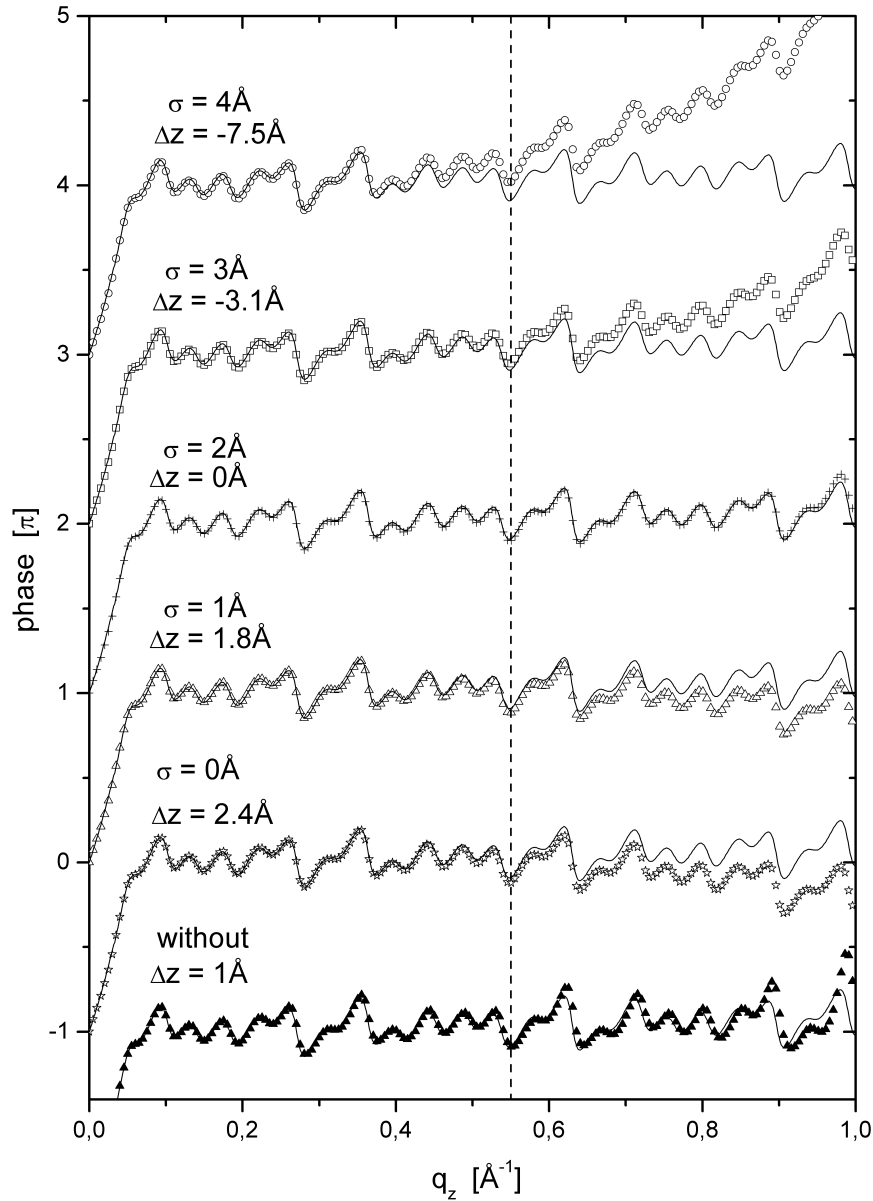
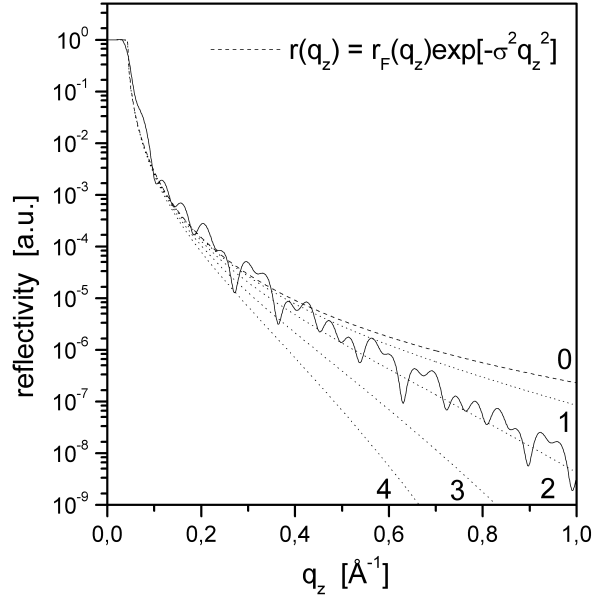


Figure 3.4: Hilbert phases calculated from the reflectivity of Fig.3.3: The exact Hilbert phase is given by the full line. The curves are shifted by π for clarity. The lowest phase (filled triangle) was calculated without any extrapolation of the reflectivity. For the five upper phases (open symbols) the reflectivity was extrapolated by $\exp(-\sigma^2 q_z^2)$ using the σ values given in the figure. For $\sigma = 2\text{\AA}$ the agreement with the exact phase is very good. Small deviations appear only close to q_{max} . If σ is chosen too high, the calculated phases differ considerably from the exact phase at higher q_z values. When σ is underestimated, the error is less pronounced. Δz is the phase offset $\Delta z q_z$ that was added to make the phases fit to the exact solution in the low q_z region.

Figure 3.5: Reflectivity of the system from Fig.3.3 (full line) and reflectivities from a single rough interface of gaussian type (dotted lines). The Fresnel reflectivity ($\sigma = 0$) is given by the dashed line. The roughness for the extrapolation of the reflectivity can be estimated to lie between 1\AA and 3\AA (see numbers at the dotted lines).



ity. Additional difficulties arise from diffuse scattering and counting statistics as present in measured reflectivities.

Throughout this section, it was assumed that the structure factor $F(q_z)$ has no zeros in the UHP and so, that $\ln F(q_z)$ is analytical in the UHP. The case of zeros in the UHP is subject of the next section.

3.2 Zeros of the complex reflection coefficient

The Paley-Wiener theorem [102] states that if $f(t)$ is a function with $f(t) \equiv 0$ for $t \notin [a, b]$ then its Fourier transform $F(x)$ is an entire function of exponential type. This applies to the structure factor $F(q)$, whose Fourier transform $d\rho(z)/dz$ vanishes in the vacuum and in the substrate, respectively. Since entire functions of exponential type are the simplest generalization of polynomials they can be represented by their zeros (Hadamard factorization theorem), see e.g. [67][121]. If the structure factor $F(q)$ has zeros $\{a_1, \dots, a_N\}$ in the upper half plane, it can be written as [153]

$$F(q) = F_H(q)B(q) \quad (3.20)$$

where $F_H(q) = |F(q)| \exp[i\phi_H(q)]$ and $B(q)$ is the so-called Blaschke product given by

$$B(q) = \prod_{j=1}^N \frac{q - a_j}{q - a_j^*} \quad (3.21)$$

For real potentials the Friedel relation

$$F^*(q) = F(-q^*) \quad (3.22)$$

holds, which reduces to $F(-q_z) = F^*(q_z)$ on the real axis, i.e. $\kappa = 0$. Then the zeros occur in pairs $(a_j, -a_j^*)$ and the Blaschke product becomes

$$B(q) = \prod_{j=1}^N \frac{q - a_j}{q - a_j^*} \frac{q + a_j^*}{q + a_j} . \quad (3.23)$$

The phase $\phi(q) = i \ln [F(q)/|F(q)|]$ is then given by

$$\phi(q) = \phi_H(q) + 2 \sum_{j=1}^N \arccos \left(\frac{2q_z \Im\{a_j\}}{q_z^2 - |a_j|^2} \right) , \quad (3.24)$$

where $\Im\{a_j\}$ denotes the imaginary part of a_j . Eq.(3.24) shows that a zero a_j in the UHP results in a shift of the phase $\phi(q)$ by 2π around $q = a_j$.

3.2.1 Zeroless reflection coefficients

The discussion in the previous section has shown that the phase of the reflection coefficient $R(q_z)$ is completely determined by the reflectivity $r(q_z)$ if $R(q_z)$ has no zeros in the upper half complex plane. The interesting question comes up whether one can formulate sufficient conditions for the potential $\rho(z)$ to have a zeroless reflection coefficient $R(q)$.

Single layer on a substrate

Let us consider the simple example of one layer of thickness d on a substrate. In the kinematical approximation, the structure factor $F(q)$ is given by

$$F(q) = \Delta\rho_0 \exp(-\sigma_0^2 q^2/2) + \Delta\rho_1 \exp(iqd) \exp(-\sigma_1^2 q^2/2) , \quad (3.25)$$

where $q = q_z + i\kappa$ is the analytical extension to the complex plane. σ_0 and σ_1 are the roughness of the surface and the substrate interface, respectively. $\Delta\rho_0$ and $\Delta\rho_1$ denote the density contrasts at the interfaces – given in units of ρ_∞ . At a zero, we have $F(q) = 0$ and thus:

$$\exp(-iqd) = -b \exp(aq^2) , \quad (3.26)$$

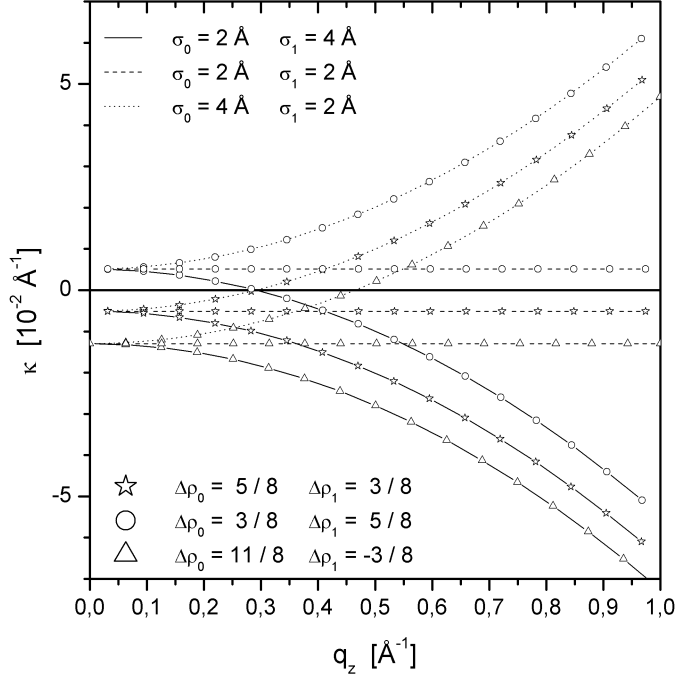
where $a := -\frac{1}{2}(\sigma_0^2 - \sigma_1^2)$ and $b := \Delta\rho_0/\Delta\rho_1$. Insertion of $q = q_z + i\kappa$ and separating real and imaginary parts yields,

$$\exp(iq_z d + 2i a \kappa q_z) = -b \exp[a(q_z^2 - \kappa^2) - \kappa d] . \quad (3.27)$$

From the imaginary part, i.e. $\sin(q_z d + 2a\kappa q_z) = 0$, we get

$$q_z = n \frac{\pi}{d + 2a\kappa} \quad \text{with } n \in \mathbb{Z} , \quad (3.28)$$

Figure 3.6: Zeros of the structure factor $F(Q)$ for a 100Å film of density $\Delta\rho_0$ on top of a substrate with density $\rho_\infty = \Delta\rho_0 + \Delta\rho_1 \equiv 1$. The roughness of the surface and of the inner interface are σ_0 and σ_1 , respectively. Zeros are located in the UHP when $\Delta\rho_0 < \Delta\rho_1$ or $\sigma_0 > \sigma_1$.



which being inserted into the real part of Eq. 3.27, leads to

$$(-1)^n = -b \exp[a(q_z^2 - \kappa^2) - \kappa d] \quad . \quad (3.29)$$

The modulus of Eq. (3.27) results in

$$\ln |b| = a(\kappa^2 - q_z^2) + \kappa d \quad . \quad (3.30)$$

From the latter equation we see immediately that the zeros are located on a hyperbola symmetric to the imaginary axis. From Eq. (3.29) follows that if $\Delta\rho_1 < 0$, that is the density of the layer is higher than that of the substrate, then $b < 0$ and Eq. (3.29) is only fulfilled for n even, whereas $b > 0$ leads to n odd. The q_z position of the zeros depends in a non-linear manner on the imaginary part if $a \neq 0$.

To have no zeros in the UHP, two conditions must be fulfilled: First, the hyperbola must be opened towards the LHP. This is the case whenever $a < 0$, i.e. $\sigma_0 < \sigma_1$ holds. Second, the maximum of the hyperbola at $q_z = 0$ must be located in the LHP, which is the case for $a \ln |b| > 0$. Since $a < 0$ we have $\ln |b| < 0$ and hence $\Delta\rho_0 > \Delta\rho_1$.

For $a = 0$, i.e. $\sigma_0 = \sigma_1$, the zeros are located on a line parallel to the q_z -axis at a distance $\ln |b|/d$, which is in accordance with Ref. [37].

Figure 3.6 shows an example for the dependency of the position of the zeros of the structure factor $F(Q)$ on the parameters of a sample consisting of a single layer on a substrate. The film is of thickness 100Å and density $\Delta\rho_0$, given in units of the substrate density ρ_∞ . Thus, the density contrast at the inner interface is

$\Delta\rho_1 = 1 - \Delta\rho_0$. The roughness of the surface and of the inner interface is σ_0 and σ_1 , respectively. The three cases $(\sigma_0, \sigma_1) = \{(2\text{\AA}, 4\text{\AA}), (2\text{\AA}, 4\text{\AA}), (4\text{\AA}, 2\text{\AA})\}$ are combined with different densities of the layer $\Delta\rho_0 = \{5/8, 3/8, 11/8\}$. The dependency of the ratio σ_0/σ_1 – and hence on the sign of a – on the bending of the hyperbola on which the zeros are located is clearly visible. For $\sigma_1 < \sigma_0$, i.e. $a < 0$, the hyperbola is bent towards the UHP and hence there are zeros in the UHP. Also the displacement of the zeros parallel to the imaginary axis – depending on the ratio $b = \Delta\rho_0/\Delta\rho_1$ – is clearly visible. Note the displacement of the zeros parallel to the q_z -axis when $b < 0$, according to Eq. (3.29).

From this derivation we see that the position of the zeros remains unchanged under certain transformations of the potential. Scaling of $\Delta\rho_{1,2}$ with a constant factor α obviously cancels out, since only the ratio b is relevant for the position of the zeros. Furthermore, the zeros do not change for $\sigma_0^2 - \sigma_1^2 = \text{const}$, which again is a hyperbola.

The above discussion is also valid within the dynamical scattering theory except for the case $\Delta\rho_1/\Delta\rho_0 > 1$. For this case it was found [161], that zeros appear in the UHP whenever $d > d_{crit}$, where the critical film thickness is given by the phenomenological formula $d_{crit} \approx (\Delta\rho_0/\Delta\rho_1)/\sqrt{4\pi(\Delta\rho_0 + \Delta\rho_1)}$.

Multiple layers on a substrate

In case of a system of N layers with interfaces located at positions z_n of gaussian roughness, the structure factor is given by

$$F(q) = \sum_{n=0}^N \Delta\rho_n \exp(-q^2\sigma_n^2/2) \exp(iqz_n) \quad . \quad (3.31)$$

If $z_0 = 0$ and $z_n > 0$, $n = 1 \dots N$, then a sufficient condition for $F(q)$ having no zeros in the UHP is $|\Delta\rho_0| > \sum_n |\Delta\rho_n|$ and $\sigma_0 \leq \sigma_n$, for which a mathematical proof is given in Appendix A.1. For arbitrary profiles an answer to the question whether the reflection coefficient has zeros in the UHP can not be given. However, the observations made in the previous section remain valid. To illustrate this a layer-structured sample system consisting of three layer on a substrate is considered: Figure 3.7 depicts such a system where all interfaces are of gaussian type and have a roughness of $\sigma = 3\text{\AA}$. The density contrast $\Delta\rho_j = \rho_{j+1} - \rho_j$ between two successive layers is given in units of the substrate density ρ_∞ . Since $\Delta\rho_0 = 10/9 > \sum_j |\rho_j| = 1$ the reflection coefficient has no zeros in the UHP. In Figures 3.8 and 3.9 the displacement of the zeros under a variation of the surface parameters $\Delta\rho_0$ and σ_0 is shown up to $q_z = 1\text{\AA}^{-1}$. In Figure 3.8 the density of the topmost layer ρ_0 is decreased from 10/9 to 7/9. This results in a vertical shift of some zeros towards the UHP. The dependence of the zero positions on the surface roughness is shown in Figure 3.9. Analogous to Fig. 3.6 an increase of σ_0 leads to a increase of the zeros imaginary parts whereas a decrease results

Figure 3.7: Density profile consisting of three layers. All interfaces have a gaussian roughness of $\sigma = 3\text{\AA}$. The density contrast between two successive layers is given in units of the substrate density ρ_∞ . Since all roughnesses are equal and $\Delta\rho_0 > \sum_j |\Delta\rho_j|$ holds, the reflection coefficient has no zeros in the UHP.

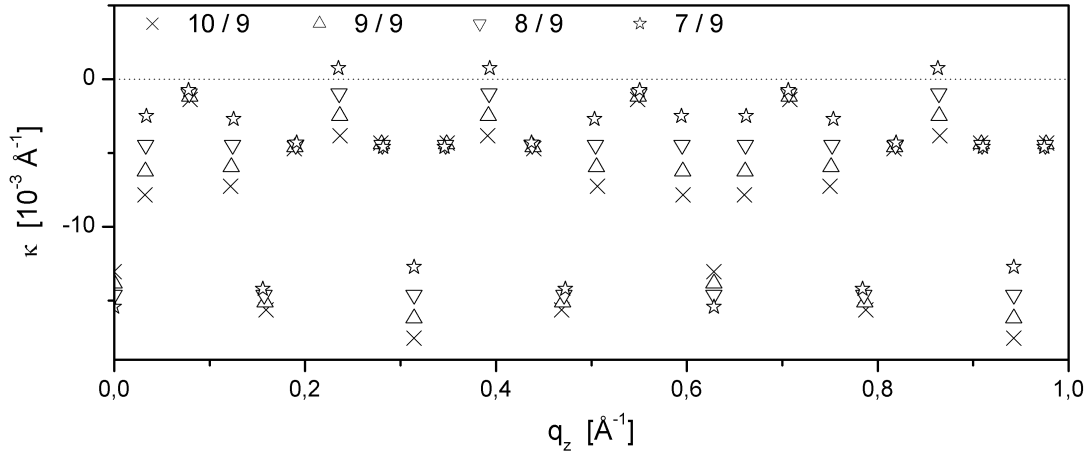
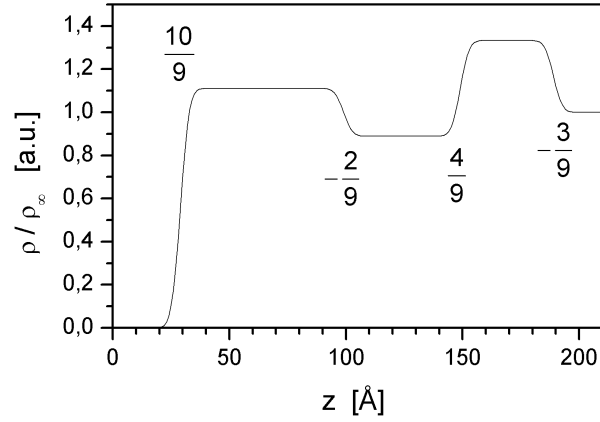


Figure 3.8: Displacement of the zeros of the reflection coefficient from the profile depict in Fig. 3.7 when $\Delta\rho_0$ is varied: A decrease of $\Delta\rho_0$ results in an increase of the imaginary part of the zeros.

in an movement of the zeros towards the LHP. For a sufficiently large value of σ_0 zeros are located in the UHP although the Clinton criterion [37], $\Delta\rho_0 > \sum_j |\rho_j|$, holds. Similarly, for a layer-structured density profile for which Clinton's criterion does not hold, all zeros can be located in the LHP, if the surface's roughness is small enough. An example is presented in Fig. 3.10, where the profile is shown in the left panel. The difference between the densities $\Delta\rho$ of the layers is given in units of the substrate density. Since $\Delta\rho_0 = 13/18 < \sum_j |\Delta\rho_j| = 17/18$, the derived criterion is not satisfied. Yet, due to the small roughness of the surface, i.e. $\sigma_0 \ll \sigma_n$, all zeros are located in the LHP.

Finally, the following fact should be noted: In the previous discussion we derived, that the reflection coefficient has no zeros in the UHP if $|\Delta\rho_0| > \sum_n |\Delta\rho_n|$. Let us now assume, that all zeros are located in the UHP. Then we can flip them all down into the LHP by simply changing the orientation of the z -axis and using

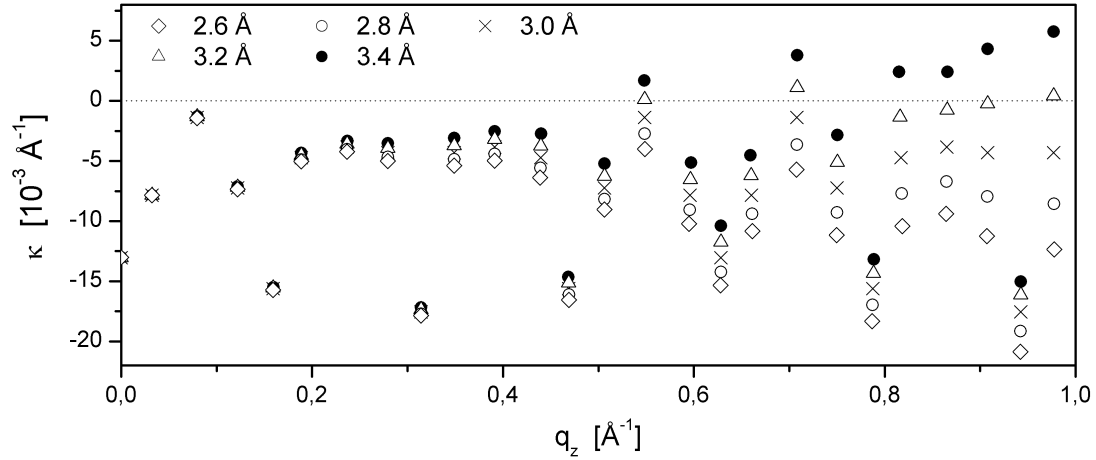


Figure 3.9: Displacement of the zeros of the reflection coefficient from the profile depict in Fig. 3.7 when σ_0 is varied: A decrease of σ_0 results in a decreases of the imaginary part of the zeros.

the kinematical approximation in the form $F(q) = \int d\rho(z)/dz \exp(-iqz) dz$, instead⁴. To fulfill the condition $z_0 < z_n$, the origin will then be at the substrate, which must have a smaller roughness than the other interfaces.

In the study of soft-matter films on substrates with small roughness, e.g. silicon-wafers, it is recommended to place the origin of the z -axis at the substrate oriented towards the surface, see e.g. Refs. [47][48][49]. But if the density variations inside the sample are small compared to the density contrast at the surface, which has the sharpest interface, then the z -axis should be chosen with the origin at the surface and oriented towards the substrate. Examples for the latter case are given in Refs. [80][82].

3.2.2 Equivalence of the phase problem and the unknown zeros

The possibility of zeros located in the UHP prevents an unambiguous determination of the complex structure factor $F(q_z)$ from its modulus $|F(q_z)| = \sqrt{r(q_z)/r_F(q_z)}$ alone. Let $F_0(q)$ be such that $|F_0(q)|^2 = r(q)/r_F(q)$, then

$$F(q) = F_0(q) \frac{q - a_j}{q - a_j^*} \quad (3.32)$$

is obviously different from $F_0(q)$, but its modulus $|F(q)|$ remains unchanged on the real axis since $|(q - a_j)/(q - a_j^*)| = 1$. Multiplication by $(q - a_j)(q - a_j^*)$ replaces

⁴In case of a complex potential the sign of the imaginary part also needs to be changed.

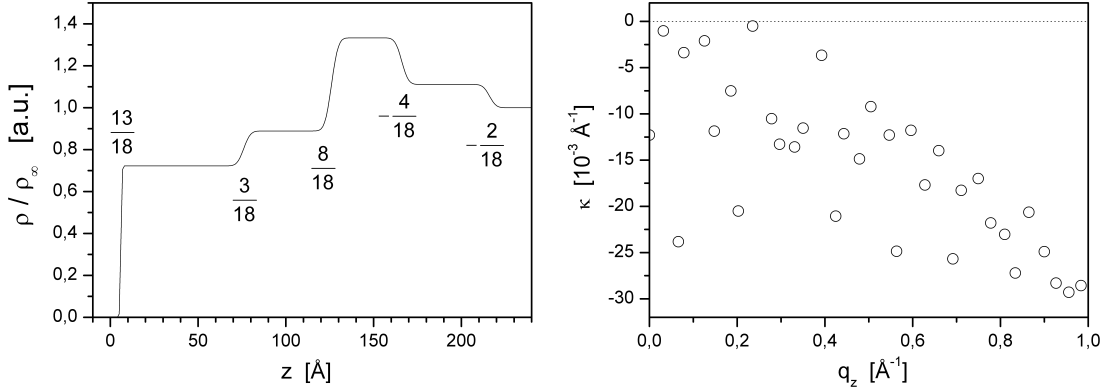


Figure 3.10: The profile depict in the left panel does not fulfill the condition $\Delta\rho_0 > \sum_j |\Delta\rho_j|$. However, the zeros (right panel) are all located in the LHP.

the zero a_j by a_j^* , that is to flip it across the q_z -axis. In case of real profiles, i.e. $F(-q^*) = F^*(q)$, the zeros at a_j and $-a_j^*$ have to be flipped simultaneously to keep $\varrho(z)$ real. If we have N pairs of zeros $(a_j, -a_j^*)$ with $\Im\{a_j\} \neq 0$ then there exist 2^N combinations, all of which have structure factors with the same modulus $\sqrt{r(q_z)/r_F(q_z)}$ on the real axis, but different phases. This is the manifestation of the *phase problem*. Zeros on the real axis do not contribute to the phase-problem, because the Blaschke factor reduces to unity and their locations are in principle ⁵ obtainable from the experiment. Another possibility to show the phase problem is to consider the reflectivity $r(q_z)$, whose analytical extension to the complex plane is given by

$$r(q) = R(q)R^*(q^*) \quad . \quad (3.33)$$

If $R(q)$ has a zero at a then $r(q)$ has a pair of zeros $\{a, a^*\}$. Multiplying $R(q)$ with the Blaschke factor $(q - a^*)/(q - a)$ does not change $r(q)$ on the q_z -axis because the zeros are flipped simultaneously across the real axis.

Now, since the phase problem is stated in terms of the sign of the imaginary part of the zeros $\Im\{a_j\}$ of the reflection coefficient $R(q_z)$, the example given at the end of the previous chapter can be discussed in more detail. The reflectivities of the profile with the higher film-density, calculated within dynamical and kinematical theory, are shown in the left panel of Figure 3.11. They differ only at small q_z values. The density profile is depicted in the inset. Since the roughness of both interfaces is identical and the density contrast at the surface is larger than that at the substrate, the reflection coefficient $R(q_z)$ has no zeros in the UHP. Hence, the phase $\phi(q_z)$ is equal to the Hilbert phase $\phi_H(q_z)$. The Hilbert phase $\phi_{H,calc}(q_z)$ calculated from the reflectivity $r(q_z)$ is in good agreement with $\phi(q_z)$. The analytical continuation of the structure factor $F(q)$ into the complex plane is presented in Figure 3.12 and the zeros are located on a line parallel to the

⁵In practice the instrumental resolution function and additional noise may prevent a precise determination of the zeros from experimental data.

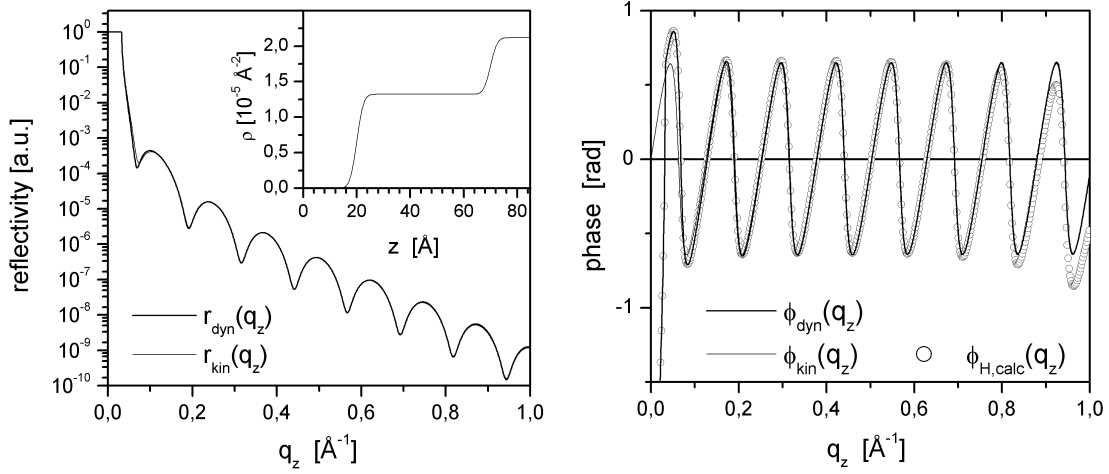


Figure 3.11: Left side: Reflectivities in dynamical (thick line) and kinematical (thin line) theory for the density profile depicted in the inset. Both differ slightly at low q_z -values. Right side: Phases of the reflection coefficient in dynamical (thick line) and kinematical (thin line) theory, respectively. The Hilbert phase (symbols) of the dynamical reflectivity agrees with the true phase. Hence the reflection coefficient has no zeros in the UHP.

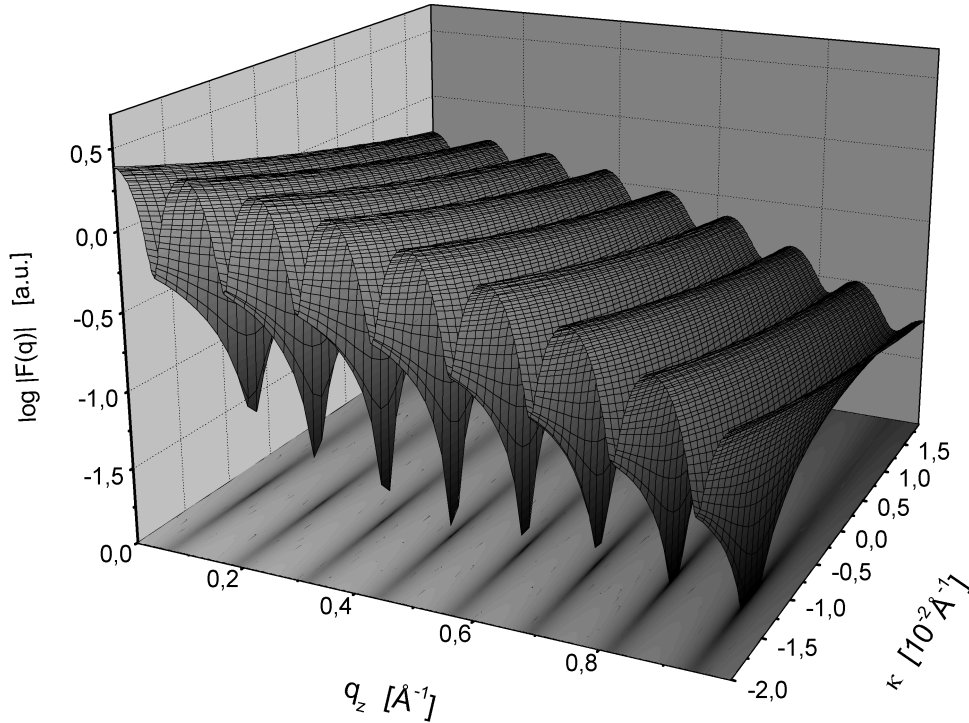


Figure 3.12: Analytical continuation of the structure factor $F(q)$ for the density profile depicted in Fig. 3.11. All zeros a_j are located in the LHP on a line parallel to the q_z -axis with $\Im\{a_j\} \approx -0.01 \text{\AA}^{-1}$.

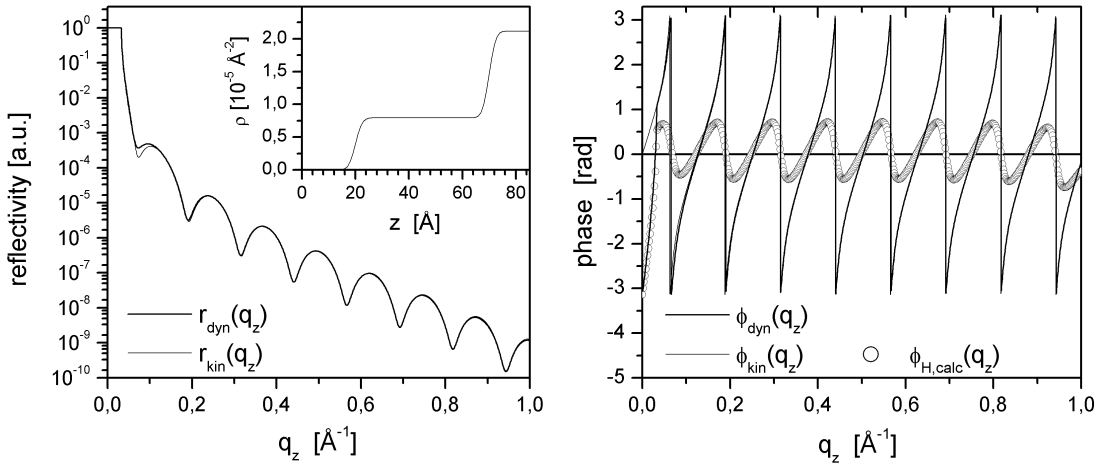


Figure 3.13: Left side: Reflectivities in dynamical (thick line) and kinematical (thin line) theory for the density profile depicted in the inset. Both differ slightly at low q_z -values. Right side: Phases of the reflection coefficient in dynamical (thick line) and kinematical (thin line) theory, respectively. The Hilbert phase (symbols) of the dynamical reflectivity differs from the true phase by the contribution of the zeros located in the UHP.

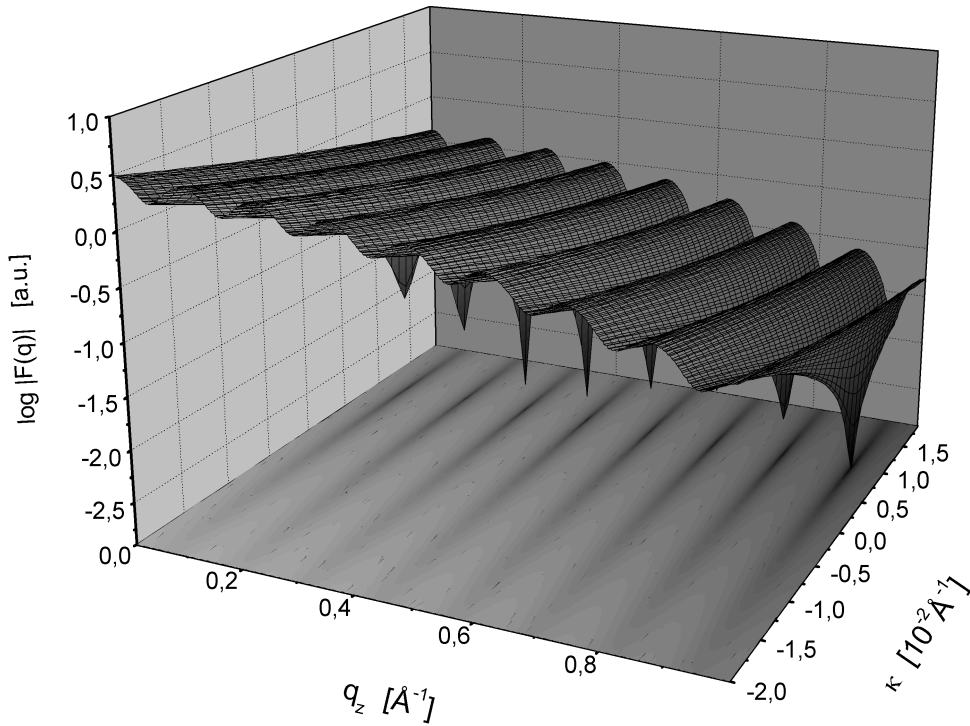


Figure 3.14: Analytical continuation of the structure factor $F(q)$ for the density profile depicted in Fig. 3.13. All zeros a_j are located in the UHP on a line parallel to the q_z -axis with $\Im\{a_j\} \approx 0.01 \text{\AA}^{-1}$.

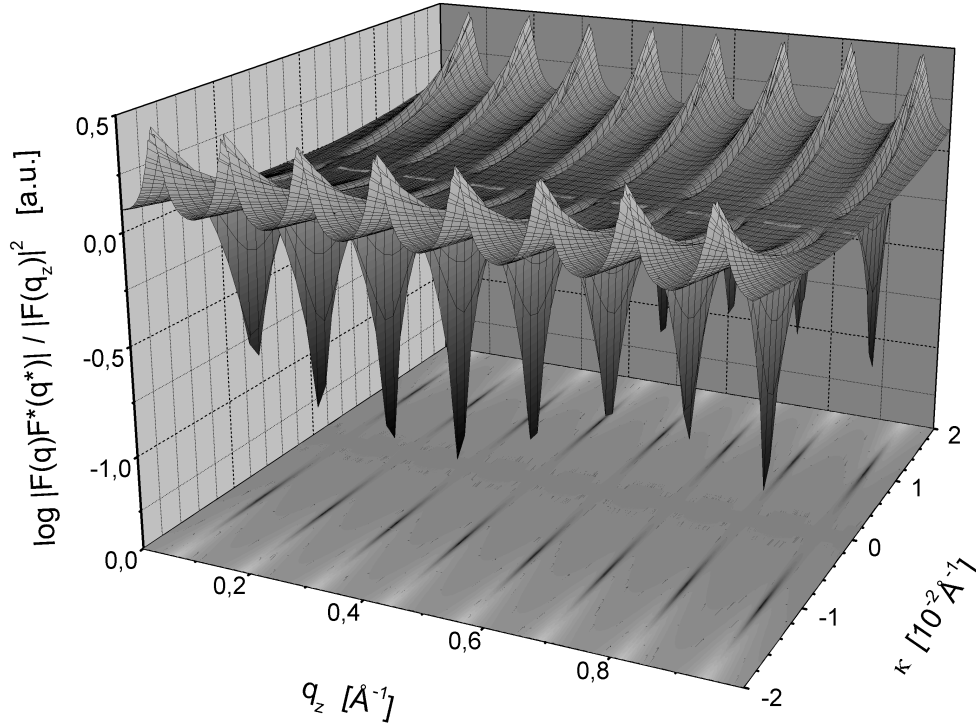


Figure 3.15: Analytical continuation of $|F(q)|^2 = F(q)F^*(q^*)$ into the complex plane: The zeros appear pairwise symmetric to the real axis. The result may be obtained either from the potential shown in Fig. 3.11 or from that presented in Fig. 3.13. For clarity $|F(q)|^2$ is normalized by $|F(q_z)|^2$.

q_z -axis with $\kappa \approx -0.01\text{\AA}^{-1}$. The case of the profile with the higher film-density is depicted in Figures 3.13 and 3.14: The dynamical and kinematical reflectivities are shown in the right panel of Figure 3.13. Now that the density contrast at the surface is smaller than that at the substrate the reflection coefficient $R(q)$ has zeros in the UHP. These show up as poles in the phase $\phi(q_z)$ according to the last term in Eq. (3.38). The phase does not agree any more with the Hilbert phase $\phi_{H,calc}$ calculated from $r(q_z)$. The analytical continuation of the structure factor $F(q)$ is presented in Figure 3.14: All zeros are located in the UHP now on a line parallel to the q_z -axis at $\kappa \approx 0.01\text{\AA}^{-1}$.

Figure 3.15 depicts the analytical continuation of $|F(q_z)|^2$ into the complex plane for $q_z > 0$. The zeros appear in pairs $\{a_j, a_j^*\}$ so that flipping two zeros a_j and a_j^* does not change $|F(q)|$ on the q_z -axis.

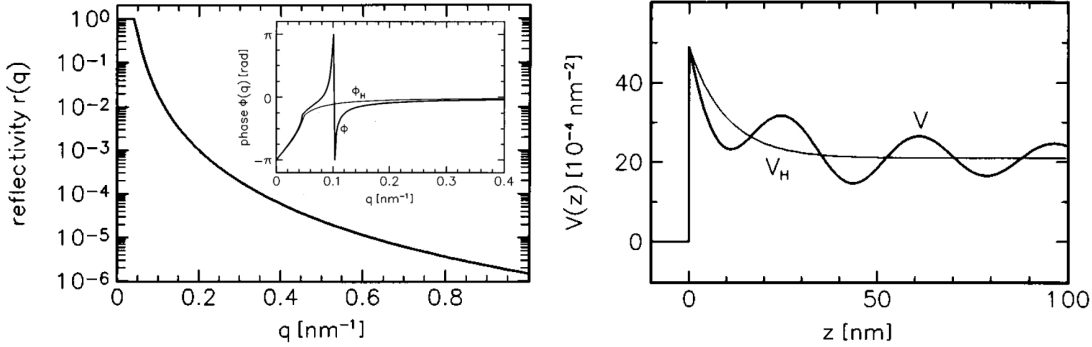


Figure 3.16: The introduction of an arbitrary pair of zeros ($\pm 0.1 + 0.005i$) leads to poles at ($\pm 0.1 - 0.005i$) and the profile has lost its compact support (taken from [116]). For details see text.

Support in the half line and compact support

The difference between the case when $\rho'(z)$ ⁶ has compact support, i.e. $\rho'(z) = 0$ for $z \notin [0, L]$, and $\rho'(z)$ supported on the half line, i.e. $\rho'(z) = 0$ for $z < 0$, is this: In the compact support case, the degree of non-uniqueness is limited by the number of non-real zeros of $F(q)$. If there are M non-real zeros, the number of solutions is 2^M . Furthermore, the density of zeros, which is defined by $D = \lim_{|q| \rightarrow \infty} N(|q|)/|q|$, is finite and approximately equal to $2\pi/L$, see e.g. [121][152].

In contrast, if $\rho'(z)$ is only supported in a half line, there are always an uncountable number of solutions, since multiplying $F(q)$ by *any* factor $(q - a)/(q - a^*)$, $a \in \text{UHP}$, produces a different $\rho'(z)$ also supported in the half line and with the same amplitude $|F(q)|$ on the real axis. Then the number of solutions is infinite. This can not be done when compact support is assumed, because of the pole that is produced at $q = a^*$. The above discussion is also valid for the case of dynamical scattering when considering the impulse response function $g(t) = \mathcal{FT} \{R(q_z)\}$ instead of $\rho'(z)$. A detailed discussion is given in Ref. [73].

In the analysis of thin films, compact support may always be assumed, because $\rho'(z)$ vanishes at the surface and in the substrate. In contrast, in case of scattering from liquid surfaces and thick soft-matter films, compact support is not given and an introduction of almost arbitrary zeros becomes possible.

This was shown by REISS ET AL. in Refs. [116][117] for the case of polymer segregation. Originally in Refs. [172][174], ZHOU ET AL. obtained a density profile consistent with the Cahn-model, $\rho(z) = a + b \exp(-z/c)H(z)$, where $a, b, c > 0$ and $H(z)$ is the Heaviside function. The reflectivity is shown in the left panel of Fig. 3.16 and the profile is represented by the thin line in the right panel. The structure factor, $F(q) = (ibcq)/(1 + icq)$, has exactly one zero, on the real axis

⁶Here $\rho'(z) = \frac{d}{dz}\rho(z)$

at $q = 0$ ⁷. Thus, the phase equals the Hilbert phase ϕ_H (thin line in the inset). The profile has a smooth transition to the bulk density a , which is practically reached at a depth of 100 nm. Then its derivative may be considered to have compact support⁸. Adding an arbitrary pair of zeros, here $(\pm 0.1 + 0.005i)$, does not change the reflectivity but leads to an oscillating profile (thick line in the right panel), whose derivative is not vanishing within the depicted z region. This is due to the two poles created simultaneously at $(\pm 0.1 - 0.005i)$ in order to keep the profile real valued.

However, when considering x-ray reflectivity experiments, compact support is given by the finite penetration of the x-ray into the sample due to absorption and by the finite resolution of the experimental setup.

3.2.3 Locating Zeros

Two methods have been reported for locating zeros. The first approach, see e.g. [99][100], makes use of the analyticity of the reflection coefficient. Since analytic functions may be represented by their roots,

$$R(q) = \prod_{j=0}^{\infty} (q - a_j) \quad , \quad (3.34)$$

throughout the complex plane, one may be tempted to fit a high order complex polynomial $p(q_z)$ to the reflection coefficient $\sqrt{r(q_z)} \exp[i\phi_H(q_z)]$, where $\phi_H(q_z)$ is the Hilbert phase. The zeros of that polynomial should then agree with those of the reflection coefficient. Taking a closer look at this procedure, the following obstacles arise: Since $r(q_z)$ is an entire function of exponential type, see the Paley-Wiener theorem [102], its number of zeros is infinity. The degree M of the polynomial we can fit to the data, and hence the maximal number of zeros we can locate, is limited by the number of collected data $r(q_{z,m})$, $m = 0 \dots M$. In addition, the density of zeros is known from the Titchmarsh theorem, see e.g. [152][154], to be approximately $\Delta q = 2\pi/L$. Hence, if $r(q_z)$ is known on the interval $0 \leq q_z \leq q_{max}$, the number of zeros within that interval is approximately given by $N = Lq_{max}/2\pi$. This means that we have to decide which N zeros of M have a physical meaning and which are *virtual* zeros [81][99]. The remaining $M - N$ zeros must be such that $\Re\{a_m\} > q_{max}$. Furthermore, the imaginary part of the Blaschke factor does not decay to zero very fast (see Fig. 3.17) and zeros with $\Re\{a_j\} \gg q_{max}$ may have an influence on the zero positions in $0 < q_z < q_{max}$. Additional difficulties arise from the computational point of view, since high-order polynomial interpolation with subsequent determination

⁷The zero at $q = 0$ is disregarded here, because it has no counterpart in dynamical scattering theory.

⁸This is not strictly true since $\exp(-z/c)$ does not vanish, but the profile can be truncated at $z \approx 100\text{nm}$ without a remarkable change of the corresponding reflectivity.

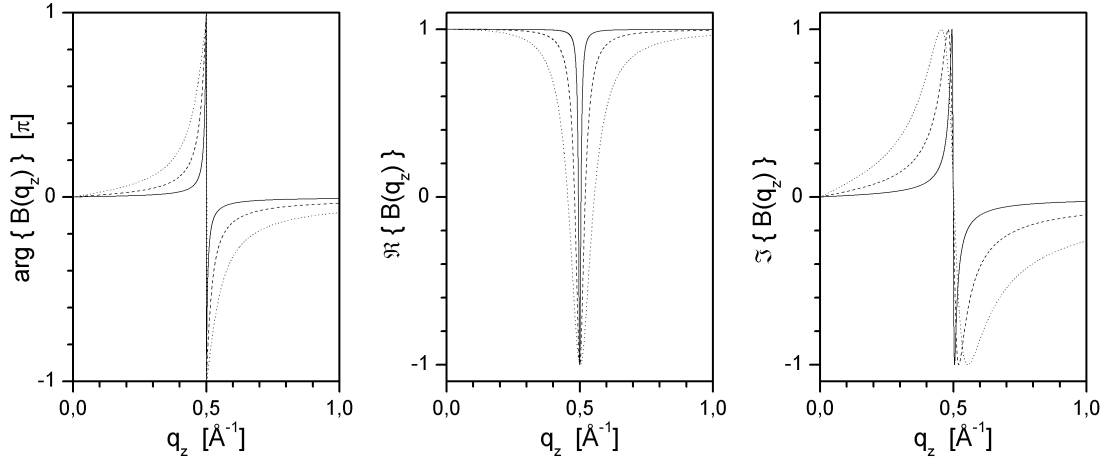


Figure 3.17: Influence of the magnitude of the imaginary part of a zero $(0.5 + i\kappa)/\text{\AA}$ on the Blaschke-product $B(q_z)$ given by Eq. (3.23): The phase of the Blaschke-product is depicted in the left panel, its real and imaginary parts are shown in the middle and right panel, respectively. The imaginary parts κ are equal to 0.005 (solid line), 0.02 (dashed line) and 0.5 (dotted line). With decreasing $|\kappa|$, $B(q_z)$ becomes more localized and reduces to unity for $\kappa = 0$.

of the zeros is numerically a difficult task.

The second method is to determine the zeros within the kinematical approximation from the condition [121]:

$$I(q) = \int_{-\infty}^{\infty} P(z) \exp(-\kappa z) \exp(iq_z z) dz = 0 \quad , \quad (3.35)$$

where

$$P(z) = \int_{-\infty}^{\infty} \frac{r(q')}{r_F(q')} \exp(-iq_z z) dq_z \quad (3.36)$$

denotes the Patterson function and $q' = \sqrt{q_z^2 + q_c^2}$. In practice, however, this method is not recommended for the following reason: Let us decide to calculate all values of $I(q)$ in the UHP to locate the zeros, i.e. for $\kappa > 0$. Then we see from the above equation that the dominating contributions in the calculation of $I(q)$ stem from the most negative part of $P(z)$, since it is amplified by $\exp(-\kappa z)$. Since $P(z)$ is obtained from the linearized measured reflectivity, it is not band-limited due to noise and the interpolation that is necessary to perform the Fourier transform. Thus, with increasing κ , the intensity $I(q)$ becomes more and more corrupted by the Fourier transform of noise and a detection of zeros is not possible any more.

The above discussion leads to the conclusion that it is difficult to locate the zeros directly from the measured intensity. Instead, it appears preferable to determine the zero positions from a density profile whose reflectivity is equal to the measured

one within the region $0 \leq q_z \leq q_{max}$.

The first method makes use of the logarithmic residuum [44]:

$$\frac{1}{2\pi i} \oint_C \frac{\frac{d}{dq} r(q)}{r(q)} dq = N_C - P_C \quad , \quad (3.37)$$

with $r(q) = R(q)R^*(q^*)$. N_C and N_P denote the number of zeros and poles of $r(q)$ inside the closed integration path C , respectively. The integration is performed on a rectangular path. Whenever $N_C \approx 0$, the area is banned from the further search, whereas the area is split in two regions of same size, if $N_C \gg 0$. If the size of the integrated area has reached a certain limit, the exact position of the zero is determined by minimization of $|r(q)|$ using conventional optimization techniques. Its disadvantage is the high computational cost when using the kinematical approximation. In this case it is more efficient to use Eq. (3.46) with

$$P(z) = ACF\{\rho'(z)\} \quad . \quad (3.38)$$

The problems described above do not arise, because $P(z)$ is band-limited now. The computation can be done by either Fast Fourier Transform or by Fast Laplace Transform, see e.g. [144].

Since the zeros of $r(q)$ appear in pairs symmetrical to the q_z -axis it is sufficient to explore only one complex half plane, e.g. the UHP. The half plane in which the zero is located can then be determined by comparing $|R(a_j)|$ and $|R(a_j^*)|$.

In principle, this method is independent from the used scattering theory and allows the localization of zeros even for the dynamical theory. However, the determination of zeros in the LHP is complicated considerably by the fact that the reflection coefficient $R(q)$ may have poles. These are due to multiple scattering and it was proven [149] that they are located only in one complex half plane, which for the notation used in this work is the LHP. An example is presented in Figure 3.18. The density profile and the corresponding reflectivity (on the q_z -axis) are shown in *a*) and *b*), respectively. Contour plots of the moduli of $T(q)$ and $R(q)$ are shown in panels *c*) and *d*) and an enlargement of the region marked by the square is presented in *e*) and *f*), respectively. The black regions indicate the positions of the poles and the zeros are located at the brightest regions. Integrating along a closed path that contains the same number of poles as zeros yields a vanishing integral and the zeros can not be localized any more using Eq. (3.37). However, one may still integrate $\frac{d}{dq} R(q)/R(q)$ in the UHP which is known to be free of poles. The remaining problem – the recovery of the zeros located in the in the LHP – can not be solved by applying Eq. (3.37).

To overcome this problem TIKHONRAROV ET. AL., see Refs. [149][150][151], introduced the spectral coefficients $S_1(q) = 1/T(q)$ and $S_2(q) = R(q)/T(q)$. The transmission coefficient $T(q)$ has no zeros and the positions of its poles is equal to those of the reflection coefficient $R(q)$, see Fig. 3.18. Hence, S_1 and S_2 are entire functions on \mathbb{C} and are uniquely determined by their zeros [79]. The zeros in the

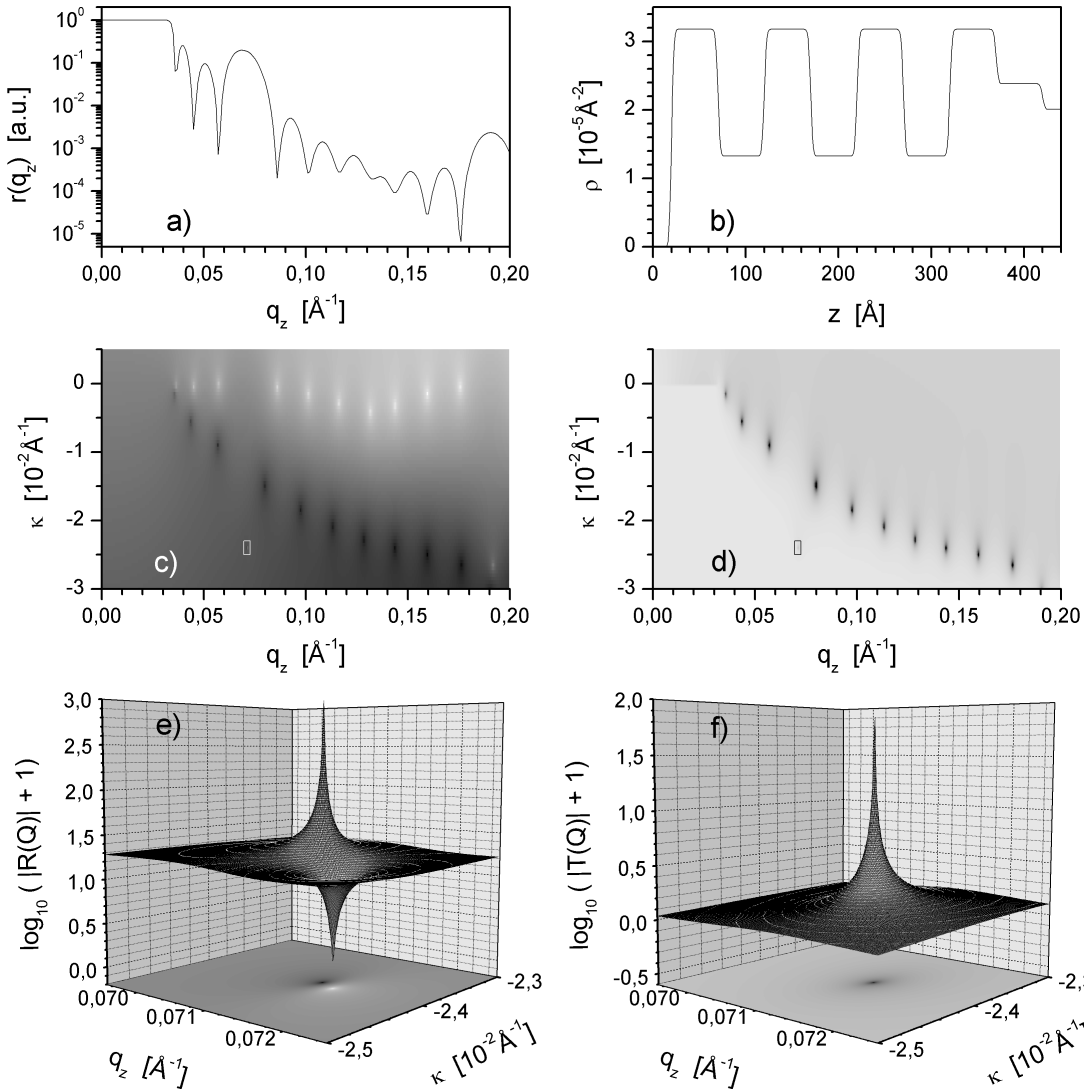


Figure 3.18: Zeros and Poles of the reflection coefficient $R(q)$ and the transmission coefficient $T(q)$ of a multilayer: a) reflectivity on the real axis. b) density-profile. c) Modulus of the reflection coefficient. d) Modulus of the transmission coefficient. e) and f) zoom of the regions in the square of c) and d), respectively.

LHP may then be located by replacing $R(q)$ by $S_2(q)$ in Eq. (3.37). However, this method requires the calculation of $R(q)$ and $T(q)$, which increases the amount of required calculations considerably.

The following procedure is helpful for locating the zeros of the dynamical reflection coefficient $R(q)$ for a given density profile $\rho(z)$: First, the zeros $\{a_j^{kin}\}$ of the structure factor $F(q)$ are computed. Next, the profile $\rho(C_0, z) = C_0\rho(z)$, where C_0 is some small positive number of order 10^{-4} . Since $\rho(C_0, z)$ is almost vanishing, the kinematical theory is valid and hence the zeros $\{a_{j,0}\}$ of the cor-

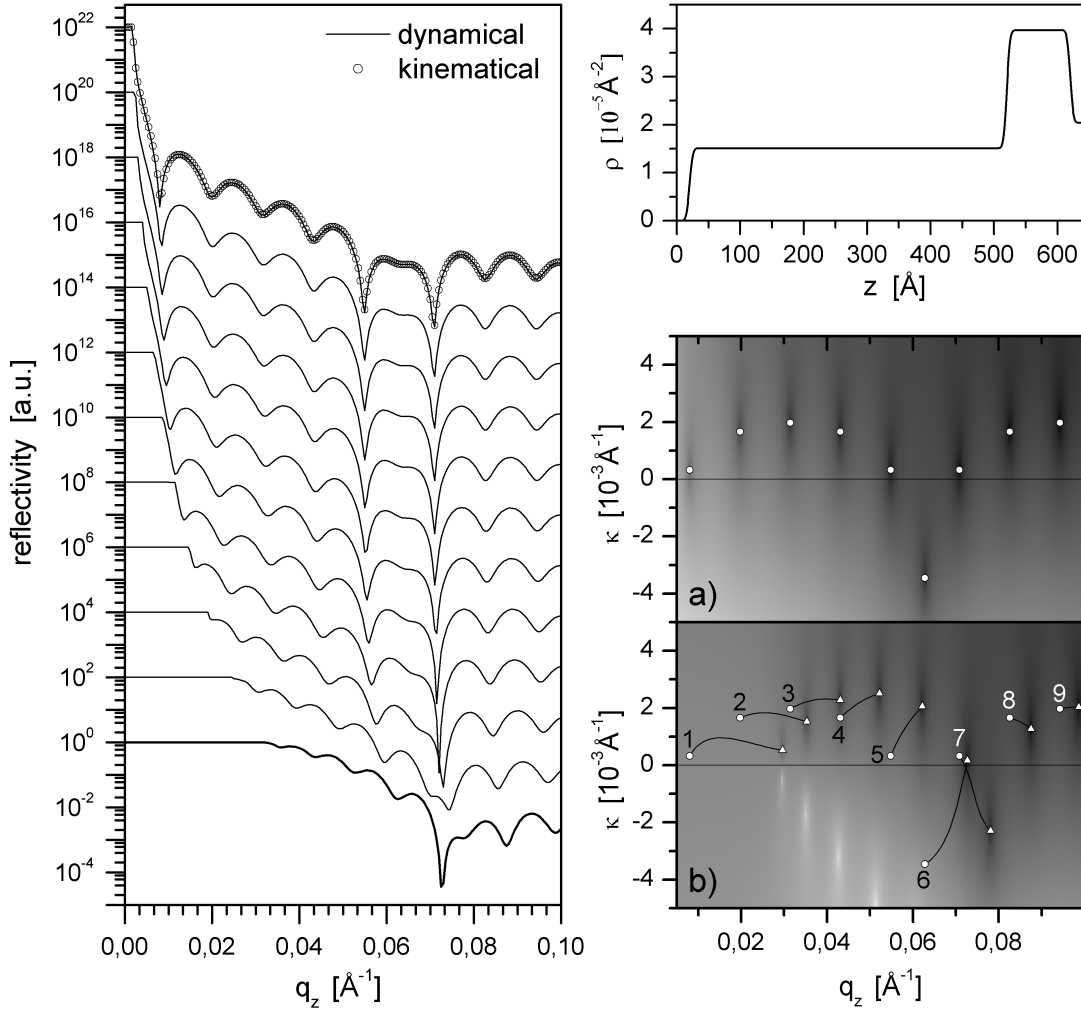


Figure 3.19: Transition from the dynamical to the kinematical reflectivity: The thick line represents the reflectivity of the profile shown in the upper right panel. For the calculation of the other reflectivities the profile was scaled by a factor 0.8^n , $n = 0, 1, \dots, 11$. The uppermost reflectivity coincides with the reflectivity calculated within kinematical approximation (symbols). The contour plots depict continuations of the a) kinematical and b) the dynamical reflectivity into the complex plane. The lines in contour plot b) indicate the displacement of the zeros from their positions in kinematical theory (circles) to their positions in dynamical theory (triangles).

responding reflection coefficient $R(C_0, q)$ are almost identical with those of $F(q)$. Then, the profile $\rho(C_1, z)$ is calculated, where C_1 is slightly larger than C_0 . The zeros of $R(C_1, q)$ are then slightly displaced and may be easily located by minimizing its modulus $|R(C_1, q)|$ provided that the displacement of $a_{j,0}$ remains within the convergence radius of $a_{j,1}$ for gradient based optimization methods. Once the

zeros $a_{j,1}$ are located, the procedure is repeated with $\rho(C_n, z)$ with $C_n \gtrsim C_{n-1}$ until $C_N = 1$.

An example is shown in Fig. 3.19: The profile with unknown zeros of the reflection coefficient is shown in the upper right panel. The reflectivity within kinematical theory, $r_F(q_z)|F(q_z)|^2$ is represented by the open circles in the left panel. The upper contour plot on the right side depicts the continuation of $|F(q)|^2$ into the complex plane. The positions of the zeros is indicated by the open circles. The solid lines in the left panel are dynamical reflectivities corresponding to density profiles $0.8^n \rho(z)$, $n = 0, 1, \dots, 11$, starting from the lowest curve. The uppermost reflectivity coincides with the kinematical reflectivity and so do their zeros. With increasing C_n , i.e. with decreasing n , the reflectivity approaches the dynamical reflectivity of $\rho(z)$ and the respective zeros undergo a continuous displacement as shown in the lower contour plot: Starting from the open triangles they move along the solid lines towards their final positions (open triangles). Inspecting the paths of the different zeros leads to the conclusion that the linearization $q_z \rightarrow \sqrt{q_z^2 + 16\pi\rho}$ does not apply to the imaginary part of the zeros. As an example, the zeros 6 and 7 move in the opposite directions along the κ -axis.

The advantage of the proposed method is that the mentioned difficulties due to the poles of the dynamical reflection coefficient do not occur and that the zeros may be located without being restricted to one complex half plane. However, it should be noted that the computational effort for tracking the zero positions is quite high and that sophisticated algorithms are required to reduce the computation time.

3.2.4 Flipping zeros

In dynamical theory and considering only real potentials, the flipping of J pairs of zeros $\{(a_j, -a_j^*)\}_{j=1\dots J}$ may be performed via a transform of Darboux type [115][116]:

$$\begin{aligned} V_0(z) &= V_H(z) \\ V_j(z) &= V_{j-1}(z) - 2 \frac{d^2}{dz^2} \ln \mathfrak{S} \left\{ f_{j-1}^-(a_j, z) \frac{d}{dz} f_{j-1}^-(-a_j^*, z) \right\} \\ V(z) &= V_J(x) \quad , \end{aligned} \tag{3.39}$$

where $f^-(q, z)$ is the Jost-solution of the Schrödinger Equation behaving like $\exp(-iqz)$ for $z < 0$ and is obtained from the second kind Volterra integral equation

$$f^-(q, z) = \exp(-iqz/2) + \frac{2}{q} \int_0^z \sin \left[\frac{1}{2} q(z-t) \right] V(t) f^-(q, t) dt \quad . \tag{3.40}$$

The above equation may be solved iteratively, using e.g. a Neumann-series, and it can be shown that the series converges for $\mathfrak{S}\{q\} > 0$ [115]. This procedure is

restricted to flipping zeros from the LHP to the UHP, which requires knowledge of the Hilbert Profile $V_H(z)$, if one wishes to compute all possible profiles. Within this work an adaptive method for the numerical solution of the Volterra integral equation [62] is used for the computation of the Jost-solution $f^-(q, z)$.

Another method for flipping zeros from the LHP to the UHP is based on the spectral coefficients S_1 and S_2 and has been proposed in Ref. [149].

Within the kinematical approximation the flipping of the zeros is much easier and straightforward via Fourier transforms:

$$\widehat{\rho}(z) = \int_0^z \mathcal{FT} \left\{ \mathcal{FT}^{-1} \left\{ \frac{d}{d\zeta} \rho(\zeta) \right\} B(q_z) \right\} d\zeta \quad , \quad (3.41)$$

with the Blaschke product $B(q_z) = \prod_j B_j(q_z)$. The Fourier transform of a single Blaschke factor $B_j(q) = (q - a_j)/(q - a_j^*)$ is given by [28][74]

$$\widetilde{B}_j(z) = \delta(z) - 2\kappa_j \exp(-ia_j^* z) H(z) \quad , \quad (3.42)$$

where $\delta(z)$ and $H(z)$ denote the Dirac function and the Heaviside function, respectively. The parameter κ_j is the imaginary part of the zero $a_j = q_j + i\kappa_j$. Flipping two zeros a_j and a_l leads to

$$\begin{aligned} \widetilde{B}_j(z) * \widetilde{B}_l(z) &= \delta(z) - 2\kappa_j \exp(-ia_j^* z) - 2\kappa_l \exp(-ia_l^* z) \\ &\quad + 4i\kappa_j \kappa_l \frac{\exp(-ia_j^* z) - \exp(-ia_l^* z)}{a_j^* - a_l^*} \quad . \end{aligned} \quad (3.43)$$

For the case of flipping the pair $(a_j, -a_j^*)$, which is necessary to keep the potential real, one obtains

$$\widetilde{B}_{j^*}(z) * \widetilde{B}_j(z) = \delta(z) + Z(z, a_j) \quad , \quad (3.44)$$

where

$$Z(z, a_j) := 4 \frac{\kappa_j}{q_j} \left(q_j \cos(q_j z) + \kappa_j \sin(q_j z) \right) \exp(-\kappa_j z) \quad . \quad (3.45)$$

The new profile $\widehat{\rho}$ is then given by

$$\widehat{\rho}(z) = \rho(z) + \int_0^z \frac{d}{d\zeta} \rho(\zeta) * Z(\zeta, a_j) d\zeta \quad . \quad (3.46)$$

Eq. (3.45) provides an insight into the influence of q_j and κ_j on the new profile. Since κ_j is typically 2 – 3 orders of magnitude smaller than q_j , the sine term can be neglected. Furthermore, κ_j/q_j decreases as q_j increases and so does $Z(z, a_j)$. Thus, the first few zeros have a dominant impact on the shape of the profile, while zeros at larger q_j contribute only oscillations of small amplitude. The exponential decay of $Z(z, a_j)$ depending on κ_j results in a localization of the influence of $Z(z, a_j)$ on the new profile, whereas for small κ_j the exponential term becomes almost constant and the influence is more global.

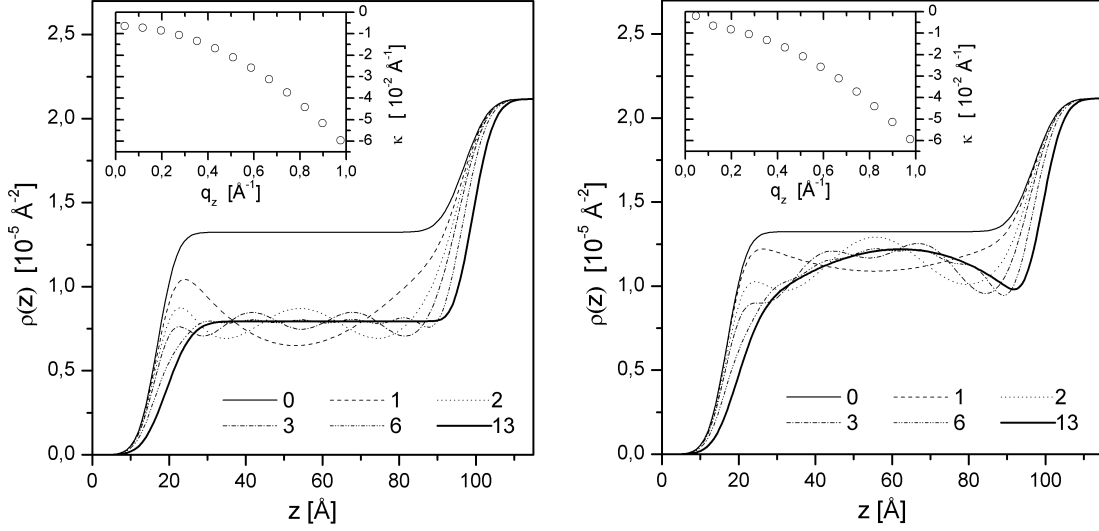
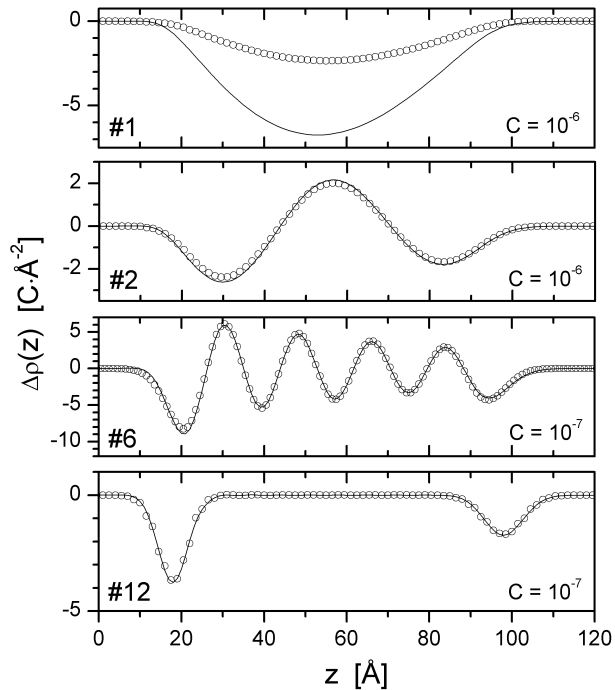


Figure 3.20: Flipping of zeros in kinematical theory (left panel) and dynamical theory (right panel): The insets depict the positions of the zeros in the LHP for $0 \text{ \AA}^{-1} \leq q_z \leq 1 \text{ \AA}^{-1}$. They differ significantly for small q_z -values. The lines represent the density profiles obtained after flipping the first n zeros where n is given in the legend. Flipping the first 13 zeros results in a density profile that coincides very well with the profile having no zeros in the LHP.

Figure 3.21: Influence of a single flipped pairs of zeros on the profile ρ_H within kinematical (line) and dynamical theory (symbols): The number of the pair is given in the lower left corner of each graph. The respective scaling factors C are shown in the lower right corner. Flipping zeros that are located in the non-linear region (#1, #2) leads to different profile modifications. For zeros located at larger q_z -values, the variations become smaller and the difference can be neglected (#6, #12). The maximal modification from flipping zero #12 is a factor 20 smaller than that of zero #1.



An example for the influence of flipped zeros on a profile is shown in Figure 3.20. The left panel depicts the kinematical case, i.e. the use of Eq. (3.41), and the right panel shows the result for the dynamical theory obtained from Eqs. (3.39) and (3.40). First, the zeros of the reflection coefficient of the Hilbert profile (thin solid line) have been located up to 1 \AA^{-1} within the respective theory. They are shown in the insets. At high q_z values the positions are almost identical whereas they differ significantly at small q_z -values where the dynamical reflection coefficient is dominated by non-linear effects and multiple scattering. Then, the zeros have been flipped in ascending order with respect to their q_z values. The numbers, given in the legends, correspond to the number of flipped zeros. The final profiles, after flipping all 13 zeros, are represented by the thick solid lines. They differ significantly due to the different positions of the first zeros. After flipping the first 6 zeros, the profiles reveal the coarse structure of the final result and the remaining zeros contribute only little variations when transferred to the UHP. Figure 3.21 shows the difference between the profile variations for the dynamical (open circles) and the kinematical case (solid lines) when only one pair of zeros is flipped to the UHP. The upper two panels depict the results when flipping zero #1 and #2, respectively. The difference is significant. The lower two plots show the modification due to the zeros #6 and #12. They are located in the kinematical region and so the difference between the results obtained via Eq. (3.41) and Eq. (3.39), respectively, is negligible. It should be noted that the flipping of a pair of zeros preserves the compact support of the profile, in contrast to the introduction of arbitrary zeros in the UHP as discussed in section 3.2.2.

Chapter 4

Analysis of reflectivities

In this section a review of methods for the analysis of x-ray reflectivities is given. In the last decades numerous, sometimes only slightly different, analysis-schemes have been published. Thus, a complete overview cannot be given here. We will mainly focus on inverse methods applied to reflectivities, where different schemes have been developed within the dynamical scattering theory and within kinematical theory. The strengths and weaknesses of the different methods will be discussed in connection with real-data interpretation.

4.1 Direct analysis methods

4.1.1 Model-dependent direct analysis

The commonly used method for analyzing x-ray reflectivity data is by *fitting* the parameters of a model to the measured data: The density profile $\rho(z) = \rho(z, \mathbf{p})$ is a function of parameters $\mathbf{p} = \{p_0, \dots, p_N\}$, for example layered structures characterized by thickness, density of the layer and roughness of the interface, or the Cahn-model for polymer segregation mentioned in Section 3.2.2. Then the direct problem, that is the calculation of the reflectivity $r_{fit}(q_z)$, or reflection coefficient $R_{fit}(q_z)$ from the density profile $\rho(z, \mathbf{p})$, is solved and compared to the experimental reflectivity $r_{obs}(q_z)$. The parameters \mathbf{p} are then varied until some functional which is related to the residuum $\|r_{obs}(q_z) - r_{fit}(q_z, \mathbf{p})\|$ becomes minimal. In a general form, this functional may be written as

$$J(\mathbf{p}) = \sum_m \mu_m \left\| \mathcal{A}_m[r_{obs}(q_z)] - \mathcal{A}_m[r_{fit}(q_z, \mathbf{p})] \right\| \quad , \quad (4.1)$$

where μ_m are weights and the $\mathcal{A}_m(\cdot)$ are operators such as $\mathcal{A}_m(\cdot) = \log(\cdot)$, $\mathcal{A}_m(\cdot) = (\cdot)/r_F(q_z)$ or $\mathcal{A}_m(\cdot) = \log[(\cdot)/r_F(q_z)]$. A comparison of the different kinds of normalization is given in Ref. [110]. While the afore mentioned examples transform the reflectivities in reciprocal-space, $\mathcal{A}_m(\cdot)$ may also be a transform

to real-space. An example is the Patterson function

$$\mathcal{A}_m(\cdot) = \int (\cdot) / r_F(q_z) \exp(iq_z z) dq_z \quad ,$$

see Section 2.4. The simultaneous refinement of the reflectivity in real-space and reciprocal-space does not only improve the sensitivity to certain parameters [128] but may also prevent the usually applied local optimization techniques from getting stuck in local minima.

To overcome the shortcomings of local minimization techniques, global optimization techniques such as simulated annealing [71] or genetic algorithms [60] have been applied to x-ray reflectivity data, see e.g. Refs. [17][158]. The advantage of genetic algorithms is that they are able find multiple global minima, whereas simulated annealing provides only one solution at a time. An extensive study on how much information can be extracted depending on the chosen model can be found in Ref. [89].

4.1.2 Model-independent methods

When tiny details in the density profile are of interest or no model is available for the sample structure under investigation, model-independent methods have to be applied to obtain a sufficient explanation of the measured reflectivity.

The main differences between model-dependent and model-independent methods are, that the choice of a model already incorporates *a-priori* information and that the solution space is therefore restricted. In contrast, model-independent methods expand the density profile in some complete set of basis functions that permits to – at least approximately – generate all possible reflectivity data.

A variety of basis functions appeared in the context of analyzing reflectivity data and the choice strongly depends on the used scattering theory and the specific problem. When dynamical scattering theory is used, it is convenient to approximate the continuous density profile by a sequence of slabs of constant electron density [29], for which the reflectivity can be easily calculated using the Parratt formalism (see Section 2.2). When the kinematical theory is used for the analysis of the reflectivity, the simple relation between real space and reciprocal space via the Fourier transform permits a wider choice of basis systems: For example, trigonometric polynomials [108][130][133], piecewise-constant slabs [123][125][169][170], cubic B-splines [107][108], and parametric B-splines [21] appear in the literature.

The Groove Track method

One model-independent analysis scheme, the so-called *Groove Track Method* (GTM), will be discussed in more detail here, since it will be used in the algorithms presented in the following chapters of this thesis. This method was first published by ZHOU ET AL.[172]. Its basic scheme is as follows:

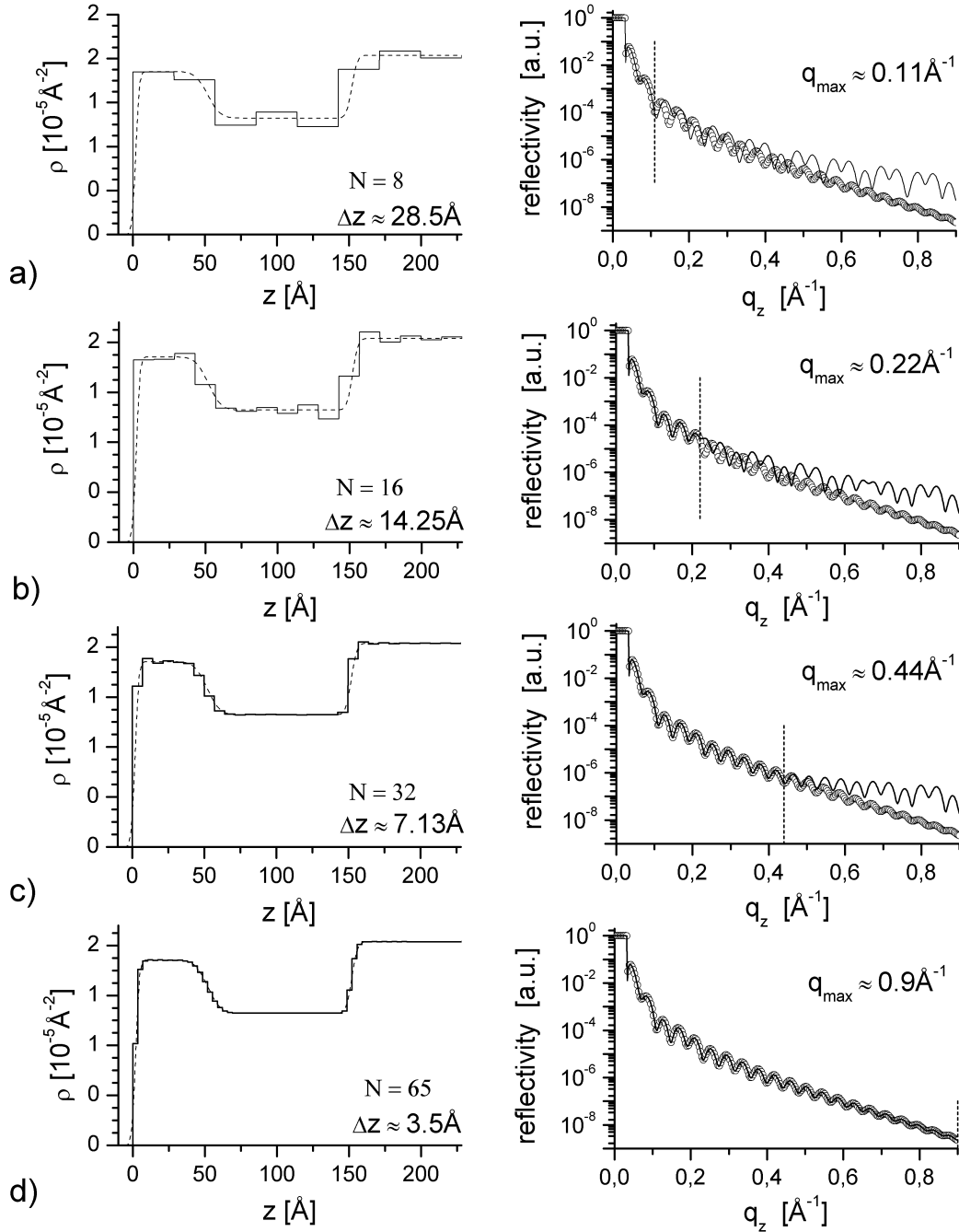


Figure 4.1: Example for the analysis of a reflectivity using the GTM : The density profile ρ_{exp} represented by the dashed line in Figs. (a) - (d) is reconstructed from its reflectivity r_{exp} (open circles). The thickness of the slabs Δz is halved and the region of the reflectivity used for the fitting is extended according to the relation $q_{\max} = \pi / \Delta z$ (vertical dotted lines) whenever the agreement between r_{exp} and the reflectivity r_{sim} calculated from the density profile is sufficiently good.

Step 1: Given is a measured reflectivity $r_{obs}(q_z)$ on $0 \leq q_z \leq q_{max}$. Estimate the critical wave-vector transfer q_c from r_{obs} . Let ρ_n^M , $n = 1, \dots, N$, denote the density of the n -th slab of constant density of the profile ρ^M at iteration step M . ρ^M consists of $N = 2^M$ slabs. Start with a single layer of thickness L , that is $M = 0$, on top of the known substrate with density ρ_∞ .

Step 2: Minimize $\|r_{obs}(q_z) - r_{sim}(q_z, \rho^M)\|_{[0, q_M]}$, where $q_M = \sqrt{(\pi/\Delta z)^2 + q_c^2}$ using some gradient-based optimization algorithm such as the Levenberg-Marquardt method [98].

Step 3: Set $M = M + 1$ and split each slab of ρ^{M-1} into two layers of thickness $\Delta z = L/2^M$ to obtain the new profile ρ^M .

Step 4: While $\Delta z \leq \pi/q_{max}$ goto Step 2.

In the following years, the GTM was constantly modified to overcome convergence problems (*Modified GTM* [32]) and to account for smoothness of the obtained profiles (*Smoothed GTM* [33][34][35][36]). In a recently published work [75], a slightly modified version of the groove track method was proposed.

An example for the analysis of the reflectivity using the GTM scheme is shown in Figure 4.1. The density profile ρ_{exp} to recover is represented by the dashed line in the left panels of subfigures a) - d). The corresponding reflectivity r_{exp} was calculated up to 0.9\AA^{-1} (open circles in the right panels). The overall length of profile L is chosen slightly larger than the actual spatial extent of ρ_{exp} , here $L = 228\text{\AA}$. According to the GTM scheme described above, the number of slabs N is doubled and the thickness Δz is halved at each step of the algorithm, $\Delta z = 228/1, 228/2, \dots, 228/32$. The maximum wavevector-transfer q_{max} (vertical dashed line in the right panels) up to which $\|r_{sim} - r_{exp}\|$ is fitted, increases according to $q_{max} = \sqrt{(\pi/\Delta z)^2 + q_c^2}$, where q_c is the critical wavevector.

The advantage of this method is that it is easy to implement and usually converges to a solution. The main drawback is the high computational effort with increasing number of slabs: For N slabs, the computation of the Jacobian matrix $J_{ij} = \partial r(q_{z,i})/\partial \rho_j$, which is required by the Levenberg-Marquardt algorithm, as well as its inversion require $\mathcal{O}(N^3)$ operations, each.

4.2 Inverse methods in the framework of dynamical scattering theory

In quantum mechanics the one-dimensional scattering problem is described by the time-independent Schrödinger equation

$$-\frac{d^2}{dz^2}\psi(z) + [q^2 + V(z)]\psi(z) = 0 \quad . \quad (4.2)$$

For a potential¹ of the form

$$V(z) = \begin{cases} 0, & \text{for } z < 0; \\ V(z), & \text{for } 0 < z < L; \\ V_\infty, & \text{for } z > L, \end{cases} \quad (4.3)$$

Eq. (4.2) has solutions in the form

$$\psi(z, q) = \exp(iqz) + R(q) \exp(-iqz) \quad , \quad z < 0 \quad (4.4)$$

$$= T(q) \exp(iQz) \quad , \quad z \rightarrow +\infty \quad , \quad (4.5)$$

$Q = \sqrt{q^2 - V_\infty}$. For a given potential $V(z)$ the reflection coefficient $R(q)$ can be obtained by solving Eq. (4.2). In Chapter 2.3.1 this has been done within the kinematical approximation. The calculation of the potential $V(z)$ from a given reflection coefficient $R(q)$, i.e. the solution of the inverse problem, is also possible. The mathematical formalism for the inverse problem in quantum scattering theory has been developed long time ago, see e.g. [52][57]. With the definition of the *impulse-response function*

$$g(z) = \frac{1}{2\pi} \int_{-\infty}^{\infty} R(q) \exp(iqz) dq \quad (4.6)$$

one has to solve the Gelfand-Levitan-Marchenkov equation [7][31][68]:

$$u(z, t) + g(z + t) + \int_{-t}^z u(z, \tau) g(\tau + t) d\tau = 0 \quad , \quad t < |z| \quad (4.7)$$

$$u(z, t) = 0 \quad , \quad t > |z|$$

for $u(z, t)$. The scattering potential $V(z)$ is then obtained from

$$V(z) = 2 \frac{d}{dz} u(z, z) \quad . \quad (4.8)$$

The determination of the scattering potential $V(z)$ requires the knowledge of the reflection coefficient $R(q)$ on the entire real q -axis. Since $R(q)$ is usually not accessible for $q < 0$, one assumes real potentials. Then $R(-q) = R^*(q)$ holds so that $g(z)$ can be calculated from $R(q)$ on the right half q -axis alone. Different numerical algorithms for the solution of Eq. (4.7) have been published in [85]. However, these methods require the reflection coefficient $R(q)$ which is not given in x-ray scattering experiments.

In the algorithm described above, the potential $V(z)$ is obtained in a direct manner by one single computation. To derive iterative reconstruction algorithms

¹In quantum scattering theory the potential $V(z)$ is used instead of the scattering length density $\rho(z)$. Both are related by $V(z) = 4\pi \rho(z)$.

the inverse scattering problem may be reformulated in the *time domain* by replacing the frequency-operator q^2 by the time-operator $-\partial^2/\partial t^2$. The potential $V(z)$ is obtained by solving the so-called *Goursat problem* [122]:

$$\left[\frac{\partial^2}{\partial t^2} - \frac{\partial^2}{\partial z^2} + V(z) \right] u(z, t) = 0 \quad , \quad 0 < z < t < \infty \quad (4.9)$$

$$\frac{\partial}{\partial z} u(0, t) - \frac{\partial}{\partial t} u(0, t) = 0 \quad , \quad t > 0 \quad (4.10)$$

$$u(z, z) + \frac{1}{2} \int_0^z V(s) ds = 0 \quad , \quad z > 0 \quad (4.11)$$

$$u(0, t) = g(t) \quad , \quad t > 0 \quad . \quad (4.12)$$

Two of the boundary conditions (4.10) – (4.12) along with Eq. (4.9) define the wavefield $u(z, t)$ uniquely. With the introduction of the functional $F(V_n) = u(0, t; V_n)$, $V(z)$ may be obtained in an iterative way via the so-called *Newton-Kantorowich algorithm* [19]

$$V_{n+1}(z) = V_n(z) + 4 \frac{d}{dt} \left\{ F[V_n(t/2)] - g(t) \right\}_{t=2z} \quad , \quad (4.13)$$

with $g(t)$ given by Eq. (4.6) and $V_0(z) \equiv 0$. A shortcoming of iterative algorithms is that convergence has to be guaranteed. For a potential of thickness L one can define the dimensionless quantity $B = ML^2$ with $M = (1/L) \int_0^L V(z) dz$. It can be shown [19][27][51] that there exists an upper limit B_{max} above which the algorithm described above becomes unstable. Numerical studies even with highly accurate "synthetic data" for $R(q)$ showed that this is the case for $B_{max} > 20$. It should be noted that for neutron scattering $V(z)$ is in general much smaller resulting in larger values for L compared to x-ray scattering. In case of "imperfect data" as obtained from experiments, B_{max} reduces and the situation becomes more difficult. Other procedures for the solution of the inverse scattering problem within the time-domain approach have been developed in Ref. [122] and the experimental feasibility of one of them, the so-called *layer-stripping technique*, has been investigated recently in detail [161][162]. An new approach for estimating the stability of the inverse problem based on so-called *Lyapunov exponents* has been published in [50].

4.2.1 Phaseless inverse scattering

All inverse methods require the complex reflection coefficient $R(q)$ as input to obtain the potential $V(z)$. But since the reflectivity $r(q) = |R(q)|^2$ is measured only its magnitude is obtained in the experiment, while the phase $\phi(q)$ gets lost. However, the analytical properties of $R(q)$ due to the limited sample size, provide at least partial information about the phase as discussed in Chapter 3. If the

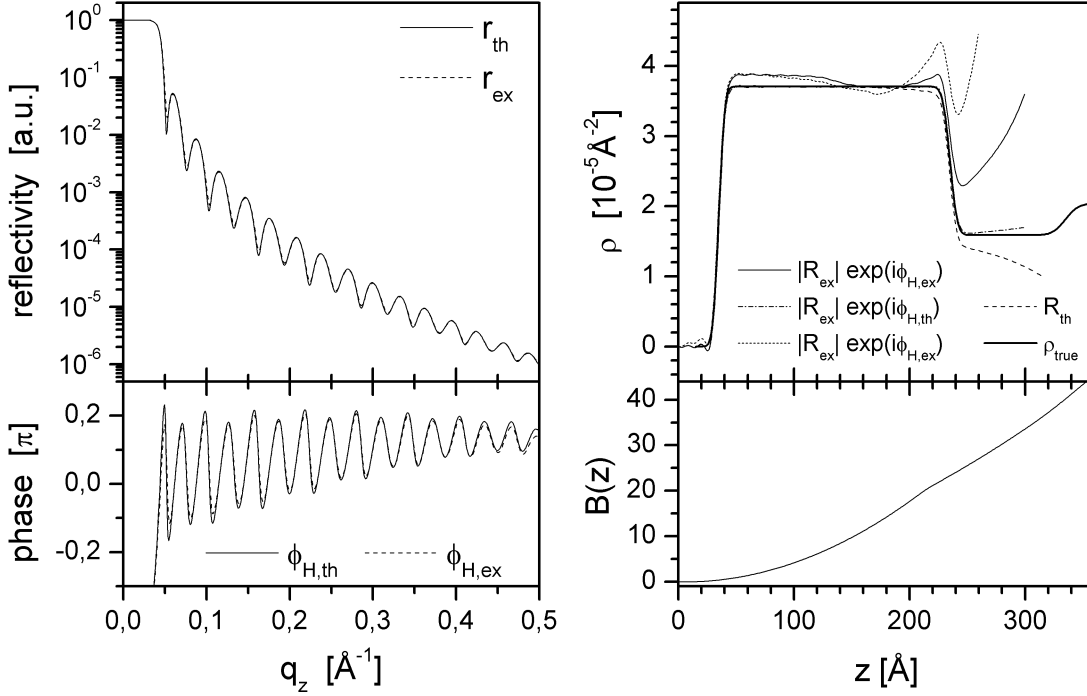


Figure 4.2: Example for inversion using the dynamical theory: The original profile (thick solid line in the upper right graph) is to be reconstructed. The upper right panel shows the corresponding reflectivity r_{th} (solid line) along with the "experimental" reflectivity r_{ex} generated from r_{th} . The lower left graphic depicts the Hilbert-phases $\phi_{H,th}$ and $\phi_{H,ex}$. They were calculated from r_{th} and r_{ex} , respectively. The lower right panel depicts the dimensionless quantity B . Different reflection coefficients $R(q_z)$, obtained by combining phases $\phi_{H,th}$ and $\phi_{H,ex}$ with the reflectivities r_{th} and r_{ex} , have been inverted. The resulting density profiles are represented by the thin lines in the upper right panel.

sample system has a structure such that one may assume that $R(q)$ has no zeros in the upper-half complex plane, then the phase is given by the Hilbert phase,

$$\phi_H(q_z) = \pi - \frac{2q}{\pi} \int_0^{+\infty} \frac{\ln|r(q')|}{q'(q' - q)} dq' \quad , \quad (4.14)$$

which is determined by the reflectivity alone. The potential $V_H(z)$ may then be calculated straightforwardly by applying the inversion algorithms described above using the reflection coefficient $R_H(q_z) = \sqrt{r(q_z)} \exp[i\phi_H(q_z)]$ as input data.

An example for the inversion within the dynamical framework is depicted in Fig. 4.2: The profile to reconstruct is represented by the thick solid line in the upper right panel. It is chosen such that its reflection coefficient has no zeros in the UHP and hence the Hilbert phase $\phi_H(q_z)$ is known to be sufficient for the inversion. The theoretical reflection coefficient $R_{th}(q_z) = \sqrt{r_{th}(q_z)} \exp[i\phi_{H,th}(q_z)]$ was calculated. An "experimental" reflectivity $r_{ex}(q_z)$ was generated by adding

noise and convoluting with a gaussian resolution function (upper left panel). Then its Hilbert phase $\phi_{H,ex}(q_z)$ was calculated. Different combinations of $\phi_{H,th}(q_z)$, $r_{th}(q_z)$ and $\phi_{H,ex}(q_z)$, $r_{ex}(q_z)$ are used to build a reflection coefficient that is then inverted using the so-called *layer-stripping technique* [122]. The obtained profiles are represented by the thin lines in the upper right panel. All profiles give a good description of the surface-near part of $\rho_{true}(z)$ but differ from it with increasing depth starting at around $100 - 110 \text{ \AA}$. This corresponds to $B = ML^2 \approx 5$ (see lower left panel). For the theoretical reflection coefficient the agreement between the original and the reconstructed profile is satisfactory up to $\approx 200 \text{ \AA}$, corresponding to $B \approx 18$.

4.2.2 Including pre-knowledge

In case of doubts about either the correctness or the uniqueness of the obtained solution $V_H(q_z)$, the influence of possibly present zeros in the UHP has to be checked.

Since all profiles obtained by flipping zeros to the UHP are equiprobable in the mathematical sense, only pre-knowledge about the sample can help to decide which profiles are the most likely ones.

Knowledge of the surface-near part of $V(z)$

Let us assume that a profile $V(z)$ with spatial extent L is known *exactly* in the surface-near region $0 \leq z \leq \epsilon L$, where $\epsilon \in [0, 1]$. Then the following procedure can be used to obtain a profile V_N with $V_N(z) = V(z)$, $0 \leq z \leq \epsilon L$ and $r(V_N) = r(V)$:

Step 1: Compute the reflection coefficient $R_H(q_z) = \sqrt{r(q_z)} \exp[i\phi_H(q_z)]$, where $\phi_H(q_z)$ is the Hilbert-phase of the given reflectivity $r(q_z)$.

Step 2: Compute $g(t)$ on $0 < t < 2\epsilon$ for V given on $[0, \epsilon]$ using Eqs. (4.10) – (4.12).

Step 3: Starting with $N = 1$, minimize the functional

$$J(A_N) = \|g(A_N) - g_0\|_{L^2(0,2\epsilon)}^2 \quad , \quad (4.15)$$

where $A_N = \{a_n | n = 1 \dots N\}$, $g(A_N) = \mathcal{FT} \{R_H(q_z)B(A_N, q_z)\}$ and $B(A_N, q_z)$ is the Blaschke product

$$B(A_N, q_z) = \prod_{n=1}^N \frac{q_z - a_n}{q_z - a_n^*} \frac{q_z + a_n^*}{q_z + a_n} \quad . \quad (4.16)$$

N is increased until $J(A_N) = 0$ or, in practice, $J(A_N)$ does not further decrease with increasing N .

Step 4: Compute V_N from $R_N(q_z) = R_H(q_z)B(A_N, q_z)$ using Eqs. (4.9) – (4.12).

The limitations of the above procedure are given by the size of ϵ , i.e. the ratio between the known and the unknown part of $V(z)$ and the amount of features in the known region $0 < z < \epsilon$. A detailed description of the algorithm along with the rationalization of the convergence and numerical examples can be found in Refs. [72][122]. The depth-dependent numerical instability of the inverse method does not cause a serious problem since the known part of the profile is in general small. In practice, however, this algorithm can be applied in very rare situations. Real samples are usually grown from a substrate and hence the surface-near part depends on the *unknown* underlying structure. Furthermore, the measurement of the reflectivity itself can lead to modifications of the surface², as will be shown in Chapter 7.

4.3 Inverse methods in the framework of kinematical scattering theory

In the dynamical theory the reflection $R(q_z)$ depends in a non-linear manner on the scattering potential $V(z)$. This non-linearity leads to inversion schemes including differential and integral equations, where numerical instabilities and error propagation become a serious problem. In the kinematical approximation, the relation between the density profile and the reflection $R(q_z)$ is linear and the resulting inversion schemes are simpler from the mathematical point of view. However, the failure of the kinematical approximation in the region of total external reflection leads to difficulties on the physics side of the inverse problem. A recovery of the potential $V(z)$ from the reflection coefficient $R(q_z)$ by a single inversion step, as described in Section 4.2, becomes impossible and iterative procedures must be used instead.

Several inversion schemes for x-ray reflectivities in the kinematical approximation have been developed in the past, most of which are based on the so-called *box-refinement technique* (see e.g. [39][40][93]), that is briefly outlined in the next section.

4.3.1 The Box-refinement technique

For a density profile of spatial extent L in the interval $[-L/2, L/2]$ the structure factor $F(q)$ is completely determined by its values at $q_n = n\Delta q$, where $\Delta q =$

²The influence of the x-rays on the sample, the so-called *radiation damage*, is a well known but often hushed up phenomenon.

$2\pi/L$, and is given by the Shannon sampling theorem

$$F(q) = \sum_{n=-\infty}^{+\infty} F(n\Delta q) \frac{\sin[\pi L(q - n\Delta q)]}{\pi L(q - n\Delta q)} . \quad (4.17)$$

For $2M + 1$ non-zero values $F(m\Delta q')$, where $\Delta q' < \Delta q$, the above equation becomes [39][40][93]

$$F(m\Delta q') = \frac{\Delta q'}{\Delta q} \sum_{n=-M}^M F(n\Delta q') \frac{\sin\left[\pi \frac{\Delta q'}{\Delta q}(m - n)\right]}{\pi \frac{\Delta q'}{\Delta q}(m - n)} . \quad (4.18)$$

or in matrix notation $\mathbf{H} \cdot \mathbf{F} = \mathbf{F}$ where the elements of the matrix \mathbf{H} are

$$H_{lk} = \frac{\Delta q'}{\Delta q} \frac{\sin\left[\pi \frac{\Delta q'}{\Delta q}(l - k)\right]}{\pi \frac{\Delta q'}{\Delta q}(l - k)} . \quad (4.19)$$

Since \mathbf{H} is hermitian, there are (orthogonal) eigenvectors \mathbf{u}_j with eigenvalues λ_j such that $\mathbf{H} \cdot \mathbf{u}_j = \lambda_j \mathbf{u}_j$. Since the \mathbf{u}_j form a complete set, there exist unique expansions for $\mathbf{H} \cdot \mathbf{F}$ and \mathbf{F} :

$$\mathbf{H} \cdot \mathbf{F} = \sum_j f_j \mathbf{H} \cdot \mathbf{u}_j = \sum_j f_j \lambda_j \mathbf{u}_j \quad (4.20)$$

$$\mathbf{F} = \sum_j f_j \mathbf{u}_j = \sum_j f_j \lambda_j \mathbf{u}_j . \quad (4.21)$$

The latter equation can only be fulfilled if the eigenvalues of the eigenvectors contributing to \mathbf{F} are unity. The box-refinement technique is then given by the iteration procedure:

Step 1: Start with an initial estimate of the sample structure $\rho_0(z)$ and the observed structure factor $|F(q_z)| = \sqrt{r(q_z)/r_F(q_z)}$.

Step 2: Calculate $F_0(q_z) = \mathcal{FT} \{\rho'_0(z)\}$.

Step 3: Calculate $F_{n+1}(q_z) = |F(q_z)| \exp\left[i \arg \left\{ \widehat{F}_n(q_z) \right\}\right]$, where $\widehat{\mathbf{F}}_{\mathbf{n}} = \mathbf{H} \cdot \mathbf{F}_{\mathbf{n}}$.

Step 4: Repeat Step 3 until $\|\widehat{\mathbf{F}}_{\mathbf{n}} - \mathbf{F}_{\mathbf{n}}\| < \epsilon$.

Step 5: Obtain the final profile $\rho_N(z) = \int_0^z \mathcal{FT}^{-1} \{F_N(q_z)\} dZ$.

The convergence of the above scheme has been rationalized [39][40] by the fact that the operation

$$\widehat{F}_{\mathbf{n}} = \mathbf{H} \cdot \mathbf{F}_{\mathbf{n}} = \mathbf{H} \sum_j f_{n,j} \mathbf{u}_j = \sum_j f_{n,j} \lambda_j \mathbf{u}_j \quad (4.22)$$

preserves the components of \mathbf{F}_n corresponding to eigenvalues $\lambda_j \approx 1$, whereas all other components will be diminished. Eq. (4.22) may be restated by

$$\mathbf{H} \cdot \mathbf{F}_n = \mathcal{FT}^{-1} \{ \Pi_L(z) \mathcal{FT} \{ F_n(q_z) \} \} = \mathcal{P}_A F_n(q_z) \quad (4.23)$$

where $\Pi_L(z) \equiv 1$ for $z \in [0, L]$ and equal to zero otherwise. Step 3 in the above procedure may then be written in terms of so-called *projectors* :

$$F_{n+1}(q_z) = \mathcal{P}_B \mathcal{P}_A F_n(q_z) \quad , \quad (4.24)$$

where \mathcal{P}_A imposes the real-space constraint, $\frac{d}{dz}\rho(z) = 0$ for $z \notin [0, L]$, and \mathcal{P}_B projects $\mathcal{P}_A F_n(q_z)$ on the space B defined by the q_z -space constraint $|F_n(q_z)| = |F(q_z)|$. Eq. (4.24) together with Eq. (4.23) is known as the *Gerchberg-Saxton* algorithm [58][103], that is successful applied to phase-retrieval problems in many fields of physics, see e.g. [38][56][67]. Although convergence has not been proven yet, the algorithm has been shown to be at least non-diverging.

It should be emphasized that the box-refinement technique is based on the linear relationship between $F(q_z)$ and $\frac{d}{dz}\rho(z)$ via the Fourier transform. Therefore it can be easily applied to the analysis of rocking curves in x-ray diffraction [83][100][99], where the momentum transfer is sufficiently large so that effects related to the non-linear relationship between $r(q_z)$ and $\rho(z)$ can be neglected. When applied to reflectivities the initial estimate of the sample structure $\rho_0(z)$ should be such that $r_{obs}(q_z) \approx r_0(q_z)$ within the q_z -region dominated by dynamical effects in order to achieve convergence [82].

Recently [20], the box-refinement technique was restated in a more mathematical way using the theory of **P**rojection **O**n **C**onvex **S**ets (POCS), see e.g. Refs. [38][67]. Compared to previous works, the constraint $\rho(z) > 0$ was taken into account and a genetic algorithm was used to search for alternative profiles. However, the shortcoming of the kinematical approximation at small q_z has not been solved and an initial profile ρ_0 is still required to achieve convergence.

4.3.2 Inversion methods proposed by Sanyal et al.

SANYAL and coworkers worked intensively on the development of inverse and model-independent analysis schemes for x-ray reflectivities. Examples are reported in Refs. [12][13][18][123][124][125]. Although many of the reported methods have been adapted to the respective sample system under investigation, two underlying basic inversion schemes exist.

Inversion within the Born approximation

Given is the reflectivity $r_{obs}(q_z)$ and an initial density profile ρ_0 that contains the pre-knowledge on the sample structure and that is typically obtained from fitting

a simple sample-model to $r_{obs}(q_z)$. In the kinematical approximation the quotient of $r_{obs}(q_z)$ and the reflectivity $r_0(q_z)$ of the profile ρ_0 is given by

$$\frac{r_{obs}(q_z)}{r_0(q_z)} = \frac{|F_{obs}(q_z)|^2}{|F_0(q_z)|^2} , \quad (4.25)$$

where the Fresnel reflectivity $r_F(q_z)$ of both reflectivities is assumed to be identical. Taking the square-root and multiplying both hand-sides by $\exp[i\phi_{obs}(q_z)]$ and $\exp[-i\phi_0(q_z)]$ yields

$$\sqrt{\frac{r_{obs}(q_z)}{r_0(q_z)}} \exp[i\Delta\phi(q_z)] = \frac{|F_{obs}(q_z)| \exp[i\phi_{obs}(q_z)]}{|F_0(q_z)| \exp[i\phi_0(q_z)]} , \quad (4.26)$$

where $\Delta\phi(q_z)$ is the difference between the known phase $\phi_0(q_z)$ and the unknown phase $\phi_{obs}(q_z)$. With $\frac{d}{dz}\rho(z) = \int F(q_z) \exp(iq_z z) dq_z$, $Q = \sqrt{q_z^2 + q_c^2}$, and making use of the convolution theorem one obtains the iterative inversion scheme

$$\frac{d\rho_{n+1}(z)}{dz} = \frac{d\rho_n(z)}{dz} * \mathcal{FT} \left\{ \sqrt{\frac{r_{obs}(Q)}{r_n(Q)}} \exp[i\Delta\phi_n(Q)] \right\} , \quad (4.27)$$

where the reflectivity r_n is calculated in dynamical theory using the Parratt-formalism (see Section 2.2). Setting the phase-difference $\Delta\phi_n(Q) \equiv 0$ and setting $\frac{d}{dz}\rho_{n+1}(z) \equiv 0$ for $z \notin [0, L]$, as reported in [12][13][124], the above formula becomes identical to the box-refinement technique, reformulated in real-space.

Inversion within the DWBA

The iterative inversion scheme described in the previous section suffers from instability: The fact that $r_{obs}(Q)/r_n(Q)$ is obtained by linearization of the dynamical reflectivities may result in an divergence of the iterative procedure.

To overcome this instability the use of the **D**istorted **B**orn **W**ave **A**pproximation (DWBA), see e.g. [66][131], was proposed, which is more accurate in the region of total external reflection but fails for large q_z . For a profile $\rho(z) = \rho_0(z) + \Delta\rho(z)$, where $\Delta\rho(z)$ is a small perturbation of $\rho_0(z)$, the reflection coefficient is given by [123][125]:

$$R(q_z) = ir_0(q_z) + (2\pi b_t/q_z) [a(q_z)^2 \Delta\tilde{\rho}(Q) + b(q_z)^2 \Delta\tilde{\rho}(Q)^*] , \quad (4.28)$$

where $b_t = e^2/mc^2 = 2.8179 \cdot 10^{-5} \text{ \AA}$ is the Thompson scattering length. $r_0(q_z)$ is the reflection coefficient of the film with average electron density ρ_0 , $a(q_z)$ and $b(q_z)$ are the coefficients for the transmitted and reflected amplitudes in this film, respectively, and $Q = \sqrt{q_z^2 - 16\pi\rho_0}$ is the wavevector-transfer inside the layer. Solving the above expression for $\Delta\tilde{\rho} = \mathcal{FT} \{\rho(z)\}$ leads to an iterative inversion scheme [104] similar to those described in the previous section. The main shortcoming of this method is its restriction to sample systems with small deviations $\Delta\rho(z)$ from a single homogeneous film on a substrate.

4.4 Previously obtained results

The inversion scheme described in this section is based on the work of SANYAL and coworkers, but makes explicit use of the known Hilbert-phase. Originally developed by A.K. DOERR, the method was first applied to study the wetting behavior of organic liquids, see e.g. [47][48][49].

A computer program for the inversion of x-ray reflectivities using the kinematical approximation was written [175] and successful applied to study the interfacial structure of metal-polymer interfaces [166][167]. Later on, the algorithm was used to study the structure and the mixing behavior of binary wetting films [111][112].

4.4.1 The inversion scheme

The algorithm requires a starting profile $\rho_0(z)$, which contains the available *a priori* information about the sample system. The profile differs from the unknown profile $\rho_{obs}(z)$ by

$$\Delta\rho(z) = \rho_{obs}(z) - \rho_0(z) \quad (4.29)$$

Fourier transforming Eq. (4.29) yields

$$\begin{aligned} \Delta\tilde{\rho}(q_z) &= \tilde{\rho}_{obs}(q_z) - \tilde{\rho}_0(q_z) \\ &= \frac{i\rho_\infty}{q_z} [F_0(q_z) - F_{obs}(q_z)] \quad , \end{aligned} \quad (4.30)$$

where $F_0(q_z)$ and $F_{obs}(q_z)$ are the complex structure factors of the initial profile $\rho_0(z)$ and unknown profile $\rho_{obs}(z)$, respectively. The structure factor $F_0(q_z)$ is obtained from $\rho_0(z)$, while for $F_{obs}(q_z)$ only its modulus $|F_{obs}(q_z)| = \sqrt{r_{obs}(q_z)/r_F(q_z)}$ is known. Splitting the structure factors in modulus and phase yields

$$\Delta\tilde{\rho}(q_z) = \frac{i\rho_\infty}{q_z} \left[|F_0(q_z)| - \sqrt{\frac{r_{obs}(q_z)}{r_F(q_z)}} \exp[i\Delta\phi(q_z)] \right] \exp[i\phi_0(q_z)] \quad , \quad (4.31)$$

where the phase-difference $\Delta\phi(q_z) = \phi_0(q_z) - \phi_{obs}(q_z)$ is the only unknown quantity. In the following, this scheme is referred to as the *phase-guessing method*[?]. In case of the simplest approximation, $\Delta\phi(q_z) \equiv 0$, Eq. (4.31) becomes equivalent to the inversion scheme proposed by SANYAL ET AL., see Eq. (4.27). A better approximation for $\Delta\phi(q_z)$ may be obtained by taking the difference of the Hilbert phases $\phi_{H,obs}(q_z)$ and $\phi_{H,0}(q_z)$, which can both be calculated from the modula of the respective scattering factors:

$$\begin{aligned} \Delta\phi(q_z) &= \phi_{H,0}(q_z) - \phi_{H,obs}(q_z) \\ &= \frac{2q_z}{\pi} \int_0^\infty \frac{1}{\zeta^2 - q_z^2} \ln \left| \frac{F_{obs}(\zeta)F_0(q_z)}{F_{obs}(q_z)F_0(\zeta)} \right| d\zeta \quad . \end{aligned} \quad (4.32)$$

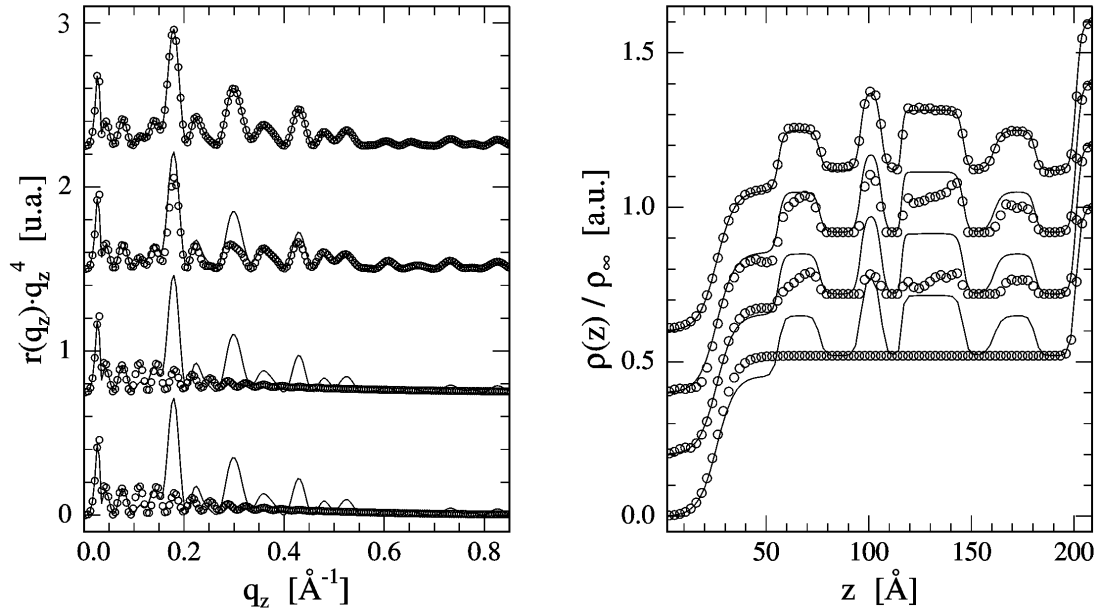


Figure 4.3: Example for inversion with the *phase-guessing method*: The solid line represents the unknown profile (right panel) and its reflectivity (left panel). The inversion starts with a one-layer profile (right panel, lowest line with symbols) and generates a new profile (right panel, second line with symbols from below). Its reflectivity (left panel, second line with symbols from below). The iterative application of the inversion step leads to a perfect reconstruction of the unknown sample structure (data taken from [176]).

The contributions of the zeros to $\Delta\phi(q_z)$ is not taken into account. Like the inversion schemes discussed before, Eq. (4.31) is used iteratively. The profile $\rho_{n+1}(z) = \rho_n(z) + \Delta\rho(z)$ serves as new input profile for the next inversion step. This method is referred to as the *phase-guessing method*.

4.4.2 Numerical examples

Fig. 4.3 shows an example for the application of the inversion scheme based on the *phase-guessing method*. The right panel contains the density profiles. The solid line represents the unknown density profile $\rho_{obs}(z)$ that has to be reconstructed. As starting profile $\rho_0(z)$ a simple one-layer model is chosen (lowest open circles). Only the overall thickness and the roughness of the surface agree with that of $\rho_{obs}(z)$. The left panel contains the corresponding reflectivities. The solid line shows the reflectivity of the unknown sample structure. The lowest line with open circles is the reflectivity $r_0(q_z)$ of the starting profile $\rho_0(z)$. Applying Eq. (4.32) once, one obtains the density profile $\rho_1(z)$ with the corresponding reflectivity $r_1(q_z)$. They are represented by the second line with circles from below.

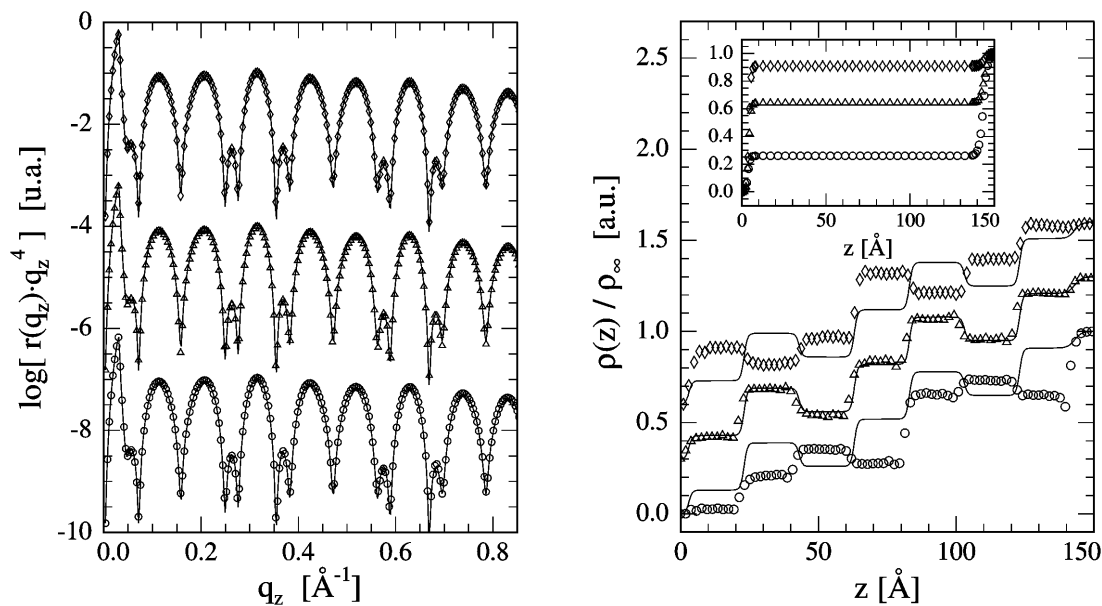


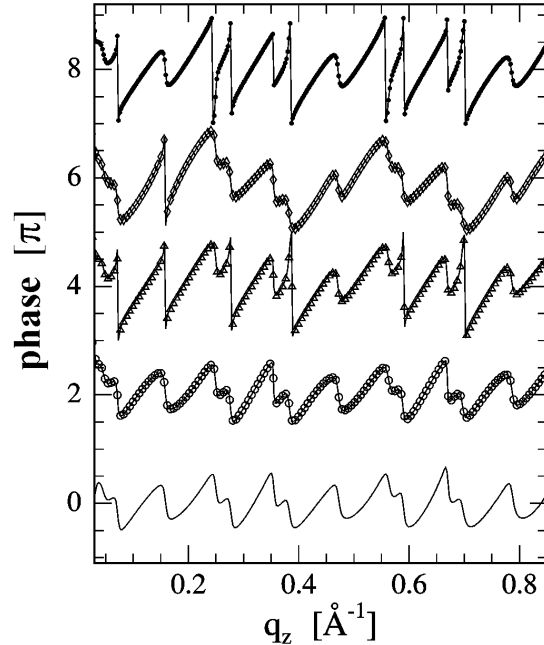
Figure 4.4: Example for the application of the *phase-guessing method* in case of insufficient pre-knowledge about the sample structure: The unknown profile is to be recovered from its reflectivity (solid line in right and left panel, respectively). Starting the inversion with profiles (inset of right panel) one obtains different solutions (symbols, right panel). Their reflectivities (symbols, left panel) are indistinguishable from that of the unknown profile. The corresponding phases are shown in Fig. 4.5 (data taken from [176]).

With increasing number of the iterations (third curves from below) the profile converges towards the unknown sample structure. The final density profile is almost indistinguishable from the solution. Note that in the presented example additional information about the unknown profile was necessary to ensure the convergence of the algorithm.

4.4.3 Determination of alternative density profiles

In the previous example the pre-knowledge about the sample structure was sufficient to ensure the convergence towards the desired solution. This is usually not the case and ambiguities about the uniqueness of the obtained density profile may arise. In such cases the result of the inversion algorithm may depend on the starting profile $\rho_0(z)$. An example is presented in Figs. 4.4 and 4.5. The solid lines in the right and the left panel of Fig. 4.4 are the profile $\rho_{obs}(z)$ to be reconstructed and its normalized reflectivity $r_{obs}(q_z)$, respectively. The sample structure consists of eight layers of equal thickness (20\AA). As starting profiles simple one-layer systems were chosen, but each with a different density of the layer (inset, right panel). The inversion algorithm leads to reflectivities (sym-

Figure 4.5: Phases of the structure factors shown in Fig. 4.4 obtained by the *phase-guessing method*: The topmost curve (black dots) is the phase belonging to unknown profile. The lowest curve (solid line) is the Hilbert phase calculated from $|F_{obs}(q_z)|$. The three phases in the middle correspond to the profiles of the respective symbol in Fig. 4.4. The phases are shifted by 2π for clarity (data taken from [176]).



bols, left panel) that are even on the logarithmic scale indistinguishable from $r_{obs}(q_z)$, while the corresponding density profiles (symbols, right panel) are all different. A perfect reconstruction of the unknown density profile $\rho_{obs}(z)$ is only achieved if the initial profile in the middle (triangles) is chosen. The other two profiles contain only characteristic features of the desired solution. Fig. 4.5 shows the corresponding phases of the reflection coefficients. The lowest phase (solid line) is the Hilbert phase calculated from $|F_{obs}(q_z)|$. The topmost curve (filled circles) is the unknown phase $\phi_{obs}(q_z)$. The other three phases correspond to the reflection coefficients of the profiles obtained from the inversion (Fig. 4.4, right panel). The phase of the bottom profile (open circles) has no zeros and is the Hilbert profile $\rho_H(z)$. The phase of the profile that agrees well with the unknown profile (open triangles) almost coincides with the exact phase.

4.5 Experimental solution of the phase problem

Throughout the previous sections the analysis of a single reflectivity from one sample system was discussed leading to the phase-problem and ambiguities of the reconstructed profile.

A reconstruction of the sample structure and hence the solution of the phase-problem becomes possible if two or more reflectivities are obtained from slightly modified experiments. In these experiments either the probing radiation is modified or some (known) part of the sample itself is modified in a controlled manner, whereas the unknown part of the sample remains unchanged. Among those schemes, polarized neutron scattering experiments were reported [84][90][91][92].

Furthermore a controlled variation of some parts of the profile has been done in Refs. [8][110][49]. However, these procedures are drastically limited to special sample systems. Anomalous scattering schemes were proposed in Ref. [125] while the use of absorption has also been discussed in Refs. [83][80][100][99]. The drawback of all these schemes is the limitation to particular systems which can not be generalized to arbitrary sample systems.

Chapter 5

Experimental influences

Most of the scientific work done on inverse scattering theory deals with perfect data as input. In practice, measured reflectivities suffer from imperfections such as finite resolution functions and the counting statistics which have to be taken into account when applying inverse or model-independent methods to measured data.

5.1 Measuring x-ray reflectivities

Figure 5.1 depicts the *in-plane* scattering geometry. The impinging x-rays enclose an angle α_i with the surface and have a wavevector \mathbf{k}_i . When the detector encloses an angle α_f with the surface, scattered photons with the momentum $\hbar\mathbf{k}_f$ are probed. The components q_x and q_z of the wavevector transfer $\mathbf{q} = \mathbf{k}_f - \mathbf{k}_i$ are given by

$$q_x = k (\cos \alpha_f - \cos \alpha_i) \quad (5.1a)$$

$$q_z = k (\sin \alpha_f + \sin \alpha_i) \quad , \quad (5.1b)$$

Figure 5.1: In-plane scattering geometry: The wavevectors of the incident and scattered x-rays are \mathbf{k}_i and \mathbf{k}_f , with the incidence and exit angles α_i and α_f , respectively. $\Phi = \alpha_i + \alpha_f$ is the scattering angle. The momentum transfer is defined by $\mathbf{q} = \mathbf{k}_f - \mathbf{k}_i = (q_x, q_z)$. For reflectivity $\alpha_i = \alpha_f$, corresponding to a q_x scan with $q_x = 0$.

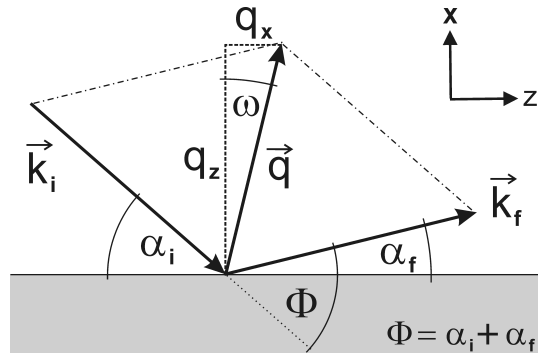
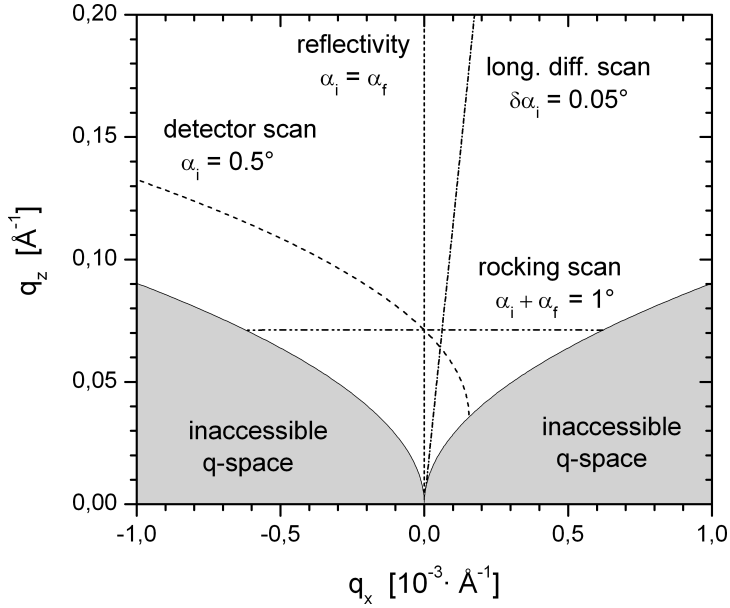


Figure 5.2: Scans in the reciprocal plane (q_x, q_z) calculated for $\lambda_{CuK\alpha} = 1.54056\text{\AA}$: Specular scan (---), longitudinal scan (—), rocking scan (—·) and detector scan (—). The shadowed region is inaccessible in experiments ($\alpha_i < 0$ or $\alpha_f < 0$).



where $k = 2\pi/\lambda$ and λ is the wavelength of the monochromatic x-rays. With the introduction of the scattering angle $\Phi = \alpha_i + \alpha_f$ ¹ and the angle $\omega = \alpha_i - \alpha_f$, different types of scans may be defined:

- *Specular Scan*: α_i and α_f are changed simultaneously such that the specular condition $\alpha_i = \alpha_f = \Phi/2$ holds. The scan runs along the q_z axis, i.e. $q_x = 0$.
- *Rocking Scan*: The scattering angle $\Phi = \alpha_i + \alpha_f$ remains constant and $\omega = \alpha_i - \alpha_f$ is changed within the limits $\pm\Phi/2$. This corresponds to a rotation of the sample at fixed x-ray source and detector positions. For small q_z the scan runs approximately parallel to the q_x axis.
- *longitudinal diffuse Scan*: α_i and α_f vary simultaneously such that the condition $\alpha_i = \Phi/2 + \delta\alpha_i$ holds. The scan runs on a line at an angle $\delta\alpha_i$ with respect to the q_z axis. $\delta\alpha_i$ should be greater than the width of the specular peak and is typically on the order of a few hundredth of a degree.
- *Detector Scan*: The incident angle α_i is kept constant and only the detector angle α_f is changed. The scan contains information about the lateral and the vertical structure of the sample.

Although the *specular scan* is of main interest in this thesis, the other types of scans are not less important for the analysis of x-ray reflectivities since they give access to information that is required for a proper extraction of the *true specular* reflectivity from the measured reflectivity, as will be discussed in section 5.3.3.

¹Often, the scattering angle Φ is also denoted by 2θ .

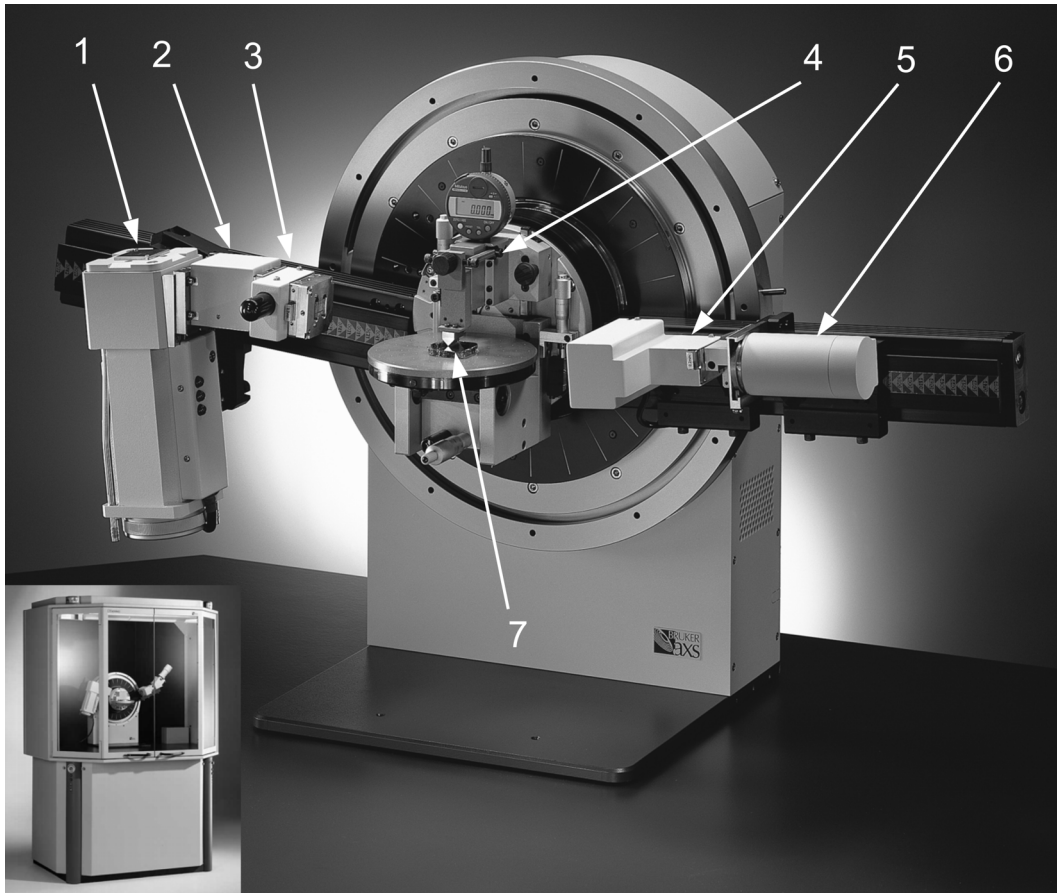


Figure 5.3: Bruker-AXS D8 ADVANCE diffractometer: Components on the primary side: x-ray tube (1), Goebel-Mirror (2) and rotary absorber (3). At the center of the diffractometer: Knife-edge collimator (KEC) (4) and the sample (7). Components on the detector-side: Slit-box (5) and detector (6). The diffractometer is set up in a radiation protection enclosure (see inset).

5.2 Experimental setup: The Bruker AXS D8 diffractometer

All measurements performed throughout this work have been performed on the D8 DISCOVER and D8 ADVANCE diffractometers from BRUKER AXS [1]. Since the experimental setup for reflectivity measurements is quite similar on both machines, only that of the D8 ADVANCE will be shortly described in the following. The x-rays are emitted by a sealed x-ray tube with a line focus copper anode running at 40kV and 40mA. The divergent and polychromomatic beam hits a parabolically bent graded multilayer, the so-called *Göbel-Mirror* [95][126] at grazing angles. If the mirror is placed in the beam path so that the line focus of the X-ray source is at the focus of the parabola, then approximately 1° of the di-

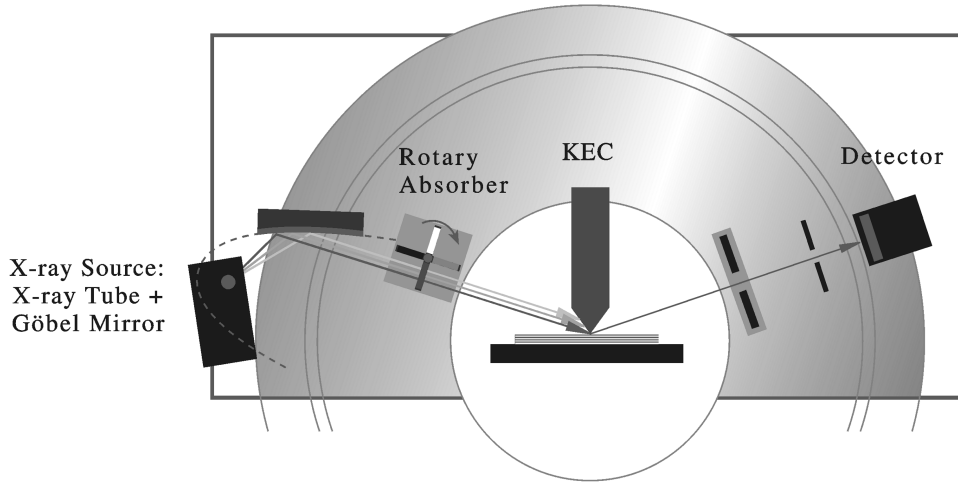


Figure 5.4: Sketch of the experimental setup depicted in Fig.5.3: Radiation emitted by the x-ray source and reflected by the Göbel mirror, irradiates the sample surface. The knife-edge collimator (*KEC*) reduces effects due to the finite sample size. The reflected beam hits the detector after passing a double-slit system, that defines the acceptance angle for the detector. An automated rotary absorber placed before the sample prevents the detector from the saturation region and avoids unnecessary irradiation of the sample.

vergent primary beam is collected and transformed into a highly parallel and quasi-monochromatic beam. All diffractometers were equipped with 3rd generation Göbel-mirrors. These mirrors have an angle of acceptance of 0.6° . The reflected beam of size $10 \times 1 \text{ mm}^2$ has a divergence $\Delta\alpha_i \approx 0.02^\circ$. The intensity integrated over the beam is $2 \cdot 10^9$ cps and the intensity ratio between Cu K_β and Cu K_α is smaller than 1 : 1000. Before hitting the sample, the beam passes an automated 4-fold absorber with (approximate) absorption factors of 1, 8, 80 and 8000, respectively. An 0.2 mm wide slit reduces the width of the beam that is used to probe the sample. The reflected beam passes two slits of width 0.2 mm. These define the acceptance angle $\Delta\alpha_f$ for the *NaI*-Detector which has a dynamical range up to $2.5 \cdot 10^5$ cps. The direct-through beam intensity of the described setup is $2 - 4 \cdot 10^8$ cps for a beam of size $10 \times 0.2 \text{ mm}^2$.

5.3 Influence of the experimental setup on the measurement

In this section the influence of the experimental setup on the measured reflectivity is discussed and procedures for the correction of these influences are discussed.

5.3.1 The resolution function

The divergence of the impinging x-rays $\Delta\alpha_i$ and the acceptance angle $\Delta\alpha_f$ of the detector determine the resolution of the experimental setup. For glancing angles α_i and α_f , the resolution in \mathbf{q} -space parallel and perpendicular to the sample surface (see Fig.5.1) is given by the total differentials of Eqs. (5.1a) and (5.1b),

$$\delta q_x = (\Delta\lambda/\lambda) q_x + k (\alpha_f \Delta\alpha_f + \alpha_i \Delta\alpha_i) \quad (5.2a)$$

$$\delta q_z = (\Delta\lambda/\lambda) q_z + k (\Delta\alpha_f + \Delta\alpha_i) \quad , \quad (5.2b)$$

where $\Delta\lambda/\lambda$ is the wavelength spread. In general $\Delta\lambda/\lambda < 10^{-4}$ and assuming a symmetrical experimental setup, i.e. $\Delta\alpha = \Delta\alpha_i = \Delta\alpha_f$, Eqs. (5.2a) and (5.2b) simplify to [59]

$$\delta q_x \approx q_x \Delta\alpha \quad \text{and} \quad \delta q_z \approx 2k \Delta\alpha \quad , \quad (5.3)$$

where $\Delta\alpha$ is given by the HWHM of the direct-through beam. Whenever $\Delta\alpha_i \approx \Delta\alpha_f$ does not hold, the calculation of δq_x and δq_z becomes more complicated (see e.g. [42][96][129]) and detailed knowledge about the optical components is required.

In the following, it is assumed that Eq. (5.3) holds and that the resolution function $g(q_z)$ is of Gaussian type, i.e.

$$g(q_z) = \exp(-q_z^2/2\delta q_z^2) \quad . \quad (5.4)$$

The *measured* reflectivity $I(q_z)$ is then given by $(r * g)(q_z)$, where the asterisk denotes the convolution.

5.3.2 Influence of the finite sample size

For very small incident angles the sample surface is almost parallel to the incident beam and parts of the incoming radiation do not hit the sample. This leads to a reduction of the reflected intensity and the measured reflectivity becomes less than unity in the region of total external reflection.

If a rectangular shaped beam of width b_i and a sample of length L is assumed, the angle of complete irradiation of the sample is given by $\alpha_b = \arcsin(b_i/L)$ and the reflected intensity is reduced by a factor

$$\beta = \begin{cases} \sin \alpha_i / \sin \alpha_b, & \alpha_i \leq \alpha_b; \\ 1, & \alpha_i > \alpha_b. \end{cases} \quad (5.5)$$

If the slit sizes b_f on the detector side are smaller than b_i , the observed intensity is further reduced by a factor b_i/b_f . A detailed description for the calculation of β in case of non-rectangular beam profiles is given in [59]. The correction factor

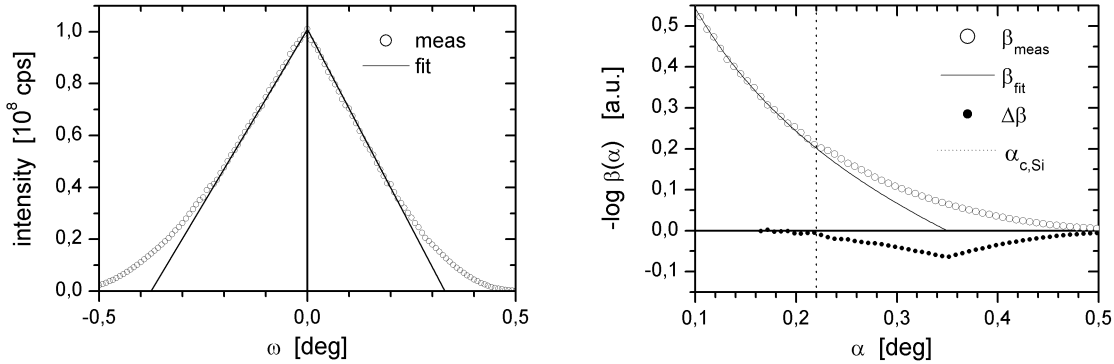


Figure 5.5: The left panel shows the measured "footprint scan" (open circles) and its triangular approximation with $\alpha_b \approx 0.35^\circ$ (line). The right panel depicts the negative logarithm of β_{meas} (open circles), β_{fit} (thin line), and their coefficient $\Delta\beta$ (thick line). The use of β_{fit} leads to a reduction of the observed intensity at angles near the tails of the "footprint scan". The critical angle of silicon $\alpha_c \approx 0.22^\circ$, indicated by the vertical dotted line, is given for comparison.

β can be easily obtained during the alignment of the sample from a rocking-curve around $\omega = 0$ with $2\theta = 0$ and is simply given by

$$\beta(\alpha) = 1 - [I(\alpha) + I(-\alpha)] / I_0 \quad . \quad (5.6)$$

The use of β obtained from the measurement appears to be advantageous since it allows arbitrary beam shapes and does not make any assumptions about the shape of the sample. As long as $\beta(\alpha) \approx 0$ for $\alpha > \alpha_c$, the impact of β restricts to the region of total external reflection and may be ignored. But if $\beta(\alpha) \gg 0$ for $\alpha > \alpha_c$, an exact estimation of β becomes necessary as illustrated in Figure 5.5. The left panel shows a "footprint scan" (open circle). The values $\alpha_b^- \approx -0.38^\circ$ and $\alpha_b^+ \approx 0.33^\circ$ are obtained by fitting lines to the left and right side of the measured triangle-like curve. The logarithms of $1/\beta(\alpha)$ calculated from Eq. (5.5) with $\alpha_b = (\alpha_b^- + \alpha_b^+)/2$ and from Eq. (5.6) are depicted in the right panel by the thin line and the open circles, respectively. The difference $\log \Delta\beta = \log(\beta_{fit}/\beta_{meas})$ is represented by the filled circles and becomes significant around 0.35° . For silicon, $\alpha_{c,Si} \approx 0.22^\circ$ (vertical dotted line), this difference is beyond the region of total external reflection. By using Eq. (5.5) instead of Eq. (5.6) one analysis a reflectivity that is slightly reduced near 0.35° would be analyzed.

In general, the differences are small, but since they affect the non-linear region of the reflectivity, they can cause significant changes in the density profile when model-independent methods are used for the data-analysis.

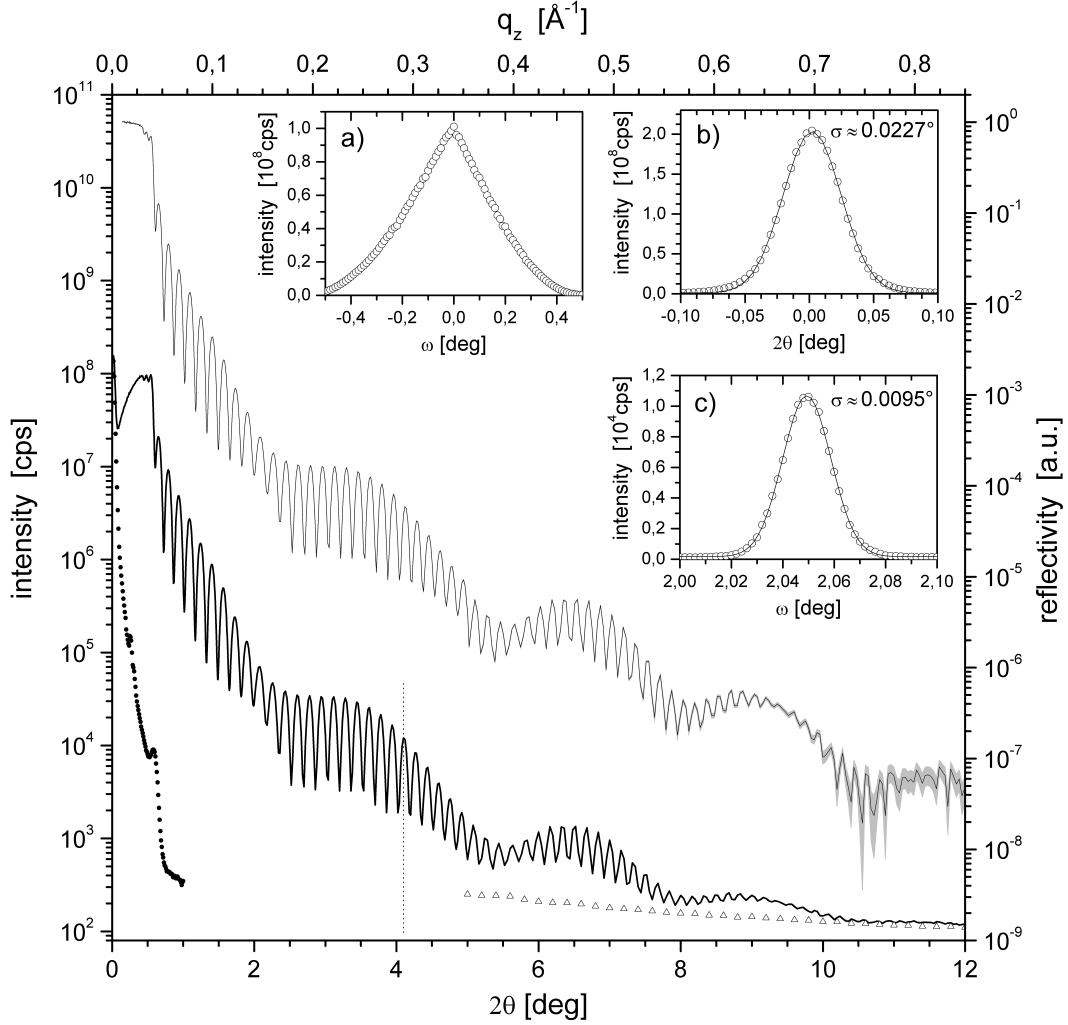


Figure 5.6: Set of measurements required for the correct analysis of the reflectivity: Measured reflectivity (lower full line), detector scan at $\omega = 0$ (filled circles) and longitudinal diffuse scan with $\delta\alpha = 0.05$ (open triangles). Additional scans are shown in the insets: a) ”footprint scan”, b) primary-beam scan (open circles) along with gaussian fit (line) and c) rocking-scan at large angles (see vertical dotted line in main plot). The upper full line depicts the *true specular* reflectivity (TSR) normalized to unity (right axis). The grey band around the TRS represents the errors due to statistics.

5.3.3 The true specular reflectivity

Besides the instrumental resolution and the geometrical factor discussed in the previous sections, additional intensity is measured under the specular condition. The measured intensity can be described by

$$I_{obs}(q_z) = I_0[\beta(q_z)r(q_z)] * g_{kw}(q_z) + I_{db}(q_z) + I_{ds}(q_z) \quad , \quad (5.7)$$

where I_0 is the intensity of the primary beam and $\beta(q_z)$ is given by Eq. (5.6). $g_{kw}(q_z)$ is the gaussian resolution function as defined Eq. (5.4) with $\delta q_z = kw$, where k is the wave vector and w is the HWHM of the direct-beam. Furthermore, I_{ds} is the contribution from diffuse scattering randomly scattered into the specular direction and

$$I_{db}(q_z) = I_0 \delta(q_z - kw/2) * g_{kw}(q_z) \quad (5.8)$$

is the intensity due to the direct-through beam hitting the detector at small angles [59]. To obtain the true specular reflectivity, the contributions I_{db} and I_{ds} are subtracted from the measured reflectivity $I_{obs}(q_z)$. I_{db} is obtained from a detector-scan (see section 5.1) around $2\theta = 0$ with $\alpha_i = 0$ and I_{ds} is estimated from a longitudinal diffuse scan with an offset $\delta\alpha$ slightly larger than the width of a specular peak in q_x -direction. At high angles the specular reflected intensity I_{obs} approaches the diffusely scattered intensity I_{ds} and, in case of poor statistics, the case $I_{obs} < I_{ds}$ may occur, resulting in a negative mean value for the true specular reflectivity, which - of course - is not possible.

At this point some comments on the counting-statistics have to be made: The measured quantity is not the scattered intensity I itself, but a discrete number of photons N falling into the detector within a time t . Thus, N is Poisson distributed with an error $\Delta N = \sqrt{N}$. For sufficiently large N , a normal distribution with $\sigma = \Delta N$ is assumed [132]. If N counts have been measured in a time t using an absorption factor A , the intensity is equal to $I = NA/t$ with an error $\Delta I = \sqrt{NA}/t$. This should be kept in mind when the inverse methods are used for the analysis of the reflectivity. If, for example, $I_0 = 2 \cdot 10^8$ cps, $A = 10000$ and $t = 0.5$ s, then $I = 10^4$ and hence $\Delta I = 100$, which is an error of 1%. For direct analysis methods, this does not cause problems since they usually refine the reflectivity on a logarithmic scale and a weighting of the data with respect to their statistical errors is easy to implement.

An example for the extraction of the true specular reflectivity from the measured reflectivity is depicted in Figure 5.6: The measured reflectivity I_{obs} is represented by the thick solid line. At small angles the contribution of the direct-through beam and the influence of the finite sample size are clearly visible. The detector scan for the subtraction of I_{db} and the longitudinal diffuse scan are represented by the filled circles and the triangles, respectively. The additional scans, depicted in the insets are required for a proper analysis of the reflectivity: The "footprint scan" is shown in inset a) and is necessary for the determination of the correction factor β as described in section 5.3.2. The detector-scan of the primary beam (see inset b)) yields $I_0 \approx 2.02 \cdot 10^8$ cps and permits an estimation of the instrumental resolution function, $\Delta\alpha \approx 0.026^\circ$ in the present case. Furthermore, rocking-scans over the specular peak - inset c) shows an example for $2\theta = 4.1^\circ$ - may be necessary if the sample is bent on a macroscopic scale². The true specular

²For details on the analysis and correction of reflectivities from bent samples see Refs. [25][59].

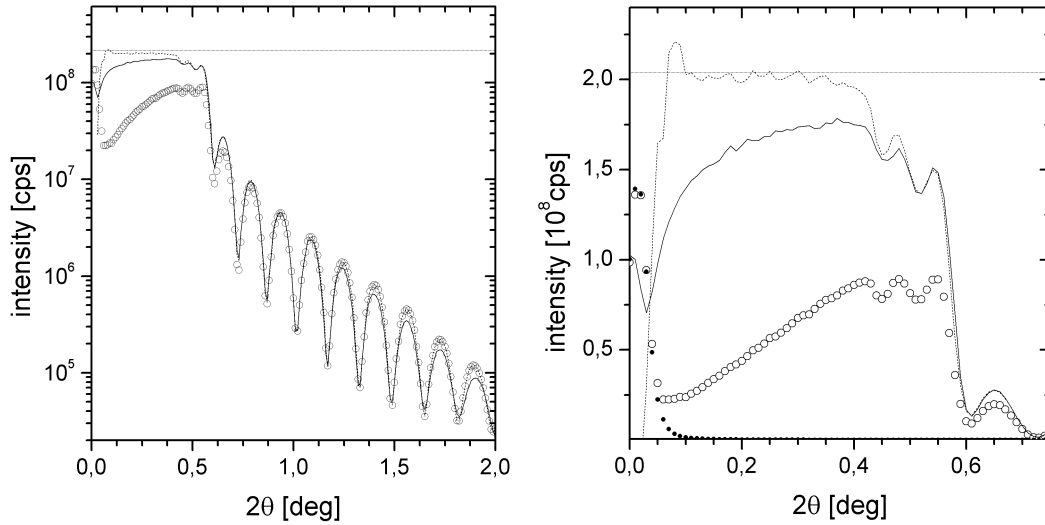


Figure 5.7: Correction of the geometrical factor vs. measurement with KEC: The left panel depicts the reflectivity measured with (symbols) and without (solid line) KEC. The footprint-corrected reflectivity is represented by the dashed line. The horizontal dotted line is the primary beam intensity I_0 . The right panel shows the region of total external reflection on a linear scale. The filled circles represent the detector-scan with $\alpha_i = 0^\circ$.

reflectivity – normalized to unity (right axis) – is represented by the thin solid line and is enclosed by a grey band indicating the statistical errors. In the presented example, the influence of the finite sample size was also corrected by dividing the true specular reflectivity with the factor $\beta(q_z)$. Note that the latter correction is not strictly correct, since it should be done after deconvolution of $I_{obs} - I_{ds} - I_{db}$ with the resolution function $g(q_z)$.

Remarks on the knife-edge collimator (KEC)

Bruker-AXS developed the so-called *knife-edge collimator* (KEC) to reduce the influence of the finite sample size on the measured reflectivity and to obtain a proper region of total external reflection. The KEC (see Fig. 5.4) consist of a "knife" that is approached to the surface of the sample up to a few μm when measuring at small angles. Since the probed quantity in x-ray reflectivity experiments is the electron density averaged over the illuminated area A ,

$$\varrho(z) = \langle \varrho(x, y, z) \rangle_A \quad , \quad (5.9)$$

the removal of the KEC causes a discontinuous change of the illuminated area A and this may lead to an abrupt change of the density profile $\varrho(z)$. This is illustrated in Fig. 5.7. The left panel depicts the reflectivity from a sample measured with (solid line) and without (symbols) KEC. At higher angles both measured

curves do not agree and hence the required scaling of the reflectivity measured with the KEC can not be performed exactly and the scaled reflectivity does not reach the primary beam intensity I_0 (dotted line). In contrast, the reflectivity obtained after correcting the influence of the footprint reaches I_0 and does not suffer from the problems due to the discontinuous transition one has to face when merging the KEC reflectivity at small angles with the reflectivity measured at higher angles without KEC.

Therefore, the use of the KEC for x-ray reflectivity measurements turns out to be disadvantageous and a correction of the reflectivity using the additional scans seems to be preferable. In Ref. [142], the difficulties of analyzing the diffuse scattering of a sample from measurements with the KEC are discussed leading to the same conclusion.

Thus, if not mentioned otherwise, all reflectivities presented in the work have been measured without the KEC and the influence of the footprint has been corrected using the additional scans as already discussed.

5.3.4 Convolution vs. Deconvolution

The measured intensity may be written as $I(q_z) = \mathcal{A}r(q_z)$. The operator \mathcal{A} contains the effects of the experimental setup. Typically, the application of inverse methods to the analysis of the reflectivity requires the true specular reflectivity $r(q_z) = \mathcal{A}^{-1}I(q_z)$ and hence the inverse operator \mathcal{A}^{-1} .

From Eq. (5.7) it follows that the true specular reflectivity $r(q_z)$ is obtained by correcting the influence of the "footprint" after deconvolution with the resolution function. Formally the inverse operator of the measurement process may be written as

$$r(q_z) = \frac{1}{I_0\beta(q_z)} \mathcal{FT}^{-1} \left\{ \mathcal{FT} \{I(q_z) - I_{db}(q_z) - I_{ds}(q_z)\} / \mathcal{FT} \{g_{k_0w}\} \right\} \quad , \quad (5.10)$$

where the deconvolution is formulated in terms of Fourier transforms. However, deconvolution is well-known to be an ill-posed and instable problem. In the present case, the simple division by $\mathcal{FT} \{g_{k_0w}\}$ will lead to an amplification of the high-frequency noise of $\mathcal{FT} \{I(q_z) - I_{db}(q_z) - I_{ds}(q_z)\}$.

Thus, more sophisticated deconvolution techniques should be applied. Often used and simple is the iterative *Lucy-Richardson* (LR) deconvolution [88][119],

$$r_{n+1} = \mathcal{P}_C \left\{ r_n \frac{I}{g * r_n} * g \right\} \quad , \quad (5.11)$$

where r_n is the deconvoluted reflectivity at the iteration step n , I is the measured intensity and g is the (gaussian) resolution function. Additional constraints, e.g. $r \leq 1$, are imposed by the projector \mathcal{P}_C . This deconvolution scheme preserves the probability and ensures the positivity of r_n .

A more sophisticated deconvolution algorithm using LR-deconvolution and *Tikhonov-regularization* (TR), see e.g. [147], is reported in [161]. The TR-algorithm seeks to minimize the functional

$$J(r) = \|I - g * r\| - \lambda \|H * r\| \quad , \quad (5.12)$$

where H is a high-pass filter. The first term expresses the fidelity to the data and the second term imposes the smoothness of the restored reflectivity. The regularization parameter λ represents the trade-off between fidelity to the data and the smoothness of the deconvoluted reflectivity. It was found [161], that the LR-deconvolution yields better results at small angles than the TR-method does. At higher angles, where the reflectivity changes only little and the signal-to-noise ratio is worse, the TR-deconvolution provides better results. The main drawback of the TR-method compared to LR-deconvolution is that it does not allow the implementation of constraints and that the positivity of the solution is not guaranteed, which is mandatory for reflectivities. Moreover, the TR-deconvolution involves operations on large matrices and is therefore much more time-consuming than LR-deconvolution.

Figure 5.8 shows an example for the deconvolution of a reflectivity using the LR-algorithm. A reflectivity r_{Theo} , represented by the dotted line, was calculated from a known sample structure and then convoluted with a gaussian resolution of $\delta\theta = 0.008^\circ$ (full line). The open circles depict the deconvoluted reflectivity r_{DC} , that agrees well with r_{Theo} except around the pronounced minima and very close to the critical angle.

It should be emphasized, that in the presented example the resolution function was known exactly. When deconvoluting real experimental reflectivities, the resolution function is only known approximately and results may differ even more from the true underlying reflectivity.

Different deconvolution algorithms are discussed in Ref. [67] and a compact overview about the most commonly used methods is given in the review article of STARK [140].

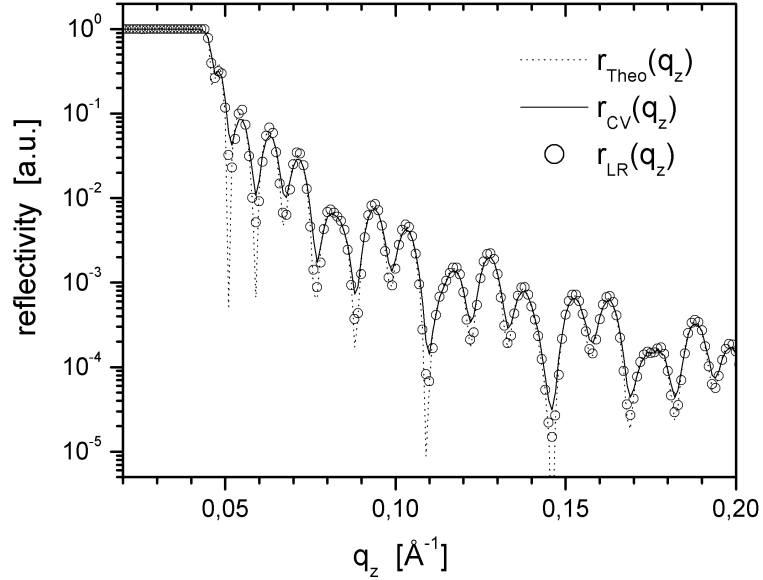
The fact that deconvolution is an unstable procedure leads to the question whether the reflectivity needs to be deconvoluted to apply inverse methods, or not. The answer depends on the used inversion schemes: Inverse methods that directly calculate the density profile by a single step require the deconvoluted reflectivity to obtain the complex reflection coefficient.

Iterative inversion techniques as well as model-independent analysis schemes do in general not require a deconvoluted reflectivity (or reflection coefficient) as input data, because they seek to minimize $\Delta r = r_{obs} - r_{calc}$. Since convolution with the resolution function is a linear transform, it is unique and then one has

$$r_n(q_z) \rightarrow r_{obs}(q_z) \quad \Leftrightarrow \quad |(\mathcal{A}r_n)(q_z) - I_{obs}(q_z)| \rightarrow \epsilon(q_z) \quad , \quad (5.13)$$

where $\epsilon(q_z)$ is some small positive number accounting for the noise. The main profit of analyzing the deconvoluted reflectivity is speed since the computation

Figure 5.8: Deconvolution of a reflectivity using the Lucy-Richardson method: Theoretical reflectivity (dotted line), convoluted reflectivity (full line) and the deconvoluted curve (open circles). A gaussian resolution function with $\delta\theta = 0.008^\circ$ was used.



of $I_n = \mathcal{A}r_n$ at each iteration step is much more time-consuming than the calculation of $r_{obs} = \mathcal{A}^{-1}I_{obs}$ only once. Furthermore, it should be noted that the deconvolution of the measured data requires several data points within the extent of the resolution function g , i.e. $\Delta q_z \approx \sigma_g$. For the region of total external reflection the scattered intensity is high and only a few seconds of measurement time per datum are necessary. But at higher angles of incidence where the reflected intensity is very small, the finer sampling results in time-consuming experiments. A reasonable and computationally efficient strategy is therefore to solve the inverse problem for $r_{obs}(qz) \approx \mathcal{A}^{-1}I_{obs}$ in a first step to obtain some approximate solution. Then, in a second step, one refines $\Delta I = I_{obs} - \mathcal{A}r_{calc}$, which involves the more time-consuming but stable convolution procedure.

Chapter 6

The new inversion algorithm

In Chapter 4 an overview over the state-of-the-art of the analysis techniques for x-ray reflectivities was given.

Inversion schemes based on the dynamical (quantum) scattering theory require the complex reflection coefficient – and hence knowledge of the phase – as input data. Furthermore, they suffer from instability even when applied to accurate, synthetic data and the required deconvolution of the measured reflectivity with the instrumental resolution function is an additional source of instability.

The second class of analysis schemes are the model-independent fitting techniques. They are stable when using the dynamical scattering theory and permit the easy implementation of the experimental influences. The main drawback is the high computational effort: Non-linear optimization techniques require the inversion of matrices. This becomes time-consuming when large sample systems are analyzed.

Inversion schemes based on the kinematical approximation have advantages: They do not require the phase of the reflection coefficient, are easy to implement and they are stable – provided that the kinematical approximation is valid. This, however, imposes a strong constraint to the sample systems they can be applied to. Almost all applications reported in the literature appear in connection with the study of soft-matter films, liquids or layers of moderate thickness, typically up to at most $100\text{\AA} - 200\text{\AA}$. The increasing instability of these methods with increasing sample thickness L follows from the fact that the number of Fourier components falling into the region of dynamical scattering at small q_z is proportional to L .

To overcome this problem, a new iterative inversion method for the analysis of x-ray reflectivity is proposed. The method is based on the kinematical approximation and is stabilized by making use dynamical scattering theory to ensure its convergence. Furthermore, this method expands the profile by a set of *eigendensities*. These eigendensities are discrete approximations of the eigenfunctions of the linear inverse problem which consists in the reconstruction of a compact

supported function from its partially known Fourier transform [14][15].

6.1 The linear inverse problem

In the following we briefly review the *linear inverse problem* which may be stated as follows:

Recover the function $f(z)$ with compact support on $[-L, L]$ from its Fourier transform $F(q) = \int f(z) \exp(-iqz) dz$ given on $[-B, B]$.

The finite Fourier transform of $F(q)$, $q \in [-B, B]$, is – up to a factor $1/2\pi$ – equal to

$$\begin{aligned} \widehat{f}(z) &= \int_{-B}^B F(q) \exp(iqz) dq \\ &= \int_{-B}^B \left(\int_{-L}^L f(\zeta) \exp(-iq\zeta) d\zeta \right) \exp(iqz) dq \\ &= 2B \int_{-L}^L f(\zeta) \operatorname{sinc}[B(z - \zeta)] d\zeta \quad . \end{aligned} \quad (6.1)$$

Next, consider the integral equation

$$\lambda_n \psi_n(z) = \int_{-L}^L \operatorname{sinc}[B(z - \zeta)] \psi_n(\zeta) d\zeta \quad (6.2)$$

where $\operatorname{sinc}(x) \equiv \sin(x)/x$ and $\psi_n(z)$ and λ_n are the eigenfunctions and the associated eigenvalues, respectively. The eigenfunctions $\psi_n(z)$ are known as *prolate spheroidal wavefunction* (PSWF). Their properties have been fully explored by D. SLEPIAN ET AL. in Refs. [77][78][135][136]. For example, the PSWF form complete bases on $[-L, L]$ and $[-\infty, \infty]$ and are doubly-orthogonal, i.e.

$$\int_{-L}^L \psi_n(z) \psi_m(z) dz = \lambda_m \delta_{m,n} \quad \text{and} \quad \int_{-\infty}^{\infty} \psi_n(z) \psi_m(z) dz = \delta_{m,n} \quad . \quad (6.3)$$

where $\delta_{m,n}$ denotes the Kronecker-delta being 1 for $m = n$ and 0 otherwise. Furthermore, they are (scaled) Fourier transforms of themselves,

$$\Psi_n(q) = \int_{-L}^L \psi_n(z) \exp(-iqz) dz = c_n \psi_n(qL/B) \quad , \quad (6.4)$$

where $c_n = i^n \sqrt{2L\lambda_n}$. The real eigenvalues λ_n fulfill

$$1 > \lambda_0 > \lambda_1 > \dots > 0 \quad (6.5)$$

and are equal to the fraction of energy of ψ_n falling into $[-B, B]$, i.e.

$$\lambda_n = \int_{-B}^B |\Psi_n(q)|^2 dq / \int_{-\infty}^{\infty} |\Psi_n(q)|^2 dq \quad . \quad (6.6)$$

The spectrum of the eigenvalues consist of three parts: About $BL/2\pi$ eigenvalues are very close to 1, followed by order $\log(2c/\pi)$ eigenvalues which decay exponentially from 1 to almost 0. The remaining eigenvalues are all very close to zero.

The recovery of $f(z)$ from $F(q)$ known on $[-B, B]$ is then given by

$$f(z) = \sum_{n=0}^{\infty} \frac{\beta_n}{\lambda_n} \psi_n(z) \quad \text{with} \quad \beta_n = \int_{-B}^B F(q) \Psi_n(q) dq \quad . \quad (6.7)$$

This may also be done by first extending $F(q)$ from $[-B, B]$ to $[-\infty, \infty]$ via

$$F(q) = \sum_{n=0}^{\infty} c_n \Psi_n(q) \quad \text{with} \quad c_n = \frac{1}{\lambda_n} \int_{-B}^B F(q) \Psi(q) dq \quad (6.8)$$

and then Fourier transforming $F(q)$ to obtain $f(z)$. Note that the instability of the inverse problem, or of the analytical continuation of $F(q)$, results from the almost vanishing λ_n in the denominators in Eqs. (6.7) and (6.8), respectively. Despite their useful properties, the PSWF are rarely used in data analysis because they are defined by the integral equation Eq. (6.2) which makes their numerical evaluation difficult. Approximations of the PSWF by a series of Legendre polynomials or by *truncated* sinc-matrices are proposed in Refs. [168] and [69], respectively.

However, much better suited for practical purposes are the *discrete prolate spheroidal sequences* (DPSS), which may be viewed as the discretization of the PWSF [137] and will be discussed in the following.

6.1.1 The Discrete Prolate Spheroidal Sequences

Consider the real-valued sequence $\{\psi(n)\}$ defined on $[0, N-1]$ with unit energy

$$\sum_{n=0}^{N-1} [\psi(n)]^2 = 1 \quad (6.9)$$

whose Fourier transform is given by

$$\Psi(f) = \sum_{n=0}^{N-1} \psi(n) \exp[-2\pi i f n] \quad . \quad (6.10)$$

From Parseval's theorem it follows that the Ψ -functions fulfill on $[-1/2, 1/2]$

$$\int_{-1/2}^{1/2} \Psi(f) \Psi^*(f) df = 1 \quad . \quad (6.11)$$

The energy¹ in the band of interest $[-W, W]$, where $0 < W < 1/2$, is given by

$$E = \int_{-W}^W \Psi(f) \Psi^*(f) df \quad . \quad (6.12)$$

Insertion of Eq. (6.10) yields

$$\begin{aligned} E &= \int_{-W}^W \left(\sum_{n=0}^{N-1} \psi(n) \exp[-2\pi i f n] \right) \left(\sum_{m=0}^{N-1} \psi(m) \exp[2\pi i f m] \right) df \\ &= \sum_{m=0}^{N-1} \sum_{n=0}^{N-1} \psi(n) \psi(m) \frac{\sin 2\pi W(n-m)}{\pi(n-m)} \end{aligned} \quad (6.13)$$

To account for the constraint of fixed energy one (see Eq. (6.11)) a Lagrange multiplier λ is used, and one seeks to maximize the quantity

$$I = \sum_{m=0}^{N-1} \sum_{n=0}^{N-1} \psi(n) \psi(m) \frac{\sin 2\pi W(n-m)}{\pi(n-m)} - \lambda \sum_{m=0}^{N-1} [\psi(m)]^2 \quad (6.14)$$

At the maximum of I the partial derivatives

$$\frac{\partial}{\partial \psi(m)} I = \sum_{n=0}^{N-1} \psi(n) \frac{\sin 2\pi W(n-m)}{\pi(n-m)} - \lambda \psi(m) \quad (6.15)$$

must vanish for all n . From the resulting eigenvalue equation

$$\lambda_k \psi_k(m) = \sum_{n=0}^{N-1} \frac{\sin 2\pi W(n-m)}{\pi(n-m)} \psi_k(n) \quad (6.16)$$

one finds N real eigenfunctions $\psi_k(m)$, known as *discrete prolate spheroidal sequences* (DPSS). The $\psi_k(m)$ are orthonormal, i.e.

$$\sum_{n=0}^{N-1} \psi_i(n) \psi_j(n) = \delta_{i,j}. \quad (6.17)$$

For the N real eigenvalues

$$1 > \lambda_0 > \lambda_1 > \dots > \lambda_{N-2} > \lambda_{N-1} > 0 \quad (6.18)$$

holds [137]. The λ_k decay exponentially from 1 to 0 for k -values around $[2WN]^2$.

The Fourier transforms Ψ_k of the k -th DPSS ψ_k are known as *discrete prolate*

¹In signal theory the energy is defined by Eq. (6.12) and is different from the term *energy* used commonly in physics.

² $X = [x]$ denotes the largest integer $X \leq x$.

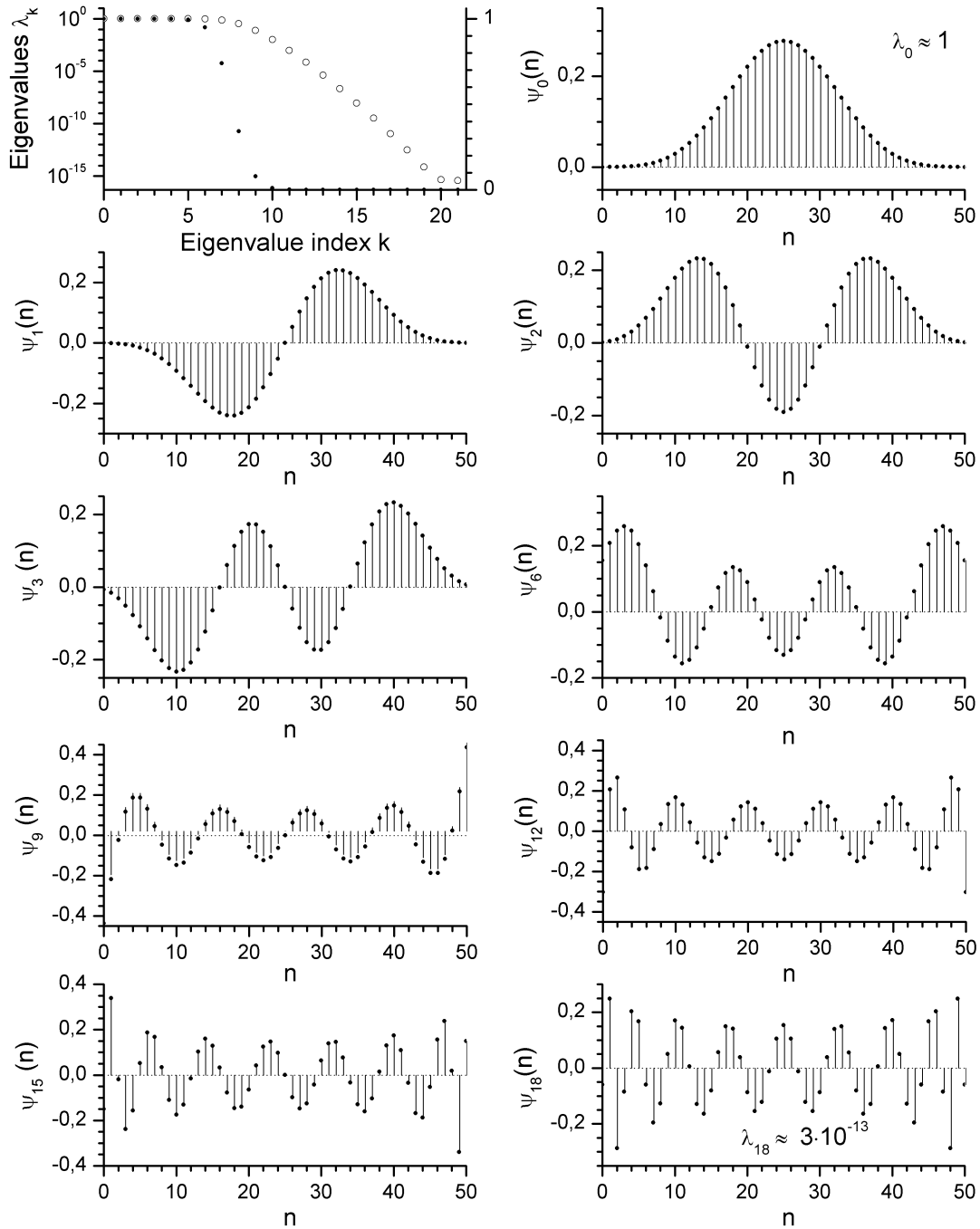


Figure 6.1: Eigenvalues λ_k and eigenvectors $\Phi_k(n)$ of the sinc-kernel for $N = 51$ and $2WN \approx 8$: The eigenvalues λ_k are shown on a logarithmic scale (left axis, open circles) and on a linear scale (right axis, filled circles). Only the Fourier transforms of the eigenvectors up to $k \approx 9$ contribute essentially to the band $[-W, W]$.

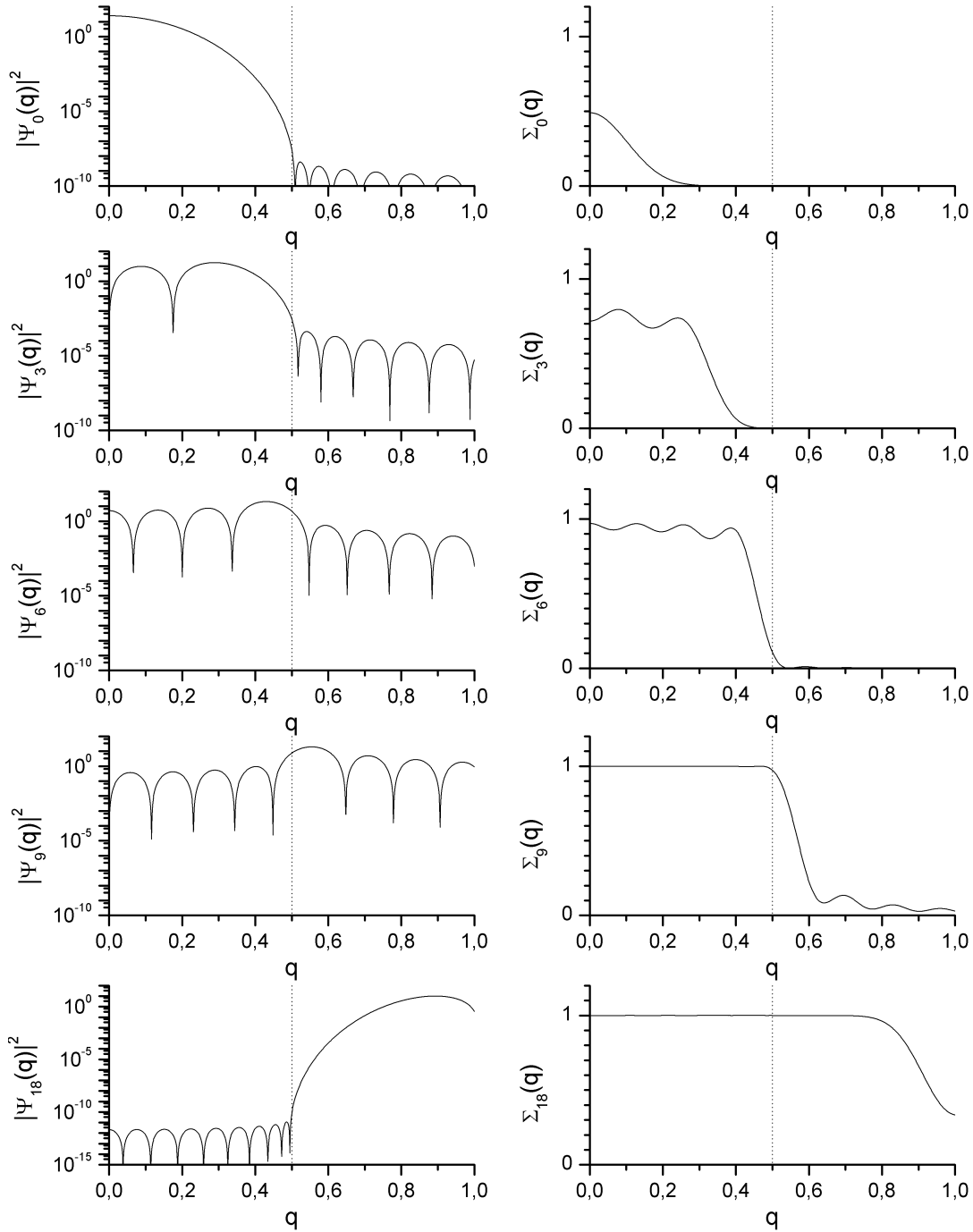


Figure 6.2: Left column: Norms $|\Psi_k(q)|^2$ of the Fourier transforms of the k -th DPSS $\psi_k(n)$. Right column: The Cumulative spectra $\Sigma_k(q)$ of the first k DPSWF $\Psi_k(q)$. The bandwidth $W = 1/32$ is depicted by the vertical dotted line. For $k > 8$, $\Sigma_k(q)$ is almost unity on $[-W, W]$.

spheroidal wave-function (DPSWF) and fulfill the orthogonality conditions

$$\frac{1}{\lambda_k} \int_{-W}^W \Psi_j(q) \Psi_k^*(q) dq = \delta_{j,k} \quad \text{and} \quad \int_{-1/2}^{1/2} \Psi_j(q) \Psi_k^*(q) dq = \delta_{j,k} \quad , \quad (6.19)$$

from which follows that the eigenvalue λ_k is equal to the fraction of spectral power of Ψ_k falling into the band $[-W, W]$, i.e.

$$\lambda_k = \int_{-W}^W |\Psi_k(q)|^2 dq / \int_{-1/2}^{1/2} |\Psi_k(q)|^2 dq \quad . \quad (6.20)$$

Since higher order $\Psi_k(q)$ have almost vanishing λ_k , i.e. have a negligible contribution to the band $[-W, W]$, the cumulative spectrum

$$\Sigma_K(q) = \sum_{k=0}^K |\Psi_k(q)|^2 \quad (6.21)$$

becomes almost unity on $[-W, W]$ for $K > 2WN$. $\psi_k(n)$ and $\Psi_k(q)$ are connected via the transforms

$$\psi_k(n) = \frac{1}{\lambda_k} \int_{-W}^W \Psi(q) \exp(2\pi i q n) dq \quad (6.22)$$

$$\Psi_k(q) = \sum_{n=0}^{N-1} \psi_k(n) \exp(-2\pi i q n) \quad . \quad (6.23)$$

As an example, the DPSS and the DPSWF are depicted in Figures 6.1 and 6.2 for the case $N = 51$ and $W = 0.5/2\pi$ so that $2WN \approx 8.12$. The eigenvalues λ_k are shown in the first panel of Fig. 6.1 on a logarithmic scale (open circles, left axis) as well as on a linear scale (filled circles, right axis). The spectrum of the eigenvalues λ_k consists of three parts. About WN eigenvalues are very close to unity, followed by order $\ln(\pi WN)$ eigenvalues which decay exponentially from 1 to almost zero. The remaining λ_k are all very close to zero, $\approx 10^{-15}$ in the presented case. For $k = 18$, $\lambda_{18} = 3 \cdot 10^{-13}$ and hence the Fourier transform $\Psi_{18}(q)$ of $\psi_{18}(n)$ does (almost) not contribute to the band $[-W, W]$. Fig. 6.2 depicts the norms $|\Psi_k(q)|^2$ along with the cumulative spectra Σ_K . It is clearly visible that the $\Psi_k(q)$ with $k < 2WN$ contribute only to the band $[-W, W]$ (vertical dotted line) whereas those with $k > 2WN$ contribute to the region $|q| > W$. The cumulative spectra $\Sigma_K(q)$ tend to unity on $[-W, W]$ with increasing K and for $K > 10$ one finds $\Sigma_K(q) \approx 1$.

6.1.2 Application of DPSS to the phase-reconstruction problem in x-ray reflectivity

The application of the DPSS to the reconstruction problem in x-ray reflectivity (XRR) is straightforward: Let the structure factor $F(q_z)$ be given on $B_q \equiv$

$[-q_{max}, q_{max}]$ and let $d\rho(z)/dz$ have compact support on $B_L \equiv [0, L]$. We approximate $\rho(z)$ by a piecewise-constant profile, i.e.

$$\rho(z) = \sum_{n=0}^N \Delta\rho_n H(z - n\Delta z) \quad , \quad \frac{d}{dz}\rho(z) = \sum_{n=0}^N \Delta\rho_n \delta(z - n\Delta z) \quad , \quad (6.24)$$

where $\Delta z = L/N \ll \pi/q_{max}$ and $H(x)$ denotes the Heaviside function. The quantity W is then given by $W = q_{max}L/2\pi N$. The DPSS $\psi_k(n) \equiv \psi_k(n\Delta z)$ are then obtained by solving the eigenvalue problem Eq. (6.16). Let us assume that the structure factor is known for all $q_z \in B_q$ and is of the form

$$F(q_z) = \sum_j \gamma_j \Psi_j(q_z) \quad , \quad (6.25)$$

with $\gamma_j = a_j/\lambda_j$. The a_j are obtained by making use of the orthogonality condition given by Eq. (6.19)

$$a_j = \int_{-q_{max}}^{q_{max}} F(q_z) \Psi_j^*(q_z) dq_z \quad . \quad (6.26)$$

The derivative $\Delta\rho(n)$ of the piecewise-constant profile is then given by

$$\Delta\rho(n) = \sum_j \gamma_j \psi_j(n) \quad . \quad (6.27)$$

In principle, the above equation allows the reconstruction of $\Delta\rho(n)$, if $F(q_z)$ is given for all $q_z \in B_q$. Since $\Delta\rho$ has compact support, $F(q_z)$ is an analytical function which has a unique extension on the real axis. However, the problem of analytical continuation is known to be highly sensitive to errors in $F(q_z)$. Eq. (6.27) gives an insight into the ill-conditioning of the reconstruction problem. A small error δa_j in the coefficient a_j with an eigenvalue $\lambda_j \approx 0$ is amplified by $1/\lambda_j$ and results in a large error in $\delta\Delta\rho(n) = \delta a_j/\lambda_j$. Vice versa, the eigenvectors ψ_j with small λ_j have a negligible impact on $F(q_z)$ for $q_z \in B_q$ and hence they can be varied without leading to a remarkable change of $F(q_z)$. Moreover, $F(q_z)$ is only available for a number of discrete q_z -values. Therefore, not all eigenvectors $\{\psi_k, \Psi_k\}$ can be used but only those with eigenvalues $\lambda_k > \epsilon$, where ϵ is some pre-defined limit.

The ψ_k are then subdivided into two groups: The first group consist of those ψ_k with $\lambda_k \approx 1$. Their Fourier transforms $\Psi_k(q_z)$ have an impact on $F(q_z)$ within the available region B_q , so that they are called *resonant* and are written as ψ_k^r . The remaining ψ_k with $\lambda_k \ll 1$ are termed *non-resonant* and denoted by ψ_k^n in the following, since the corresponding $\Psi_k(q_z)$ do not contribute to $F(q_z)$ on B_q . Thus, the resonant ψ_k^r are needed for the reconstruction of $F(q_z)$ on B_q , while the non-resonant ψ_k^n may be used to impose constraints and for regularization purposes.

Construction of the initial profile

Iterative inversion schemes require an initial profile that contains the *a-priori* information about the sample. If no profile is available, the Groove Track Method (GTM) discussed in Section 4.1.2 can be used to obtain a profile $\rho_G(z)$ that fits the measured reflectivity within the region of dynamical scattering. Let this profile consist of N_G slabs with density $\rho_{G,n}$, $n = 1, \dots, N_G$, and thickness $\Delta z_G = \pi/q_G$. Its derivative is given by

$$\frac{d}{dz}\rho_G(z) = \sum_{n=0}^{N_G} \Delta\rho_{G,n}\delta(z - n\Delta z_G) \quad . \quad (6.28)$$

The inversion of the total reflectivity $r(q_z)$ measured on $[0, q_{max}]$ requires a finer spatial resolution. The new z -grid is given by $\Delta z = \Delta z_G/w$, where $w \in \mathbb{N}$ such that $\Delta z < \pi/q_{max}$. The eigendensities ψ_j are then constructed by solving the eigenproblem (6.16) and $d\rho_G(z)/dz$ is projected on the space spanned by the ψ_j . The representation of $d\rho_G(z)/dz$ as a series expansion of the ψ_j is then given by

$$\frac{d}{dz}\rho(n\Delta z) = \sum_{j=0}^J \beta_j \psi_j(n) \quad \text{with} \quad \beta_j = \sum_{n=0}^{N_G} \Delta\rho_{G,n} \psi_j(n) \quad . \quad (6.29)$$

Inversion step using the DPSS

The measured reflectivity $I_{obs}(q_z)$ is only given on a discrete grid $q(m)$ with $m = 0, \dots, M$. At the n -th iteration, the difference of the structure factor $\Delta F(q_z)$ is given by

$$\Delta F_n(m) = \frac{1}{|R_F(m)|} \left(\sqrt{I_{obs}(m)} - \sqrt{(g * r_n)(m)} \right) \exp[i\phi_n(m)] \quad , \quad (6.30)$$

where r_n is the reflectivity of the profile ρ_n calculated within dynamical theory, g is the resolution function and ϕ_n is the phase of the reflection coefficient R_n . The q_z -grid on which $\Delta F_n(m)$ is given is not the same as the grid given by the measurement with I_{obs} and $g * r_n$. It is the grid obtained via the already mentioned transform $q(m) \rightarrow \sqrt{q(m)^2 - q_c^2}$, where q_c is the critical wave-vector transfer estimated from the initial profile ρ_0 . Note that Eq. (6.30) is not exact because the difference between intensities I_{obs} and $g * r_n$ is used. However, in the case of convergence, i.e. $\Delta F_n \rightarrow 0$, we have $g * r_n \rightarrow I_{obs}$ from which $r_n \rightarrow r_{obs}$ follows.

From the equations

$$\Delta F_n(m) = \sum_j \Psi_j(m) \Delta\beta_j^n \quad ; \quad m = 0 \dots M \quad , \quad (6.31)$$

or in matrix notation $\Delta \mathbf{F}_n = \mathbf{P} \cdot \Delta \beta^n$, the variation $\Delta \beta^n$ is simply given by

$$\Delta \beta^n = \tilde{\mathbf{P}} \cdot \Delta \mathbf{F}_n \quad , \quad (6.32)$$

where $\tilde{\mathbf{P}}$ is the pseudo-inverse of \mathbf{P} . The matrix $\tilde{\mathbf{P}}$ has to be computed only once as long as q_c remains unchanged so that the time-consuming inversion of \mathbf{P} can be avoided within the iteration procedure. The change of the profile's derivative³ $\Delta \rho'$ is equal to

$$\Delta \rho' = \sum_j \psi_j \cdot \Delta \beta_j \quad , \quad (6.33)$$

and has to fulfill the boundary condition

$$\int_0^L \Delta \rho'(z) dz = \sum_j \left(\sum_{n=0}^N \psi_j(n) \right) \Delta \beta_j = 0 \quad (6.34)$$

or in matrix notation $\mathbf{a}^T \cdot \Delta \beta = 0$, where $a_j = \sum_{n=0}^N \psi_j(n)$. Note that the latter boundary condition should be fulfilled automatically, since $\Delta F(0) \equiv 0$ always holds and hence $\sum_n \Delta \rho'_n = 0$.

Taking a closer look at the inversion step described above reveals two shortcomings: Let us assume that $I_n(q_z) = I_{obs}(q_z)$ holds for $q_z \in B_G \equiv [-q_G, q_G]$. Then $\Delta F(q_z)$ and hence $|\Delta F(q_z)|$ will vanish for $q_z \in B_G$. The first problem is that the projection onto the solution-space $\{\psi_j\}_{j=0}^J$ does not necessarily preserve $|\Delta F(q_z)| = 0$. Secondly, even if the profile-modification was such that $|\Delta F(q_z)| = 0$ holds on B_G , it follows from the analyticity of $F(q_z)$, that any modification of $|F(q_z)|$ outside B_G will lead to a change of the phase of $F(q_z)$ inside B_G . This is also clear from inspection of the expression of the Hilbert-phase

$$\phi_H(q_z) = -\frac{2q_z}{\pi} \int_0^{+\infty} \frac{\ln |F(q')| - \ln |F(q_z)|}{q'^2 - q_z^2} dq' \quad . \quad (6.35)$$

It then follows, that due to the non-linear relation between $F(q_z)$ and the dynamical reflectivity $r(q_z)$ for $q_z \in B_G$, a variation of $\arg\{F(q_z)\}$ will in general lead to a change of $|r(q_z)|$ and convergence of the iteration procedure is not guaranteed anymore. Therefore, the modification $\Delta \rho'$ must be such that the dynamical reflectivity $r(q_z)$ remains unchanged for $q_z \in B_G$.

For the efficient implementation of this constraint, and also with regard to following sections, a bases for expanding the profile difference $\Delta \rho$, instead of its derivative $\Delta \rho'$, will be derived.

³In the following, the profile's derivative $d\rho(z)/dz = \Delta \rho_n$, see Eq. (6.24), is denoted by ρ' and the change of the profiles derivative $\Delta(d\rho(z)/dz)$ is denoted by $\Delta \rho'$.

6.1.3 Eigendensities for the piecewise-constant density profile

In the kinematical approximation the structure factor is equal to

$$F(q) = \int_0^L \frac{d}{dz} \rho(z) \exp(iqz) dz = iq \int_0^L \rho(z) \exp(iqz) dz \quad , \quad (6.36)$$

where $\rho(z)$ is given in units of the substrates density ρ_∞ . For a variation of the profile $\Delta\rho(z)$ on $[0, L]$ the quantity

$$\Delta\widehat{F}(q) = \frac{\Delta F(q)}{iq} = \int_0^L \Delta\rho(z) \exp(iqz) dz \quad (6.37)$$

is band-limited and we wish to construct bases $\{\psi_k\}$ and $\{\Psi_k\}$ for the expansion of $\Delta\rho(z)$ and $\Delta\widehat{F}(q)$, respectively. Note that the boundary condition $\int_0^L \Delta\rho(z) dz = 0$ is automatically fulfilled. For a piecewise-constant profile consisting of N slabs of thickness d and density $\rho(n)$, the profile variation $\Delta\rho(z)$ may be written as

$$\Delta\rho(z) = \sum_{n=1}^N \Delta\rho(n) H(1/2 - |z/d - n + 1/2|) \quad , \quad (6.38)$$

where $H(x)$ denotes the Heaviside function and $\Delta\rho(n)$ is the variation of the density in the n -th slab. The constraint of unit energy (see Eq. (6.9)) becomes

$$d^2 \sum_{n=1}^N [\Delta\rho(n)]^2 = 1 \quad . \quad (6.39)$$

As in section 6.1.1 we seek to maximize the energy E in the region of interest $[-Q, Q]$ defined by

$$E = \int_{-Q}^Q \Psi(q) \Psi^*(q) dq \quad . \quad (6.40)$$

The Fourier transform $\Psi(q)$ of $\Delta\rho(z)$ is given by

$$\begin{aligned} \Psi(q) &= \int_0^L \Delta\rho(z) \exp(iqz) dz \\ &= \sum_{n=1}^N \Delta\rho(n) \exp[iqd(n - 1/2)] \int_{-d/2}^{d/2} \exp(iqz) dz \\ &= d \operatorname{sinc}(qd/2) \sum_{n=1}^N \Delta\rho(n) \exp[iqd(n - 1/2)] \end{aligned} \quad (6.41)$$

where $\text{sinc}(x) \equiv \sin(x)/x$. Inserting the latter equation in Eq. (6.40) yields

$$\begin{aligned} E &= \sum_{n,m} \Delta\rho(n)\Delta\rho(m) \int_{-Q}^Q \exp[iqd(n-m)] d^2 \text{sinc}^2(qd/2) dq \\ &= \sum_{n,m} \Delta\rho(n)\Delta\rho(m) S_{n,m}(Q, d) \end{aligned} \quad (6.42)$$

with

$$S_{n,m}(Q, d) = \frac{2}{Q} \left\{ f_{n,m+1}(Qd) + f_{n,m-1}(Qd) - 2f_{n,m}(Qd) \right\} \quad (6.43)$$

and

$$f_{n,m}(x) = x(n-m) \text{Si}[x(n-m)] + \cos[x(n-m)] \quad , \quad (6.44)$$

where $\text{Si}(x) \equiv \int_0^x \text{sinc}(t) dt$. Maximization of E requires $\partial E/\partial\Delta\rho(m) = 0$ and applying the constraint Eq. (6.39) leads to

$$\frac{\partial}{\partial\Delta\rho(n)} \left(E - \lambda d^2 \sum_n [\Delta\rho(n)]^2 \right) = 0 \quad (6.45)$$

from which the eigenvalue equation

$$\frac{1}{d^2} \sum_m S_{n,m}(Q, d) \Delta\rho(m) = \lambda \Delta\rho(n) \quad (6.46)$$

follows. Since $S_{n,m}(x) = S_{m,n}(x)$, the matrix \mathbf{S} is hermitian and hence the eigenvalues λ_k and the eigenvectors $\Delta\hat{\rho}_k$ are real.

As an example, selected eigendensities $\psi_k(z)$ and the moduli squared $|\Psi_k(q)|^2$ of their Fourier transforms $\Psi_k(q)$ are shown in Figures 6.3 and 6.4 for a density profile consisting of 50 slabs of thickness $d = 1$ and with $Q = 0.5$, respectively. The uppermost left panel in Fig. 6.3 depicts the eigenvalues λ_k on a linear scale (right axis, filled circles) and on a logarithmic scale (left axis, open circles). The λ_k decay rapidly at $k = 50Qd/\pi \approx 8$. For $k = 18$ the eigenvalue is $\approx 1.4 \cdot 10^{-13}$. The moduli squared of the Ψ_k are shown on a logarithmic scale in the left panels of Fig. 6.4. The vertical dotted line represents $Q = 0.5$. For $k < 8$ the Ψ_k are concentrated in the interval $[-Q, Q]$ and only little power spectral density is outside that interval. For $k \gg 8$, $\Psi_k(q)$ vanishes almost on $[-Q, Q]$, as shown in the lowermost left panel for $k = 18$. The right panels depict the cumulative spectra $\Sigma_k(q)$ which are smooth and almost⁴ equal to unity on $[-Q, Q]$ for $k > 9$.

⁴The reason why $\Sigma_k(q)$ does not converge to 1, but decreases slowly, is not investigated further here.

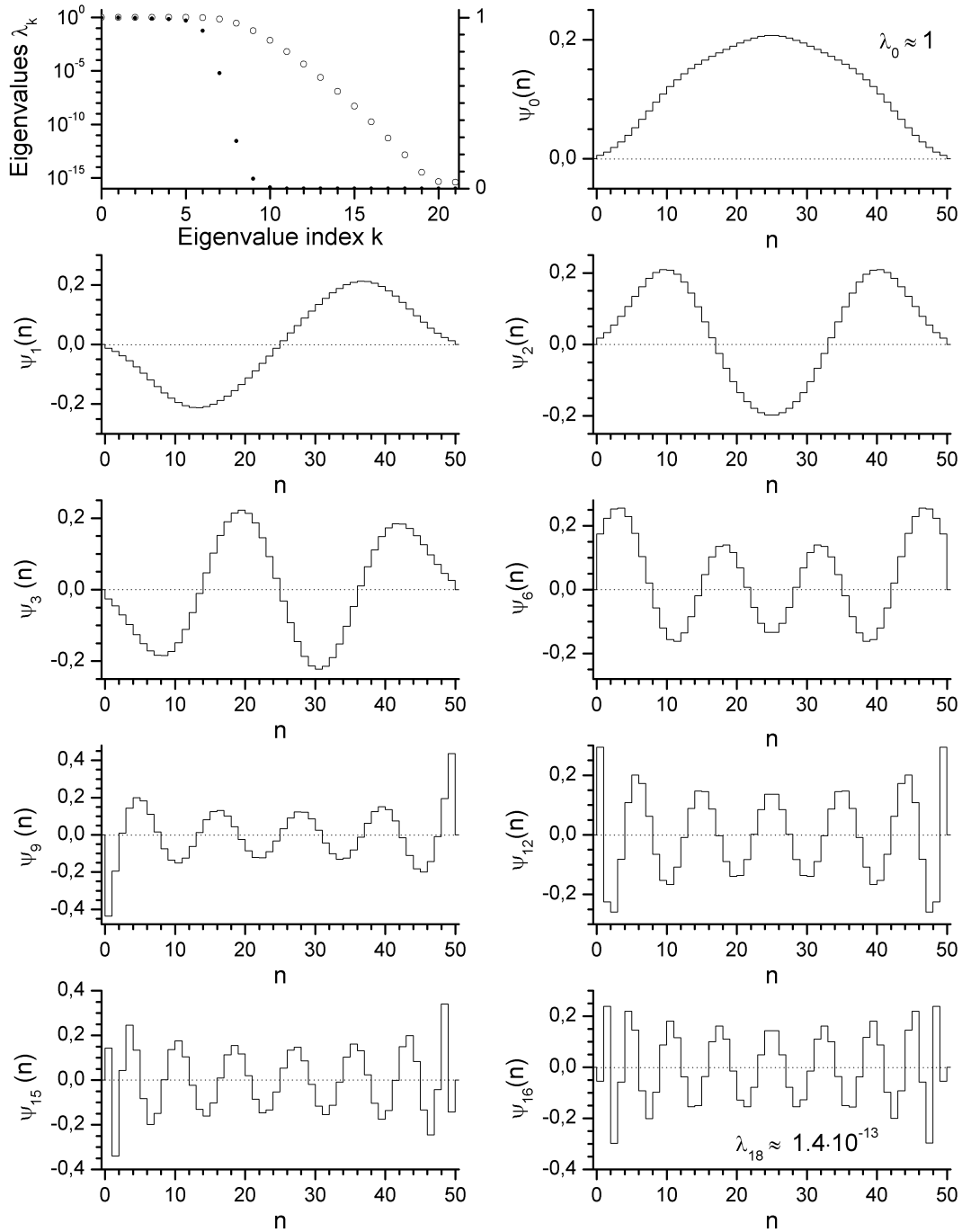


Figure 6.3: Eigendensities $\psi_k(z)$ of a piecewise-constant density profile consisting of 50 slabs of thickness $d = 1$ for $Q = 0.5$: The uppermost left panel depicts the eigenvalues λ_k on a logarithmic scale (left axis, open circles) and on a linear scale (right axis, filled circles). Around $k = 50Qd/\pi \approx 8$ the λ_k decay rapidly. The corresponding Ψ -functions are shown in Fig. 6.4.

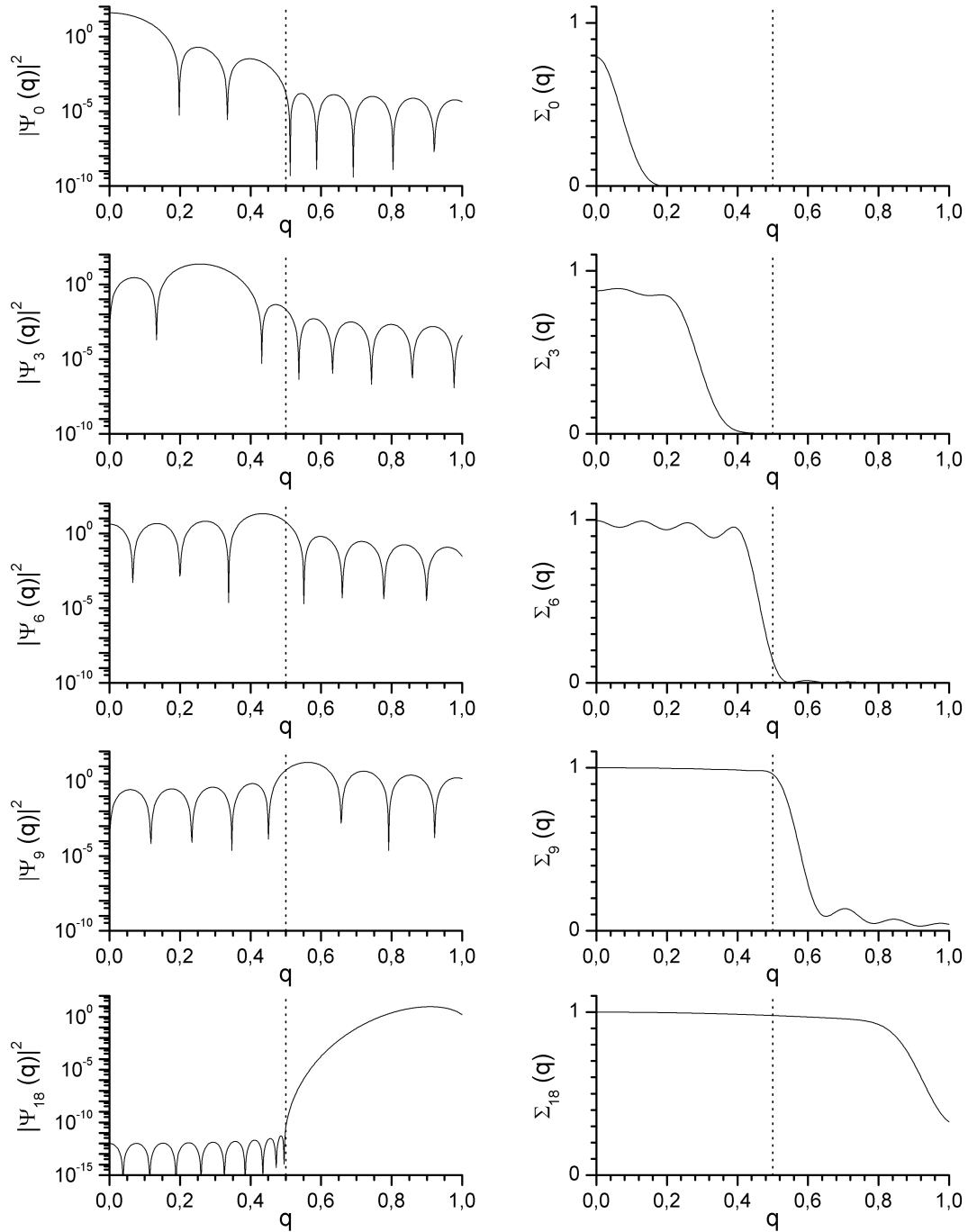


Figure 6.4: Squared moduli $|\Psi_k(q)|^2$ (left panels) and cumulative spectra $\Sigma_k(q)$ (right panels) for the eigendensities $\psi_k(z)$ depicted in Fig.6.3: For $k < 8$, the $|\Psi_k|^2$ are concentrated almost completely in $[-Q, Q]$ (vertical dotted line), whereas for $k \gg 8$ only little energy falls into $[-Q, Q]$. The $\Sigma_k(q)$ are smooth and almost unity on $[-Q, Q]$.

6.1.4 Analytical expression for $\partial R(q_z)/\partial \rho_n$

Parratt's formula for the calculation of the reflection coefficient $R(q_z)$ of a system consisting of N homogeneous layers of thickness d with density ρ_j is given by [105]:

$$R_{j-1} = \frac{r_j + R_j \exp(2ik_{z,j}d)}{1 + r_j R_j \exp(2ik_{z,j}d)} \quad (6.47)$$

with

$$r_j = \frac{k_{z,j-1} - k_{z,j}}{k_{z,j-1} + k_{z,j}} \quad (6.48)$$

and $k_{z,j} = \sqrt{k_z^2 - 4\pi\rho_j}$. $d_j = z_j - z_{j-1}$ is the thickness of layer j . The partial derivative of the reflectivity $r = R_0^* R_0$ with respect to the density ρ_n of a layer n is given by

$$\frac{\partial}{\partial \rho_n} r = \frac{\partial R_0}{\partial \rho_n} R_0^* + R_0 \frac{\partial R_0^*}{\partial \rho_n} = 2\Re \left\{ \frac{\partial R_0}{\partial \rho_n} R_0^* \right\} \quad (6.49)$$

With the introduction of the quantities

$$P_j = \exp(2ik_{z,j}d) \quad (6.50a)$$

$$A_j = 1 + r_j R_j P_j \quad (6.50b)$$

$$B_j = \frac{P_j}{A_j^2} (1 - r_j^2) \quad (6.50c)$$

$$C_{j,n} = \frac{1}{A_j^2} \left[(1 - R_j^2 P_j^2) \frac{\partial r_j}{\partial \rho_n} + R_j (1 - r_j^2) \frac{\partial P_j}{\partial \rho_n} \right] \quad (6.50d)$$

the derivative of the reflection coefficient inside the layer j with respect to the density ρ_n is given by

$$\frac{\partial R_{j-1}}{\partial \rho_n} = B_j \frac{\partial R_j}{\partial \rho_n} + C_{j,n} \quad (6.51)$$

The remaining non-zero partial derivatives in the latter equations are given by

$$\frac{\partial P_n}{\partial \rho_n} = 2id \frac{\partial k_{z,n}}{\partial \rho_n} P_n \quad (6.52a)$$

$$\frac{\partial r_{n+1}}{\partial \rho_n} = \frac{\partial k_{z,n}}{\partial \rho_n} \frac{2k_{z,n+1}}{(k_{z,n} + k_{z,n+1})^2} \quad (6.52b)$$

$$\frac{\partial r_n}{\partial \rho_n} = -\frac{\partial k_{z,n}}{\partial \rho_n} \frac{2k_{z,n-1}}{(k_{z,n-1} + k_{z,n})^2} \quad (6.52c)$$

where $\partial k_{z,n}/\partial \rho_n = -2\pi/k_{z,n}$. From the above equations, it follows that for fixed n all $C_{j,n}$ vanish, except for $C_{n,n}$ and $C_{n+1,n}$. From $R_{N+1} = 0$, i.e. no reflected wave

comes from the substrate, one obtains the boundary condition $\partial R_{N+1}/\partial \rho_n = 0$. Writing down the derivatives of the reflection coefficient in each layer j , one finds:

$$\frac{\partial R_N}{\partial \rho_n} = \frac{\partial R_{N-1}}{\partial \rho_n} = \dots = \frac{\partial R_{n+1}}{\partial \rho_n} = 0 \quad (6.53a)$$

$$\frac{\partial R_n}{\partial \rho_n} = C_{n+1,n}, \quad \frac{\partial R_{n-1}}{\partial \rho_n} = B_n \frac{\partial R_n}{\partial \rho_n} + C_{n,n} \quad (6.53b)$$

$$\frac{\partial R_{n-2}}{\partial \rho_n} = B_{n-1} \frac{\partial R_{n-1}}{\partial \rho_n}, \dots, \quad \frac{\partial R_0}{\partial \rho_n} = B_1 \frac{\partial R_1}{\partial \rho_n} \quad (6.53c)$$

Rewriting the above equations in a more compact form, the derivative of the reflection coefficient with respect to the density ρ_n becomes [29]

$$\frac{\partial R_0}{\partial \rho_n} = (B_n C_{n+1,n} + C_{n,n}) D_n, \quad D_n = \prod_{l=1}^n B_l \quad (6.54)$$

with $D_1 = 1$. Since the calculation of the Jacobian matrix requires $\partial R_0/\partial \rho_n$ for $n = 1, \dots, N$, the coefficients D_n may be computed most efficiently in reverse order, i.e. $n = 0, 1, \dots, N$, by making use of the relation $D_{n+1} = D_n B_{n+1}$.

The computational cost of the above procedure for the calculation of the $N \times N$ Jacobian is of the order of $\mathcal{O}(N^2)$, while the use of finite difference methods leads to algorithms requiring $\mathcal{O}(N^3)$ operations. Besides the gain of computation time, this method provides the exact Jacobian and not an approximation.

6.1.5 Stabilization of the inversion step

The fact that the dynamical reflectivity $r(q_z)$ must remain constant for $q_z \in B_G$ under any variation $d\beta$ requires in first order approximation

$$dr_m \equiv dr(q_{z,m}) = \sum_{j=1}^J \frac{\partial r_m}{\partial \beta_j} d\beta_j = 0, \quad 0 < m < G \quad (6.55)$$

or in matrix notation $\mathbf{J} \cdot d\boldsymbol{\beta} = \mathbf{0}$. The elements of the Jacobian matrix \mathbf{J} are given by

$$J_{mn} = \frac{\partial r_m}{\partial \beta_n} = 2 \Re \left\{ R_m \frac{\partial}{\partial \beta_n} R_m^* \right\}. \quad (6.56)$$

Instead of directly calculating latter equation, it is preferable to first calculate

$$\hat{J}_{mn} = \frac{\partial r_m}{\partial b_l} \quad (6.57)$$

via the recursive procedure presented in the previous section and then making use of the relation

$$db_l = \sum_m \psi_m(l) d\beta_m \quad (6.58)$$

so that $\mathbf{J} = \widehat{\mathbf{J}} \cdot \mathbf{P}$, where $P_{m,l} = \psi_m(l)$ ⁵. The advantage is that the number of computations involving trigonometric and exponential functions is reduced. It is also preferable to consider the Jacobian

$$J_{mn} = \frac{\partial}{\partial \beta_n} \ln r_m = \frac{1}{r_m} \frac{\partial}{\partial \beta_n} r_m \quad , \quad (6.59)$$

where we assume, that $r_m > 0$. The construction of the normal equations $dr(q_z) = 0$ requires the calculation and inversion of the Jacobian matrix $J_{mn} = \partial R(q_m) / \partial \beta_n$ at each iteration step. Since the computational cost for the singular value decomposition of the Jacobian \mathbf{J} is quite expensive⁶ a reduction of the dimension is desirable. To do so, eigendensities $\{\psi_{D,n}\}$ are constructed for $Q_D \approx 4q_c \ll Q$. The $\Psi_{D,n}$ corresponding to eigenvalues $\lambda_{D,n} \approx 0$, will then have a negligible impact on the dynamical reflection coefficient for $|q_z| < Q_D$. It is then sufficient to ask for $\mathbf{J}_D \cdot d\beta_D = \mathbf{0}$ so that one dimension of the Jacobian is reduced by $N_D/N \approx Q_D/Q$. Let us define the two spaces

$$\mathcal{S} = \text{span}\{\psi_n\}_{n=0}^N \quad \text{and} \quad \mathcal{S}_D = \text{span}\{\psi_{D,m}\}_{m=0}^{N_D} \quad . \quad (6.60)$$

\mathcal{S} is the space of the eigendensities ψ_n with non-vanishing eigenvalues λ_n for $q_z \in [-Q, Q]$ and \mathcal{S}_D is span by the eigendensities $\psi_{D,m}$, whose $\Psi_{D,m}$ contribute to the region of dynamical scattering $[-Q_D, Q_D]$. Their Fourier transformed spaces are denoted by $\tilde{\mathcal{S}}$ and $\tilde{\mathcal{S}}_D$, respectively. Next, consider some profile variation $\Delta\rho \in \mathcal{S}$ given by

$$\Delta\rho(z) = \sum_n \psi_n(z) d\beta_n \quad . \quad (6.61)$$

The projection of $\Delta\rho$ on \mathcal{S}_D is equal to

$$\mathcal{P}_{\mathcal{S}_D}\{\Delta\rho\} = \sum_m \psi_{D,m}(z) d\beta_{D,m} \quad \text{where} \quad d\beta_{D,m} = \sum_n W_{m,n} d\beta_n \quad (6.62)$$

and

$$W_{m,n} = \int_0^L \psi_n(z) \psi_{D,m}(z) dz = \sum_{k,l} \psi_n(l) \psi_{D,m}(k) \tilde{B}_{kl} \quad (6.63)$$

with $\tilde{B}_{kl} = \int B_k(z) B_l(z) dz$. Since both, $\psi_{D,m}$ and ψ_n , are either symmetric or anti-symmetric, all $W_{m,n}$ with $(m+n)$ odd are equal to zero so that the projection of the even and odd parts can be performed separately.

⁵Note that the number of required multiplications can be reduced by a factor 2 when making use of the symmetry properties of the ψ_m .

⁶The singular value decomposition of a $N \times M$ matrix using the *Golub-Reinsch algorithm* [61] requires $4N^2M + 8NM^2 + 9M^3$ operations.

Let $\Delta\widehat{F}(q_m) \equiv \Delta F(q_m)/(iq_m)$, where $\Delta F(q_m)$ is the guessed difference of the structure factor and let $\Delta\widehat{F}_{\widetilde{\mathcal{S}}} = \mathcal{P}_{\widetilde{\mathcal{S}}}\{\Delta\widehat{F}\}$ denote the projection of $\Delta\widehat{F}$ onto $\widetilde{\mathcal{S}}$. Up to now it was assumed that the derivative of density profile $d\rho(z)/dz$ has compact support on $[0, L]$. This is a natural choice, because the surface of the sample is, besides the beginning of the substrate, an appropriate choice for the origin of the z -axis. Moreover, the concept of the impulse-response function $g(t)$, see Section 4.2, requires causality, i.e. $\rho(z) = 0$ for $z < 0$. However, since the eigendensities are either even or odd with respect to $L/2$, it is preferable to set the origin to $L/2$, i.e.

$$\Delta\widehat{F}(q_m) \rightarrow \Delta\widehat{F}(q_m) \exp(-iq_m L/2) \quad , \quad (6.64)$$

so that the real and imaginary parts of $\Delta\widehat{F}(q_m)$ may be projected separately on the spaces $\widetilde{\mathcal{S}}_e$ and $\widetilde{\mathcal{S}}_o$ that are spanned by the pure real and imaginary Ψ_n of the even and odd ψ_n of \mathcal{S} , respectively. Thus, from

$$\Delta\widehat{F}_{\widetilde{\mathcal{S}}} = \mathcal{P}_{\widetilde{\mathcal{S}}}\{\Delta\widehat{F}\} = \mathcal{P}_{\widetilde{\mathcal{S}}_e}\{\Re\{\Delta\widehat{F}\}\} + i \mathcal{P}_{\widetilde{\mathcal{S}}_o}\{\Im\{\Delta\widehat{F}\}\} \quad (6.65)$$

one obtains the coefficients $\Delta\beta_e$ and $\Delta\beta_o$. The projectors $\mathcal{P}_{\widetilde{\mathcal{S}}_e}$ and $\mathcal{P}_{\widetilde{\mathcal{S}}_o}$ are constructed by singular value decomposition of $\Psi_n(q_m)$, with n even and odd. Note, if q_c does not change, the grid $\{q_m\}$ remains unchanged and hence $\mathcal{P}_{\widetilde{\mathcal{S}}_e}$ and $\mathcal{P}_{\widetilde{\mathcal{S}}_o}$ have to be computed only once.

Next, $\Delta\widehat{F}_{\widetilde{\mathcal{S}}}$ is projected onto \mathcal{S}_D and the remaining part $\Delta\widehat{F}_{\widetilde{\mathcal{S}}} - \mathcal{P}_{\mathcal{S}_D}\{\Delta\widehat{F}_{\widetilde{\mathcal{S}}}\}$ can be transformed directly to real space, since it does not affect the dynamical region:

$$\begin{aligned} d\rho_{D^\perp}(z) &= \sum_n \psi_n(z) d\beta_n - \sum_m \psi_{D,m}(z) d\beta_{D,m} \\ &= \sum_n \left(\psi_n(z) - \sum_m W_{m,n} \psi_{D,m}(z) \right) d\beta_n \quad . \end{aligned} \quad (6.66)$$

The fraction falling into the dynamical region, $\mathcal{P}_{\mathcal{S}_D}\{\Delta\widehat{F}_{\widetilde{\mathcal{S}}}\}$, is then to be projected onto the space fulfilling $\mathbf{J}_D \cdot d\boldsymbol{\beta}_D = \mathbf{0}$: By Singular value decomposition, $\mathbf{J}_D = \mathbf{U} \cdot \boldsymbol{\Sigma} \cdot \mathbf{V}^T$, one constructs the (right-side) null-space of the Jacobian,

$$\mathcal{N}(\mathbf{J}_D) = \text{span}\{\mathbf{v}_n\}_{n=N_\epsilon}^{N_D} \quad (6.67)$$

with $\sigma_n = \Sigma_{nn} < \epsilon$ for all $n > N_\epsilon$. \mathbf{v}_n denotes the n -th column vector of \mathbf{V} . The projection of $d\boldsymbol{\beta}_D$ on $\mathcal{N}(\mathbf{J}_D)$ is given by

$$d\widehat{\boldsymbol{\beta}}_D = \mathcal{P}_{\mathcal{N}(\mathbf{J}_D)}\{d\boldsymbol{\beta}_D\} = \sum_{n=N_\epsilon}^{N_D} (\mathbf{v}_n^T d\boldsymbol{\beta}_D) \mathbf{v}_n \quad . \quad (6.68)$$

Finally, one obtains the total profile modification $d\rho(z) = d\rho_D(z) + d\rho_{D^\perp}(z)$ with

$$d\rho_D(z) = \sum_m \psi_{D,m}(z) d\widehat{\beta}_{D,m} \quad . \quad (6.69)$$

The density profile for the next iteration is then given by $\rho_{n+1}(z) = \rho_n(z) + d\rho(z)$.

6.2 Smoothness

For $d < \pi/q_{z,max}$, the construction of a step-like profile from the structure factor $F(q_z)$ given on $[0, q_{max}]$ will not provide a unique solution because the system of linear equations to solve is under-determined. Then additional constraints are required to pick the desired profile from the solution space. Typically, one expects the density profile to be smooth and non-oscillating, so that one seeks to minimize the functional

$$U_s = \int_0^L \left[\frac{d}{dz} \rho(z) \right]^2 dz \quad , \quad (6.70)$$

as proposed for example in Refs. [75][107][108][148]. The partial derivative of U_s with respect to some coefficient b_k becomes

$$\frac{\partial}{\partial b_k} U_s = 4b_k - 2b_{k-1} - 2b_{k+1} \quad . \quad (6.71)$$

If the reflectivity corresponding to the density profile $\rho(z)$ agrees already with the experimental reflectivity $r_{obs}(q)$ for $|q| \leq Q$, then any variation $d\rho(z)$ reducing the functional U_s must not change the reflectivity on $[-Q, Q]$. Within kinematical theory and assuming a density profile of thickness L this constraint becomes

$$d|F_n|^2 = \sum_k \frac{\partial}{\partial b_k} |F_n|^2 db_k = 0 \quad , \quad n = 0 \dots N \quad . \quad (6.72)$$

where $F_n = F(q_n)$, $q_n = n(2\pi/L)$. The partial derivative of $|F_n|^2$ with respect to some b_k is equal to

$$\frac{\partial}{\partial b_k} |F_n|^2 = 2\Re \left\{ F_n^* \frac{\partial}{\partial b_k} F_n \right\} \quad (6.73)$$

where

$$F_n^* = \sum_m b_m \left[\exp(-iq_n z_{m-1}) - \exp(-iq_n z_m) \right] \quad (6.74a)$$

$$\frac{\partial}{\partial b_k} F_n = \exp(iq_n z_{k-1}) - \exp(iq_n z_k) \quad . \quad (6.74b)$$

The functional U_s is then minimized in the Null-space of the set of equations given by Eq. (6.72).

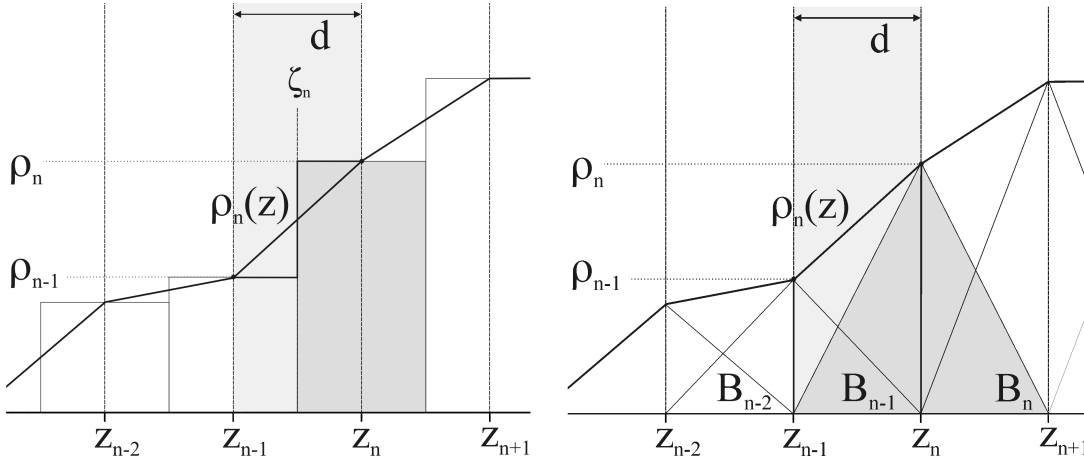


Figure 6.5: Two ways of constructing a linear-graded density profile: In the left panel the profile is built of slabs of constant density with thickness d in order to model a linear transition layer of width d at each interface position ζ_n . The right panel depicts the same profile but constructed by first order B-splines B_n^1 . The splines are of triangular form and centered at the positions z_n .

6.3 Representation of the profile by a polygon

In the previous sections an inversion algorithm for x-ray reflectivity was developed, using a piecewise-constant density profile. The algorithm requires the calculation of eigendensities for the expansion of the profile modification $\Delta\rho(z)$ and the total differential $dr(q_z)$ of the reflectivity in dynamical theory with respect to the coefficients β_n of the expansion

$$\Delta\rho(z) = \sum_n \beta_n \psi_n(z) \quad . \quad (6.75)$$

In this section, the density profile will be represented by a polygon, so that it is continuous. In Figure 6.5, two different ways to describe such a density profile are presented. The profile is represented by the thick solid line in both panels, respectively. In the left panel, the profile is constructed by slabs of constant electron density ρ_n and thickness d as indicated by the rectangles. The slabs are centered at the positions z_n . In order to model the polygon, a linear transition of width d at the positions ζ_n between the layers $n-1$ and n is assumed. The density $\rho(z)$ at a position $z \in [z_{n-1}, z_n]$ is then simply given by

$$\rho(z) = \rho_{n-1} + \frac{\rho_n - \rho_{n-1}}{d}(z - z_{n-1}) \quad . \quad (6.76)$$

In the right panel of Figure 6.5 the polygon-profile is represented by first order B-splines. For two reasons the B-spline representation is introduced here:

First, results may be derived directly from the well-known properties of B-splines [41][160]. Second, in the next Section, the profile will be represented by second order B-splines.

In the following $B_n^1(z)$ denotes the first order B-spline centered at the position $z_n = nd$. It is given by

$$B_n^1(z) = \begin{cases} Z - n + 1 & , \quad Z \in [n - 1, n] ; \\ -Z + n + 1 & , \quad Z \in [n, n + 1] ; \\ 0 & , \quad \text{otherwise.} \end{cases} \quad (6.77)$$

where $Z = z/d$. Expanded in first order B-splines, the polygon profile and its derivative become

$$\rho(z) = \rho_\infty \sum_{n=1}^N b_n B_n^1(z) \quad \text{and} \quad (6.78)$$

$$\frac{d}{dz} \rho(z) = \frac{\rho_\infty}{d} \sum_{n=1}^N (b_n - b_{n-1}) H(z_n - z) H(z - z_{n-1}) \quad , \quad (6.79)$$

respectively. The coefficients b_n are equal to 0 for $n \leq 0$ and equal to 1 for $n > N$, so that $d\rho(z)/dz$ vanishes for $z \notin [0, L]$. The structure factor $F(q_z)$ is given by

$$\begin{aligned} F(q_z) &= \frac{1}{d} \sum_{n=1}^N (b_n - b_{n-1}) \int_{z_{n-1}}^{z_n} \exp(iq_z z) dz \\ &= \exp(-iq_z d/2) \operatorname{sinc}(q_z d/2) \sum_{n=1}^N (b_n - b_{n-1}) \exp(inq_z d) \quad . \end{aligned} \quad (6.80)$$

6.3.1 Modified Fresnel coefficients for the linear-graded interface

Parratt's formula for the calculation of the reflection of an system consisting of N homogeneous layers of equal thickness d and density ρ_n is given by [105]:

$$R_{n-1} = \frac{r_n + R_n \exp(2ik_{z,n}d)}{1 + r_n R_n \exp(2ik_{z,n}d)} \quad (6.81)$$

with

$$r_n = \frac{k_{z,n-1} - k_{z,n}}{k_{z,n-1} + k_{z,n}} \quad . \quad (6.82)$$

$k_{z,n} = \sqrt{k_z^2 - 4\pi\rho_n}$ is the z -component of the wavevector inside the layer n . For a gradient layer of arbitrary form the modified reflection coefficient \tilde{r}_n (see Section 2.2.2) is given by (see e.g. Refs. [30][155])

$$\tilde{r}_n = \frac{f_n(k_{z,n} + k_{z,n-1})}{f_n(k_{z,n} - k_{z,n-1})} r_n \quad , \quad (6.83)$$

with

$$f_n(k) = \exp(ik\mu_n) \int_{-\infty}^{\infty} P_n(z) \exp(ikz) dz \quad , \quad (6.84)$$

where $P_n(z)$ is the probability distribution function of the transition region and $\mu_n = \int z P_n(z) dz$ is mean position the n -th interface.

From the left panel in Figure 6.5 we see that the polygon profile can be represented by a profile with constant densities and a linear interfacial gradient, corresponding to a box-like probability distribution function of width d centered at $\mu = 0$, i.e.

$$P(z) = \frac{1}{d} H(d/2 - |z|) \quad , \quad (6.85)$$

where $H(x)$ denotes the Heaviside function and d is the width of the box. Then Eq. (6.84) becomes $f_n(k) = 2 \sin(kd/2)/kd$ and hence

$$\tilde{r}_n = \frac{\sin[(k_{z,n} + k_{z,n-1})d/2]}{\sin[(k_{z,n} - k_{z,n-1})d/2]} r_n^2 \quad . \quad (6.86)$$

For $k_{z,n} - k_{z,n-1} = 0$, i.e $\rho_n = \rho_{n-1}$, one obtains $\tilde{r}_n = 0$, since $\lim_{x \rightarrow 0} \sin(x)/x = 1$. The first order partial derivatives of \tilde{r}_n with respect to ρ_n and ρ_{n-1} are given by

$$\frac{\partial}{\partial \rho_n} \tilde{r}_n = 2 \frac{\tilde{r}_n}{r_n} \frac{\partial r_n}{\partial \rho_n} - r_n^2 \frac{d \sin(k_{z,n-1}d)}{\cos[(k_{z,n-1} - k_{z,n})d] - 1} \frac{\partial k_{z,n}}{\partial \rho_n} \quad (6.87)$$

$$\frac{\partial}{\partial \rho_n} \tilde{r}_{n+1} = 2 \frac{\tilde{r}_{n+1}}{r_{n+1}} \frac{\partial r_{n+1}}{\partial \rho_n} + r_{n+1}^2 \frac{d \sin(k_{z,n+1}d)}{\cos[(k_{z,n} - k_{z,n+1})d] - 1} \frac{\partial k_{z,n}}{\partial \rho_n} \quad . \quad (6.88)$$

For $k_{z,n} \rightarrow k_{z,n-1}$ one finds

$$\lim_{k_{z,n-1} \rightarrow k_{z,n}} \frac{r_n^2}{\cos[(k_{z,n-1} - k_{z,n})d] - 1} = -\frac{2}{(2k_{z,n}d)^2} \quad (6.89)$$

and $\lim_{k_{z,n-1} \rightarrow k_{z,n}} \tilde{r}_n/r_n = \text{sinc}(k_{z,n}d)$. The reflection coefficient $R(q_z)$ of the entire sample is then equal to $R_0 \exp(-iq_z d/2)$, where the phase-shift stems from the displacement of the ζ_n relative to the z_n .

Note, the calculation of the modified reflection coefficients \tilde{r}_n via Eqs. (6.83) and (6.84) is an approximation as discussed in Refs. [30] and [54]. The exact solution for the reflection coefficient $R(q_z)$ may be obtained by solving the Schrödinger equation: For a linear-graded profile, $V(z) = bz + c$, the time-independent Schrödinger equation (see Eq. (4.2)) has solutions of the form⁷

$$\psi(z) = C_1 \text{Ai}[\alpha(z)] + C_2 \text{Bi}[\alpha(z)] \quad , \quad (6.90)$$

with $\alpha(z) = (bz + c)/(-b)^{2/3}$ and the Airy functions $\text{Ai}(x)$ and $\text{Bi}(x)$, see [6]. The constants C_1 and C_2 are then determined from the required continuity of

⁷The wavevector-transfer q_z is included in the constant c .

$\psi(z)$ and its derivative $d\psi(z)/dz$ at the positions z_n . However, in the following we do not use the exact solution for the reflection coefficient for two reasons: First, the use of the modified Fresnel coefficients fails only at small q_z -values and only if d , which is equal to the width of the interface, is too large. This does not occur because d is typically of the order of a few Å. Furthermore, even if d was too large, then the \tilde{r}_n may still be used by splitting the graded region in two interfaces of width $d/2$ and twice applying Parratt's formula. The second reason for not using the exact solution is of practical nature: The effort for the numerical evaluation of the Airy functions $\text{Ai}(x)$ and $\text{Bi}(x)$ is too high compared to the fast calculation of $\sin(x)$.

6.3.2 Eigendensities for the linear-graded density profile

As in Section 6.1.3, it is assumed the density profile $\rho(z)$ differs from the true profile by $\Delta\rho(z)$, which in this section is represented by first order B-splines, i.e.

$$\Delta\rho(z) = \sum_{n=1}^{N-1} \Delta b_n B_n^1(z) \quad , \quad (6.91)$$

Note that sum goes from 1 to $N - 1$, since $\Delta\rho(0)$ and $\Delta\rho(L)$ are equal to zero and hence $\Delta b_0 = \Delta b_N = 0$. $\Delta\rho(z)$ has compact support on $[0, L]$ and so one considers the (bandlimited) function

$$\Psi(q) = \frac{\Delta F(q)}{iq} = \int_0^L \Delta\rho(z) \exp(iqz) dz \quad . \quad (6.92)$$

Inserting Eq. (6.91) yields

$$\Psi(q) = \frac{d}{2} \text{sinc}^2(qd/2) \left(\sum_{n=1}^{N-1} \Delta b_n \exp(inqd) \right) \quad . \quad (6.93)$$

Again, one seeks to maximize the energy $E = \int_{-Q}^Q \Psi^*(q)\Psi(q) dq$ and inserting Eq. (6.93) yields

$$\begin{aligned} E &= d^2 \sum_{n,m} \Delta b_n \Delta b_m \int_{-Q}^Q \text{sinc}^4(qd/2) \cos[qd(n-m)] dq \\ &= 2d^2 \sum_{n,m} \Delta b_n \Delta b_m S_{n,m}(Q) \quad , \end{aligned} \quad (6.94)$$

where the integral $S_{n,m}(Q)$ is given by

$$\begin{aligned} S_{n,m}(q) &= 6f_{n-m}(q) - 4f_{n-m+1}(q) - 4f_{n-m-1}(q) \\ &\quad + f_{n-m+2}(q) + f_{n-m-2}(q) \end{aligned} \quad (6.95)$$

with

$$f_j(q) = \frac{j^3}{6d} \left(-2 \frac{\cos(jqd)}{(jqd)^3} + \frac{\sin(jqd)}{(jqd)^2} + \frac{\cos(jqd)}{jqd} + \text{Si}(jqd) \right) . \quad (6.96)$$

If the eigendensities ψ_n should fulfill the condition

$$\int_{-\infty}^{\infty} [\psi_n(z)]^2 dz = 1 \quad , \quad (6.97)$$

then one finds

$$\int_{-\infty}^{\infty} [\psi_n(z)]^2 dz = \sum_{n,m} \Delta b_n \Delta b_m \tilde{B}_{n,m} \quad , \quad (6.98)$$

or in matrix notation $\Delta \mathbf{b}^T \tilde{\mathbf{B}} \Delta \mathbf{b} = 1$, where $\tilde{B}_{n,m}$ denotes the overlap-integral between two B-splines $B_n^1(z)$ and $B_m^1(z)$ and is given by

$$\tilde{B}_{n,m} = \int_{-\infty}^{\infty} B_n^1(z) B_m^1(z) dz = \begin{cases} \frac{2}{3}d, & m = n; \\ \frac{1}{6}d, & m = n \pm 1; \\ 0, & \text{otherwise.} \end{cases} \quad (6.99)$$

The matrix $\tilde{\mathbf{B}}$ is positive definite and has band structure. For the maximum of the energy one obtains under the use of a Lagrangian multiplier λ

$$U = 2d^2 \sum_{n,m} \Delta b_n \Delta b_m S_{n,m}(Q) - \lambda \sum_{n,m} \Delta b_n \Delta b_m \tilde{B}_{n,m} \quad (6.100)$$

and minimization of U with respect to the Δb_n leads to the generalized eigenvalue problem

$$2d^2 \sum_n \Delta b_n S_{n,m}(Q) = \lambda \sum_n \Delta b_n \tilde{B}_{n,m} \quad (6.101)$$

or in matrix notation $\mathbf{S} \Delta \mathbf{b} = \lambda \tilde{\mathbf{B}} \Delta \mathbf{b}$.

The main difference between this eigenvalue equation and that obtained for the piecewise constant profile is, that here the matrix $\tilde{\mathbf{B}}$ appears on the right-hand side. In case of the piecewise constant profile, the basic functions are rectangles of width d , which are the B-splines of first order. Then the overlap-integral $\int B_n^1(z) B_m^1(z) dz$ vanishes except for $m = n$ so that $\tilde{\mathbf{B}} = d^2 \mathbb{1}$ and hence $\tilde{\mathbf{B}} \Delta \mathbf{b} = d^2 \Delta \mathbf{b}$.

As an example, selected eigendensities $\psi_k(z)$ and their Fourier transforms $\Psi_k(q)$ are shown in Figures 6.6 and 6.7 for a density profile consisting of 50 slabs of thickness $d = 1$ and with $Q = 0.5$, respectively. The uppermost left panel in Fig. 6.6 depicts the eigenvalues λ_k of a linear scale (right axis, filled circles) and on a logarithmic scale (left axis, open circles). The λ_k decay rapidly at $k = 50Qd/\pi \approx 8$.

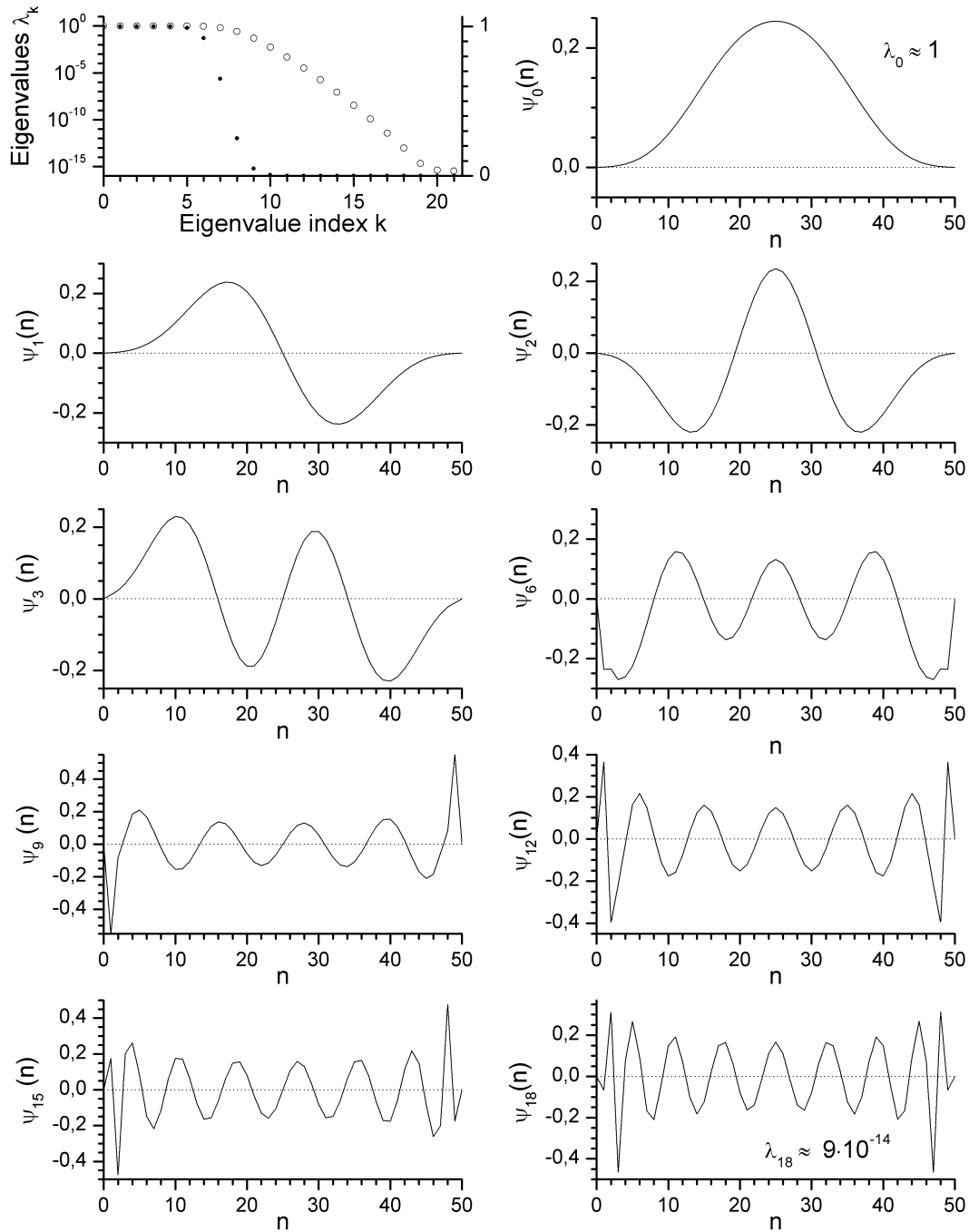


Figure 6.6: Eigendensities $\psi_k(z)$ of a linear-graded density profile consisting of 50 slabs of thickness $d = 1$ for $Q = 0.5$: The uppermost left panel depicts the eigenvalues λ_k on a logarithmic scale (left axis, open circles) and on a linear scale (right axis, filled circles). Around $k = 50Qd/\pi \approx 8$ the λ_k decay rapidly. The corresponding Ψ -functions are shown in Fig. 6.7.

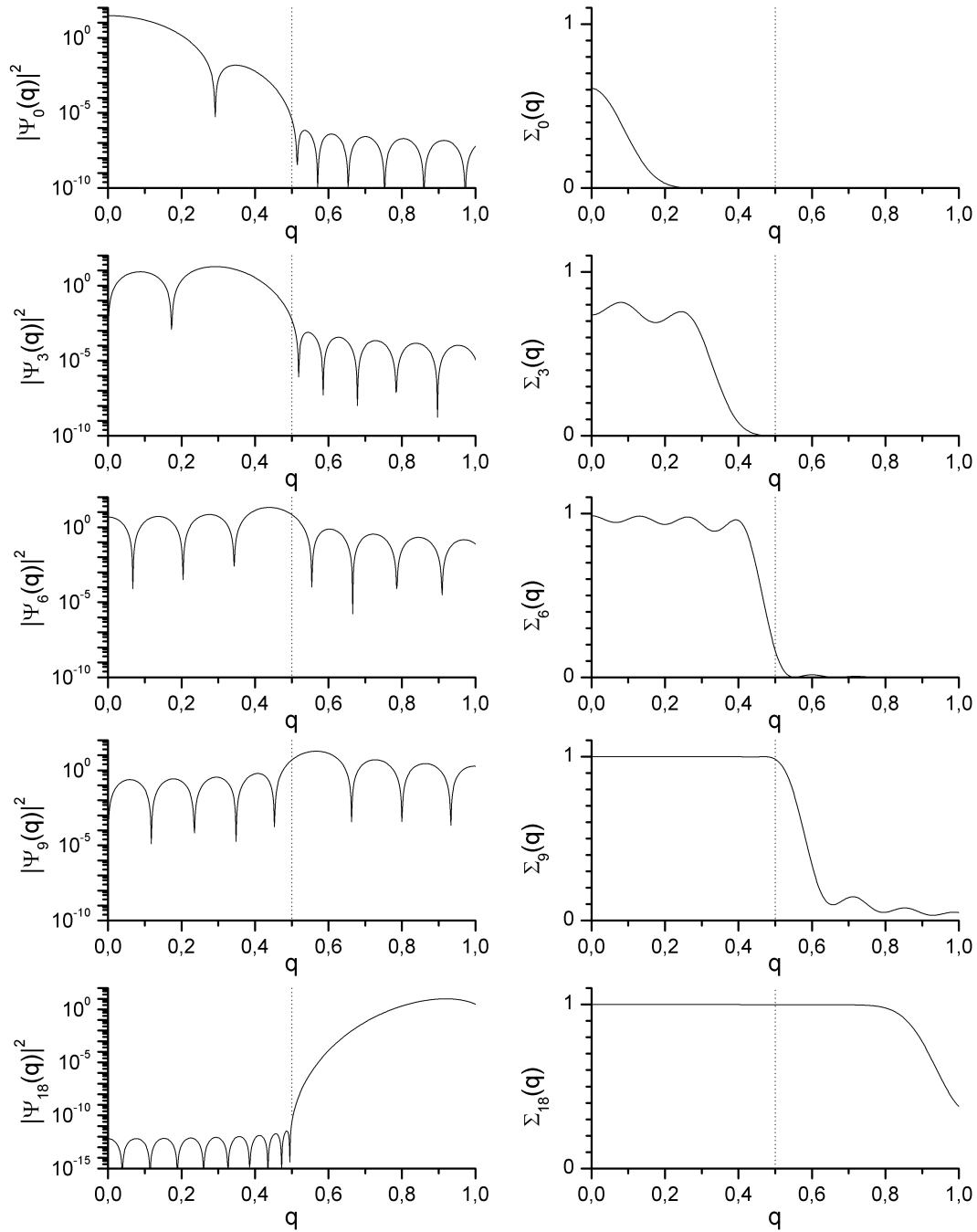


Figure 6.7: Squared moduli $|\Psi_k(q)|^2$ (left panels) and cumulative spectra $\Sigma_k(q)$ (right panels) for the eigendensities $\psi_k(z)$ depicted in Fig. 6.6: For $k < 8$, the $|\Psi_k|^2$ are concentrated almost completely in $[-Q, Q]$ (vertical dotted line), whereas for $k \gg 8$ only little energy falls into $[-Q, Q]$. The $\Sigma_k(q)$ are smooth and almost unity on $[-Q, Q]$.

For $k = 18$ the eigenvalue is $\approx 1.4 \cdot 10^{-13}$. The moduli squared of the Ψ_k are shown on a logarithmic scale in the left panels of Fig. 6.7. The vertical dotted line represents $Q = 0.5$. For $k < 8$ the Ψ_k are concentrated in the interval $[-Q, Q]$ and only little power spectral density is outside that interval. For $k \gg 8$, $\Psi_k(q)$ vanishes almost on $[-Q, Q]$, as shown in the lowermost left panel for $k = 18$. The right panels depict the cumulative spectra $\Sigma_k(q)$ which are smooth and converge to unity on $[-Q, Q]$ for $k > 9$.

6.4 Profile representation by second order B-splines

In the previous sections two different sets of eigen-densities for the piecewise-constant profile and the linear-graded profile, have been presented that can be used for the iterative inversion algorithm. However, both cases do not fulfill an important demand on the reconstructed densities profile – *smoothness*. Mathematically this means that the density profile and its derivative have to be continuous.

In this section the profile is represented by second order B-splines which fulfill this condition. An overview of their properties can be found in Refs. [41][159], for example.

In the following, the second B-splines are denoted by $B_n^2(z)$ and defined by

$$B_n^2(z) = \begin{cases} (Z - n + 2)^2/2 & , \quad Z \in [n - 2, n - 1]; \\ -(Z - n + 2)(Z - n - 1) - 3/2 & , \quad Z \in [n - 1, n]; \\ (Z - n - 1)^2/2 & , \quad Z \in [n, n + 1]; \\ 0 & , \quad \text{otherwise} \quad , \end{cases} \quad (6.102)$$

where $Z = z/d$ and d is the distance between the knots. The left panel of Figure 6.8 depicts some B-splines as defined above. The n -th B-spline B_n^2 is centered at $z_n - d/2$ and extends from z_{n-2} to z_{n+1} . The reason for using these *shifted* B-splines is, that the density ρ_n at the position z_n simplifies to $\rho_n = \rho_\infty(b_n + b_{n+1})/2$. A density profile $\rho(z)$ built of second B-splines and with $d\rho(z)/dz$ supported on $[0, L]$, where $L = Nd$, is given by

$$\rho(z) = \rho_\infty \sum_n b_n B_n^2(z) \quad , \quad (6.103)$$

where $b_n \equiv 0$ for $n \leq 2$ and $b_n \equiv 1$ for $n \geq N - 1$. In the following a profile built of second order B-splines is referred to as a *BS2-profile*. Its derivative is equal to

$$\frac{d}{dz}\rho(z) = \frac{\rho_\infty}{d} \sum_n b_n [B_{n-1}^1(z) - B_n^1(z)] \quad , \quad (6.104)$$

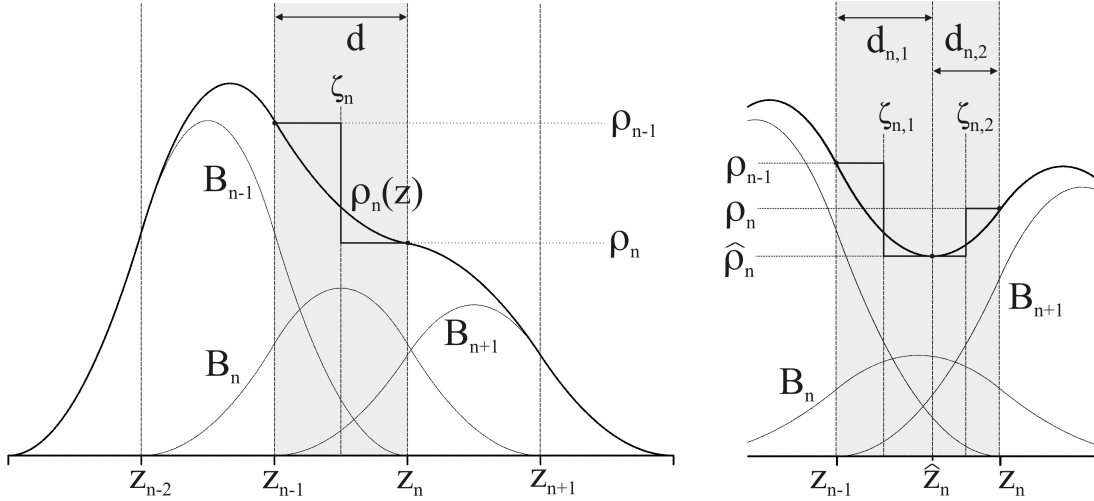


Figure 6.8: Representation of the density profile by second order B-splines: The n -th spline has support on $[z_{n-2}, z_{n+1}]$ and its center is located at $z_n - d/2$. For the case depicted in the left panel, the reflection from the region $[z_{n-1}, z_n]$ can be calculated by *one* modified Fresnel coefficient \tilde{r}_n , whereas the situation shown in the right panel requires the splitting of the interval $[z_{n-1}, z_n]$ in two intervals $[z_{n-1}, \hat{z}_n]$ and $[\hat{z}_n, z_n]$.

where $B_n^1(z)$ is the first order B-spline defined by Eq. (6.77). For the structure factor $F(q_z)$ of a BS2-profile one obtains from Eq. (6.104)

$$\begin{aligned}
 F(q_z) &= \frac{1}{d} \sum_n (b_{n+1} - b_n) \int_{-\infty}^{\infty} B_n^1(z) \exp(iq_z z) dz \\
 &= \text{sinc}^2(q_z d/2) \sum_n (b_{n+1} - b_n) \exp(inq_z d) \quad . \quad (6.105)
 \end{aligned}$$

6.4.1 Modified Fresnel coefficient for the second order B-spline profile

In this section the modified Fresnel coefficients \tilde{r}_n for the calculation of the reflection coefficient $R(q_z)$ within dynamical scattering theory will be derived. Two situations have to be distinguished. They are illustrated in Figure 6.8: In the first case, depicted in the left panel, the density profile is monotonic on the interval $[z_{n-1}, z_n]$ and we can calculate \tilde{r}_n by treating $\rho(z)$ as a *single* transition layer. But when $\rho(z)$ has an extremum on $[z_{n-1}, z_n]$ as shown in the right panel, the interval has to be split and two modified Fresnel coefficients have to be calculated to obtain the reflection from $\rho(z)$ on $[z_{n-1}, z_n]$. This case is referred to as the *two-layer case*.

The single-layer case

For $z \in [z_{n-1}, z_n]$, the profile is given by

$$\rho(z) = \rho_\infty \sum_{j=n-1}^{n+1} b_j B_j^2(z) \quad , \quad (6.106)$$

which can be rewritten as

$$\rho(z) = \rho_\infty \left(\frac{a_1}{2} Z^2 + a_2 Z + \frac{a_3}{2} \right) \quad (6.107)$$

where $Z = z/d$ and

$$a_1 = b_{n-1} - 2b_n + b_{n+1} \quad (6.108a)$$

$$a_2 = b_{n+1} - b_n - na_1 \quad (6.108b)$$

$$a_3 = (2n+1)b_n - (2n-1)b_{n+1} - n^2 a_1 \quad . \quad (6.108c)$$

At the position z_n the above equation simplifies to $\rho_n = \rho_\infty(b_n + b_{n+1})/2$. If one considers the region between z_{n-1} and z_n as an interface of width d located at $\zeta_n = z_n - d/2$ between two materials $(n-1)$ and n with densities ρ_{n-1} and ρ_n , respectively, then the function

$$p_n(z) = \frac{\rho(z) - \rho_{n-1}}{\rho_n - \rho_{n-1}} \quad (6.109)$$

describes this transition. It varies from 0 at z_{n-1} to 1 at z_n and is equal to the fraction of material n at the position z . The corresponding probability distribution $P_n(z) = \frac{d}{dz} p_n(z)$ is then given by

$$P_n(z) = \frac{2}{d^2(b_{n-1} - b_{n+1})} \left[a_1(z_n - z) + d(b_n - b_{n+1}) \right] \quad (6.110)$$

for $z_{n-1} \leq z \leq z_n$ and 0 otherwise. The mean value of $P_n(z)$ relative to ζ_n is equal to

$$\mu_n = \int_{z_{n-1}}^{z_n} (z - \zeta_n) P(z) dz = \frac{d}{6} \frac{a_1}{b_{n+1} - b_{n-1}} \quad . \quad (6.111)$$

The function $f_n(k)$ defined by

$$f_n(k) = \exp(ik\mu_n) \int_{z_{n-1}}^{z_n} P_n(z) \exp \left[-ik(z - \zeta_n) \right] dz \quad , \quad (6.112)$$

is needed for the calculation of the modified Fresnel coefficients $\tilde{r}_{n-1,n}$. Carrying out the integration yields

$$f_n(k) = \left\{ \frac{2i \left[2b_n \cos(kd/2) - b_{n-1} \exp(ikd/2) - b_{n+1} \exp(-ikd/2) \right]}{(b_{n-1} - b_{n+1})kd} + \frac{4i a_1 \sin(kd/2)}{(b_{n-1} - b_{n+1})(kd)^2} \right\} \exp(ik\mu_n) \quad (6.113)$$

with the limit $f(0) = 1$. The modified reflection coefficient $\tilde{r}_{n-1,n}$ is then given by

$$\tilde{r}_{n-1,n} = \frac{f_n(k_{n-1} + k_n)}{f_n(k_{n-1} - k_n)} r_n = \exp(-2ik_n \mu_n) \frac{g_n(k_{n-1} + k_n)}{g_n(k_{n-1} - k_n)} [r_{n-1,n}]^3 \quad (6.114)$$

where

$$g_n(k) = a_1 k d \cos(kd/2) - \left[2a_1 - ikd(b_{n+1} - b_{n-1}) \right] \sin(kd/2) \quad . \quad (6.115)$$

Note that in the case $a_1 = 0$, i.e. without quadratic term, one obtains $\mu_n = 0$ and $g_n(k) \propto k \sin(kd/2)$ so that \tilde{r}_n reduces to that of the linear transition layer given by Eq. (6.86). Furthermore, the Parratt formalism has to be slightly modified to account for the non-vanishing first moments μ_n of $P_n(z)$ and becomes

$$R_n = \exp(2ik_n Z_n) \frac{\tilde{r}_{n,n+1} + R_{n+1} \exp(-2ik_{n+1} Z_n)}{1 + \tilde{r}_{n,n+1} R_{n+1} \exp(-2ik_{n+1} Z_n)} \quad , \quad (6.116)$$

with $Z_n = \zeta_n + \mu_n$.

The two-layer case

The above method for calculating the reflection coefficient from a B-spline interface has limitations: First, when $b_{n+1} = b_{n-1} \neq b_n$ holds, the function $p_n(z)$, see Eq. (6.109), describing the interface transition is undefined because then $\rho_n = \rho_{n-1}$. Second, if either

$$b_n > \max(b_{n+1}, b_{n-1}) \quad \text{or} \quad b_n < \min(b_{n+1}, b_{n-1}) \quad , \quad (6.117)$$

then $\rho(z)$ will have an extremum on $[z_{n-1}, z_n]$. The position \hat{z}_n of that extremum is given by

$$\hat{z} = z_n + d \frac{b_n - b_{n+1}}{a_1} \quad . \quad (6.118)$$

The notation used in this section is given in the right panel of Fig. 6.8. In order to calculate the reflection coefficient, the interval $[z_{n-1}, z_n]$ is split into the intervals $\mathcal{I}_1 = [z_{n-1}, \hat{z}_n]$ and $\mathcal{I}_2 = [\hat{z}_n, z_n]$. The density at \hat{z}_n is equal to

$$\hat{\rho}_n = \rho_\infty \left(\frac{b_n}{2} + \frac{b_{n-1} b_{n+1} - b_n^2}{2a_1} \right) \quad . \quad (6.119)$$

The interface transition functions $p_{n,1}$ and $p_{n,2}$ are then given by

$$p_{n,1}(z) = \frac{\rho(z) - \rho_{n-1}}{\hat{\rho}_n - \rho_{n-1}} \quad \text{and} \quad p_{n,2}(z) = \frac{\rho(z) - \hat{\rho}_n}{\rho_n - \hat{\rho}_n} \quad . \quad (6.120)$$

For the functions $f_{n,1}(k)$ and $f_{n,2}(k)$ one obtains

$$f_{n,1}(k) = \exp(-ik\mu_{n,1}) \int_{\mathcal{I}_1} P_{n,1}(z) \exp[-ik(z - \zeta_{n,1})] dz \quad (6.121a)$$

$$f_{n,2}(k) = \exp(-ik\mu_{n,2}) \int_{\mathcal{I}_2} P_{n,2}(z) \exp[-ik(z - \zeta_{n,2})] dz \quad , \quad (6.121b)$$

where $\zeta_{n,1} = (z_{n-1} + \hat{z}_n)/2$ and $\zeta_{n,2} = (z_n + \hat{z}_n)/2$ are the position and

$$\mu_{n,1} = \int_{\mathcal{I}_1} (z - \zeta_{n,1}) P_{n,1}(z) dz = \frac{d}{6a_1} (b_n - b_{n-1}) \quad (6.122a)$$

$$\mu_{n,2} = \int_{\mathcal{I}_2} (z - \zeta_{n,2}) P_{n,2}(z) dz = \frac{d}{6a_1} (b_{n+1} - b_n) \quad (6.122b)$$

are the mean values of the probability distribution $P_{n,1/2}(z) = dp_{n,1/2}(z)/dz$ of the respective sublayer. Explicit calculation of $f_{n,1}(k)$ and $f_{n,2}(k)$ yields :

$$\tilde{f}_{n,1}(k) = C_1 \frac{\exp(ik\mu_{n,1})}{k^2} \left[\eta_{n,1} \exp(-i\eta_{n,1}) - \sin(\eta_{n,1}) \right] \quad (6.123a)$$

$$\tilde{f}_{n,2}(k) = C_2 \frac{\exp(ik\mu_{n,2})}{k^2} \left[\eta_{n,2} \exp(-i\eta_{n,2}) - \sin(\eta_{n,2}) \right] \quad (6.123b)$$

where $\eta_{n,1} = -3k\mu_{n,1}$ and $\eta_{n,2} = -3k\mu_{n,2}$ and $C_{1,2}$ are constants that do not depend on k . The modified reflection coefficients are then given by

$$\tilde{r}_{n-1,n(1)} = \exp(-2i\hat{k}_n\mu_{n,1}) \frac{g_{n,1}(k_{n-1} + \hat{k}_n)}{g_{n,1}(k_{n-1} - \hat{k}_n)} [r_{n-1,n(1)}]^3 \quad (6.124a)$$

$$\tilde{r}_{n-1,n(2)} = \exp(-2ik_n\mu_{n,2}) \frac{g_{n,2}(\hat{k}_n + k_n)}{g_{n,2}(\hat{k}_n - k_n)} [r_{n-1,n(2)}]^3 \quad (6.124b)$$

where

$$g_{n,1}(k) = \eta_{n,1} \exp(-i\eta_{n,1}) - \sin(\eta_{n,1}) \quad (6.125a)$$

$$g_{n,2}(k) = \eta_{n,2} \exp(-i\eta_{n,2}) - \sin(\eta_{n,2}) \quad (6.125b)$$

and $r_{n-1,n(1)}(k)$ and $r_{n-1,n(2)}(k)$ are the Fresnel coefficients for a sharp interface between two materials with the densities $\{\rho_{n-1}, \hat{\rho}_n\}$ and $\{\hat{\rho}_n, \rho_n\}$, respectively. The overall reflection from the region $[z_{n-1}, z_n]$ is then obtained by twice applying Parratt's recursion formula as given by Eq. (6.116).

Examples for reflectivities from second order B-spline profiles

Two examples for reflectivities from second order B-spline profiles are presented in Figure 6.9. The right panels depict the density profiles. The upper profile is

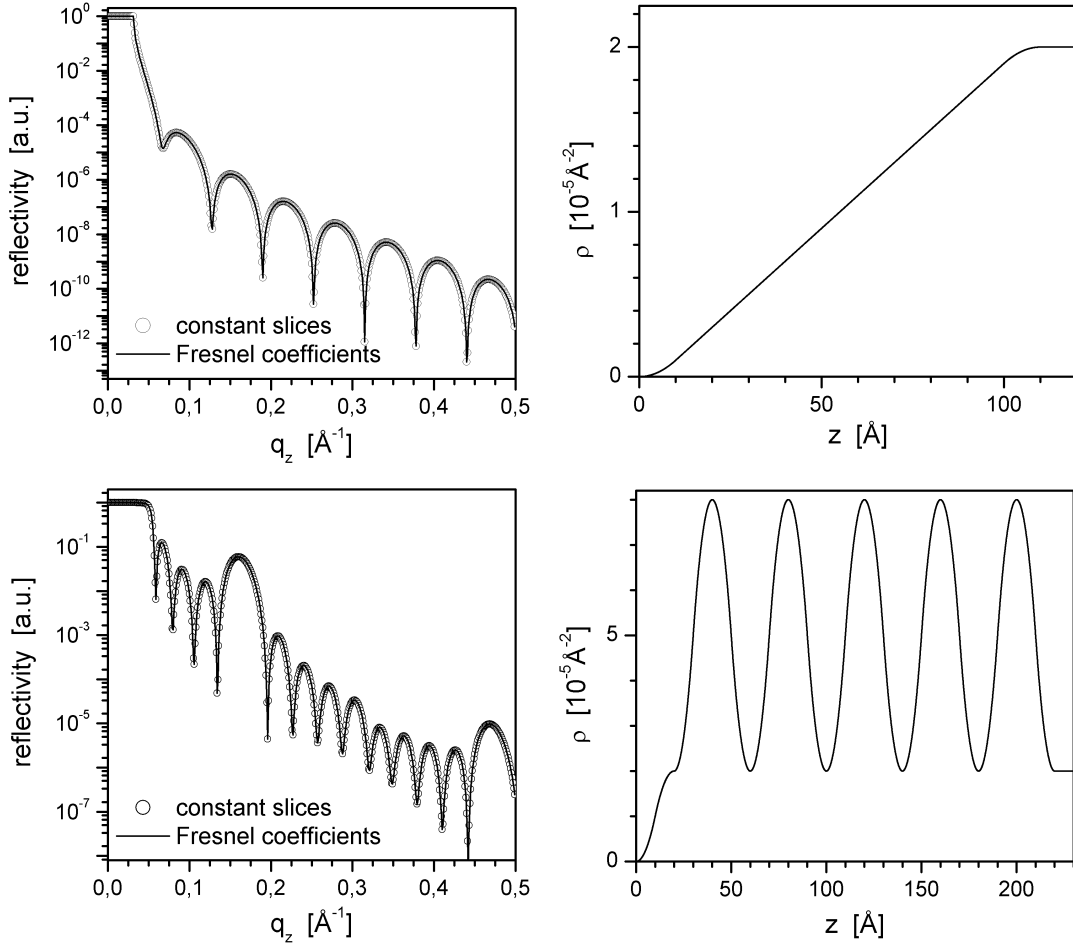


Figure 6.9: Comparison between reflectivities calculated with modified Fresnel coefficients (lines) and by approximating the profile with thin slices of constant electron density and thickness 0.1\AA (open circles). Both reflectivities are virtually indistinguishable. The corresponding density profiles are depicted on the right side.

a smooth transition layer of width 100\AA , whereas the second example is a multi-layered structure with large density variations inside the sample. In both cases the thickness d was equal to 10\AA . The corresponding reflectivities (left panels) have been calculated in two different ways: The reflectivities represented by the open circles are obtained by subdividing the B-spline profile in thin layers of constant electron-density and thickness 0.1\AA , which is sufficiently fine to obtain the correct result within dynamical scattering theory for the depicted q_z -region. The reflectivities calculated using the modified Fresnel-coefficients for the B-splines are shown as solid lines. Both curves are indistinguishable which shows that the presented B-spline method is a powerful tool for calculating x-ray reflectivities in dynamical theory.

Remarks on the solution of the Schrödinger equation for the second order B-spline profile

The reflection coefficient $R(q_z)$ from a density profile constructed by second order B-splines may also be calculated by solving the Schrödinger equation. For a profile $V(z) = az^2 + bz + c$, the time-independent Schrödinger equation (see Eq. (4.2)) has solutions for the form

$$\psi(z) = \exp[-z(az + b)/2\sqrt{a}] \left(C_1 {}_1F_1[\alpha, 1/2, \beta(z)] + C_2(2az + b) {}_1F_1[1/2 + \alpha, 3/2, \beta(z)] \right), \quad (6.126)$$

where ${}_1F_1(x)$ denotes the hypergeometric confluent function of the first kind (see e.g. [6]) and

$$\alpha = 1/2 + (4ac - b^2)/16a^{3/2}, \quad \beta(z) = (2az + b)^2/4a^{3/2}. \quad (6.127)$$

The constants C_1 and C_2 are determined by the boundary conditions resulting from the required continuity of the wave-field $\psi(z)$ and its derivative $d\psi(z)/dz$ at the positions z_n . $R(q_z)$ may then be obtained by applying the matrix-transfer method [5]. The poles of α and $\beta(z)$ at $a = 0$, i.e. a linear profile, are handled by making use of the asymptotic behavior $\lim_{x \rightarrow \infty} {}_1F_1(x)$ as given in Ref. [6], which involves the Airy functions $\text{Ai}(x)$ and $\text{Bi}(x)$ – the solutions of the Schrödinger equation for the linear graded profile.

Although the briefly sketched analytical solution is exact, we will not make use of it because the modified Fresnel coefficients provide a sufficiently accurate approximation. Furthermore, the computational cost of the numerical evaluation the above mentioned special functions, ${}_1F_1(x)$, $\text{Ai}(x)$ and $\text{Bi}(x)$, is too high to justify its use.

If anyhow, the width d of the B-splines is too large, the calculation of the reflection may become inaccurate. To overcome this problem, one may calculate the reflection from a profile built of second order B-splines of width $d/2$. The representation of a second order B-spline of width d , denoted⁸ by $B_d^2(z - md)$, by second order B-splines of width $d/2$, denoted by $B_{d/2}^2(z - md)$, is given by

$$\begin{aligned} B_d^2(z - md) &= \frac{1}{4} B_{d/2}^2 \left[z - md - \frac{3}{4}d \right] + \frac{3}{4} B_{d/2}^2 \left[z - md - \frac{1}{4}d \right] \\ &+ \frac{3}{4} B_{d/2}^2 \left[z - md + \frac{1}{4}d \right] + \frac{1}{4} B_{d/2}^2 \left[z - md + \frac{3}{4}d \right] \end{aligned} \quad (6.128)$$

from which follows that a profile

$$\rho(z) = \sum_{m=0}^M b_m B_d^2(z - md)$$

⁸This notation differs from that of the rest of the thesis: Here, the subscript gives the *grid-size* d , whereas it gives the *position* of the spline elsewhere.

may be reexpressed as

$$\begin{aligned} \rho(z) = & \frac{1}{4} \sum_{m=0}^{M+1} (b_m + 3b_{m-1}) B_{d/2}^2(z - md - 3d/4) \\ & + (3b_m + b_{m-1}) B_{d/2}^2(z - md - d/4) \quad . \end{aligned} \quad (6.129)$$

Accelerated calculation of the reflection coefficient

Since the calculation of the reflection coefficient $R(q_z)$ within dynamical theory turns out to be time-consuming compared to the case of the linear-graded and the piecewise profile an acceleration is desirable. For sufficiently large wavevector-transfers q_z , say $q_z > 2q_c$, the so-called **W**eighted-**S**uperposition **A**pproximation (WSA), see e.g. Refs. [65][171], yields highly accurate results. Within this approximation the reflection coefficient is calculated via

$$R(q_z) = 4\pi \int_0^L \frac{1}{q_z(z)^2} \frac{d\rho(z)}{dz} \exp \left[i \int_0^z q_z(Z) dZ \right] dz \quad (6.130)$$

where $q_z(z) = \sqrt{q_z^2 - 16\pi\rho(z)}$, see also Eqs. (2.38) and (2.40). For the B-spline profile the above formula is replaced by the sum over the intervals $\mathcal{I}_n = [nd, (n+1)d]$. The profile is of the form $\rho(z) = \rho_\infty(\alpha_n z^2 + \beta_n z + \gamma_n)$ and the wavevector-transfer is approximated by $q_{z,n} = \sqrt{q_z^2 - 16\pi\bar{\rho}_n}$, $\bar{\rho}_n$ being the mean density on \mathcal{I}_n given by

$$\bar{\rho}_n = \alpha_n d^2 (n^2 + n + 1/3) + \beta_n d (n + 1/2) + \gamma_n \quad (6.131)$$

so that the reflection coefficient becomes

$$R(q_z) = 4\pi\rho_\infty \sum_{n=0}^{N-1} \frac{P_n(q_z)}{q_{z,n}^2} \int_{nd}^{(n+1)d} (2\alpha_n z + \beta_n) \exp [iq_{z,n}(z - nd)] dz \quad (6.132)$$

where $P_n(q_z) = \prod_{l=0}^{n-1} \exp(iq_{z,l}d)$. Carrying out the integration yields

$$R(q_z) = 4\pi\rho_\infty \sum_{n=0}^{N-1} P_n(q_z) \left[(A_n - iB_n) \exp(iq_{z,n}d) - A_n \right] \quad (6.133)$$

with

$$A_n = \frac{2\alpha_n}{q_{z,n}^4} - i \frac{2\alpha_n nd + \beta_n}{q_{z,n}^3} \quad \text{and} \quad B_n = \frac{2\alpha_n d}{q_{z,n}^3} \quad . \quad (6.134)$$

6.4.2 Derivation of the partial derivatives $\partial R(q_z)/\partial b_j$

To calculate the partial derivatives of the reflection coefficient $R(q)$ with respect to some parameter b_j of a profile with second order B-spline representation

$$\rho(z) = \rho_\infty \sum_n b_n B_n(z) \quad ,$$

the formalism presented in Section 6.1.4 must be adapted. In Section 6.4.1 we obtained

$$R_j = \exp(2ik_j Z_j) \frac{\tilde{r}_{j,j+1} + R_{j+1} \exp(-2ik_{j+1} Z_j)}{1 + \tilde{r}_{j,j+1} R_{j+1} \exp(-2ik_{j+1} Z_j)} \quad , \quad (6.135)$$

with $Z_j = \zeta_j + \mu_j$. The quantities ζ_j and μ_j are defined in Section 6.4.1. The partial derivative of the reflection coefficient R_j with respect to a coefficient b_n is then given by the recursion formula

$$\frac{\partial}{\partial b_n} R_j = R_j \frac{\partial}{\partial b_n} (2ik_j Z_j) + Q_j \left[B_j \frac{\partial}{\partial b_n} R_{j+1} + C_{j,n} \right] \quad , \quad (6.136)$$

with

$$\begin{aligned} Q_j &= \exp(2ik_j Z_j) & P_j &= \exp(-2ik_{j+1} Z_j) \\ A_j &= 1 + \tilde{r}_{j,j+1} R_{j+1} P_j & B_j &= (1 - \tilde{r}_{j,j+1}^2) P_j / A_j^2 \end{aligned} \quad (6.137)$$

and

$$C_{j,n} = \frac{1}{A_j^2} \left[(1 - R_{j+1}^2 P_j^2) \frac{\partial \tilde{r}_{j,j+1}}{\partial b_n} + R_{j+1} (1 - \tilde{r}_{j,j+1}^2) \frac{\partial P_j}{\partial b_n} \right] \quad . \quad (6.138)$$

The modification of b_n changes the profile on the interval $[z_{n-2}, z_{n+1}]$, thus, affecting only those reflection coefficients $\tilde{r}_{j,j+1}$ with $j \in \{n-2, n-1, n\}$. The partial derivatives $\partial P_j / \partial b_n$ are equal to zero for $j \notin \{n-2, n-1\}$. Then, for fixed n , all coefficients $C_{j,n}$ vanish, except for $C_{n-2,n}$, $C_{n-1,n}$ and $C_{n,n}$, so that Eq. (6.136) simplifies to $\partial R_j / \partial b_n = 0$ for $j > n$ and

$$\frac{\partial}{\partial b_n} R_j = Q_j B_{j+1} \frac{\partial}{\partial b_n} R_{j+1} \quad \text{for } j < n-2 \quad . \quad (6.139)$$

Carrying out the recursion up to $n=0$, one obtains

$$\frac{\partial}{\partial b_n} R_0 = D_n \frac{\partial}{\partial b_n} R_{n-1} \quad \text{where} \quad D_n = \prod_{l=1}^n Q_l B_{l+1} \quad . \quad (6.140)$$

In contrast to the case of the step-like profile and the linear-graded profile, the non-vanishing partial derivatives $\partial\tilde{r}_n/\partial b_j$ are not derived in analytical form. Instead, they are calculated numerically using finite difference methods of first order,

$$\frac{\partial}{\partial b_n} R_{n-1} = \frac{R_{n-1}(b_n + \epsilon) - R_{n-1}(b_n)}{\epsilon} \quad , \quad (6.141)$$

where $R_{n-1}(b_n)$ is known and $R_{n-1}(b_n + \epsilon)$ is obtained by triple recursion of the Parratt algorithm as given by Eq. (6.135), starting from R_{n+1} .

This decision is justified by the fact that the main profit, namely the fast calculation of the Jacobian matrix, results from avoiding the $\mathcal{O}(N^2)$ operations via the recursion given by Eq. (6.140). Furthermore, due to the complexity of the analytical expressions for the above-mentioned derivatives, the use of finite difference methods is not expected to lead to a significant loss in speed.

When using the WSA for the calculation of the reflection coefficient, the partial derivatives simplify significantly and may be calculated analytically. The explicit formulae for $\partial R(q)/\partial b_n$ are derived in Appendix A.2.

6.4.3 Eigendensities for the second order B-spline profile

The calculation of the eigendensities is performed analogous to Sections 6.1.3 and 6.3.2: We want to obtain the eigendensities for a profile variation with compact support on $[0, L]$, where $L = Nd$. From the boundary conditions $\Delta\rho(0) = \Delta\rho(L) = 0$ follows that Δb_0 , Δb_1 and Δb_N must be equal to zero, so that $\Delta\rho(z)$ is given by

$$\Delta\rho(z) = \sum_{n=2}^{N-1} \Delta b_n B_n^2(z) \quad (6.142)$$

and the Fourier-transform of $\Delta\rho(z)$ becomes

$$\begin{aligned} \Psi(q) &= \frac{\Delta F(q)}{iq} = \int_{-\infty}^{\infty} \Delta\rho(z) \exp(iqz) dz \\ &= \frac{d}{4} \text{sinc}^3\left(\frac{qd}{2}\right) \exp(-iqd/2) \left(\sum_{n=2}^{N-1} \Delta b_n \exp(inqd) \right) \quad . \quad (6.143) \end{aligned}$$

We seek to maximize the energy $E = \int_{-Q}^Q \Psi^*(q)\Psi(q) dq$. Inserting the above equation yields

$$\begin{aligned} E &= \frac{d^2}{16} \sum_{n,m} \Delta b_n \Delta b_m \int_{-Q}^Q \text{sinc}^6(qd/2) \cos[qd(n-m)] dq \\ &= \frac{d^2}{8} \sum_{n,m} \Delta b_n \Delta b_m S_{n,m}(Q) \quad . \quad (6.144) \end{aligned}$$

The elements of the matrix $S_{n,m}(Q)$ are given by

$$\begin{aligned} S_{n,m}(Q) = & f_{n-m+3}(Q) + f_{n-m-3}(Q) - 6[f_{n-m+2}(Q) + f_{n-m-2}(Q)] \\ & + 15[f_{n-m+1}(Q) + f_{n-m-1}(Q)] - 20f_{n-m}(Q) \end{aligned} \quad (6.145)$$

with

$$\begin{aligned} f_j(Q) = & \frac{j^5}{60} \left[24 \frac{\cos(jQd)}{(jQd)^5} - 6 \frac{\sin(jQd)}{(jQd)^4} - 2 \frac{\cos(jQd)}{(jQd)^3} \right. \\ & \left. + \frac{\sin(jQd)}{(jQd)^2} + \frac{\cos(jQd)}{jQd} + \text{Si}(jQd) \right]. \end{aligned} \quad (6.146)$$

Again, the eigenvectors should have unit norm, i.e.

$$\int_{-\infty}^{\infty} [\psi_n(z)]^2 dz = \sum_{n,m} \Delta b_n \Delta b_m \tilde{B}_{n,m} = 1 \quad (6.147)$$

or in matrix notation $\mathbf{\Delta b}^T \tilde{\mathbf{B}} \mathbf{\Delta b} = 1$. The elements of the matrix $\tilde{\mathbf{B}}$ are given by

$$\tilde{B}_{n,m} = \int_{-\infty}^{\infty} B_n(z) B_m(z) dz = \begin{cases} \frac{11}{20}d, & m = n; \\ \frac{13}{60}d, & m = n \pm 1; \\ \frac{1}{120}d, & m = n \pm 2; \\ 0, & \text{otherwise.} \end{cases} \quad (6.148)$$

The matrix $\tilde{\mathbf{B}}$ is positive definite and has band structure. For the minimization of the energy E subject to the constraint $\|\psi(z)\| = 1$, we define the functional

$$U = 2d^2 \sum_{n,m} \Delta b_n \Delta b_m S_{n,m}(Q) - \lambda \sum_{n,m} \Delta b_n \Delta b_m \tilde{B}_{n,m} \quad (6.149)$$

with the Lagrangian-Multipliers λ . Minimization of U with respect to the coefficients Δb_n leads to the generalized eigenvalue-problem

$$2d^2 \sum_n \Delta b_n S_{n,m}(Q) = \lambda \sum_n \Delta b_n \tilde{B}_{n,m} \quad (6.150)$$

or in matrix notation $\mathbf{S} \mathbf{\Delta b} = \lambda \tilde{\mathbf{B}} \mathbf{\Delta b}$ from which the $(N - 2)$ eigendensities ψ_k with eigenvalues λ_k are obtained.

As an example, selected eigendensities $\psi_k(z)$ and their Fourier transforms $\Psi_k(q)$ are shown in Figures 6.10 and 6.11 for a density profile consisting of 50 slabs of thickness $d = 1$ and with $Q = 0.5$, respectively. The uppermost left panel in Fig. 6.10 depicts the eigenvalues λ_k of a linear scale (right axis, filled circles) and on a logarithmic scale (left axis, open circles). The λ_k decay rapidly at

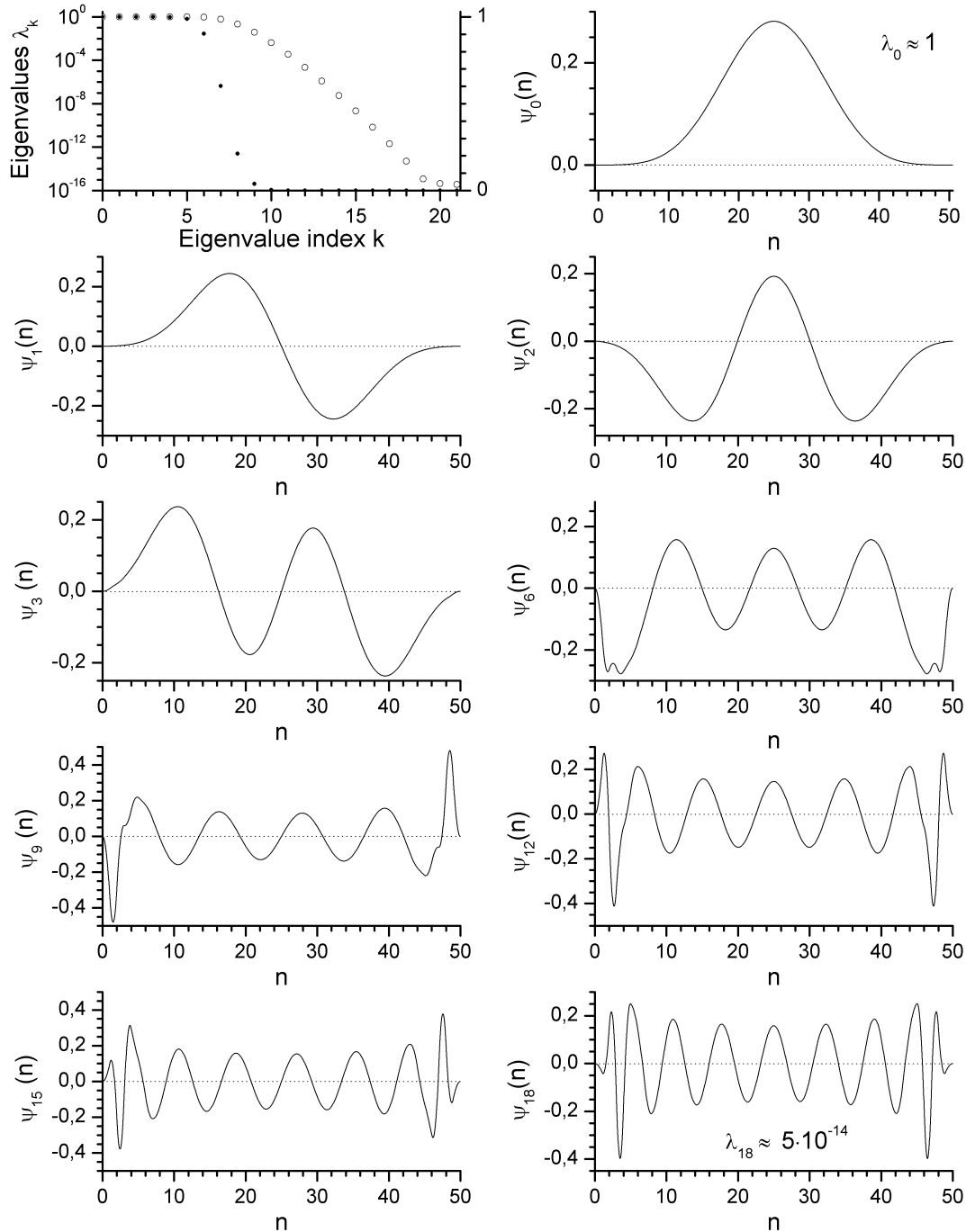


Figure 6.10: Eigendensities $\psi_k(z)$ of a second-order B-spline profile consisting of 50 slabs of thickness $d = 1$ for $Q = 0.5$: The uppermost left panel depicts the eigenvalues λ_k on a logarithmic scale (left axis, open circles) and on a linear scale (right axis, filled circles). Around $k = 50Qd/\pi \approx 8$ the λ_k decay rapidly. The corresponding Ψ -functions are shown in Fig. 6.11.

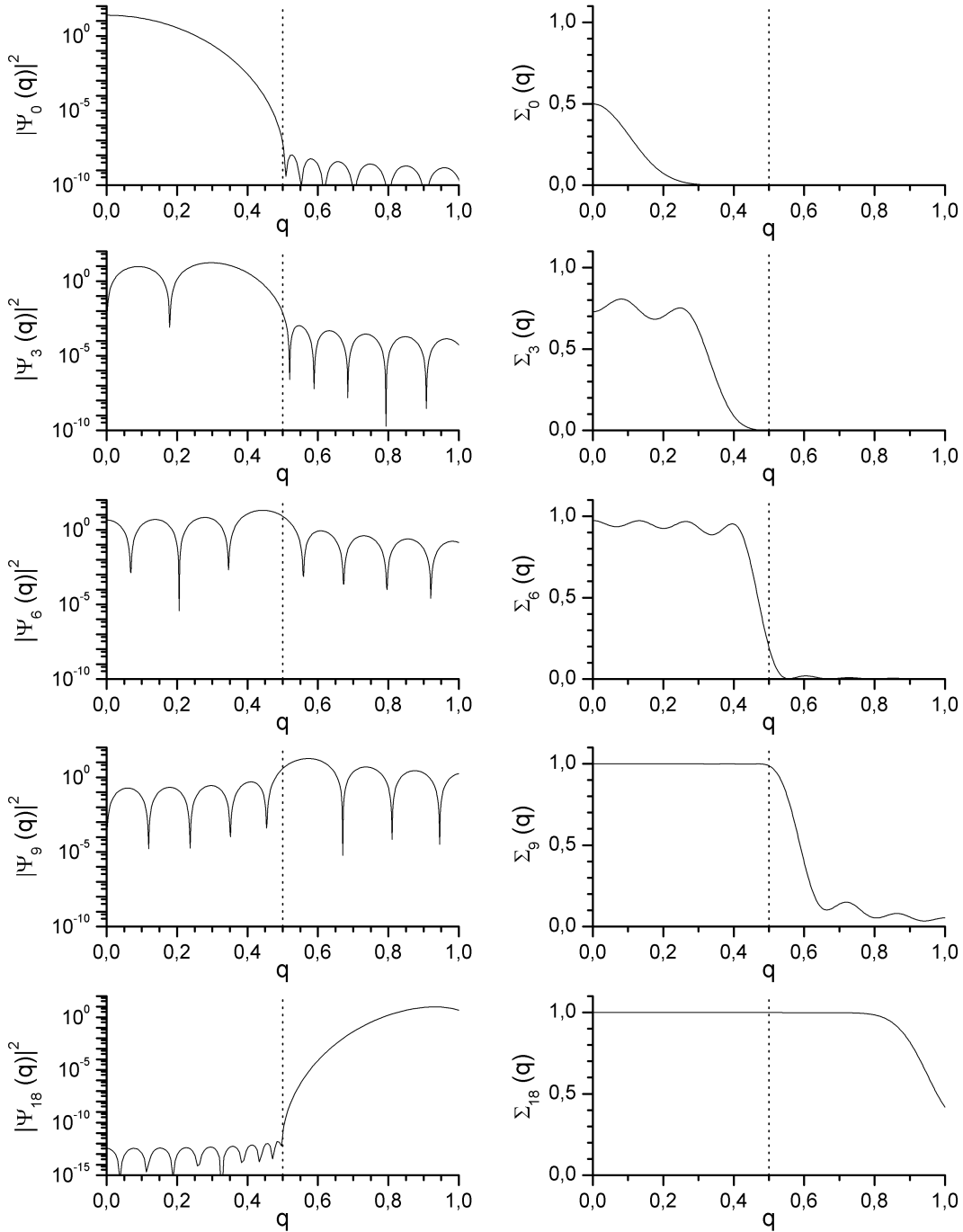


Figure 6.11: Squared moduli $|\Psi_k(q)|^2$ (left panels) and cumulative spectra $\Sigma_k(q)$ (right panels) for the eigendensities $\psi_k(z)$ depicted in Fig.6.10: For $k < 8$, the $|\Psi_k|^2$ are concentrated almost completely in $[-Q, Q]$ (vertical dotted line), whereas for $k \gg 8$ only little energy falls into $[-Q, Q]$. The $\Sigma_k(q)$ are smooth and almost unity on $[-Q, Q]$.

$k = 50Qd/\pi \approx 8$. For $k = 18$ the eigenvalue is $\approx 9 \cdot 10^{-14}$. The moduli squared of the Ψ_k are shown on a logarithmic scale in the left panels of Fig. 6.11. The vertical dotted line represents $Q = 0.5$. For $k < 8$ the Ψ_k are concentrated in the interval $[-Q, Q]$ and only little power spectral density is outside that interval. For $k \gg 8$, $\Psi_k(q)$ vanishes almost on $[-Q, Q]$, as shown in the lowermost left panel for $k = 18$. The right panels depict the cumulative spectra $\Sigma_k(q)$ which are smooth and converge to unity on $[-Q, Q]$ for $k > 9$.

Remarks on the solution of the eigenproblems

At this point some remarks on the computation of the eigenvalues and the eigenvectors will be made.

Since the matrices \mathbf{S} and $\tilde{\mathbf{B}}$ are both real and symmetric Toeplitz matrices, the matrix $\tilde{\mathbf{B}}^{-1}\mathbf{S}$ is centrosymmetric. It then follows, see e.g. [165], that its eigenvectors are either symmetric or skew-symmetric. For large N the eigenvalues are clustered at 1. Then for two eigenvalues $\lambda_n + \varepsilon = \lambda_m$, where ε is close to the machine-precision, if ψ_n and ψ_m are eigenvectors of $\tilde{\mathbf{B}}^{-1}\mathbf{S}$, any linear combination $a\psi_n + b\psi_m$, $a^2 + b^2 = 1$, will also be an eigenvector within machine-precision.

For the piecewise-constant profile this problem does not arise, because the clustering of the eigenvalues is not very strong. But for the linear-graded profile and for the second order B-spline profile, the clustering of the eigenvalues is very strong and it was found, that for $N \gtrsim 200$ the eigenvectors do not obey the desired symmetry properties anymore. To give an example, the eigenvalue spectra for the case $N = 300$, $d = 1\text{\AA}$ and $Q = 1\text{\AA}^{-1}$ have been calculated for the three types of eigenproblems. They are shown in Fig. 6.12. The decay of the the eigenvalues of the piecewise-constant eigendensities is clearly visible in the left panel, whereas the other two seem to be almost constant at 1. The right panel depicts the spectra around 1, now the decay of the eigenvalues of the linear-graded eigenproblem is clearly visible, but those of the second order B-spline case are still almost unity. This is not unexpected, since the side-lobes of the function $\text{sinc}(qd/2)^l$ decay faster as the degree l of the used B-spline increases and hence the concentration of energy in the band $[-Q, Q]$ increases.

The eigenvalue problems have been solved using the standard linear algebra package LAPACK [2]. One limiting factor is the precision of the routine for the computation of the sine integral $\text{Si}(x)$. It turns out that the use of standard routines with 16-digit precision leads to numerical instabilities resulting in eigenvalues $\lambda_k < 0$ or $\lambda_k > 1$, which is wrong since by definition $\lambda_k \in]0, 1[$. This problem was overcome by using an extended precision library [3] providing ≈ 33 digits of precision.

The problem due to the clustering of the eigenvalue around one is handled by transforming the original eigenvalue-problem to

$$\mathbf{T} \cdot \mathbf{b}_n = \mu_n \mathbf{b}_n \quad (6.151)$$

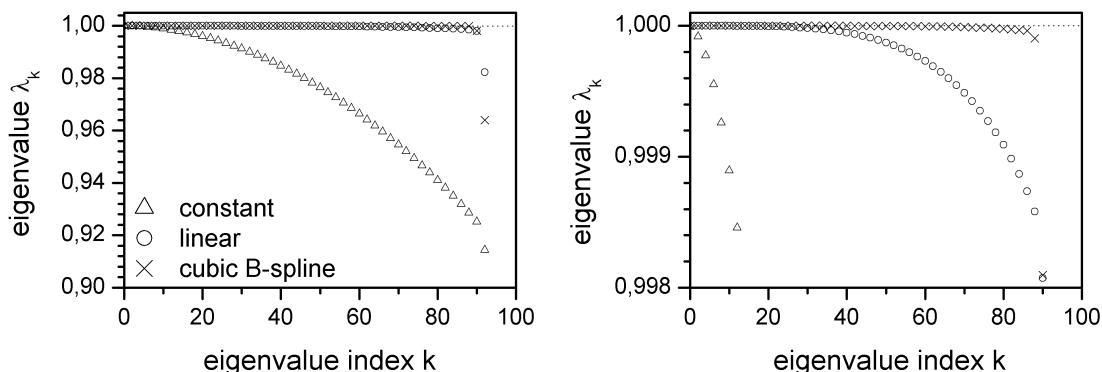


Figure 6.12: Eigenvalue spectra for the piecewise-constant (triangles), the linear-graded (circles) and the second order B-spline (crosses) eigendensities calculated for the case $N = 300$, $d = 1.0\text{\AA}$ and $Q = 1.0\text{\AA}^{-1}$. They decay at $k = 300/\pi \approx 94$. The eigenvalues of the piecewise-constant eigendensities are little clustered (left panel), whereas those of the second order B-spline eigendensities are strongly clustered at 1 (right panel). The eigenvalues for the linear-graded profile are less clustered (right panel). The dotted line represents $\lambda_k = 1$. For clarity only every second eigenvalue is shown.

where $\mathbf{T} = (\mathbf{S} - \sigma\tilde{\mathbf{B}})^{-1} \cdot \tilde{\mathbf{B}}$, $\sigma \approx 1 + \varepsilon$ and $\mu_n = 1/(\lambda_n - \sigma)$. ε is some small positive number. Note that $\mathbf{S} - \sigma\tilde{\mathbf{B}}$ is a Toeplitz matrix so that the computation of its inverse can be done quite efficiently, see e.g. [61][157].

In the following it is assumed that $\mathbf{T} \in \mathbb{R}^{2M \times 2M}$ with $M \in \mathbb{N}$. In order to enforce the afore-known symmetry and skew-symmetry of the eigenvectors, the matrix \mathbf{T} is written as

$$\mathbf{T} = \begin{bmatrix} \mathbf{C} & \mathbf{J} \cdot \mathbf{D} \cdot \mathbf{J} \\ \mathbf{D} & \mathbf{J} \cdot \mathbf{C} \cdot \mathbf{J} \end{bmatrix}, \quad (6.152)$$

where \mathbf{J} , \mathbf{C} , $\mathbf{D} \in \mathbb{R}^{M \times M}$. \mathbf{J} denotes the exchange matrix whose elements are equal to 1 on the anti-diagonal and zero otherwise and $\mathbf{J} \cdot \mathbf{D} \cdot \mathbf{J}$ is equal to \mathbf{D} rotated by 180° . The eigenvectors \mathbf{b}_n are reexpressed by a vector $\mathbf{a} \in \mathbb{R}^M$ and the matrix \mathbf{J} so that Eq. (6.151) takes the form

$$\mathbf{T} \begin{bmatrix} \mathbf{a} \\ \pm \mathbf{J} \cdot \mathbf{a} \end{bmatrix} = \mu \begin{bmatrix} \mathbf{a} \\ \pm \mathbf{J} \cdot \mathbf{a} \end{bmatrix} \quad (6.153)$$

for the symmetric (+) and the skew-symmetric (−) case, respectively. Making use of the relation $\mathbf{J} \cdot \mathbf{J} = \mathbb{1}$ above eigenproblems become

$$(\mathbf{C} \pm \mathbf{J} \cdot \mathbf{D}) \mathbf{a} = \mu \mathbf{a} \quad (6.154)$$

for the symmetric (+) and the skew-symmetric (−) case, respectively. Note that by splitting the eigenproblem in two eigenproblems for the symmetric and skew-symmetric eigenvectors, respectively, the clustering of the eigenvalues in the original eigenproblem has also been relaxed. However, this method is only suitable

for computing the eigenvalues/eigenvectors near the shift σ , because the matrix $\mathbf{C} \pm \mathbf{J} \cdot \mathbf{D}$ in Eq. (6.154) is non-symmetric and so the computed eigenvalues become complex, which is evidently false.

Therefore, the eigenvectors of the non-clustered eigenvalues, say $\lambda_n < 0.999$, are computed by solving the standard-eigenvalue problem

$$\tilde{\mathbf{B}}^{-1} \mathbf{S} \cdot \mathbf{b}_n = \lambda_n \mathbf{b}_n \quad . \quad (6.155)$$

Less effort is spent in the computation of the *non-resonant* eigendensities $\psi^{nr}(z)$. When using Eq. (6.155) the $\psi^{nr}(z)$ do not possess any symmetry properties because their eigenvalues are clustered at 0. However, they are still quasi-orthonormal, i.e.

$$\left| \int_0^L \psi_n^{nr}(z) \psi_m(z) dz \right| \lesssim 10^{-14} \quad (6.156)$$

holds for arbitrary m and n , which is sufficiently accurate.

6.5 Connection between the different types of profile representation

In the previous sections three types of density profiles, piecewise constant, linear-graded and second order B-spline, have been considered and the respective eigenproblems to obtain the eigendensities for the solution of the linear inverse problem have been derived. In this section the different approaches will be compared and conclusion for the application will be drawn.

Recall that the structure of a profile built of B-splines of order l is given by

$$F_l(q) = \exp(iZq) G_l(q) F_1(q) \quad (6.157)$$

where $\exp(iZq)$ is an arbitrary phase shift and

$$F_1(q) = \sum_{n=0}^N (b_{n+1} - b_n) \exp(inqd) \quad (6.158)$$

is the structure factor of the piecewise constant profile and the function

$$G_l(q) = \text{sinc}^{l-1}(qd/2) \quad (6.159)$$

accounts for the degree l of the used B-spline. Since $G_l(q) \in \mathbb{R}$, $\phi_G(q) = j\pi$, $j \in \mathbb{N}$, and hence all B-spline profiles with the identical coefficients b_n have the phase $\phi_{pc}(q)$ of the piecewise-constant profile. Moreover, since $G_l(Q)$ with $l > 1$ has only zeros on the real axis located at $|q_z| = n2\pi/d$, $n \in \mathbb{N}^+$, all these profiles have identical zeros apart from those of $G_l(Q)$, which are known beforehand. Note that the zeros on the real axis do not introduce additional ambiguities to

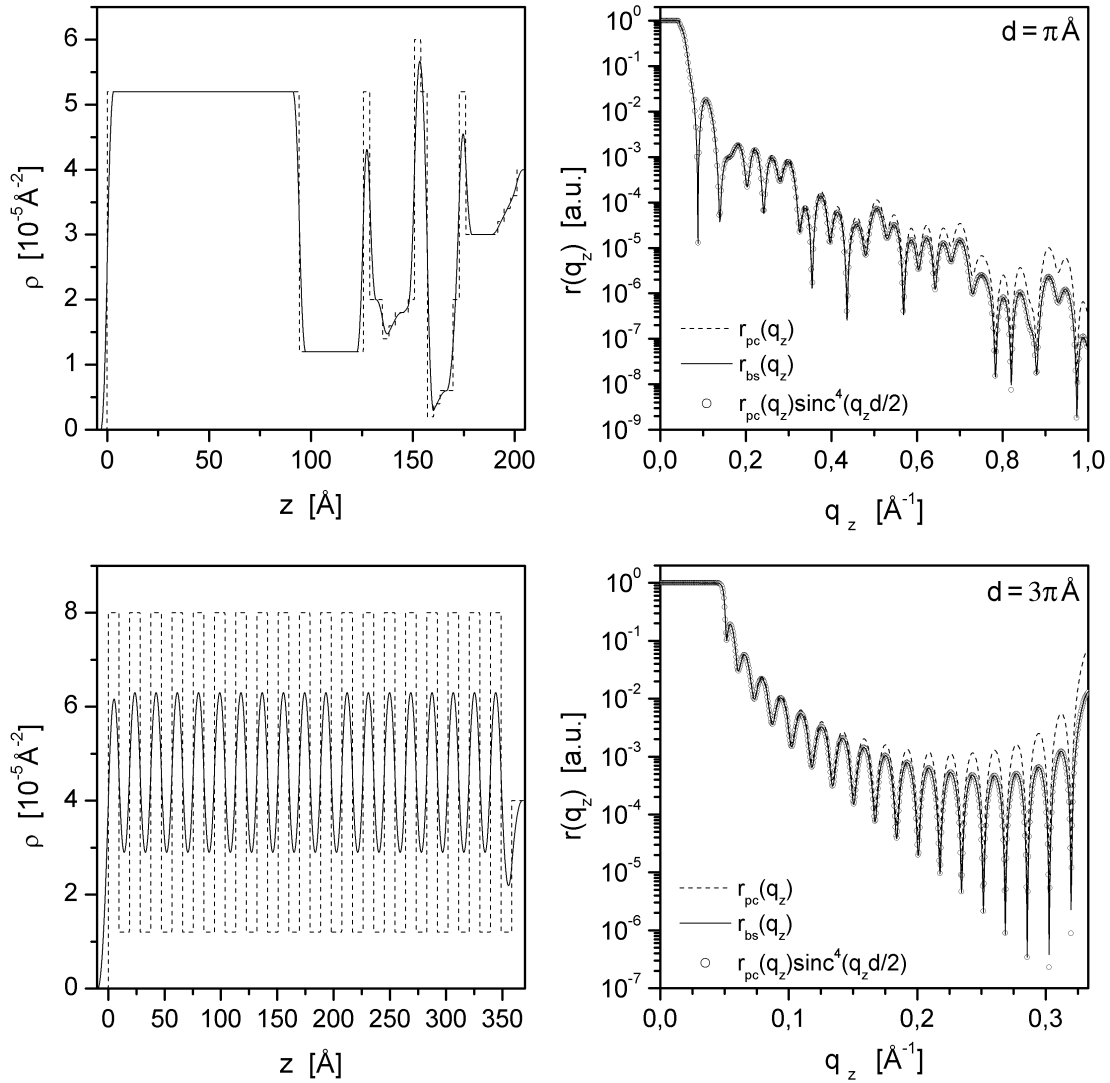


Figure 6.13: Comparison of the reflectivities from a piecewise-constant profile and a profile built of second order B-splines: The left panels show the density profiles and the right panels depict the reflectivities. Multiplying the reflectivity of the piecewise constant (dashed line) profile by $\text{sinc}^4(q_z d/2)$ yields a reflectivity (symbols) that is virtually indistinguishable from that of the second order B-spline profile (solid line).

the phase-problem and hence do not cause any problems, as discussed in Section 3.2.

Above observations can be extended to dynamical scattering theory, provided that $q_c \ll \pi/d$ holds. Two examples are given in Figure 6.13: The left panels depict the piecewise constant profiles (dashed lines) and the second order B-splines profiles (solid lines), constructed from the same coefficients b_n . The right panels

show the respective reflectivities. The dotted lines represent the reflectivities of the piecewise constant profile, but multiplied by $\text{sinc}^4(q_z d/2)$. They agree very well with those of the second order B-spline profiles. A further improvement may be achieved by using the function

$$G_l(q_z) = H(q_c - |q_z|) + H(|q_z| - q_c) \text{sinc}^{l-1}(q_d/2) \quad , \quad (6.160)$$

where $q = \sqrt{q_z^2 - q_c^2}$ accounts for non-linear effects. The phase of the respective reflection coefficients of the second example are presented in the left panel of Fig. 6.15 and they are in excellent agreement.

Thus, if we wish to analyze a reflectivity $r(q)$ given on $[-Q, Q]$, we have two possibilities. Let us assume that we would like to obtain a second order B-spline profile. Then, the first possibility is to analyze $\hat{r}(q) = r(q)/|G_l(q_z)|^2$ instead of $r(q)$ using the eigendensities of the piecewise-constant profile. The resulting coefficients b_n should then be such that the respective second order B-spline profile corresponds to a reflectivity $r(q_z)$. The second possibility is to analyze $r(q)$ using the piecewise-constant eigendensities and then to convert the obtained profile into a second order B-spline profile. Using Eqs. (6.157)–(6.159), the conversion can be performed straightforward by solving the set of linear equations

$$S(q_m) = \sum_{n=1}^N b_n \exp(i n q_m d) \quad (6.161)$$

with

$$S(q_m) = \frac{F^1(q_m) \text{sinc}^{1-l}(q_m d/2) \exp(-i Z q_m) - \exp(i q_m L)}{-2i \sin(q_m d/2) \exp(-i q_m d/2)} \quad . \quad (6.162)$$

The upper two panels in Fig. 6.14 give an example for the conversion of a piecewise-constant profile into a second order B-spline profile. Given is the piecewise-constant profile shown in the right panel (thin line). The corresponding reflectivity is represented by the symbols in the left panel. The obtained second order B-spline profile (thick line, right panel) is smooth and the reflectivity (solid line, left panel) agrees up to $q_z = 0.5 \text{\AA}^{-1}$, but decays much faster at larger q_z -values.

It should be emphasized that, the different (finite-dimensional) sets of eigendensities do not form a complete basis for the space they have support on. For example, a simple step-like profile $\rho(z) = \rho_\infty H(z)$ can not be expanded in higher-order B-splines. More generally, since the structure factor is an analytical function, two different profiles can not have identical structure factors on some domain⁹. Thus, the solution \mathbf{b} obtained from Eqs. (6.161) and (6.162) is actually the least-square solution of $\|S(q_m) - \sum_n b_n \exp(i n q_m d)\|$.

⁹The trivial case $\rho(z) \equiv 0$ for all z is excluded.

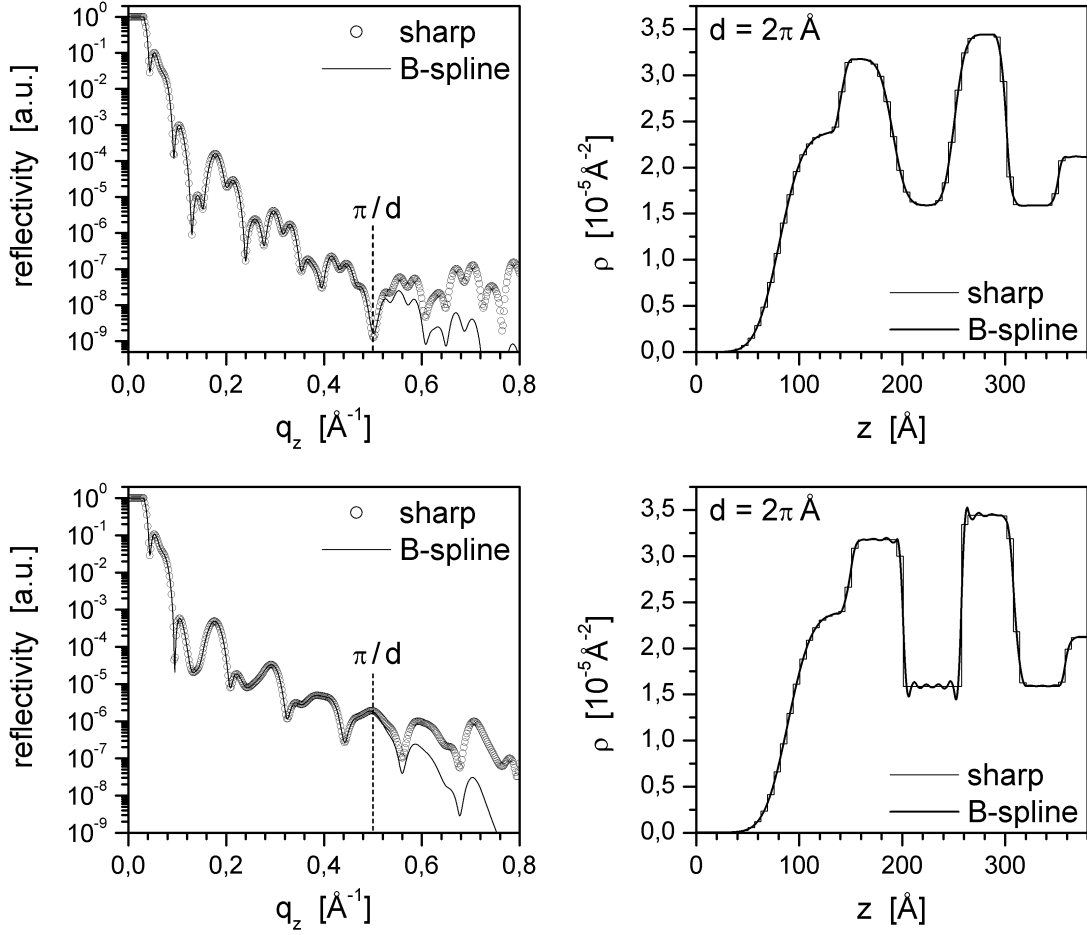


Figure 6.14: Conversion of piecewise-constant profiles in second order B-spline profiles: In the upper example the roughness of the internal interfaces is 10\AA and 8\AA , respectively. The lower right panel depicts the conversion of a profile with sharp interfaces (both $\sigma = 1\text{\AA}$). The *intrinsic* roughness of the second order B-splines with grid $d = 2\pi\text{\AA}$ is too large to obtain a non-oscillating profile around the sharp interfaces.

In general, we expect the profile to be smooth and non-oscillating. This requires that the basis functions must have an *intrinsic* roughness smaller than that corresponding to the asymptotic behavior of the reflectivity. Consider, for example, a substrate with gaussian roughness σ . Its structure factor is given by $F_{DW}(q_z) \propto \exp(-q_z^2 \sigma^2 / 2)$. The structure factor of an interface given by a single B-spline of degree l is $F_{BS}(q_z) \propto \text{sinc}^{l-1}(q_z d / 2)$. From the respective expansions of the structure factors for small q_z ,

$$F_{DW}(q_z) \approx 1 - \sigma^2 / 2 q_z^2 + \mathcal{O}(q_z^4) \quad (6.163a)$$

$$F_{BS}(q_z) \approx 1 - (l-1)d^2 / 24 q_z^2 + \mathcal{O}(q_z^4) \quad , \quad (6.163b)$$

we see that $d \ll \sqrt{12/(l-1)}\sigma$ must hold in order to describe the gaussian interface properly. In the second example depicted in Fig. 6.14, the roughness of two internal interfaces has been reduced – from 10Å and 8Å to 1Å for both. Since $d = 2\pi \text{Å} \gg \sqrt{6} \text{Å}$, strong oscillations show up at the sharp interfaces of the obtained second order B-spline profile. From this follows that if the reflectivity $r(q_z)$ is only known up to $q_{max} < \pi/d$, then the *non-resonant* eigendensities, i.e. those with vanishing eigenvalues, have to be involved to reduce the oscillations in the density profile by making use of the functional U_s given in Section 6.2.

The extension of the presented method for the calculation of the reflection coefficient and the construction of the eigendensities can be easily extended to higher order B-splines. If the B-splines are of degree m , the profile can have up to $m - 1$ extrema on an interval $[z_{n-1}, z_n]$. The reflection from that interval may then be calculated by splitting it as described in Section 6.4.1 for the case $m = 2$. The respective eigenproblems can be stated straightforward by comparison of the respective formulae for the linear-graded and the second order B-spline case. Although higher order B-spline profiles possess smooth higher-order derivatives, their disadvantages predominate: All calculations performed in dynamical scattering theory will be much more time-consuming compared to those for the lower order B-spline profiles. Furthermore, the computation of the eigendensities will be complicated by the stronger clustering of the eigenvalues at 1. Thus, their use does not seem to be justified.

6.6 Computation of the Hilbert-phase of a B-spline profile

Let us assume that we obtained a profile whose reflectivity agrees with the measured one. To investigate the influence of the zeros of the reflection coefficient on this profile, the Hilbert-profile is required.

6.6.1 The Hilbert-phase of a B-spline profile

From the discussion of the last section it follows that for the calculation the Hilbert-phase of a B-spline profile, it is sufficient to calculate that of the corresponding piecewise constant profile. In the following $F(q)$ denotes the structure factor of the piecewise-constant profile.

Since

$$F(q) = \sum_{n=0}^N (b_{n+1} - b_n) \exp(inqd)$$

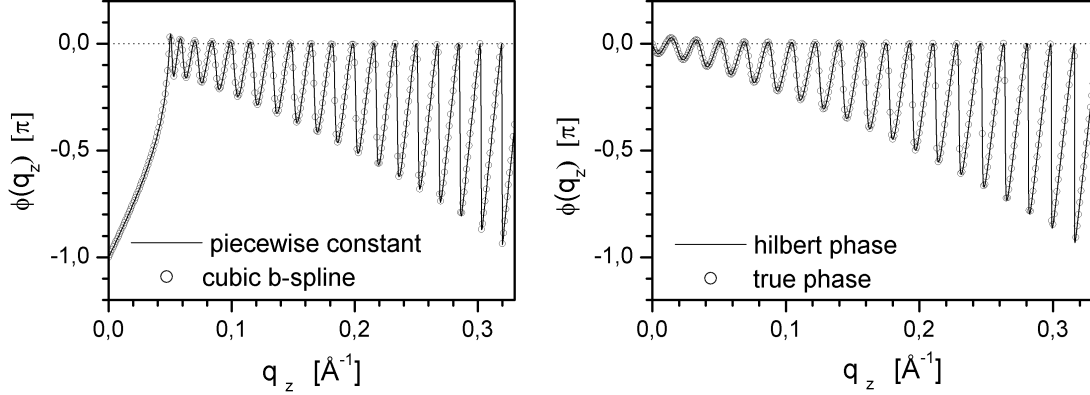


Figure 6.15: Phases for the lower example presented in Fig. 6.13. Left side: Phases of the piecewise constant and the second order B-spline profile. Right side: True phase of the structure factor $F(q_z)$ and the corresponding Hilbert-phase obtained from Eq. (6.166).

is periodic, i.e. $F(q) = F(q + 2Qn)$, where $Q = \pi/d$ and $n \in \mathbb{Z}$, the Hilbert-phase may be written as

$$\begin{aligned} \phi_{H,pc}(q_z) &= -\frac{q_z}{\pi} \int_{-\infty}^{\infty} \frac{\ln |F(q')| - \ln |F(q_z)|}{q'^2 - q_z^2} dq' \\ &= -\frac{q_z}{\pi} \int_{-Q}^Q \ln \left| \frac{F(q')}{F(q_z)} \right| \sum_{n=-\infty}^{\infty} \frac{1}{(q' + 2Qn)^2 - q_z^2} dq' \quad (6.164) \end{aligned}$$

Substitution of $q' = 2Qa$ and $q_z = 2Qb$ and making use of the relation

$$f(a, b) = \frac{b}{\pi} \sum_{n=-\infty}^{\infty} \frac{1}{(a+n)^2 - b^2} = \frac{\cos(\pi b) \sin(\pi b)}{\cos^2(\pi b) - \cos^2(\pi a)} \quad (6.165)$$

the Hilbert-phase becomes

$$\phi_{H,pc}(q_z) = -\frac{1}{Q} \int_0^Q \ln \left| \frac{F(q')}{F(q_z)} \right| f\left(\frac{q'}{2Q}, \frac{q_z}{2Q}\right) dq' \quad , \quad (6.166)$$

where the singularity of $f(a, b)$ at $b = \pm a$ is removed by $\ln |F(q')/F(q_z)|$. It is worth noting that it is sufficient to calculate $\phi_{H,pc}(q_z)$ for $q_z \in [0, Q]$, because of the symmetry property $\phi_{H,pc}(-q_z) = -\phi_{H,pc}(q_z)$ and the $2Q$ -periodicity, that is $\phi_{H,pc}(q_z + 2Qn) = \phi_{H,pc}(q_z)$, $n \in \mathbb{N}$. The right panel in Figure 6.15 depicts the Hilbert-phase obtained from the profiles of the second example in Fig. 6.13 using Eq. (6.166) and the phase of their structure factors $F(q_z)$. Both phases agree perfectly. It is worth noting that no additional phase-shift $\exp(iq_z\Delta)$ is required to obtain the depicted Hilbert-phase, in contrast to the Hilbert-phases presented

in the Section 3.1.3.

To calculate the Hilbert-phase within dynamical scattering theory,

$$\phi_{H,dyn}(q_z) = \phi_F(q_z) - \frac{2q_z}{\pi} \int_0^\infty \frac{\ln f(q') - \ln f(q_z)}{q'^2 - q_z^2} dq' \quad , \quad (6.167)$$

where $f(q_z) = r(q_z)/r_F(q_z)$ and $\phi_F(q_z)$ is the phase of the Fresnel reflection $R_F(q_z)$, the integral is split: The first integral extends over the q_z -region dominated by dynamical scattering effects and for the second integral the kinematical approximation is assumed to be valid:

$$\phi_{H,dyn}(q_z) = \phi_F(q_z) - \frac{2q_z}{\pi} \left(\int_0^{Q(N_d)} + \int_{Q(N_d)}^\infty \right) \frac{\ln f(q') - \ln f(q_z)}{q'^2 - q_z^2} dq' \quad (6.168)$$

where

$$Q(n) = \sqrt{(2n-1)^2 Q^2 + q_c^2} \quad (6.169)$$

$Q = \pi/d$ and N_d is chosen sufficiently large so that

$$r(q_z) \approx r_F(q_z) |F(q)|^2 \quad , \quad (6.170)$$

$q = \sqrt{q_z^2 - q_c^2}$, holds for $q_z \geq Q(N_d)$. The first integral is solved by numerical integration and by making use of Eq. (6.170) the second integral, in the following denoted by $\hat{\phi}(q_z)$, becomes

$$\hat{\phi}(q_z) = -\frac{2q_z}{\pi} \int_{Q(N_d)}^\infty \frac{\ln |F(\sqrt{q'^2 - q_c^2})|^2 - \ln f(q_z)}{q'^2 - q_z^2} dq' \quad (6.171)$$

and a change of variables, $\zeta = \sqrt{q'^2 - q_c^2}$, leads to

$$\hat{\phi}(q_z) = -\frac{2q_z}{\pi} \int_{(2N_D-1)Q}^\infty \frac{\ln |F(\zeta)|^2 - \ln f(q_z)}{\zeta^2 + q_c^2 - q_z^2} \frac{\zeta}{\sqrt{\zeta^2 + q_c^2}} d\zeta \quad . \quad (6.172)$$

Splitting the interval $[(2N_D-1)Q, \infty]$ into intervals $[(2n-1)Q, (2n+1)Q]$, $n = N_D, \dots, \infty$, yields

$$\hat{\phi}(q_z) = -\frac{2q_z}{\pi} \int_{-Q}^{+Q} [\ln |F(\zeta)|^2 - \ln f(q_z)] S(\zeta, q_z, q_c) d\zeta \quad (6.173)$$

with

$$S(\zeta, q_z, q_c) = \sum_{n=N_D}^\infty \frac{1}{(\zeta + 2Qn)^2 + q_c^2 - q_z^2} \frac{\zeta + 2Qn}{\sqrt{(\zeta + 2Qn)^2 + q_c^2}} \quad . \quad (6.174)$$

Since $q_c \ll \zeta + 2Qn$, we approximate the last term by its series expansion¹⁰ and obtain

$$S(\zeta, q_z, q_c) \approx \sum_{n=N_D}^{\infty} \frac{1}{(\zeta + 2Qn)^2 - (q_z^2 - q_c^2)} \left(1 - \frac{1}{2} \left(\frac{q_c}{\zeta + 2Qn} \right)^2 \right) . \quad (6.175)$$

The above expression can be solved analytically by making use of the formulae

$$S_1(a, b) = \sum_{n=N_D}^{\infty} \frac{1}{(a+n)^2 - b} = -\frac{1}{2\sqrt{b}} g(a, b) \quad (6.176)$$

$$S_2(a, b) = -\sum_{n=N_D}^{\infty} \frac{1}{((a+n)^2 - b)(a+n)^2} = \frac{1}{2b\sqrt{b}} g(a, b) + \frac{\Psi_1(N_D + a)}{b} \quad (6.177)$$

where $g(a, b)$ is given by

$$g(a, b) = \Psi(N_D + a - \sqrt{b}) - \Psi(N_D + a + \sqrt{b}) \quad (6.178)$$

and $\Psi_0(x) = \frac{d}{dx} \Gamma(x)/\Gamma(x)$ is the digamma function and $\Psi_1(x) = \frac{d}{dx} \Psi_0(x)$ is the first polygamma function, see e.g. [6]. For $b = 0$, i.e. $q_z = q_c$, the above sums simplify to

$$S_1(a, 0) = \Psi_1(N_D + a) \quad \text{and} \quad S_2(a, 0) = \frac{1}{6} \Psi_3(N_D + a) \quad , \quad (6.179)$$

where $\Psi_3(x) = \frac{d^3}{dx^3} \Psi_0(x)$. Finally, Eq. (6.175) becomes

$$S(\zeta, q_z, q_c) \approx \frac{1}{4Q^2} \left[S_1 \left(\frac{\zeta}{2Q}, \frac{q_z^2 - q_c^2}{4Q^2} \right) + \frac{q_c^2}{8Q^2} S_2 \left(\frac{\zeta}{2Q}, \frac{q_z^2 - q_c^2}{4Q^2} \right) \right] . \quad (6.180)$$

Note that the digamma function $\Psi(x)$ has poles at $-1, -2, \dots$. Thus, the stable calculation of the above formula requires positive arguments for $\Psi(x)$ in Eq. (6.178) so that N_D should be sufficiently large compared to q_z .

To illustrate the difference between calculating the Hilbert-phase by simply truncating the integral, the Hilbert-phase of the dynamical reflection coefficient for the second example in Fig. 6.13 is shown in Fig. 6.16: The upper panel shows the correct phase of the reflection coefficient (solid line) calculated from the density profile. The symbols represent the Hilbert-phase obtained by integrating over the limited interval $[0, Q(N_D)]$ with $N_D = 2$. The value for q_c was estimated¹¹ from the reflectivity to be approximately 0.045\AA^{-1} so that the integration was performed up to $\approx 1 \text{\AA}^{-1}$ which is twice as far as the depicted q_z -region. It can be

¹⁰ $1/\sqrt{1+x} \approx 1 - x/2$ for $x \ll 1$.

¹¹The q_c may also be obtained from the condition $\phi_H(q) = 0$ for $q = \sqrt{(nQ)^2 + q_c^2}$, $n \in \mathbb{N}^+$, which follows from the $2Q$ -periodicity of $F(q_z)$ and $F(-q_z) = F(q_z)^*$.

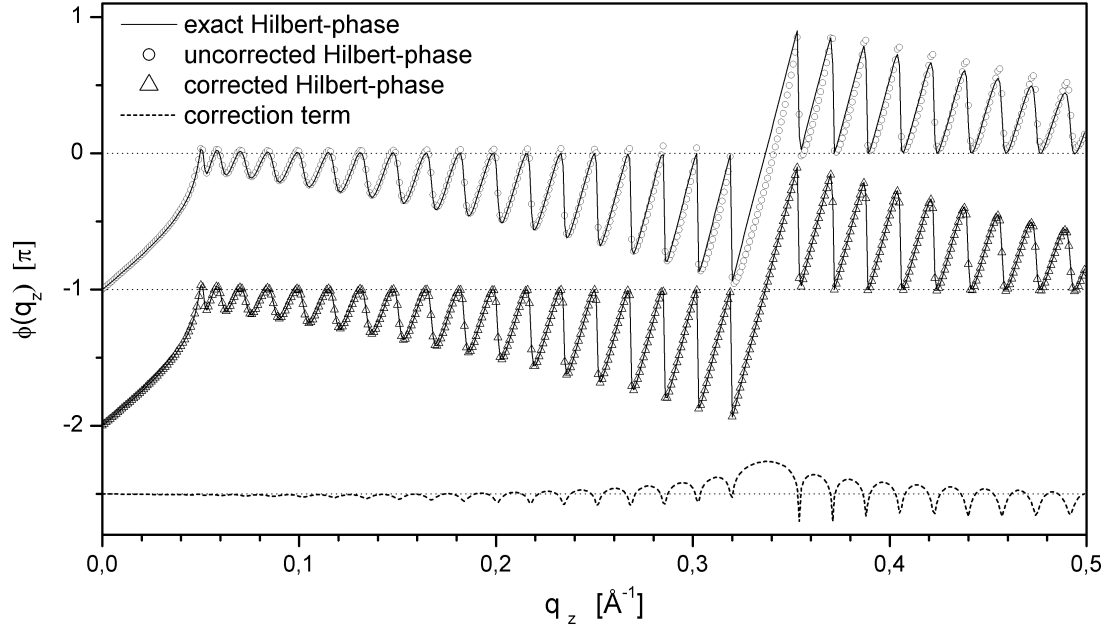


Figure 6.16: Calculation of the Hilbert-phase of the dynamical reflectivity from a piecewise-constant density profile: The corresponding reflectivity and the density profile are depicted in the lower panels in Fig. 6.13. The Hilbert-phase obtained by truncating the integration in Eq. (6.167) at $\approx 1\text{\AA}^{-1}$ (open circles) differs from the exact Hilbert-phase (solid line). The correction term $S(\zeta, q_z, q_c)$ calculated via Eq. (6.180) is represented by the dashed line, shifted by $-3/2\pi$ for clarity. Inclusion of this correction term results in the Hilbert-phase (open triangles, shifted by $-\pi$) that is in excellent agreement with the exact Hilbert-phase.

seen that the calculated Hilbert-phase begins to deviate from the exact solution at $\approx 0.25\text{\AA}^{-1}$. The dashed line, shifted by $-3/2\pi$ for sake of clarity, represents the phase-correction $\widehat{\phi}(q_z)$ calculated by Eq. (6.168) with q_c and N_D as given above. By including this phase-correction one obtains a Hilbert-phase (open triangles) that is in excellent agreement with the exact Hilbert-phase (solid line). Note again, that no additional phase-factor was required to obtain the depicted Hilbert-phase.

Now, that we are able to calculate Hilbert-phase to the reflectivity of a B-spline profile $\rho(z)$, we can use inverse methods of dynamical scattering theory to obtain the Hilbert-profile $\rho_H(z)$. This will be done in the next section.

6.6.2 Computation of the Hilbert-profile for B-spline profiles

The input quantity of the layer-stripping method is the impulse response function $g(t)$. In the following, its sine representation is used

$$g(t) = -\frac{2}{\pi} \int_0^\infty \Im \{R(q)\} \sin(qt) dq \quad . \quad (6.181)$$

The reason for choosing the sine transform is that $g(0) = 0$ is always fulfilled and that the use of the sine transform reduces the ringing due to Gibbs' phenomenon for profiles with a discontinuity at $z = 0$, such as the piecewise-constant profile. If the scattering potential is of extent L then $g(t)$ must be known for $0 \leq t \leq 2L$. At this point we give some details on the *layer-stripping technique* [122] that was already mentioned in Section 4.2. If the density profile is of extent L and wanted on the discrete grid $\hat{z} = i\Delta z$, $i = 0, \dots, N$ with $N\Delta z = L$ then $g(t)$ must be given on a discrete grid $t = j\Delta t$ with $\Delta t = 2L/(3N)$. The factor 3 is required for the extrapolation of $g(t)$ to zero grid size, see Refs. [27][122]. The accuracy of this method is $\mathcal{O}((\Delta z)^2)$. Therefore Δt and hence Δz should be sufficiently small and we choose \hat{z} to be a subgrid of z , $\Delta z = d/N_\Delta$.

Thus, the reflection coefficient $R(q_m)$ is required up to $q_{max} = N_\Delta Q$ with $q_m = m\Delta q = m(\pi/L)$. To reduce the computational effort, the calculation of $R(q_z)$ is performed in dynamical theory only for small q_z values. For the remaining q_z -region $R(q_z)$ is calculated in the kinematical approximation, i.e.

$$R(q_z) = (q_c/2q_z)^2 F_l(q_z) \quad (6.182)$$

with the structure factor $F_l(q)$ of a profile of B-spline degree l given by

$$F_l(q + 2Qn) = F_1(q) \left(\frac{\sin [(q + 2Qn)d/2]}{(q + 2Qn)d/2} \right)^{l-1} \quad . \quad (6.183)$$

Let us assume a profile $\rho(z)$ is available that provides a reflectivity that coincides with the reflectivity to analyze on $[-Q, Q]$ and let $d\rho(z)/dz$ have compact support on $[0, L]$, then we know from the previous chapters, that the flipping of a zero does not change the support properties.

Thus, if we apply the layer-stripping technique to the reflection coefficient

$$R_H(q_z) = \sqrt{r(q_z)} \exp[i\phi_H(q_z)] \quad ,$$

where ϕ_H is the Hilbert-phase calculated as described in Section 6.6, then the resulting profile $\rho_H(z)$ will also have support on $[0, L]$. Unfortunately, it is unlikely to be a Hilbert-profile having an expansion of the form $\rho_H(z) = \sum_n b_n B_n^l(z)$, for the following reason: If the reflection coefficient of $\rho(z)$ has zeros in the UHP

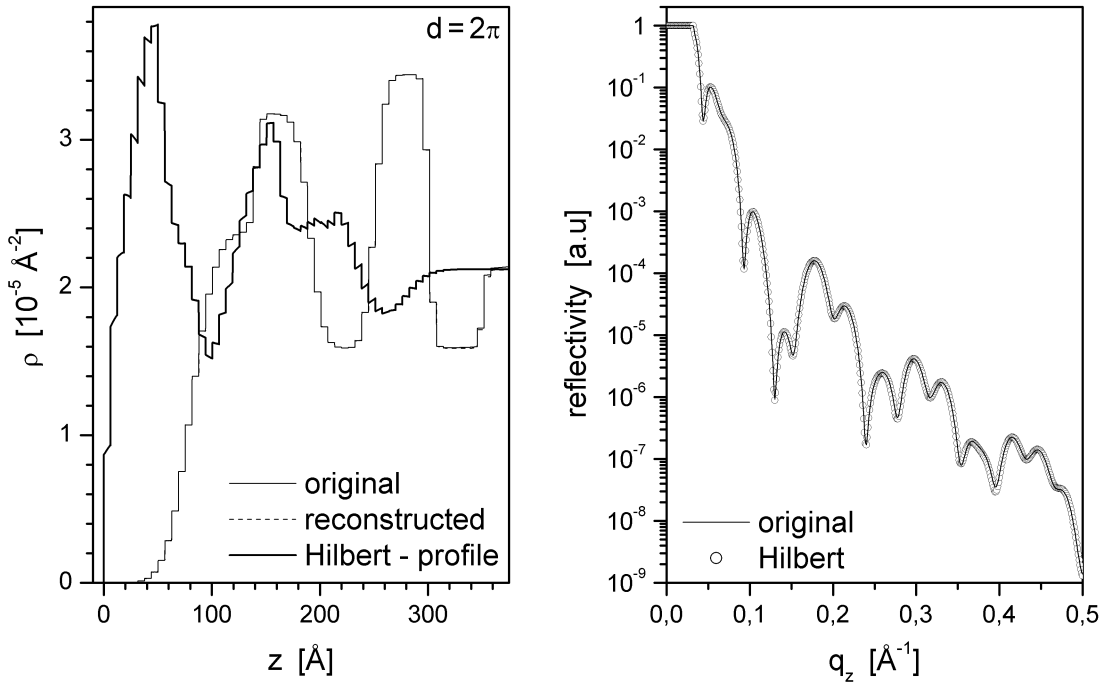


Figure 6.17: Reconstruction of the Hilbert-profile of a piecewise-constant profile: The original density profile (thin solid line) is piecewise-constant. The corresponding reflectivity is shown in the right panel (thin line). The dashed line represents the profile obtained by applying the layer-stripping technique to the reflection coefficient of the profile. The thick solid line represents the Hilbert-profile. It is no longer piecewise-constant. The phase of the reflection coefficient as well as the Hilbert-phase are depicted in Fig.6.18. The reflectivity of the Hilbert-profile (open circles, right panel) is in good agreement with the original reflectivity.

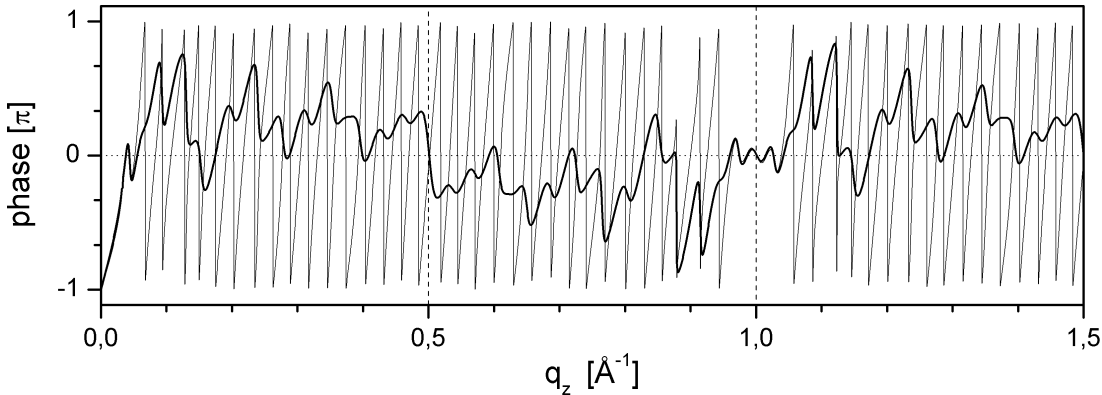
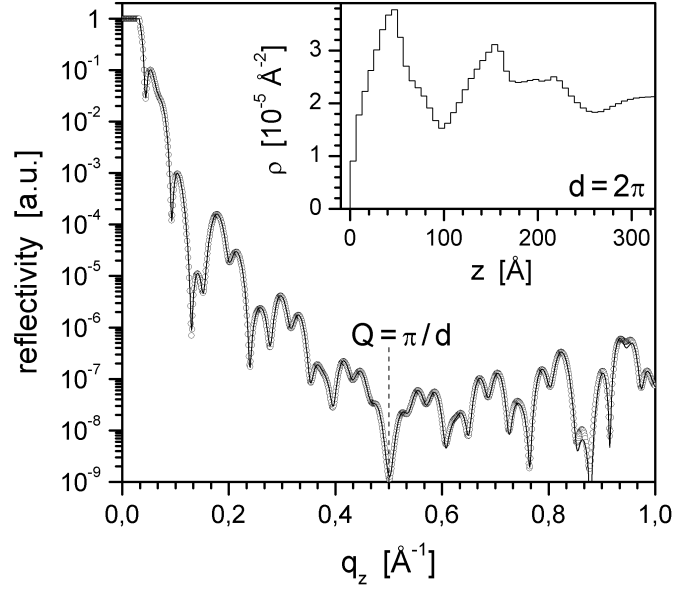


Figure 6.18: True phase (thin line) and Hilbert-phase (thick line) of the reflectivity depicted in Fig. 6.17. The vertical dashed lines represent $q_z = n\pi/d$.

Figure 6.19: The inset depicts the piecewise-constant profile obtained from the Hilbert-profile $\rho_H(z)$ shown in Fig.6.17. Its reflectivity (line) is identical with that from $\rho_H(z)$ (open circles) on $[-Q, Q]$ but different for $|q_z| > Q$, because the corresponding structure factor $F(q_z)$ changed on $[-Q, Q]$.

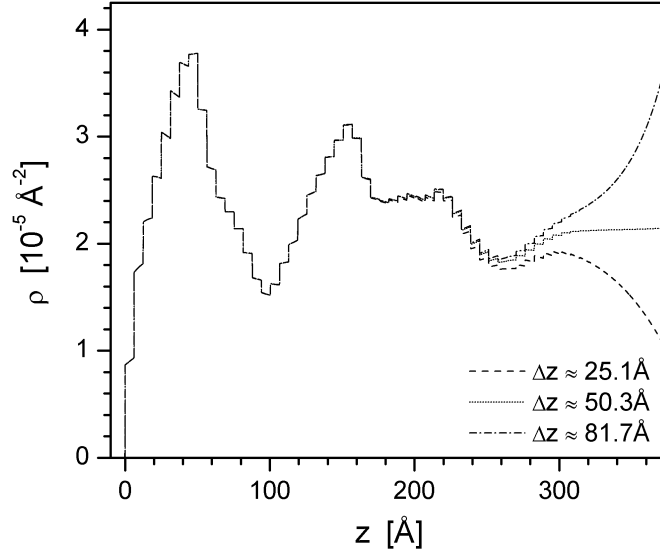


with small q_z -values, where the reflection is non-linear, then the flipping of these zeros into the LHP, by using the Hilbert-phase, will change the corresponding structure factor $F(q_z)$. The reflectivity of the Hilbert-profile does not change on $[-Q, Q]$, but for $|q_z| > Q$, the reflectivity will change around $q_z \approx 2nQ$, $n \in \mathbb{N}$, due to the non-linearity of the reflection-coefficient.

This effect is strongest for piecewise-constant profiles, whereas for higher-order B-spline profiles the reflectivity is damped around $q_z \approx 2nQ$ by the factor $\text{sinc}^{2(l-1)}(qd/2)$ so that this problem is weakened. From another point of view, higher order B-spline profiles provide a much better approximation of the smooth profile modifications due to the displacement of the zeros that are located in the region of dynamical scattering.

To illustrate this, an example is depicted in Figs.6.17 and 6.18: Given is a piecewise-constant density profile $\rho(z)$ (thin solid line, left panel) which is smooth in the surface-near region and has some sharp features inside, so that its reflection coefficient $R(q_z)$ must have zeros in the UHP. The corresponding reflectivity $r(q_z)$ is represented by the line in the right panel. The phase $\phi(q_z)$ of $R(q_z)$ is depicted in Fig. 6.18 (thin line). Then the Hilbert-phase $\phi_H(q_z)$ was calculated (thick line in Fig. 6.18) from $\rho(z)$ and the reflection coefficient $R_H(q_z) = \sqrt{r(q_z)} \exp[i\phi_H(q_z)]$ was inverted using the layer-stripping technique. The obtained density profile $\rho_H(z)$ is represented by the solid line in the left panel of Fig. 6.17. It is no longer piecewise-constant. The corresponding reflectivity (open circles, right panel) is in good agreement with that of the original profile. The piecewise-constant profile with $R(q_z)$ having no zeros in the UHP on $[-Q, Q]$ is then recovered by averaging the density inside the intervals $[z_n, z_{n+1}]$, i.e. $\rho_{n+1} = (1/d) \int_0^d \rho_H(z + nd) dz$. The obtained profile is depicted in the inset of the Fig. 6.19. The corresponding reflectivity (solid line) coincides with the reflectivity of $\rho_H(z)$ for $q_z \in [-Q, Q]$.

Figure 6.20: Different solutions obtained from the layer-stripping technique when adding some phase-shift $\exp(iq_z\Delta z)$ to the reflection coefficient $R_H(q_z)$. The different profiles coincide well up to $z \approx 200\text{\AA}$ after being translated by $-\Delta z$. At larger depths, $z \gg 200\text{\AA}$, the profiles differ significantly from each other due to the instability of the inverse method.



But for $|q_z| > Q$ the reflectivities differ from each other, because the respective structure factors are different due to the non-linearity of the reflection coefficient for small q_z -values.

It should also be noted that there exist piecewise-constant profiles for which a piecewise-constant Hilbert-profile does not exist. If, for example, the reflection coefficient $R(q_z)$ has a zero located at small q_z -values in the UHP, but the corresponding structure factor $F(q_z)$ no zeros in the UHP, then the flipping of this zero into the LHP will result in a density profile which has no zeros in the UHP, but is not piecewise-constant. But if the corresponding structure factor has zeros in the UHP, then the projection of this profile onto the space of piecewise-constant profiles yields a profile with zeros in the UHP at $|q_z| > Q$.

In the previous discussion, it was assumed that the inverse method used to obtain the Hilbert-profile $\rho_H(z)$ from the reflection coefficient $R_H(q_z)$ works sufficiently stable on $[0, L]$. In the presented example, this was the case – under some restrictions: Instead of inverting $R_H(q_z) = \sqrt{r(q_z)} \exp[i\phi_H(q_z)]$, where $\phi_H(q_z)$ is the Hilbert-phase depicted in Fig. 6.18, the reflection coefficient $R_H(q_z) \exp(iq_z\Delta z)$, with $\Delta z = 50\text{\AA}$, was used as input data for the inversion. Thus, the Hilbert-profile shown in Fig. 6.17 was translated by $-\Delta z$. From the theoretical point of view, the parameter Δz should not have an impact on the result of the inverse method. However, this is not the case as illustrated in Fig. 6.20. The three depicted profiles have been obtained from the layer-stripping technique after multiplying $R_H(q_z)$ with different phase-shifts Δz and then translating the profile by Δz . The three solutions agree well up to $z \approx 200\text{\AA}$ and differ significantly for $z > 200\text{\AA}$. The value for the quantity $B = 4\pi z \int_0^z \rho(Z) dZ$, see Section 4.2.1, is ≈ 13 for $z \approx 200\text{\AA}$.

The onset of this instability provides a simple possibility to estimate up to what

depth the obtained profile is trustworthy. This depth is denoted by \hat{L} is the following. Two cases have to be distinguished: $\hat{L} > L$ and $\hat{L} < L$. In the first case the profile is sufficiently small¹² and the layer-stripping technique is sufficient to recover the full Hilbert-profile. But if the inverse method provides only some fraction of the profile, additional work is required to recover the missing part of the profile on $[\hat{L}, L]$.

The easiest way to obtain the missing fraction of the profile ρ_H is by optimization:

- Given is the density profile $\rho_H(z)$ on $[0, Kd]$, where $K \equiv \lfloor \hat{L}/d \rfloor$, and the structure factor $F_H(q_z)$ as well as the (dynamical) reflection coefficient $R_H(q_z)$ on $[-Q, Q]$, $Q = \pi/d$.
- Generate a start-profile $\rho(z)$ by transforming the surface-near fraction $\rho_H(z)$, $z \in [0, Kd]$ into a piecewise-constant profile and complete the remaining part on $[Kd, Nd]$ by some profile, in the simplest case $\rho_n \equiv \rho_\infty$, $n = K + 1, \dots, N$. Note that the difference $\Delta\rho = \rho_H - \rho$ has compact support on $[Kd, Nd]$.
- Construct the set of linear equations

$$\Delta F(q_m) = \sum_{n=K+1}^N A_{mn} \Delta\rho_n \quad , \quad (6.184)$$

where $\Delta F(q_m) = F_H(q_m) - F(q_m)$ and $q_m = m\Delta q$ with $\Delta q = 2Q/(N - K)$ and $m = 1, \dots, (N - K)/2$. $F(q_m)$ is the structure factor of the profile $\rho(z)$. For the piecewise-constant profile, the elements of the matrix \mathbf{A} are given by

$$A_{mn} = iq_m d \operatorname{sinc}(q_m d/2) \exp[-iq_m d/2] \exp(iq_m n d) \quad . \quad (6.185)$$

The corresponding formulae for the linear-graded and the second order B-spline profile may be obtained from Eq. (6.93) and Eq. (6.143), respectively. Since the matrix A_{mn} is not singular, $\Delta\rho_n$ may be obtained straightforward via $\Delta\rho = \mathbf{A}^{-1} \cdot \Delta\mathbf{F}$.

The stability of the described method depends on the size the known part of the profile and the properties of the profile. Let us assume that the kinematical approximation fails for $q_z \lesssim 4q_c$. If $\rho_H(z)$ is known for $z \in [0, Kd]$, then $\Delta q = 2Q/(N - K)$ and hence $K_D \approx 2(q_c/Q)(N - K)$ grid-points are located in the region of dynamical scattering so that the respective equations in Eq. (6.185) are not valid anymore. Thus, they have to be replaced by their counterparts from dynamical theory,

$$\Delta \hat{F}_m \equiv \frac{R_H[q(m)] - R[q(m)]}{R_F[q(m)]} = \sum_{n=K+1}^N J_{mn} \Delta\rho_n \quad , \quad (6.186)$$

¹²Here "small" refers to the quantity B , see Section 4.2.1.

where $J_{mn} = (\partial R[q(m)]/\partial \rho_n)/R_F[q(m)]$ with $q(m) = \sqrt{(m\Delta q)^2 + q_c^2}$ and $m = 1, \dots, K_D$. The partial derivatives are calculated using the accelerated method described in Section 6.1.4. Then, the system of linear equations to solve becomes

$$\widehat{\mathbf{A}} \cdot \Delta \boldsymbol{\rho} = \begin{bmatrix} \Delta \widehat{\mathbf{F}} \\ \Delta \mathbf{F} \end{bmatrix} \quad \text{where} \quad \widehat{\mathbf{A}} = \begin{bmatrix} \mathbf{J} \\ \widetilde{\mathbf{A}} \end{bmatrix} . \quad (6.187)$$

The matrix $\widetilde{\mathbf{A}}$ consists of the last rows of \mathbf{A} for which the kinematical approximation is assumed to be valid. Since the problem is non-linear now, the above equation is used iteratively.

In order to avoid the inversion of the entire matrix $\widehat{\mathbf{A}}$ at each iteration step, the *Sherman-Morrison* formula¹³, see e.g. Refs. [61][113], is used:

$$(\mathbf{A} + \mathbf{e}_l \cdot \mathbf{J}_l^T)^{-1} = \mathbf{A}^{-1} - \frac{(\mathbf{A}^{-1} \cdot \mathbf{e}_l) \cdot (\mathbf{J}_l^T \cdot \mathbf{A}^{-1})}{1 + \lambda} , \quad (6.188)$$

where $\lambda \equiv \mathbf{J}_l^T \cdot \mathbf{A}^{-1} \cdot \mathbf{e}_l$. \mathbf{e}_l are the unit vectors and \mathbf{J}_l is the l -th row vector of \mathbf{J} . The above formula is applied $2K_D$ times – for real and imaginary part – starting with the matrix \mathbf{A}^{-1} and updating the l -th row at the l -th run. The overall effort for updating the matrix $\widehat{\mathbf{A}}^{-1}$ is of the order of $\mathcal{O}(K_D(N - K)^2)$ and hence the resulting gain in speed is $\approx (N - K)/K_D$.

Note, that the method works even for the case where no surface-near fraction of the Hilbert-profile is available, i.e. $K = 0$, so that one may ask, why using the layer-stripping technique at all. The reason is computational efficiency: The most time-consuming step is the calculating of the Hilbert-phase $\phi_H(q_z)$ in dynamical scattering theory¹⁴. In comparison to this, the computational cost of the layer-stripping technique is negligible so that the surface-near fraction of $\rho_H(z)$ is obtained for *almost* free. Furthermore, even if this fraction is small, the resulting reduction of the dimension of the Jacobian \mathbf{J} leads to a gain in speed.

6.6.3 Computation of the *conjugate* profile ρ_{H^*}

Once the Hilbert-profile ρ_H is known, access to all profiles with the same reflectivity $r(q_z)$ on $[-Q, Q]$ is possible, provided that all zeros $\{a_j\}$ of $R(q_z)$ have been determined. Various methods for locating the zeros have been discussed in Section 3.2.3. Zeros with sufficiently large real parts can be efficiently located within the kinematical approximation, whereas the detection of zeros located in the region of dynamical scattering turned out to be time-consuming.

Let us assume that the Hilbert-profile ρ_H is known and that we seek the *conjugate*¹⁵ profile ρ_{H^*} having all zeros in the UHP. In kinematical approximation $\rho_{H^*}^{kin}$

¹³Similarly, a *QR-decomposition* may be used, for which efficient update algorithms exist as well, see e.g. Refs. [61][113].

¹⁴This refers to the current stage of the numerical implementation.

¹⁵*conjugate* refers to the zeros of its reflection coefficient.

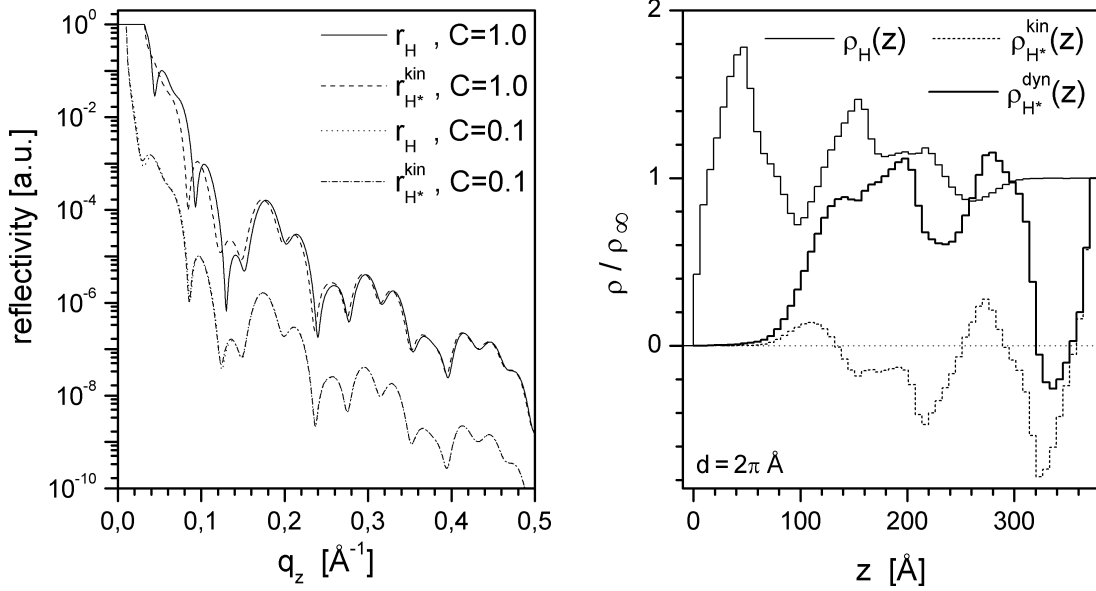


Figure 6.21: Left panel: Reflectivities from the scaled Hilbert-profile $C\rho_H(z)$ and the profile $C\rho_{H^*}^{kin}$ for $C = 1$ and $C = 0.1$. For small C both reflectivities differ little. Right panel: Hilbert-profile (thin solid line) and $\rho_{H^*}^{kin}$ (dashed line). The thick solid line represents the profile $\rho_{H^*}^{dyn}$ that was obtained by minimizing $\|r_H(q_z) - r_{H^*}^{dyn}(q_z)\|$, $q_z \in [0, \pi/d]$, while increasing the scaling factor C from ≈ 0 to 1.

can be obtained straightforward because the simultaneous flipping of all zeros corresponds to the operation $\rho_{H^*}^{kin}(z) = \rho_\infty - \rho_H(L - z)$, which becomes

$$\rho_H(z) = \rho_\infty \sum_{n=1}^N b_n B_n(z) \implies \rho_{H^*}^{kin}(z) = \rho_\infty \sum_{n=1}^N (1 - b_{N-n+1}) B_n(z) \quad (6.189)$$

for the B-spline profiles. Of course, the reflectivities from the profiles ρ_H and $\rho_{H^*}^{kin}$ are not identical due to non-linear effects, but we can use $\rho_{H^*}^{kin}$ as a starting-point for an iterative procedure to recover the profile $\rho_{H^*}^{dyn}$ with the reflectivity $r_{H^*}^{dyn}(q_z) = r_H(q_z)$ for $q \in [-Q, Q]$:
occur

Step 1: Given is the Hilbert-profile $\rho_H(z)$, the *conjugate* profile $\rho_{H^*}^{kin}(z)$ obtained from by Eq.(6.189) and the number of scaling-steps M . Set $m = 1$ and $\widehat{\rho}_{H^*}^{dyn}(C_0, z) = \rho_{H^*}^{kin}(z)$.

Step 2: Calculate the profile

$$\rho_{H^*}^{dyn}(C_m, z) = \frac{C_m}{C_{m-1}} \widehat{\rho}_{H^*}^{dyn}(C_{m-1}, z) \quad (6.190)$$

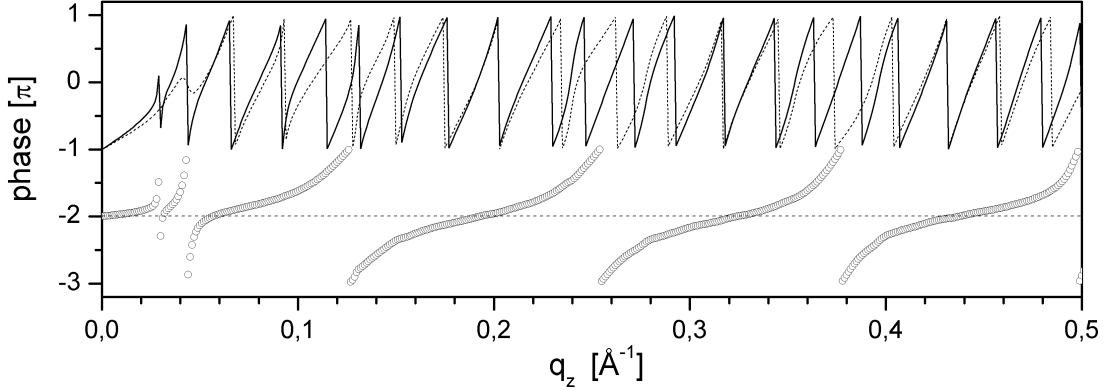


Figure 6.22: Phases of the reflection coefficients from the *original* profile depicted in Fig. 6.17 (thin line) and from the profile $\rho_{H^*}^{dyn}$ (thick line). The difference between the phases is represented by the symbols, shifted by -2π for clarity. The additional zeros of $R_{H^*}^{dyn}$ in the UHP are clearly visible as they appear as poles.

with the scaling-factor $C_m = (m/M)^2$ so that $q_{c,m} - q_{c,m-1} \approx \sqrt{16\pi\rho_\infty}/M$ remains almost constant. For $m = 1$, $C_0 \equiv 1$. Calculate the reflectivity $r_H(C_m, q_z)$ from the density profile $\rho_H(C_m, z) = C_m\rho_H(z)$.

Step 3: Starting from $\rho_{H^*}^{dyn}(C_m, z)$, minimize $\|r_H(C_m, q_z) - r_{H^*}^{dyn}(C_m, q_z)\|$ for $q_z \in [-Q, Q]$ and obtain the profile $\widehat{\rho}_{H^*}^{dyn}(C_m, z)$.

Step 4: If $m < M$, increase m and goto Step 2.

The procedure described above has been applied to the Hilbert-profile ρ_H shown in the right panel Fig. 6.21 (thin solid line, cf. inset of Fig. 6.19). The *conjugate* profile $\rho_{H^*}^{kin}(z)$ is represented by the dashed line. The left panel depicts the reflectivities $r_H(C, q_z)$ and $r_{H^*}^{kin}(C, q_z)$, for $C = 1$ and $C = 0.1$, respectively. The thick solid line in the right panel is the profile $\rho_{H^*}^{dyn}(z)$, obtained with $M = 10$. The phase of the reflection coefficient $R_{H^*}(z)$ is depicted in Fig. 6.22 (thick solid line) along with the phase of the "original" profile (thin line in Fig. 6.17). The difference between both phases is represented by the symbols (shifted by 2π). The additional zeros in the UHP are clearly visible. It must be emphasized that $R_{H^*}(z)$ can not have exactly the same Hilbert-phase of $R_H(z)$ because the reflectivity $r_{H^*}(z)$ differs from $r_H(z)$ for $q_z > Q$. However, since $r_{H^*}(z) \approx r_H(z)$ holds for $Q \leq q_z \ll 2Q$, the difference between the exact Hilbert-phase of $R_{H^*}(z)$ and that of $R_H(z)$ should be small on $[-Q, Q]$ and is neglected in the following.

Now that the profile $\rho_{H^*}^{dyn}(z)$ is given, the access to the zeros is facilitated by considering the function

$$Y(q_z) \equiv \frac{R_{H^*}(q_z)}{R_H(q_z)} = \exp(iq_z Z)B(q_z) \quad (6.191)$$

where $B(q_z) = \prod_j B_j(q_z)$ is the product of the Blaschke-factors (see Section 3.2),

$$B_j(q_z) = \frac{q_z - a_j}{q_z - a_j^*} \frac{q_z + a_j^*}{q_z + a_j} \quad , \quad (6.192)$$

of the zeros $\{a_j\}$, $a_j = \alpha_j + i\beta_j$, that are located in the UHP and Z is some unknown phase-shift introduced through the refinement procedure described above. The recovery of the zeros is performed in two steps:

Step 1: Determine the position of the N_k zeros $\{a_j^{kin}\}$ located in the region of kinematical scattering, say $Q > q_z \gg 5q_c$. This can be efficiently done by first locating the zeros of the structure factor $F(q_z)$ using the grid-search algorithm described in Section 3.2.3 and then refining their positions within dynamical theory.

Step 2: Remove the zeros $\{a_j^{kin}\}$ from the function $Y(q_z)$. Remember that if a zero is located at $a_j = \alpha_j + i\beta_j$, $q_c \ll \alpha_j < Q$, then there is another zero close to $2Q - \alpha_j + i\beta_j$. The Blaschke-factor of this zero may contribute essentially to $B(q_z)$ on $[-Q, Q]$, see Fig. 3.17, and therefore it must be removed, too. The obtained function is denoted by $Y_{dyn}(q_z)$.

Step 3: Under the assumption that the impact of the remaining zeros with $|\alpha_j| > Q$ is negligible, the function $Y_{dyn}(q_z)$ may be well approximated by a finite Blaschke-product

$$\widehat{Y}(N_D, a_1, \dots, a_{N_D}, Z, q_z) = \exp(iq_z Z) \prod_{j=1}^{N_D} B_j(q_z) \quad (6.193)$$

where N_D is the estimated number of remaining zeros in the dynamical region. The offset Z may be estimated as follows: If all zeros in the kinematical region around Q have been removed, the overall change of the phase, $\int_{q_{kin}} \phi(q_z) dq_z$, must be smaller than 2π . This, together with the condition $\phi(Q) \approx 0$, permits the estimation of an interval $[Z_{low}, Z_{up}]$ for Z .

To locate these zeros, $\Delta Y = Y_{dyn}(q_z) - \widehat{Y}(\dots, q_z)$ is minimized. The positivity constraints, $\beta_j \geq 0$ and $\alpha_j \geq 0$, are imposed by introducing new variables γ_j and δ_j with $\alpha_j = \gamma_j^2$ and $\beta_j = \delta_j^2$, respectively, so that the minimization may be performed by Newton-steps,

$$\mathbf{J} \cdot \begin{bmatrix} \Delta Z \\ \Delta \gamma \\ \Delta \delta \end{bmatrix} = \begin{bmatrix} \Re \{ \Delta \mathbf{Y} \} \\ \Im \{ \Delta \mathbf{Y} \} \end{bmatrix} \quad , \quad (6.194)$$

where \mathbf{J} is the Jacobian of $\widehat{Y}(\dots, q_z)$. The required partial derivatives of

$B(q_z)$ with respect to γ_j and δ_j are given by

$$\frac{\partial}{\partial \gamma_j} B(q_z) = \frac{-16 i q_z \gamma_j^3 \delta_j^2}{[(q_z + \gamma_j^2)^2 + \delta_j^4] [(q_z - \gamma_j^2)^2 + \delta_j^4]} B(q_z) \quad (6.195a)$$

$$\frac{\partial}{\partial \delta_j} B(q_z) = \frac{-8 i q_z \delta_j (q_z^2 - \gamma_j^4 + \delta_j^4)}{[(q_z + \gamma_j^2)^2 + \delta_j^4] [(q_z - \gamma_j^2)^2 + \delta_j^4]} B(q_z) \quad (6.195b)$$

The number of zeros N_D should be chosen large enough. Since the density of zeros is known to be $\approx 2\pi/L$, the number of remaining zeros in the dynamical region is approximately $N_D \approx 2Q\pi/L - N_k$. The *unnecessary* zeros should disappear automatically from the Blaschke-product when their imaginary parts β_j tend to zero so that $B_j(q_z) = 1$. Note also, that whenever $r(q_z)$ has a local minimum at q_z , there exist a zero a_j with $\alpha_j \approx q_z$, so that additional constraints are available.

An example for the procedure described above is not given here, since the computational algorithm is still under construction.

Chapter 7

Application of inverse iteration schemes to experimental data

The ongoing decrease of the structure dimensions in semiconductor-industry and surface-coating technology led to an increased need of thin-film reference samples in research and industry. One of the demands on such a sample is the long-time stability under ambient conditions in- and outside the x-ray beam. Roughly speaking: Two reflectivities taken from the same sample should be identical – except for the counting-statistics. Furthermore, the sample structure should be simple enough to be well described by a parameterized layer-model so that one could use traditional fitting-techniques for the data-analysis.

In this chapter the structural investigation of possible candidates for such a thin-film reference sample by x-ray reflectometry is reported. First experiments, which will not be presented here, revealed that the high intensity of the x-ray beam cracks organic molecules in the air which then partially deposit on the sample surface and lead to the growth of an organic film. This effect plays an important role in the design of x-ray optics for synchrotron radiation sources [145], which are kept under vacuum to avoid its occurrence.

By taking series of reflectivities the growth this organic film serves as a phase constraint and may permit the unambiguous determination of the underlying sample structure. A similar way of dealing with the phase-problem was used by DOERR ET AL. where the controlled variation of the thickness of liquid films on a substrate allowed the unambiguous determination of the density profiles at the liquid/substrate interface [48][49].

Preparation of the samples

All samples except for the SiGe sample, which will be discussed at the end of this chapter, have been prepared by the group of R. DIETSCH from the Fraunhofer IWS/Dresden using *pulsed laser deposition* (PLD) [45][46]. This method permits

material	Si	SiO ₂	Si _{0.9} Ge _{0.1}	SiC	C	Ni	Ti	TiC
density [g/cm ³]	2.33	2.2	2.69	3.21	2.32	8.9	4.54	4.92
SLD [10^{-5}\AA^{-2}]	2.01	1.89	2.17	2.75	1.97	6.43	3.58	3.94
q_c [10^{-2}\AA^{-1}]	3.18	3.08	3.30	3.72	3.15	5.70	4.24	4.45

Table 7.1: Density, scattering length density (SLD) for $\lambda = 1.54056\text{\AA}$ and critical wavevector-transfer q_c for the materials [4].

the preparation of ultra-thin layers (<1 nm) with very small interfacial roughness and constant film thicknesses over areas of several cm². The optical properties and the mass density of the materials in the samples are presented in Table 7.1. It should be mentioned that the density of Carbon is strongly depending on the structure and the ratio between sp^2 and sp^3 bonds which itself depends on the preparation parameters [55][86][87]. The value given in Table 7.1 refers to carbon films prepared by PLD.

7.1 Single Carbon layer on a Silicon substrate

The first sample discussed in this chapter consist of a Carbon layer with a nominal thickness of 340\AA on a silicon substrate.

A series of reflectivities has been measured on a Bruker AXS D8 Advance diffractometer with a primary beam intensity of $2 \cdot 10^8$ cps and an angular resolution of about 0.018° . Each reflectivity took 180 min, followed by an off-specular scan (60 min) and a detector-scan (400 min) with an incident angle of 0.6° to ensure a homogenous irradiation of the entire sample. The latter was done to reduce the relative influence of the reflectivity measurement – the probing method – on the effect to be observed. The overall time of the experiment was about 85 1/3 hours. The true specular reflectivities – obtained by subtraction of the diffusely scattered intensity and correction of footprint (see Chapter 5) – are depicted in Figure 7.1 as symbols. For clarity they are shifted by 1.5 orders of magnitude and have been multiplied by q_z^4 ¹. The numbers given at the right border correspond to the measuring order so that the vertical axis may also be considered as a time-axis. It should be noted that the total measured q_z range was larger than given in the graph, but for larger q_z -values a separation of the true specular reflectivity and the contribution from diffuse scattering is not possible.

The corresponding Patterson functions (see Section 2.4) calculated from the true specular reflectivities are presented in Figure 7.2, shifted for clarity. At small

¹The multiplication by q_z^4 is often done instead of taking $r(q_z)/r_F(q_z) \approx |F(q_z)|^2$. However, for sufficiently large q_z the difference can be neglected.

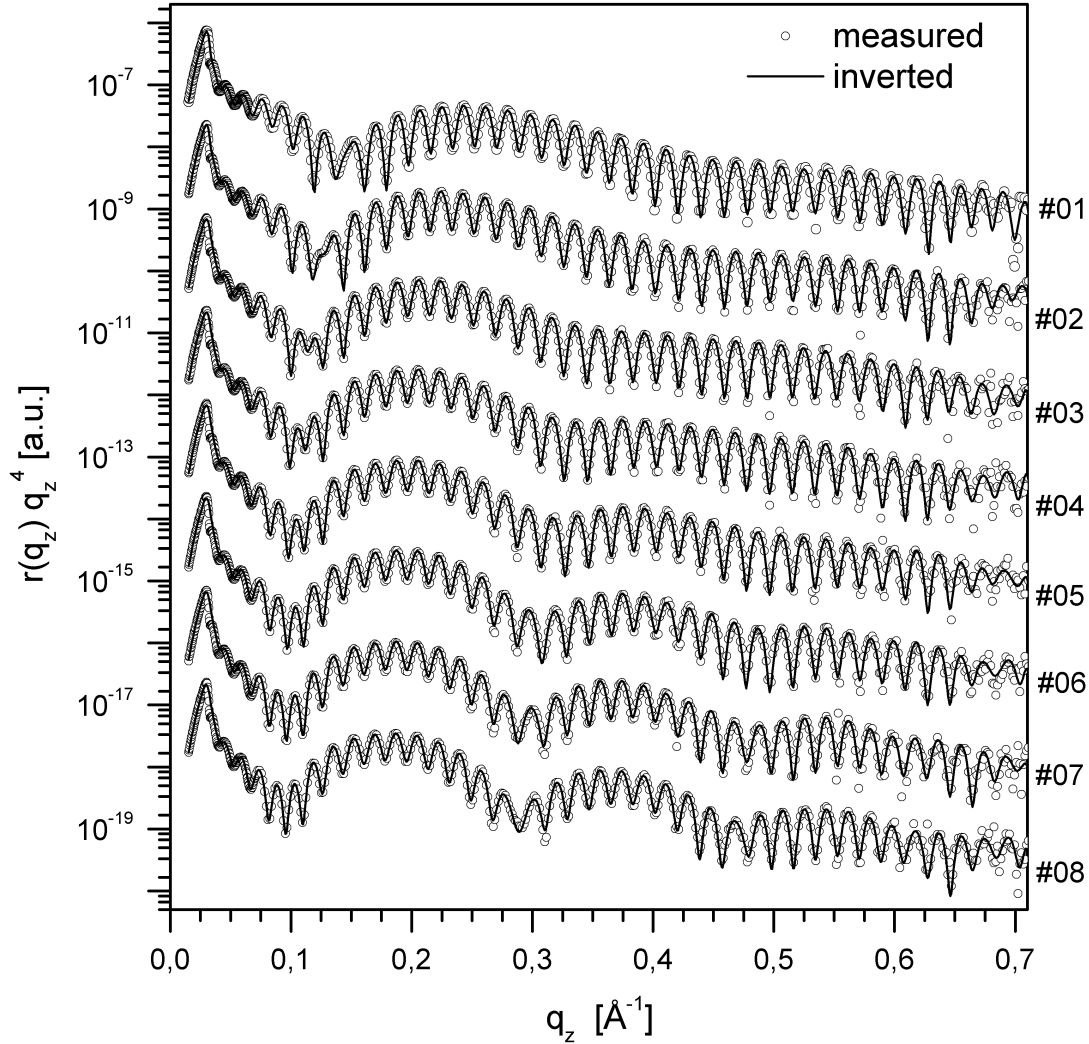
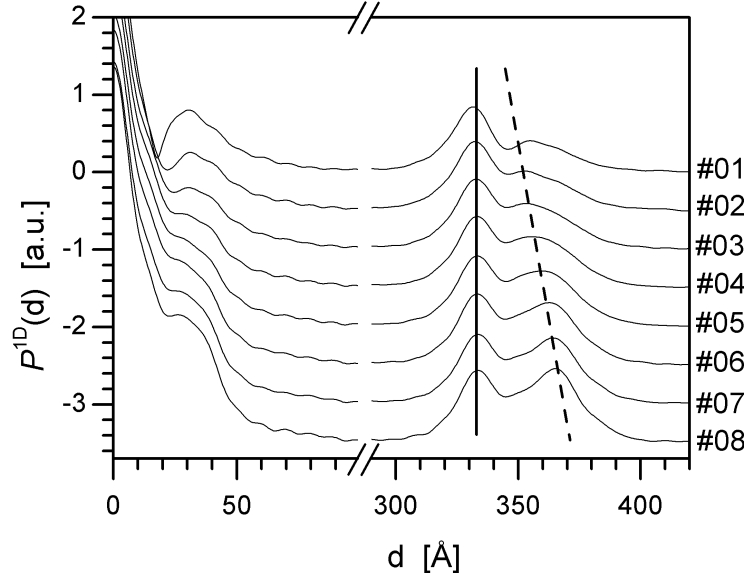


Figure 7.1: Series of reflectivities taken from sample v1098 – 340Å carbon on a silicon wafer. The true specular reflectivity (\circ) and the reflectivities obtained by inversion ($-$) are in good agreement.

d several peaks overlap and cannot be distinguished properly². At large d all Patterson functions have a peak at $d \approx 334\text{\AA}$ that does not change (vertical solid line), whereas strong variations show up in the region between 350Å and 390Å. The dashed line indicates the shift of a peak. The region between 100Å and 290Å is not presented here since all Patterson functions practically vanish therein. The true specular reflectivities have been analyzed using an iterative inversion scheme very similar to that described in the previous chapter with the difference

²Furthermore, the imperfect linearization of the dynamical reflectivity causes additional spectral power density at small d .

Figure 7.2: Patterson functions calculated from the true specular reflectivities depicted in Fig.7.1: The peak at $\approx 334\text{\AA}$ (line vertical line) remains stable, while the rightmost peak (dashed line) changes height and position. The region between 100\AA and 300\AA is featureless and not shown for clarity.



that the eigendensities ψ_n have not been used. Instead, the quantity

$$\Delta\tilde{\rho}(q) = \frac{1}{iq} \frac{\sqrt{I_{obs}(q) - I_n(q)}}{r_F(q)} \arg \left\{ R_n(q) \right\} , \quad (7.1)$$

$q = \sqrt{q_z^2 - q_c^2}$ and $I_n(q)$ is the reflectivity $|R(q)|^2$ – calculated within dynamical scattering theory from the profile ρ_n at the n -th iteration – convoluted with the instrumental resolution function, was directly Fourier transformed on a fine grid ($d \ll 1\text{\AA}$) and the fraction of $\Delta\rho(z)$ falling into the spatial interval $[0, L]$ was then projected onto the Null-space of the Jacobian $\partial r_m / \partial \rho_n$ to stabilize the algorithm (see Section 6.1.5). Furthermore, the interior of the Carbon layer was assumed to be constant. This assumption is justified by the fact that the Patterson functions do not have spectral power in the respective region (see Fig.7.2).

The first reflectivity was inverted using a layer-structured sample model based on the nominal preparation parameter (340\AA C on a Silicon substrate) and gaussian interfaces with a roughness $\sigma = 3\text{\AA}$. The resulting profile is then used as the initial profile for the inversion of reflectivity #2, and so on. By this procedure one obtains a series of profiles that follow the variations in the reflectivities. The profiles are depicted in Figure 7.3. The corresponding reflectivities are shown as solid lines in 7.1. The density profiles show a continuous variation with increasing irradiation time. Practically all changes take place at the surface, where the formation of a layer can be clearly observed. The dashed line indicates the (virtual) position of the upper Carbon interface ($\sigma \approx 2.8\text{\AA}$). The initial thickness of this film is about 17\AA and increases to $\approx 28\text{\AA}$ over the entire experiment. Additionally, the electron density of the film increases from $\rho \approx 1.1 \cdot 10^{-5}\text{\AA}^{-2}$ with increasing film thickness by about 30% to $\approx 1.46 \cdot 10^{-5}\text{\AA}^{-2}$ (horizontal dotted lines) whereas the depletion zone at $z_1 \approx 35\text{\AA}$ does not change significantly. Be-

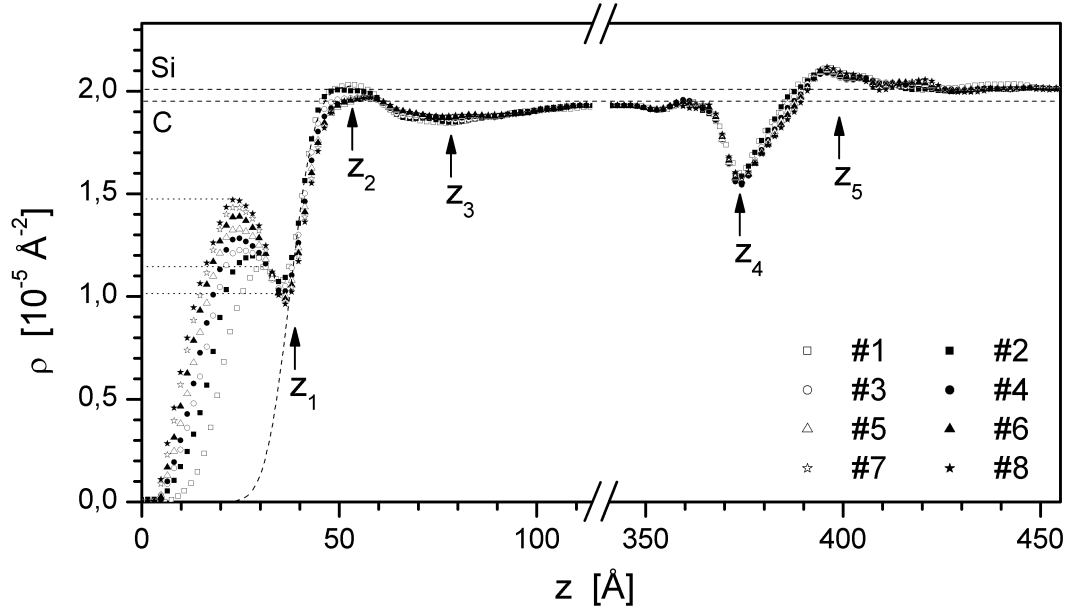


Figure 7.3: Density profiles obtained from the reflectivities of depicted in Fig. 7.1: The growth of a layer on top of the Carbon surface (dashed line) is clearly visible. The substrate-near part of the density profiles remains practically constant. The electron density near the substrate is slightly increased compared to the bulk value of Silicon.

fore reaching the constant electron density of the Carbon layer ($\approx 1.97 \cdot 10^{-5} \text{ \AA}^{-2}$, horizontal dashed line), a small region of increased electron density was found in profiles #1 and #2 at the position z_2 , followed by a region with reduced electron density of that extends over $\approx 50 \text{ \AA}$ around the position z_3 .

Near the substrate, all profiles show a region of decreased electron density at z_4 that remains completely unchanged during the entire experiment. This region is likely to be Silicon oxide which is always present on un-treated Silicon surfaces. The region of increased electron density around the position z_5 is then inside the substrate and may be explained by the diffusion of C atoms into the substrate and the formation of Silicon Carbide, which has a higher electron density than Si (see Table 7.1).

A comparison of the region at z_3 and that between z_4 and z_5 shows, that the profiles #1 and #2 differ from the rest in both regions. Since the remaining profiles #3 – #8 are almost identical on that region, these deviations do not seem to be very trust-worthy. A possible explanation of these features is the fact that the variations of the density profiles also take place during the reflectivity measurement. This may cause small oscillations and other artificial features in the profiles [53].

7.2 Structural investigation of Ti–C samples

In this section the results of the analysis of two samples – denoted by *pl366* and *pl367* – consisting of Titanium and Carbon layers on Silicon substrates will be presented. As the samples presented in the previous section, they have been prepared by PLD. Their nominal preparation data are given in Table 7.2. *pl366* consist of $\approx 80\text{\AA}$ Ti on a Si substrate with about 340\AA C on top. *pl367* is identical but has an additional Ti layer of thickness 20\AA at the surface.

X-ray reflectivities have been taken from both samples directly after the preparation process. They are shown in the left panel of Fig.7.4 along with simulated reflectivities obtained by fitting layer structured models according to the preparation parameter to the measured data. The obtained parameters are presented in the table of Figure 7.4. The layer thicknesses are in good agreement with the respective nominal values given in Table 7.2.

In the following, the experiments performed on both samples as well the analysis will be first discussed separately, followed by a comparison of the obtained results.

7.2.1 Sample *pl366*

The measurements on the sample *pl366* have been performed on a Bruker AXS D8 Advanced diffractometer with a primary-beam intensity of $3.8 \cdot 10^8$ cps and an angular resolution of 0.018° . The relatively poor resolution is explained by a reduction of the beam path on tube- and detector-side. This was done to decrease the absorption in the air and expose the sample to a maximum of intensity. Series of reflectivities have been taken. Each reflectivity took ≈ 2.5 hours. In addition, between the reflectivity measurements the sample has been irradiated for 3 hours with an angle of incidence of 0.6° .

The obtained true specular reflectivities are depicted in Figure 7.5 – multiplied by q_z^4 – on a logarithmic scale. The most significant change in the reflectivity series is the continuous displacement of oscillation knots to smaller q_z values as indicated by the dashed lined arrow.

The corresponding Patterson functions are presented in Fig.7.6. The large peak at $\approx 80\text{\AA}$ corresponds to the thickness of the Titanium layer. This peak remains unchanged (dashed line) in all Patterson functions. At higher d -values two peak

sample	substrate	layer 1		layer 2		layer 3	
		Σ	d [\AA]	Σ	d [\AA]	Σ	d [\AA]
<i>pl366</i>	Si / SiO ₂	Ti	80	C	340	—	
<i>pl367</i>	Si / SiO ₂	Ti	80	C	340	Ti	20

Table 7.2: Nominal preparation data of the samples *pl366* and *pl367*.

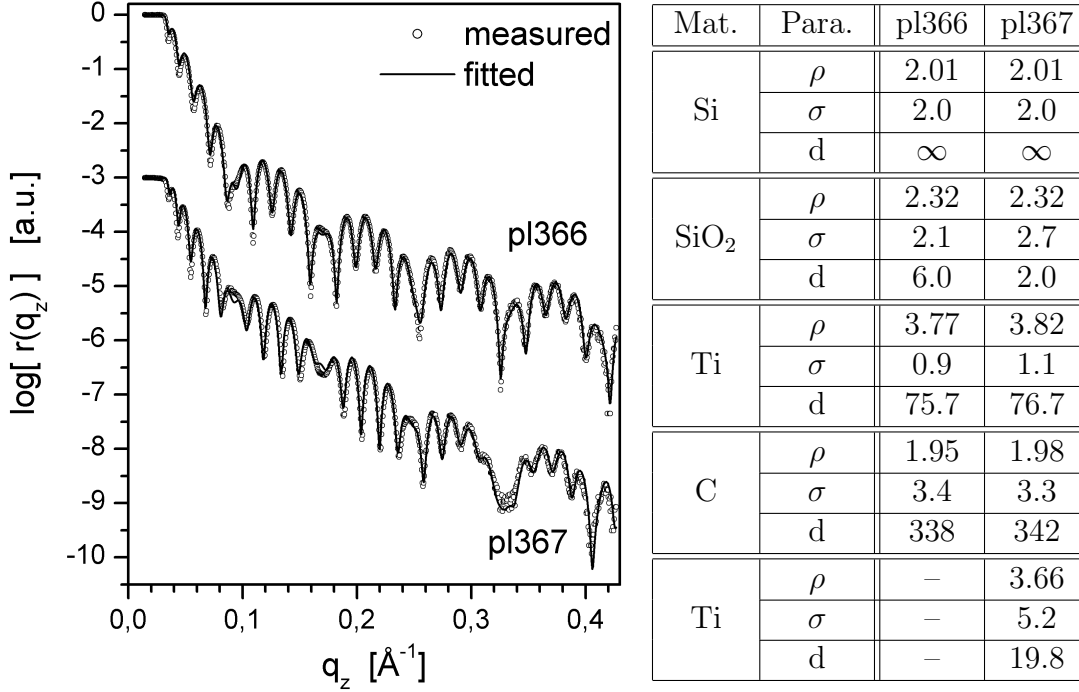


Figure 7.4: Left side: Reflectivities from the samples pl366 and pl367 taken directly after the preparation process. A good explanation of both data sets can be achieved by fitting a simple layer model. The parameters of the layer models are presented in the table. The scattering length density ρ is given in 10^{-5}\AA^{-2} , interfacial roughness σ and the layer thickness d are given in \AA .

doublets can be found. The left peak in the doublets does not change whereas the right peak shifts to larger d -values (solid line). In the grey shaded region at small d several small peaks appear, but a continuous behavior of single peaks can not be clearly identified. The reflectivities have been inverted starting with an initial profile based on the preparation parameters given in Table 7.2 and the scattering length density for Ti from Table 7.1. The Carbon layer was assumed to have a SLD of $\approx 2 \cdot 10^{-5} \text{\AA}^{-2}$ and to remain unchanged during the entire experiment. This is justified by the fact that no features show up in the respective regions of the Patterson functions. The obtained profiles are depicted in Figure 7.7 and the corresponding reflectivities are represented by the solid lines in Fig. 7.5.

The most significant changes in the profiles are found at the surface, where the growth of layer with low density ($\approx 1.5 \cdot 10^{-5} \text{\AA}^{-2}$) can be observed. The increase of its thickness is about 9.5\AA over the entire experiment. The remaining parts of the profiles changes only little. The Carbon–Titanium interface has a very small roughness and a region of width 7\AA – 8\AA with increased electron density shows up. The density inside the Ti film is almost constant. The right interface of the Titanium layer has a slightly larger roughness than the left one. Between the

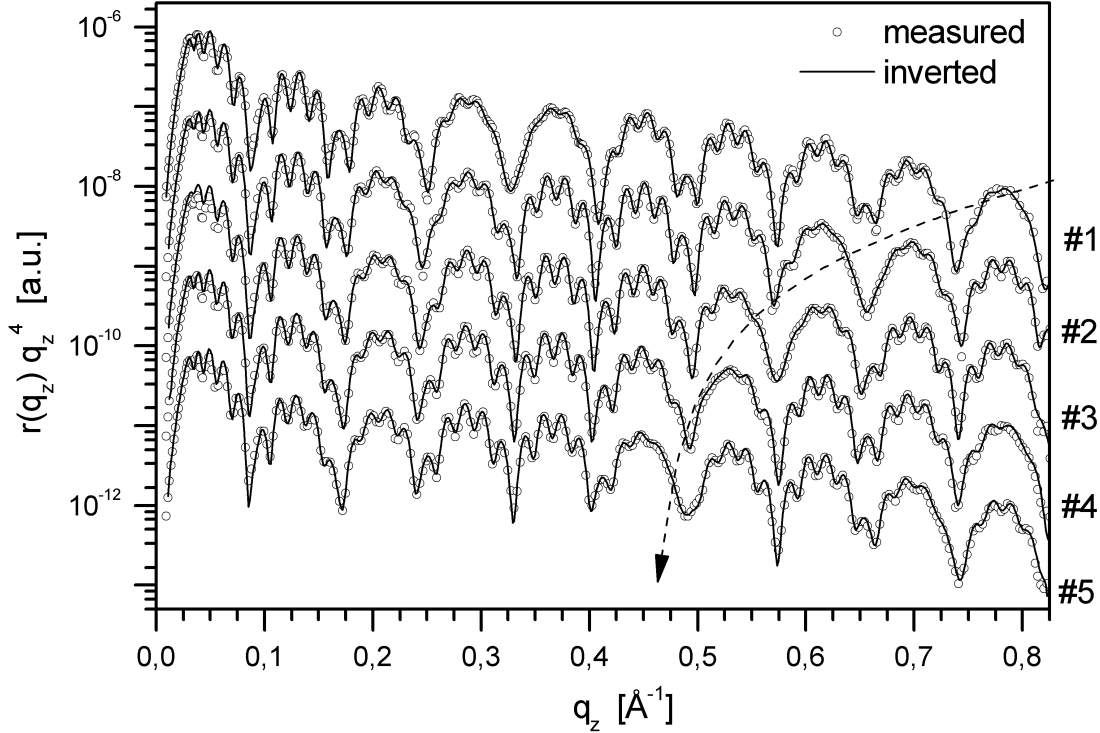


Figure 7.5: Series of reflectivities taken from sample pl366: The curves are shifted by -1 for clarity. The true specular reflectivities are represented by the symbols. The reflectivities obtained by inversion are shown as lines. The dashed line indicates the position of an oscillation knot.

Ti layer and the substrate a region with an electron density higher than that of Silicon was found.

The density profiles are in good agreement with the parameters of sample model given in Fig. 7.4. The horizontal dotted lines indicate the SLD values for Ti and TiC from Literature (see Table 7.1). The density of the Ti layer found by inversion is close to the value found by fitting (dashed line) as given in Table 7.4. The density of the small intermediate layer between C and Ti is in good agreement with the theoretical value of TiC.

7.2.2 Sample pl367

The measurements on the sample pl367 have been performed on a Bruker AXS D8 Advanced diffractometer with a primary-beam intensity of $3.8 \cdot 10^8$ cps but – compared to the setup used for pl366 – with a much better angular resolution of about 0.011° . Again, a series of reflectivities was recorded each taking 3 hours. The irradiation time in between was 6 hours.

Figure 7.8 depicts the obtained true specular reflectivities (open circles) nor-

Figure 7.6: Patterson functions of sample pl366 obtained from the reflectivities depicted in Fig.7.5. The curves are shifted for clarity. The solid and dashed lines indicate the stable and changing peaks, respectively. In the shaded region several peaks of low intensity overlap. The featureless region between 130\AA and 300\AA is not shown. At larger d , the amplitudes of the peaks are damped by the poor experimental resolution.

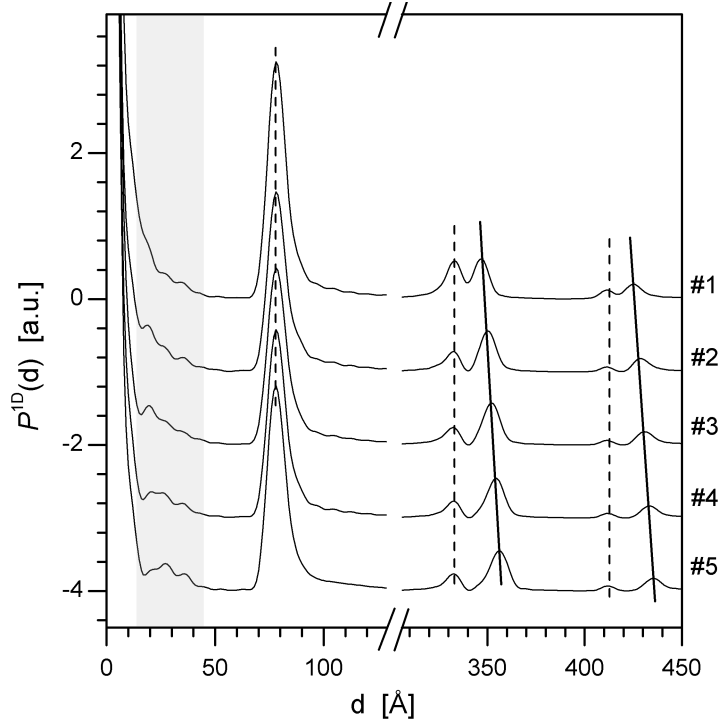
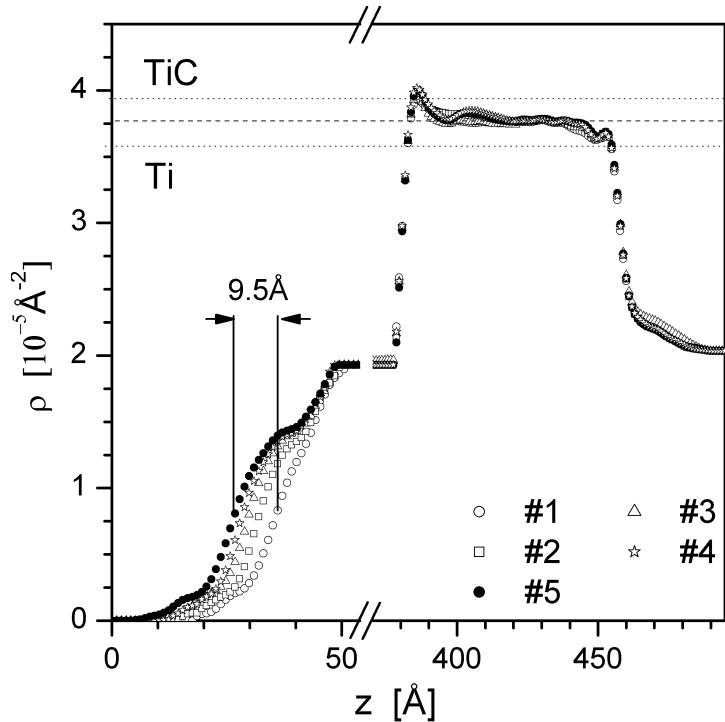


Figure 7.7: Density profiles of sample pl366 obtained from the measured reflectivities depicted in Fig.7.5: The growth of the organic layer at the surface is clearly visible. The C layer is homogeneous and not shown for clarity. At the C/Ti interface the electron density is increased due to the formation of TiC. The small transition layer at the Ti/Si interface causes the asymmetry of the peak at $d \approx 80\text{\AA}$ in the Patterson functions.



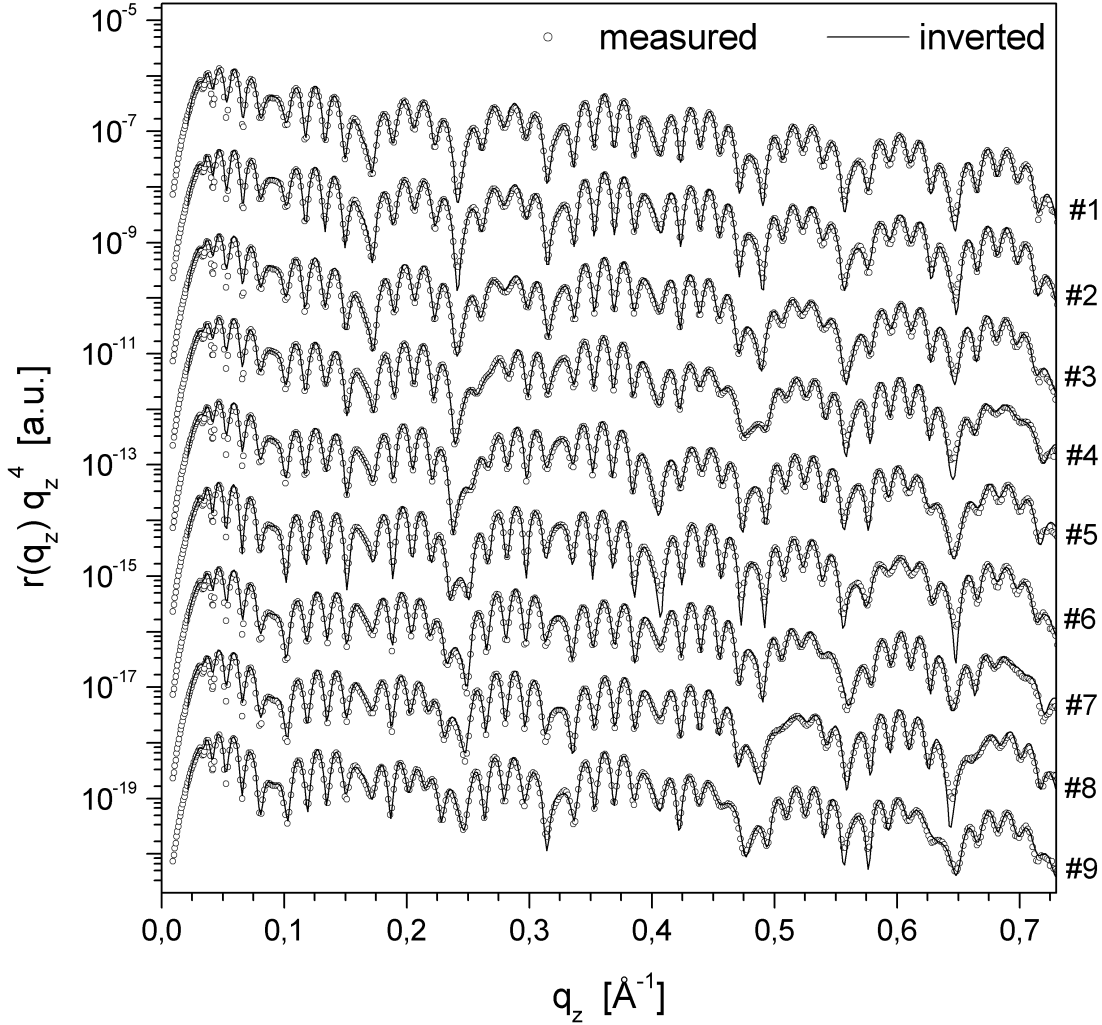


Figure 7.8: Series of reflectivities taken from sample pl367: Measured data (\circ) and the reflectivities obtained by inversion ($-$). The curves are shifted by 1.5 orders of magnitude for clarity. The numbers at the right border give the order in which the reflectivities have been measured.

malized to $1/q_z^4$. The curves are shifted by 1.5 orders of magnitude for clarity. The numbers at the right border indicate the order in which the reflectivities have been measured. The change of the reflectivities with increasing irradiation time can be clearly observed. The corresponding Patterson functions are presented in Figure 7.9: Some peaks (solid lines) are shifted by $\approx 20\text{\AA}$, while others (dashed lines) remain stable in intensity and position. In addition, there exist peaks that do not displace but increase in intensity (dotted line). The featureless region between 110\AA and 300\AA is not shown for clarity. From a comparison of the preparation data (see Table 7.2) and/or the sample parameters given in the table of Figure 7.4 it can be concluded that the strongly shifting peaks cannot

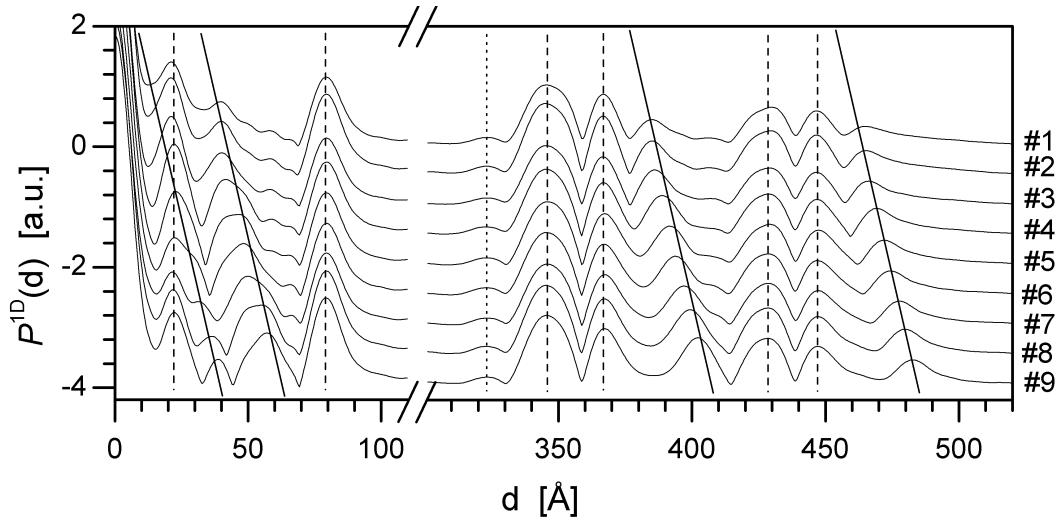


Figure 7.9: Patterson functions of the reflectivities shown in Fig. 7.8: The curves are shifted for clarity. The peaks connected to surface (solid lines) are shifted with ongoing irradiation while those resulting from internal interfaces (dashed lines) remain stable in position and shape. The dotted line indicates a peak that does only change in intensity.

result from the above mentioned structures so that there must exist at least one additional interface.

The reflectivities have been analyzed in the same way as sample pl366. The initial profile for the inversion of reflectivity #1 was based on the preparation parameters (see Table 7.2). Figure 7.10 depicts the obtained density profile, the corresponding reflectivities are shown in Figure 7.8 as lines.

The profiles show the growth of a low-density film at the surface where almost all variation in the profiles takes place. The thickness of that film increases from initially $\approx 7\text{\AA}$ by $\approx 22\text{\AA}$. The displacement of the interfaces is in accordance with the shift of the peaks in the Patterson function (solid lines in Fig.7.9). The remaining part of the density profiles remains almost unchanged over the entire experiment. The structure obtained for the 20\AA deposited Titanium is located between the positions z_1 and z_4 and can be separated in three regions of different electron density, which are considered as layers in following. The first layer – between the interfaces z_1 and z_2 has a density of $\approx 2.85 \cdot 10^{-5}\text{\AA}^{-2}$, followed by a 12\AA thick layer with an electron density between that of Ti and TiC (horizontal dotted lines). The third layer, between the positions z_3 and z_4 , has a density slightly higher than that of the Carbon layer. The obtained structure can be explained as follows: When Titanium particles hit the Carbon surface, they form TiC with preference directly at the surface but also –although less probable – at greater depths. This explains that the electron density between z_2 and z_3 is higher than of Titanium. The region between z_3 and z_4 may then be considered

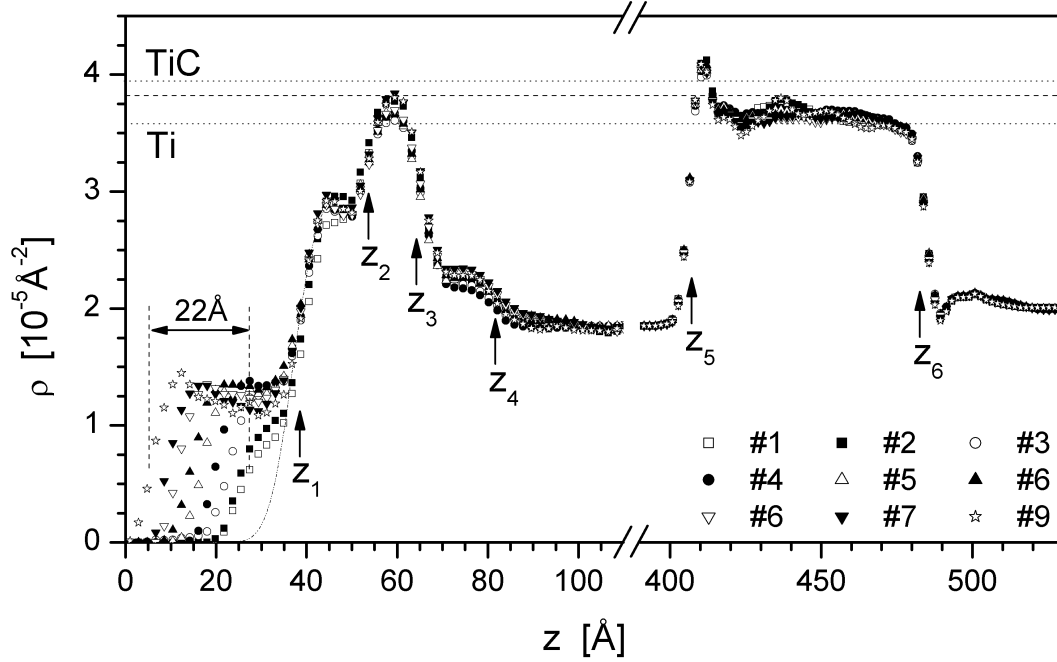
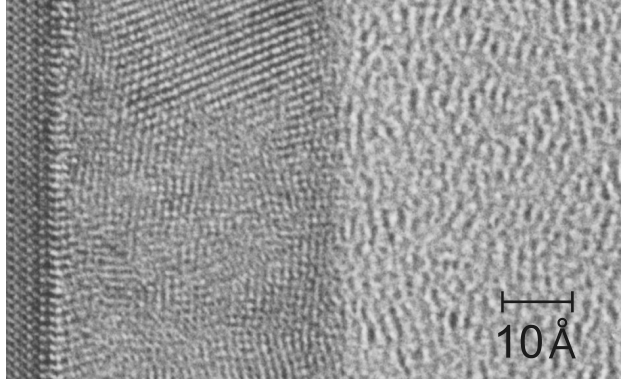


Figure 7.10: Density profiles of sample pl367 obtained from the reflectivities depicted in Fig. 7.8: The growth of the organic layer at the surface from profile #1 to profile #9 is clearly visible. The dashed-dotted line indicates its interface. Near the substrate, the electron density is slightly increased at the interfaces between Carbon and Titanium due to the formation of TiC. The density inside the carbon layer is constant and is not shown for clarity. The numbers in the legend refer to those given at the right borders in Figs. 7.8 and 7.9. Further details are given in the text.

as a diffusion tail. Once enough TiC is formed at the surface, it acts as a diffusion barrier so that the impinging Ti atoms remain at the surface and form an oxide layer. Notice that this complex structure can not be identified from the Patterson functions because the peaks from the interfaces $\{z_2, z_5\}$ and $\{z_3, z_5\}$ overlap and form the broad peak at $d = 345\text{\AA}$. Whereas a peak related to the smooth transition at z_4 can be found at $d \approx 323\text{\AA}$ (vertical dotted line).

The substrate-near part of the profiles is very similar to that obtained for sample pl366: The interface between the Carbon and the Titanium has a very small roughness. At the interface at z_5 is a region of width 6\AA – 7\AA where the density is about 10% higher than in rest of the Ti layer. The roughness of the interface between Ti and substrate at z_6 is slightly larger than that at z_5 . Furthermore a smooth transition layer with a density slightly higher than that of Si was found near the substrate.

Figure 7.11: HR-TEM picture of a 40Å Titanium layer on a Sapphire substrate (left side) with an amorphous Carbon layer on top (right side). The slightly darker region of width $\approx 10\text{\AA}$ at the Ti/C-interface indicates the formation of Titanium Carbide whose electron density is slightly higher than that of Ti.



7.2.3 Comparison of the obtained profiles

The density profiles obtained from both samples by inversion of the reflectivities are consistent and can be reasonably explained. The growth of a film with an electron density of $1.4 - 1.6 \cdot 10^{-5} \text{\AA}^{-2}$ at the surface was found for both samples. Furthermore, very similar features have been found at the substrate-near Titanium layer: At the C-Ti interface the formation of a $6\text{\AA} - 8\text{\AA}$ thick TiC layer was observed. The interface between this TiC layer and the Carbon has a very small roughness whereas the TiC-Ti interface is much rougher. The observed formation of TiC at the interface between Titanium and Carbon layers is in accordance with the real space picture from such an interface, obtained by High Resolution Transmission Electron Microscopy (HR-TEM) in cross-section mode, presented in Fig. 7.11: At the left border a Sapphire substrate is depicted. The perfect single crystal structure is clearly visible. The layer in the middle consists of about 40Å Titanium with 3 preferred orientations. The right side shows an amorphous Carbon layer. In between is a transition layer of width $8\text{\AA} - 10\text{\AA}$ that is slightly darker than the Titanium layer and which is, hence, Titanium Carbide. It can be seen that the TiC/C interface is extremely sharp, whereas the Ti/TiC interface has a higher roughness. This is in perfect agreement with the density profiles obtained for both samples.

7.3 Structural investigation of Ni-C samples

In this section results obtained from x-ray reflectivity series taken from two Nickel-Carbon samples – labeled NiC1 and NiC2 in the following – are reported. The nominal preparation parameters are given in Table 7.3. Both samples consist of a silicon substrate with a Carbon layer and a 100\AA Nickel layer on top. The difference between both samples is, that the substrate-near Carbon layers have different thicknesses and that sample NiC2 has an additional Carbon layer at the surface.

The primary-beam intensity was about $8 \cdot 10^7$ cps for both setups and the angular

resolution was about 0.016° . Series of reflectivities have been taken from both samples: In the case of sample NiC1 each reflectivity took 1h20 followed by an irradiation of 3h20 with an incident angle of 60° for the x-rays. The reflectivities for sample NiC2 took 45min followed by 3h20 of irradiation under the same angle of incidence. The overall duration of the experiments is much smaller compared to experiments performed on the Titanium Carbon samples.

The obtained true specular reflectivities are depicted Figure 7.12 as symbols. For clarity they are shifted by one order of magnitude. The lines represented the reflectivities obtained by inversion. The Patterson functions calculated from the measured reflectivities are depicted in Figs. 7.13 and 7.14: Multiple peaks show up indicating a more complex sample structure than expected from the preparation parameter in Table 7.3. For example, if NiC1 had 3 interfaces only 3 peaks would show up in the Patterson function. Stable peaks are indicated by dashed lines, shifting peaks by solid lines and peaks that change the shape, but do not shift, are indicated by dotted lines. The observed changes in the Patterson functions over the entire series are very small. For both samples the displacement of the shifting peaks is only of the order of 5\AA – 8\AA .

The applied inversion scheme was identical to that used for the inversion of the Titanium–Carbon samples in the previous section with the difference that no part of the profiles was kept fixed. The initial profiles have been chosen according to the preparation parameters (see Table 7.3). The obtained densities profiles are shown in Figs. 7.15 and 7.16. For clarity only the profiles #1, #3, #5 and #7 are depicted. The horizontal dashed lines represent the scattering length densities of Silicon and Nickel given in Table 7.1. The vertical dotted lines indicate the positions z_j given at the bottom of the graph. As one may already expect from the Patterson functions, both profiles do not show large variations.

Density profiles obtained for sample NiC1

The Nickel layer can be clearly identified and has a thickness of $z_3 - z_2 \approx 93\text{\AA}$. Its density is almost constant and in good agreement with the value given in the literature (see Table 7.1). At the surface, the profiles show the presence of an additional layer with a density of about $2.3 \cdot 10^{-5}\text{\AA}^{-2}$ and a thickness of 10\AA – 20\AA on top of the Nickel. The roughness of this layer is higher than that of the Nickel interfaces. The layer is likely to be Nickel Oxide. At the lower interface

sample	substrate	layer 1		layer 2		layer 3	
		Σ	d [\AA]	Σ	d [\AA]	Σ	d [\AA]
NiC1	Si / SiO ₂	C	50	Ni	100	—	
NiC2	Si / SiO ₂	C	20	Ni	100	C	35

Table 7.3: Nominal preparation data of the Ni-C samples

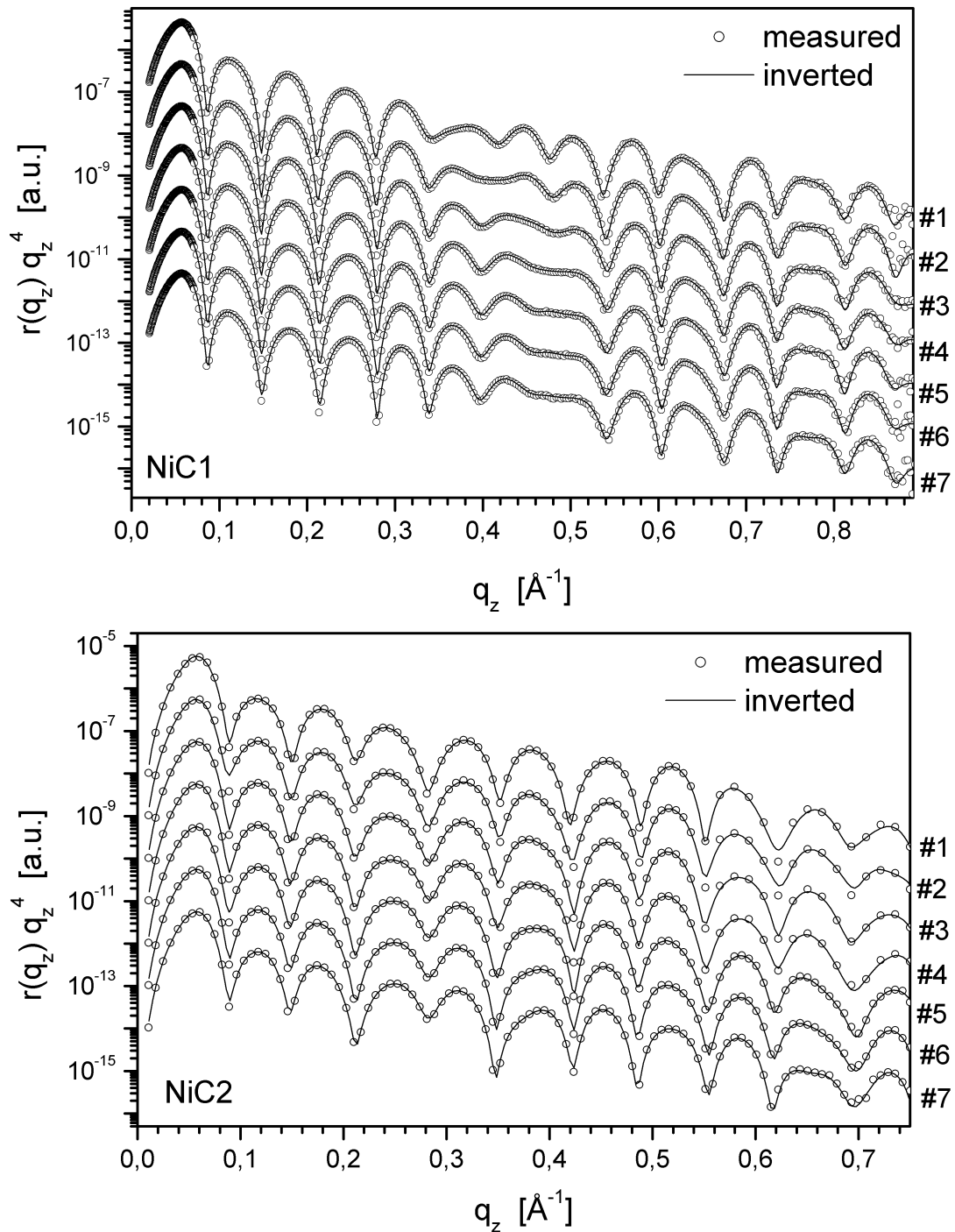


Figure 7.12: Series of reflectivities taken from the samples NiC1 (upper panel) and NiC2 (lower panel). The true specular reflectivities are represented by the symbols, the reflectivities obtained through inversion by lines. The curves are shifted for clarity. The numbers at the right border correspond to the measuring order.

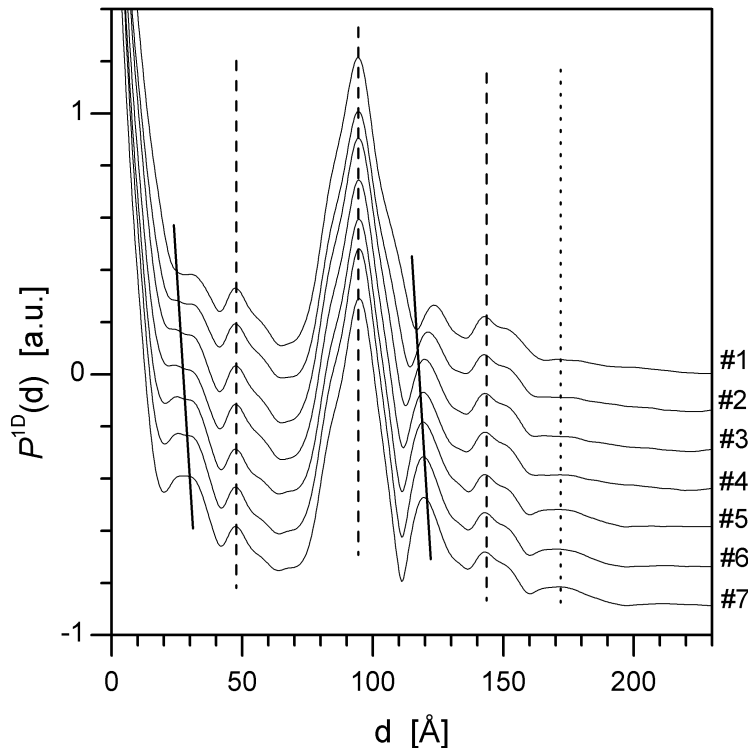


Figure 7.13: Patterson functions calculated from the measured reflectivities depicted in the upper panel of Fig. 7.12: The dashed lines indicate correlation of unchanged interfaces and the dotted line indicates a peak that changes its height, whereas its position remains stable. The solid lines indicated shifting peaks.

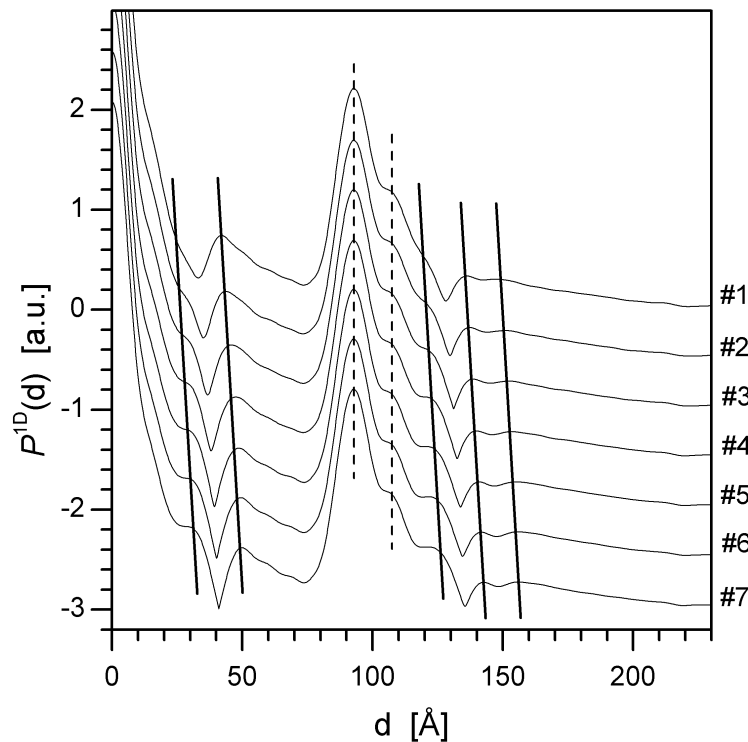


Figure 7.14: Sample NiC2: Patterson functions calculated from the measured reflectivities shown in the lower graphic of Fig. 7.12. The curves are shifted for clarity. The numbers at the right border correspond to those in Fig. 7.12. Some peaks (solid lines) change with continued irradiation, while others (dashed lines) do not.

Figure 7.15: Density profiles of sample NiC1 obtained by inversion from the measured reflectivities depicted in the upper panel of Fig.7.12: For clarity not all profiles are shown. At a depth of 210\AA a complex structure with a density slightly higher than that of the Silicon substrate. Further details are given in the text.

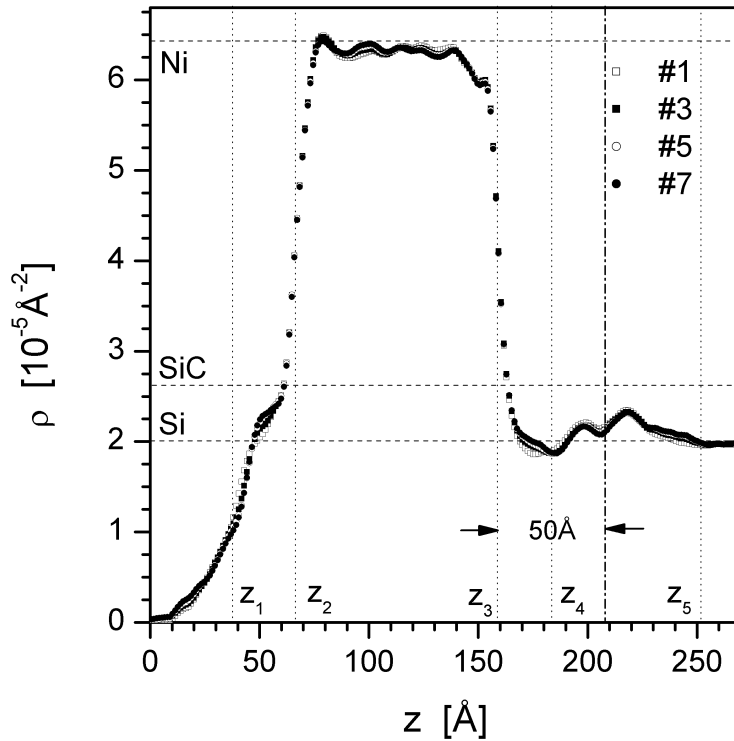
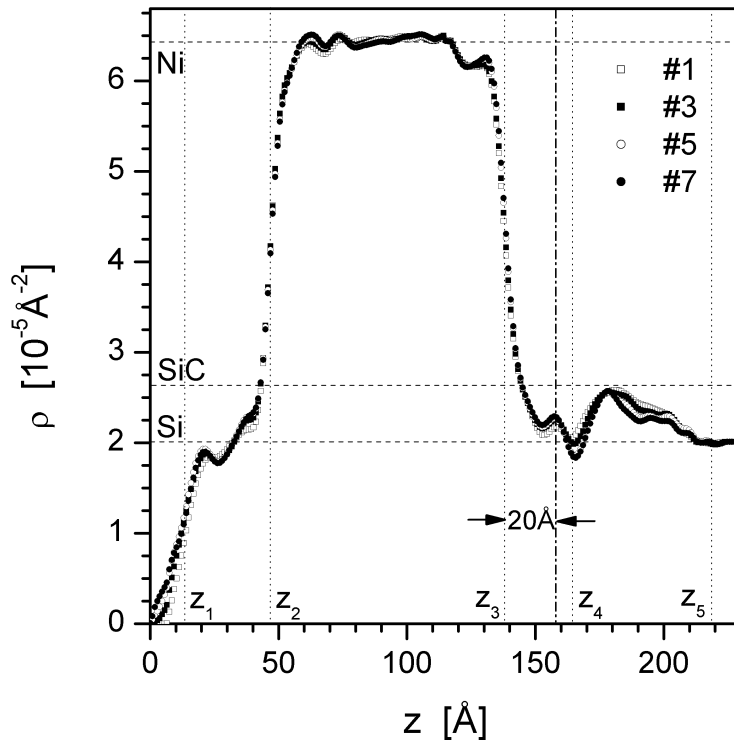


Figure 7.16: Density profiles of sample NiC2 obtained by inversion of the measured reflectivities depicted in the lower panel of Fig.7.12: The curves are shifted for clarity. The growth of the layer at the surface can be observed. The Nickel layer does not change significantly, whereas slight variations show up in the substrate-near part of the profiles. Further details are given in the text.



(z_3) the density is slightly decreased. Near the substrate a complex structure with multiple minima and maxima was found: The electron density decays monotonic from the Nickel layer down to a minimum at z_4 where the density is slightly smaller than that of Si (horizontal dashed line). Between z_4 and z_5 the electron density is much higher than that of Si followed by a smooth transition into the substrate.

Density profiles obtained for sample NiC2

The Nickel layer has a thickness of $\approx 95\text{\AA}$ and is homogenous. Its density agrees almost perfectly with the value given in Table 7.1 over the entire layer, except near the interface at z_3 , where the profiles show a significant reduction of the density. In the surface-near region the profiles show a layer of thickness of $z_2 - z_1 \approx 35\text{\AA}$ whose density is close to that of Carbon. Furthermore, a continuous – even though weak – increase of the electron density can be observed between 0 and z_1 . The substrate-near region of the profiles shows a complex structure similar to that found in the profiles of sample NiC1: Starting from the Nickel interface at z_3 the density decays down to a density lower than that of Si at the position z_4 – after passing a small local maximum at 155\AA . Between z_4 and z_5 the electron density is much higher than that of the Silicon. This is also the region where most of the variation in the profile series takes place. Finally, the profiles decay smoothly to the substrate level around z_5 .

Comparison and discussion of the results

A comparison of the obtained profiles reveals several similarities: The reduction of the density at the substrate-near interface of the Nickel layer appears in both profiles. Furthermore, the regions between this interface and the substrate resemble each other. In both cases the density decays slightly below the Silicon density followed by a region with increased electron density and thickness of 40\AA – 50\AA . Before continuing with the interpretation, some thoughts about the correctness of the profiles should be spent, because the growth of an organic layer at the surface, that served as a kind of phase-constraint in the previous analysis, is not observable. In contrast, the most significant changes appear in the region near the substrate. Keeping in mind that the samples have been irradiated under an incident angle of 60° between the reflectivities, the absorbed energy per area is much higher than under grazing angles as this was the case in the experiments presented in the previous sections. This may activate diffusion or other processes at the Ni–C and C–Si(SiO_2) interfaces. Diffusion and Nickel–Carbide formation are reported in Ref. [76]. Chemical reactions between Nickel and SiC have been observed in Ref. [70]. Furthermore, the overall irradiation time of the samples was short compared (NiC1: 31.5h, NiC2: 28.h) to the experiments where a significant growth of the organic layer was observed. Sample pl366(pl367) was exposed

to the x-rays for 27.5(81) hours causing an increase of 9(22) Å of the organic layer. Thus, a significant change of the surface is not very likely which increases the probability of the correctness of the observed substrate-near variations. Note also, that a region of increased electron density with similar shape was found – although less pronounced – for the single Carbon layer on a Silicon substrate discussed at the beginning of this chapter³.

The dashed-dotted lines in Figs. 7.15 and 7.16 indicate the expected position of the C-Si interface, if the nominal deposited Carbon was forming a homogenous layer. But since the region of high electron density is located at greater depths, diffusion of Carbon into the substrate is the only plausible explanation. This also explains the smooth, tail-like transition down to the substrate density. Furthermore, from Table 7.1 we see that the density of SiC is much higher than that of the Silicon substrate.

The above discussion shows the consistency of the profiles obtained for the samples NiC1 and NiC2 and fits the results obtained for the sample with the single Carbon layer (see Section 7.1).

7.4 The SiGe standard-sample from Bruker AXS

The standard-sample from Bruker AXS consist of an epitaxial grown SiGe layer of approximate thickness of 680Å on a Silicon substrate. The sample was prepared in the research laboratories of Texas Instruments/Freising. By High Resolution X-ray Diffraction (HRXRD) the Ge content was found to be 11% [143].

The measurements were performed on a *Bruker AXS D8 Advance SuperSpeed*⁴ diffractometer from running at 18kW (45kV/400mA). The primary beam intensity was $\approx 1.2 \cdot 10^9$ cps using 0.1mm slits on tube and detector side and the angular resolution was estimated from the direct-through beam to be 0.020°. Each reflectivity measurement took about 3h10 followed the measurement of the longitudinal-diffuse scan (0h50) and additional 2h of irradiation at angles small enough to illuminate the entire sample. The true specular reflectivities extracted from the measured data are depicted in Figure 7.17 – multiplied by q_z ⁴. They have an unexpected complicated structure: A Bragg-like peak is located at $q_z \approx 0.9 \text{ \AA}^{-1}$ and complex oscillation patterns show up (see arrows in Figure 7.17). Moreover, two knots are located at 0.14 \AA^{-1} and 0.58 \AA^{-1} .

The Patterson functions calculated from the true specular reflectivities are presented in Figure 7.18. To suppress the strong oscillations that would result from the Bragg peak, the reflectivities have truncated at $q_z \approx 0.85 \text{ \AA}^{-1}$. However, the Patterson functions are dominated by the next peak around 0.68 \AA^{-1}

³Similar structures have also been found at the C-Si interface of other samples, which are not presented here.

⁴*SuperSpeed* = rotating anode x-ray source.

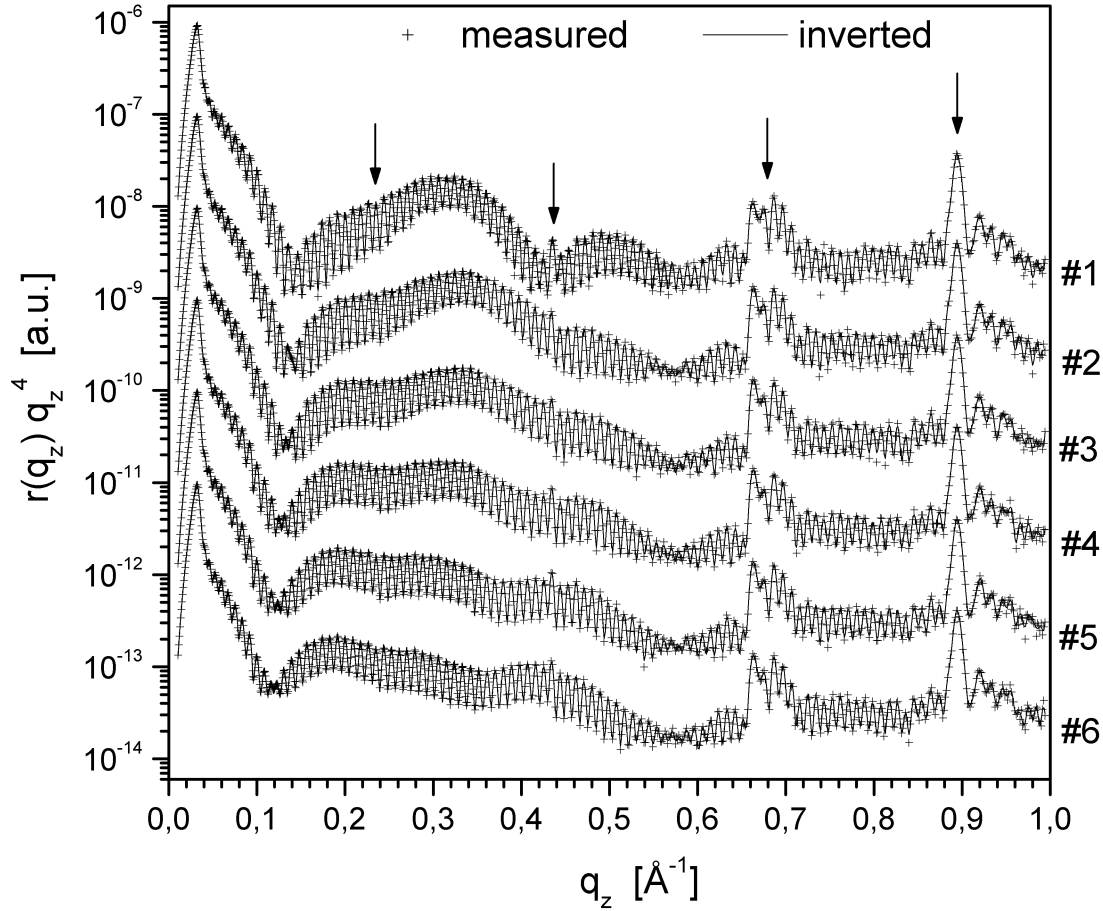


Figure 7.17: Series of reflectivities from the SiGe sample measured on a *D8 Advance SuperSpeed* at 18kW (45kV/400mA): The measured data (symbols) and reflectivities obtained by inversion (lines) are multiplied by q_z^4 and shifted for clarity. The arrows indicate positions where the internal periodical structure of the epitaxial grown SiGe layer shows up.

and therefore the region of small d is dominated by a series of equidistant peak with $\Delta d = 9.5 \text{ \AA}$ so that no helpful information about the sample structure can be extracted. At greater lengthscales three peaks appear, two of which – at $d = 670 \text{ \AA}$ and $d = 690 \text{ \AA}$ – do not change (dashed lines) whereas the third peak (solid line) at about 720 \AA displaces slightly by $\approx 8 \text{ \AA}$.

In contrast to the previous sections, the algorithm proposed in Chapter 6 with the piecewise constant eigendensities, was used for the inversion of the reflectivity series. For technical reasons, the algorithm was always started from the same sample system: A $\text{Si}_{0.9}\text{Ge}_{0.1}$ ($\rho = 2.17 \cdot 10^{-5} \text{ \AA}^{-2}$, see Table 7.1) layer of thickness 730 \AA on a silicon substrate, both with an gaussian interface of roughness 3 \AA . It should be noted, that although composition and density of the SiGe layer are

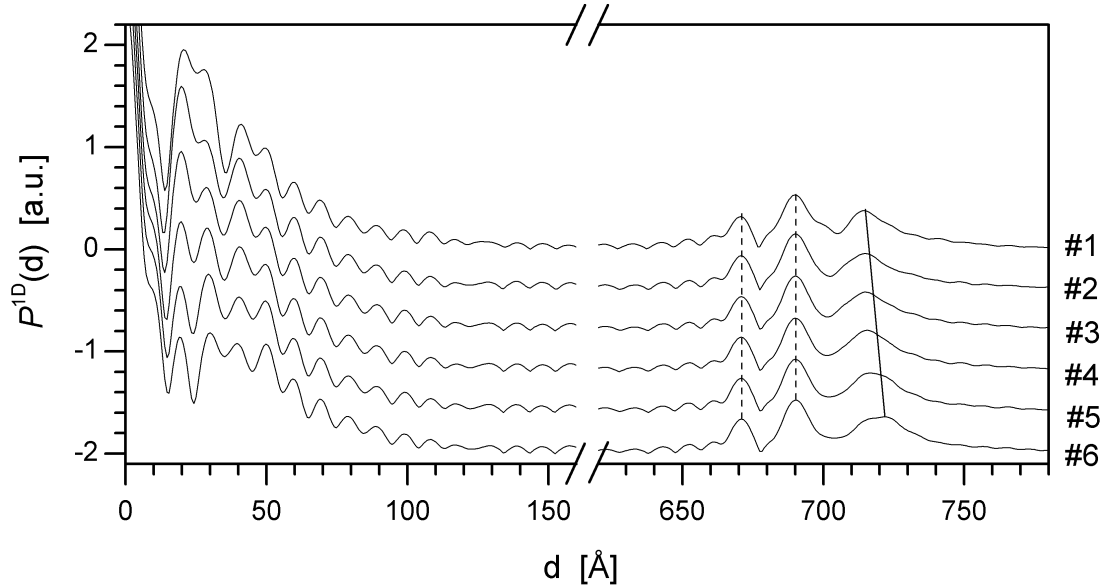


Figure 7.18: Patterson functions calculated from the reflectivities depicted in Figure 7.17 with $0\text{\AA}^{-1} < q_z < 0.85\text{\AA}^{-1}$: The curves are shifted for clarity. The dashed lines indicates peaks that remain constant. The solid line is a peak that shifts by $\approx 8\text{\AA}$. The periodical appearing peaks ($\Delta z \approx 9.5$) result from the superlattice-like structure inside the SiGe layer and correspond to the peak around 0.67\AA^{-1} .

known a-priori from the HRXRD experiments, no part of the density profile could be kept fixed, because of the internal (unknown) fine-structure of the SiGe that dominates the reflectivity. The thickness of the slabs for the construction of the eigendensities was chosen to be $d = 2\text{\AA}$ ⁵. A perfect agreement (see Fig. 7.17) between measured and inverted reflectivity was achieved after ≈ 10 iterations.

Results and discussion

The obtained density profiles are depicted in Fig. 7.19. For the sake of clarity only the profiles #1, #2, #4 and #6 are shown and the SiGe layer is not fully presented. The profile #2, #4 and #6 are represented by solid lines of increasing thickness, profile #1 is represented by a dotted line. The obtained profiles remain almost constant over the entire SiGe film. The long-period oscillation inside the SiGe layer (not shown) may be due to small imperfections in either the experimental setup or the data correction procedure of the true specular reflectivity around the critical angle (see Section 5.3.3).

At the surface, a structure consisting of multiple thin layers was found: A layer with low electron density and thickness of 25\AA is on top of a layer with

⁵It might be preferable to use a grid adapted to the Bragg-like peak at $\approx 0.9\text{\AA}^{-1}$ instead.

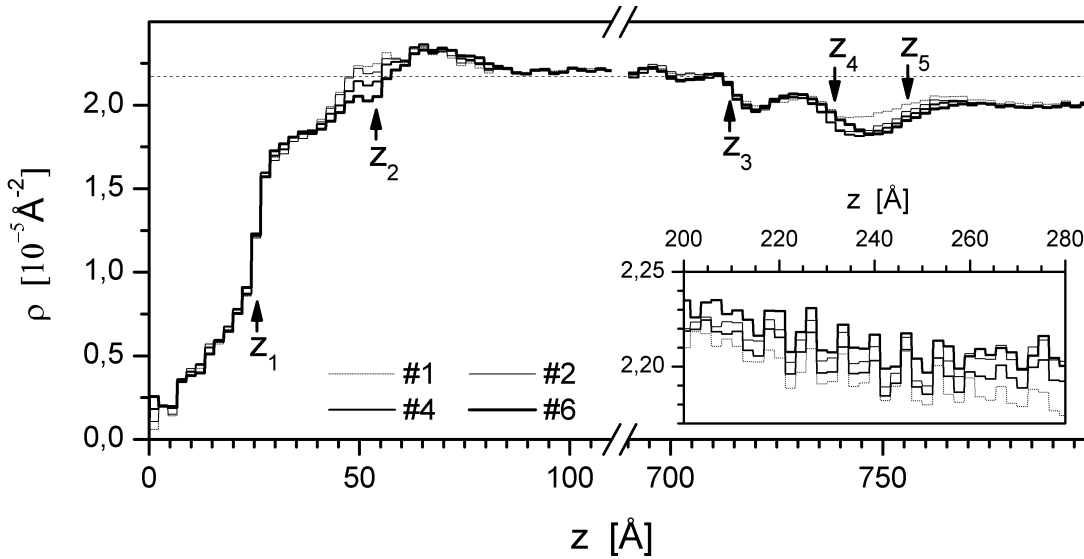


Figure 7.19: Density profiles obtained by inversion of the measured reflectivities depicted in Figure 7.17: For clarity only the profiles #1, #2, #4 and #6 are shown. The density inside the SiGe-layer is almost constant and does not change significantly. The horizontal dashed line corresponds to the theoretical bulk density of $\text{Si}_{0.9}\text{Ge}_{0.1}$. Small periodical density variations can be observed inside the layer (see inset).

intermediate density and a very sharp interface at the position $z_1 \approx 25 \text{ \AA}$. The next interface may be located at $z_2 \approx 55 \text{ \AA}$. In between is a transition layer with increased electron density, where the electron density decreases constantly from profile #1 to profile #6. Before (approximately) reaching the bulk-density of $\text{Si}_{0.9}\text{Ge}_{0.1}$ (vertical dashed line) a region of increased density shows up. Inside the SiGe layer all profiles have a very similar oscillation structure as presented in the inset of Fig. 7.19.

In the substrate-near region of the profiles, a well defined interface is located at $z_3 \approx 715 \text{ \AA}$ which – together with the interface at z_1 – causes the intense peak in the Patterson functions at 690 \AA . It follows a region of lower electron density between z_4 and z_5 before profiles reach the bulk density of the Silicon substrate. The variation of the density profiles is continuous with one exception: In the substrate-near region around $z = 750 \text{ \AA}$ a remarkable reduction of the electron density occurs from profile #1 to profile #2, while this region remains almost constant for profiles #2 – #6. The reflectivities do also show an abrupt change between the reflectivities #1 and #2, such as the knot at $q_z \approx 0.58 \text{ \AA}^{-1}$ that does not exist in the first reflectivity. This may be explained as follows: In measurement #1, the region of small q_z -values is scanned quite fast and the sample has

not been exposed to much radiation so far⁶. It may then happen that the impinging x-rays initiate some process that reaches a stable state after a sufficiently long irradiation. One possible explanation may be the emission of photo-electrons either from the silicon substrate or from the layer structure between the $\text{Si}_{0.9}\text{Ge}_{0.1}$ layer and substrate.

A physical explanation for the observed reduction of the electron density around the position z_2 can not be given here. In contrast, it is contradictory to the expected growth of an organic layer at sample surface. Although hints for the latter exists in the profiles, doubts about the correctness of the obtained solution remain.

7.5 Summary and concluding remarks

In this chapter iterative inversion schemes have been successfully applied to experimental x-ray reflectivity data.

For the investigated Titanium-Carbon samples, the obtained profiles yield a consistent picture of the sample structures. The expected growth of the organic layer at the surface was found. The observed formation of TiC as well as the roughnesses at the Ti/C and C/Ti interfaces are in perfect agreement with results obtained by TEM.

In case of the Nickel-Carbon samples strong indications for the formation of SiC inside the substrate have been found in the density profile. This is in accordance with the density profiles obtained for the single Carbon film on the Si-substrate. Furthermore, hints for the diffusion of the Nickel into the Carbon have been found in the profiles of both samples. In the last example, reflectivities from a SiGe film of thickness $\approx 700 \text{ \AA}$ on a Silicon substrate are analyzed. Reasonable density profiles have been obtained without imposing any constraints to the inversion and with a very rough guess of the initial profile. The inversion scheme converged rapidly (≈ 10 iterations) towards a solution. However, a plausible explanation of the observed details in the density profiles could not be given – showing the limitation of inverse methods in the analysis of x-ray reflectivities.

This Chapter concludes with a warning to the reader: Although the use of inverse methods has lead to the recovery of tiny details – partially close to the spatial resolution limited by the q_z -region accessible in the experiment – the user should always be aware of an over-interpretation of the profiles obtained by inverse methods. The high sensitivity of these methods with respect to noise, errors in the experimental setup and ambiguities due to the always present phase-problem may produce features in the profiles, which have to be carefully checked.

⁶Keep in mind that the measurements have been performed using a rotation-anode system providing one order of magnitude more in x-ray intensity than a conventional sealed-tube x-ray source

Chapter 8

Summary and Outlook

Today Nanoscience combines the efforts of a whole set of formerly separated disciplines of science: Physics, Chemistry, Biology, Material Science and Engineering. The common goal is to produce layers, structures and finally devices in the nanometer scale. The used materials reach from organic, polymer, ceramic, semiconducting up to metallic. All the layers require the characterization on the nano and subnano – Ångstroem – level.

The progress in x-ray instrumentation – especially new types of x-ray sources – allows the characterization by x-ray reflectometry down to 1Å. The goal of this thesis is to provide some tools, so that the advances in the measurement techniques are followed by a progress in data evaluation for samples in which interfaces, layers and surfaces are hard to distinguish.

The first part of this thesis addresses the phase-problem in x-ray reflectivity: As only amplitudes are measured in x-ray scattering experiments, the direct calculation of the electron density profile of the sample is impossible. The phase, which is required for the solution of this inverse problem, is lost in the experiment.

The analytical properties of the reflection coefficient imply that the phase is completely determined by 1. the Hilbert transform of the logarithm of the modulus and 2. the zeros in the upper half complex plane (UHP). The calculation of the Hilbert-phase from a reflectivity which is only known up to some maximum wavevector, requires the extrapolation over the entire q_z -axis to infinity. The existing formulation [117] uses the asymptotic behavior of a Fresnel reflectivity. To account in addition for interfacial roughness, a new formula for the Hilbert-phase is derived. In the following, the conditions for which the reflection coefficient has zeros in the UHP is discussed and the existing sufficient condition [37] is extended to rough multi-layer systems. Procedures for locating these zeros are developed. While the zeros located in the region of kinematical scattering can be located very efficiently by a divide-and-conquer algorithm, the detection of the zeros in the region of dynamical scattering remains a time-consuming and

difficult task. The transfer of the zeros into the UHP can be performed either in dynamical theory via Darboux-transforms [116] or in kinematical theory using Fourier transforms. The comparison of both methods shows that the much more time-consuming Darboux-transforms only need to be applied to a limited number of zeros. Furthermore, the dependency of the position of the flipped zero on the resulting profile variation shows that only a small number of zeros causes a significant change of the profile when flipped across the q_z -axis. This can reduce the number of important phase solutions dramatically.

The second part of this thesis introduces a new iterative inversion method for x-ray reflectivity. This method overcomes the shortcomings of existing model-independent analysis schemes and inverse methods: It expands the profile in a set of eigenfunctions, which are discrete approximations of the eigenfunction of the classical reconstruction problem of a compact supported function from its partially known Fourier-transform [15]. In this work, piecewise constant functions, polygons and second-order B-splines are used to expand the density profile. The eigenvalue problems for the calculation of the above mentioned approximations are stated and solved. The formalism for the calculation of the reflection coefficients for these profiles is developed in dynamical and single-scattering theory. The stabilization of the linear inversion scheme is achieved by projecting the proposed profile modification onto the space which does not change the reflectivity in the region of dynamical scattering. The required partial derivatives of the reflectivity can be calculated efficiently in dynamical as well as single-scattering theory. The explicit formulas for the Hilbert-phase of the reflectivity from a piecewise-constant profile have been derived in kinematical and dynamical theory. In addition, procedures are developed to obtain – from a given profile – the profile having no zeros in the UHP. Finally, a method for locating the zeros of its reflection coefficient is proposed.

In the experimental part of this work iterative inverse schemes are applied to the analysis of x-ray reflectivity. The samples under investigation are exposed to x-rays under ambient conditions. Repeated reflectivity measurements show a continuous change caused by the absorption of organic molecules at the sample surface. This effect can serve as a phase-constraint and provides the possibility of an unambiguous determination of the density profiles. Different sample systems are instigated: For two Titanium-Carbon samples tiny details at the Ti/C interfaces such as the formation of a thin TiC layer can be observed. The obtained density profiles can be well explained and are in agreement with results from transmission electron microscopy studies. The density profiles obtained from the reflectivities taken from Nickel-Carbon samples show the formation of SiC inside the substrate. This was confirmed for a single Carbon layer on a Si-substrate. Finally, the new inversion scheme is applied to a series of reflectivities from a 700Å SiGe film on a substrate. The obtained profiles show highly localized modifications.

Based on the achievements of this thesis, future work could address different topics: As the locating of the zeros of the reflection coefficient at small q_z is still problematic and time-consuming, further numerical improvement could be helpful. Moreover, efficient strategies for the selection of zeros as well as the improvement of the flipping-produce itself are important topics. The latter requires the Jost-solution of the profile, if the Darboux-transform has to be applied. Analytical solutions for B-spline profiles would be desirable.

Finally, the influence of imperfections in the measured reflectivities on the density profiles could be investigated, as it is of fundamental importance for the interpretation of the obtained density profiles and the application of x-ray reflectometry in Nanoscience.

Appendix A

A.1 Sufficient condition for zero-free UHP for layer-stack with gaussian interfaces

For a system of N layers, the structure factor is given by

$$F(Q) = \sum_{n=0}^N \Delta\rho_n \exp\left[-\frac{1}{2}\sigma_n^2 Q^2\right] \exp[iQz_n] \quad , \quad (\text{A.1})$$

where $Q = q_z + i\kappa$. Let $z_0 = 0$ and $z_n > 0$, $n = 1\dots N$, then the real and the imaginary part of $F(Q)$ are given by

$$\begin{aligned} \Re\{F(Q)\} &= \Delta\rho_0 \cos(q_z \kappa \sigma_0^2) \exp\left[-(q_z^2 - \kappa^2)\sigma_0^2/2\right] \\ &+ \sum_{n=1}^N \Delta\rho_n \cos(q_z z_n + q_z \kappa \sigma_n^2) \times \\ &\quad \times \exp\left[-\kappa z_n - (q_z^2 - \kappa^2)\sigma_n^2/2\right] \quad (\text{A.2}) \end{aligned}$$

and

$$\begin{aligned} \Im\{F(Q)\} &= \Delta\rho_0 \sin(q_z \kappa \sigma_0^2) \exp\left[-(q_z^2 - \kappa^2)\sigma_0^2/2\right] \\ &+ \sum_{n=1}^N \Delta\rho_n \sin(q_z z_n + q_z \kappa \sigma_n^2) \times \\ &\quad \times \exp\left[-\kappa z_n - (q_z^2 - \kappa^2)\sigma_n^2/2\right] \quad , \quad (\text{A.3}) \end{aligned}$$

respectively. A sufficient condition for a zero in the UHP is $|F(Q)|^2 = 0$, from which follows:

$$\begin{aligned}
& |\Delta\rho_0|^2 \exp[-(q_z^2 - \kappa^2)\sigma_0^2] \\
= & \left| \sum_{n=1}^N \left(\Delta\rho_n^2 \exp[-\kappa z_n - (q_z^2 - \kappa^2)\sigma_n^2] \right. \right. \\
& + 2 \sum_{m=n+1}^N \Delta\rho_n \Delta\rho_m \cos[q_z(z_n - z_m) + q_z \kappa(\sigma_n^2 - \sigma_m^2)] \times \\
& \left. \left. \times \exp[-\kappa(z_n + z_m) - (q_z^2 - \kappa^2)(\sigma_n^2 + \sigma_m^2)/2] \right) \right| \quad (\text{A.4})
\end{aligned}$$

In the UHP we have $\kappa > 0$. Let us assume that $|\Delta\rho_0| > \sum_{n=1}^N |\Delta\rho_n|$ and $\sigma_0 \leq \sigma_n$, $n = 1 \dots N$, holds. Then the following inequalities are valid for $\kappa \leq |q_z|$:

$$\begin{aligned}
& |\Delta\rho_0|^2 \exp[-(q_z^2 - \kappa^2)\sigma_0^2] \\
> & \left(\sum_{n=1}^N |\Delta\rho_n| \right)^2 \exp[-(q_z^2 - \kappa^2)\sigma_0^2] \\
= & \left(\sum_{n=1}^N \left(|\Delta\rho_n|^2 + 2 \sum_{m=n+1}^N |\Delta\rho_n \Delta\rho_m| \right) \right) \exp[-(q_z^2 - \kappa^2)\sigma_0^2] \\
\geq & \sum_{n=1}^N \left(\Delta\rho_n^2 \exp[-(q_z^2 - \kappa^2)\sigma_n^2] \right. \\
& \left. + 2 \sum_{m=n+1}^N |\Delta\rho_n \Delta\rho_m| \exp[-(q_z^2 - \kappa^2)(\sigma_n^2 + \sigma_m^2)/2] \right) \\
> & \sum_{n=1}^N \left(\Delta\rho_n^2 \exp[-\kappa z_n - (q_z^2 - \kappa^2)\sigma_n^2] \right. \\
& \left. + 2 \sum_{m=n+1}^N |\Delta\rho_n \Delta\rho_m| \exp[-\kappa(z_n + z_m) - (q_z^2 - \kappa^2)(\sigma_n^2 + \sigma_m^2)/2] \right) \\
\geq & \sum_{n=1}^N \left(\Delta\rho_n^2 \exp[-\kappa z_n - (q_z^2 - \kappa^2)\sigma_n^2] \right. \\
& \left. + 2 \sum_{m=n+1}^N |\Delta\rho_n \Delta\rho_m \cos(X)| \exp[-\kappa(z_n + z_m) - (q_z^2 - \kappa^2)(\sigma_n^2 + \sigma_m^2)/2] \right) \\
\geq & \dots
\end{aligned}$$

$$\begin{aligned}
&\geq \dots \\
&\geq \left| \sum_{n=1}^N \left(\Delta\rho_n^2 \exp \left[-\kappa z_n - (q_z^2 - \kappa^2) \sigma_n^2 \right] \right. \right. \\
&\quad \left. \left. + 2 \sum_{m=n+1}^N \Delta\rho_n \Delta\rho_m \cos(X) \times \right. \right. \\
&\quad \left. \left. \times \exp \left[-\kappa(z_n + z_m) - (q_z^2 - \kappa^2)(\sigma_n^2 + \sigma_m^2)/2 \right] \right) \right| \quad (\text{A.5})
\end{aligned}$$

where X is an arbitrary real number. Latter inequality is identical to the right hand-side of Eq. A.4. Thus, Eq. A.4 can never be satisfied and hence $F(Q) \neq 0$ for any $Q \in \{Q = q_z + i\kappa \in \mathbb{C} | \kappa > 0 \wedge |q_z| \geq \kappa\}$.

Next we consider the case $|q_z| < \kappa$. Again, we start with the necessary condition for a zero $|F(Q)|^2 = 0$:

$$\begin{aligned}
&\Im \{F(Q)\}^2 + \Re \{F(Q)\}^2 \\
&= \sum_{n=0}^N \left(\Delta\rho_n^2 \exp \left[-\kappa z_n - (q_z^2 - \kappa^2) \sigma_n^2 \right] \right. \\
&\quad \left. + 2 \sum_{m=n+1}^N \Delta\rho_n \Delta\rho_m \cos \left(q_z(z_n - z_m) + q_z \kappa (\sigma_n^2 - \sigma_m^2) \right) \times \right. \\
&\quad \left. \times \exp \left[-\kappa(z_n + z_m) - (q_z^2 - \kappa^2) (\sigma_n^2 + \sigma_m^2) / 2 \right] \right) = 0 \quad (\text{A.6})
\end{aligned}$$

Collecting all terms with $\Delta\rho_0$ on the right hand-side yields

$$\begin{aligned}
&\sum_{n=1}^N \left(\Delta\rho_n^2 \exp \left[-\kappa z_n - (q_z^2 - \kappa^2) \sigma_n^2 \right] \right. \\
&\quad \left. + 2 \sum_{m=n+1}^N \Delta\rho_n \Delta\rho_m \cos \left(q_z(z_n - z_m) + q_z \kappa (\sigma_n^2 - \sigma_m^2) \right) \times \right. \\
&\quad \left. \times \exp \left[-\kappa(z_n + z_m) - (q_z^2 - \kappa^2) (\sigma_n^2 + \sigma_m^2) / 2 \right] \right) \\
&= -\Delta\rho_0^2 \exp \left[- (q_z^2 - \kappa^2) \sigma_0^2 \right] \\
&\quad - 2 \sum_{m=1}^N \Delta\rho_0 \Delta\rho_m \cos \left(-q_z z_m + q_z \kappa (\sigma_0^2 - \sigma_m^2) \right) \times \\
&\quad \times \exp \left[-\kappa z_m - (q_z^2 - \kappa^2) (\sigma_0^2 + \sigma_m^2) / 2 \right] \\
&< |\Delta\rho_0|^2 \exp \left[- (q_z^2 - \kappa^2) \sigma_0^2 \right] \quad , \quad (\text{A.7})
\end{aligned}$$

where the inequality is obtained from

$$\begin{aligned}
& \Delta\rho_0^2 \exp[-(q_z^2 - \kappa^2) \sigma_0^2] + 2 \sum_{m=1}^N \Delta\rho_0 \Delta\rho_m \cos(-q_z z_m + q_z \kappa (\sigma_0^2 - \sigma_m^2)) \times \\
& \quad \times \exp[-\kappa z_m - (q_z^2 - \kappa^2) (\sigma_0^2 + \sigma_m^2) / 2] \\
\geq & \Delta\rho_0^2 \exp[-(q_z^2 - \kappa^2) \sigma_0^2] - 2 \sum_{m=1}^N |\Delta\rho_0 \Delta\rho_m| \times \\
& \quad \times \exp[-\kappa z_m - (q_z^2 - \kappa^2) (\sigma_0^2 + \sigma_m^2) / 2] \\
> & \Delta\rho_0^2 \exp[-(q_z^2 - \kappa^2) \sigma_0^2] - 2|\Delta\rho_0| \sum_{m=1}^N |\Delta\rho_m| \exp[-(q_z^2 - \kappa^2) \sigma_0^2] \\
= & \Delta\rho_0^2 \exp[-(q_z^2 - \kappa^2) \sigma_0^2] - 2|\Delta\rho_0| \exp[-(q_z^2 - \kappa^2) \sigma_0^2] \sum_{m=1}^N |\Delta\rho_m| \\
> & \Delta\rho_0^2 \exp[-(q_z^2 - \kappa^2) \sigma_0^2] - 2|\Delta\rho_0|^2 \exp[-(q_z^2 - \kappa^2) \sigma_0^2] \\
= & -|\Delta\rho_0|^2 \exp[-(q_z^2 - \kappa^2) \sigma_0^2] \quad . \tag{A.8}
\end{aligned}$$

But then Eq. A.4 and Eq. A.7 cannot be satisfied simultaneously and hence $F(Q) \neq 0$ for any $Q \in \{Q = q_z + i\kappa \in \mathbb{C} | \kappa > 0 \wedge |q_z| < \kappa\}$.

A.2 Partial derivatives $\partial R(q)/\partial b_m$ for the second-order B-spline profile within the WSA

When using the weighted superposition approximation (WSA) for the calculation of the reflectivity, the partial derivative of the reflection coefficient with respect to profile parameter b_m is given by

$$\frac{\partial R(q_z)}{\partial b_m} = 4\pi\rho_\infty \left[\sum_{n=m-1}^{N-1} S_n \frac{\partial}{\partial b_m} P_n(q_z) + \sum_{n=m-1}^{m+1} P_n \frac{\partial}{\partial b_m} S_n \right] \quad (\text{A.9})$$

where $S_n = (A_n - iB_n) \exp(iq_{z,n}d) - A_n$. The derivatives in the first sum are equal to

$$\frac{\partial}{\partial b_m} P_n(q_z) = idP_n(q_z) \sum_{l=m-1}^{m+1} \frac{\partial q_{z,l}}{\partial b_m} \quad \text{where} \quad \frac{\partial q_{z,l}}{\partial b_m} = -\frac{8\pi}{q_{z,l}} \frac{\partial \bar{\rho}_l}{\partial b_m} \quad (\text{A.10})$$

and

$$\frac{\partial \bar{\rho}_{m-1}}{\partial b_m} = \frac{3m}{2} + \frac{1}{6}, \quad \frac{\partial \bar{\rho}_m}{\partial b_m} = -3m - \frac{4}{3} \quad \text{and} \quad \frac{\partial \bar{\rho}_{m+1}}{\partial b_m} = \frac{3m}{2} + \frac{13}{6}. \quad (\text{A.11})$$

The derivatives in the second sum of Eq. (A.9) become

$$\frac{\partial}{\partial b_m} S_n = \exp(iq_{z,n}d) \left[\frac{\partial}{\partial b_m} (A_n - iB_n) + id(A_n - iB_n) \frac{\partial q_{z,n}}{\partial b_m} \right] - \frac{\partial A_n}{\partial b_m} \quad (\text{A.12})$$

with

$$\begin{aligned} \frac{\partial}{\partial b_m} A_n &= 2 \left(\alpha_n \frac{32\pi}{q_{z,n}^6} \frac{\partial \bar{\rho}_n}{\partial b_m} + \frac{1}{q_{z,n}^4} \frac{\partial \alpha_n}{\partial b_m} \right) \\ &\quad - i \left\{ (2nd\alpha_n + \beta_n) \frac{24\pi}{q_{z,n}^5} \frac{\partial \bar{\rho}_n}{\partial b_m} + \frac{1}{q_{z,n}^3} \frac{\partial}{\partial b_m} (2nd\alpha_n + \beta_n) \right\} \end{aligned} \quad (\text{A.13})$$

and

$$\frac{\partial}{\partial b_m} B_n = 2d \left(\alpha_n \frac{24\pi}{q_{z,n}^5} \frac{\partial \bar{\rho}_n}{\partial b_m} + \frac{1}{q_{z,n}^3} \frac{\partial \alpha_n}{\partial b_m} \right) \quad (\text{A.14})$$

The non-vanishing derivatives of α_n and β_n are given by

$$\frac{\partial \alpha_n}{\partial b_m} = \frac{1}{d^2} \cdot \begin{cases} 1/2, & n = m \pm 1; \\ -1, & n = m. \end{cases} \quad \text{and} \quad \frac{\partial \beta_n}{\partial b_m} = \frac{1}{d} \cdot \begin{cases} 2, & n = m - 1; \\ -3, & n = m; \\ 1, & n = m + 1. \end{cases} \quad (\text{A.15})$$

Note that when computing the entries of the Jacobian matrix, most of the above calculations do not depend on q_z and hence have to be carried out only once before looping over the q_z -values for which $\partial R(q)/\partial b_m$ is requested.

A.3 Modification of the proposed algorithm

The way of constructing the eigendensities ψ_n for the linear profile and for the BS2-profile, as given in Sections 6.3.2 and 6.4.3 was done under the assumption that orthonormality of the ψ_n on $[0, L]$ is required. However, in the proposed algorithm this is not mandatory. Thus, the following modification of the proposed method results in significant simplifications: For a profile expanded in B-splines of degree l , one may consider the function

$$\frac{\Delta F(q)}{iq} \frac{\exp(i\Delta zq)}{\text{sinc}^l(qd/2)} = \sum_{n=0}^{N-1} \Delta b_n \exp(inqd) \quad (\text{A.16})$$

and then use the DPSS (see Section 6.1.1) for the expansion of the profile modification $\Delta\rho$. This would have the following advantages: First, the respective eigendensities $\psi_n(z)$ are much easier to compute and the energy concentration of the $|\Psi_n(q)|$ within the band of interest $[-Q, Q]$ improves significantly. Moreover, the sensitivity to $\Delta F(q)$ at higher q is improved because of the sinc-function in the denominator in the above equation.

References

- [1] <http://www.bruker-axs.de>.
- [2] <http://www.netlib.org/lapack>.
- [3] <http://www.nerisc.gov/~dhbaileys>.
- [4] http://cindy.lbl.gov/optical_constants/.
- [5] F. ABÈLES, *Recherches sur la propagation des ondes électromagnétiques sinusoidales dans les milieux stratifiés*, Ann. Physique (Paris), 5 (1950), p. 596.
- [6] M. ABRAMOWITZ AND I. STEGUN, *Handbook of Mathematical Functions*, Dover, New York, 1965.
- [7] Z. S. AGRANOVICH AND V. A. MARCHENKOW, *The inverse Problem of Scattering Theory*, Gordon and Breach, New York, 1963.
- [8] T. AKTOSUN AND P. E. SACKS, *Inversion of reflectivity data for nondecaying potentials*, SIAM J. Appl. Math., 60 (2000), p. 1340.
- [9] S. BANERJEE, S. FERRARI, D. CHATEIGNER, AND A. GIBAUD, *Recent advances in characterization of ultra-thin films using specular x-ray reflectivity technique*, Thin Solid Films, 450 (2004), p. 23.
- [10] S. BANERJEE, S. FERRARI, R. PIAGGA, AND S. SPANDONI, *Determination of density profile of ultrathin $SiO_2/Si_3N_4/SiO_2/Si(001)$ multilayer structures using x-ray reflectometry technique*, Appl. Phys. Lett., 84 (2004), p. 3798.
- [11] S. BANERJEE, Y. J. PARK, D. R. LEE, Y. H. JEONG, K.-B. LEE, S. B. Y. C, H. CHOI, J.-C. PARK, J. ROH, AND M. SANYAL, *Anomalous x-ray reflectivity study of metal oxide thin films*, Appl. Surf. Sci., 136 (1998), p. 41.
- [12] S. BANERJEE, G. RAGHAVAN, AND M. K. SANYAL, *Study of interdiffusion in thin Fe film deposited on Si(111) by x-ray reflectivity and secondary ion mass spectrometry*, J. Appl. Phys., 85 (1999), p. 7135.

-
- [13] S. BANERJEE, M. K. SANYAL, AND A. DATTA, *X-ray-reflectivity study of Ge-Si-Ge films*, Phys. Rev. B, 54 (1996), p. 16377.
- [14] R. BARAKAT AND G. NEWSAM, *Algorithms for reconstruction of partially known, band-limited Fourier-transform pairs from noisy data*, J. Opt. Soc. Am., A2 (1985), p. 2027.
- [15] —, *Algorithms for reconstruction of partially known, band-limited Fourier-transform pairs from noisy data. I. the prototypical linear problem*, J. Integral Eq., 9 (Suppl.) (1985), p. 49.
- [16] —, *Algorithms for reconstruction of partially known, band-limited Fourier-transform pairs from noisy data. II. the nonlinear problem of phase retrieval*, J. Integral Eq., 9 (Suppl.) (1985), p. 77.
- [17] A. BASILLE, E. ZIEGLER, C. FERRERO, J. REVILLARD, AND C. MORAWE, *Determination of multilayer structures from grazing incidence x-ray reflectometry measurements using a simulated annealing algorithm.*, Conference Talk, The 4th International Conference on the Physics of X-Ray Multilayer Structures, Breckenridge, Colorado, USA, March 1998.
- [18] J. K. BASU AND M. K. SANYAL, *Capillary waves in langmuir-blodgett interfaces and formation of confined CdS layers*, Phys. Rev. Lett., 79 (1997), p. 4617.
- [19] A. C. BAYLISS, Y. LI, AND C. S. MORAWETZ, *Scattering by a potential using hyperbolic methods*, Math. Comp., 52 (1989), p. 321.
- [20] E. BENGU, M. SALUD, AND L. D. MARKS, *Model-independent inversion of x-ray or neutron reflectivity data*, Phys. Rev. B, 63 (2001), p. 195414.
- [21] N. F. BERK AND C.F. MAJKRZAK, *Using parametric B-splines to fit specular reflectivities*, Phys. Rev. B, 51 (1995), p. 11296.
- [22] M. BERTERO, C. DE MOL, AND G. A. VIANO, *The stability of inverse problems*, in Inverse scattering problems in optics, H. P. Baltes, ed., Springer-Verlag, Berlin, 1979.
- [23] J. K. BLASIE, S. ZHENG, AND J. STRZALKA, *Solution to the phase problem for specular x-ray or neutron reflectivity from thin films on liquid surfaces*, Phys. Rev. B, 67 (2003), p. 224201.
- [24] M. BORN AND E. WOLF, *Principles of Optics*, Pergamon, Oxford, 1993.
- [25] F. BRIDOU AND B. PARDO, *Grazing x-ray reflectometry data processing by Fourier transform*, Journal of X-Ray Science and Technology, 4 (1994), p. 200.

-
- [26] —, *Use of Fourier transform in grazing X-ray reflectometry*, J. Phys. III France, 4 (1994), p. 1523.
- [27] K. P. BUBE, *Numerical methods for reflection inverse problems: Convergence and nonimpulsive sources*, SIAM J. Numer. Anal., 23 (1986), p. 227.
- [28] R. E. BURGE, M. A. FIDDY, A. GREENAWAY, AND G. ROSS, *The phase problem*, Proc. Roy. Soc. London, A350 (1976), p. 191.
- [29] V. A. BUSHUEV, A. A. LOMOV, AND A. G. SUTYRIN, *Reconstruction of the Surface Layer Density Profile by the X-ray Reflectometry Method*, Cryst. Rep., 47 (2002), p. 683.
- [30] A. CATICHA, *Reflection and transmission of x-rays by graded interfaces*, Phys. Rev. B, 52 (1995), p. 9214.
- [31] K. CHADAN AND P. C. SABATIER, *Inverse Problems in Quantum Scattering Theory*, Text and Monographs in Physics, Springer, Berlin, 2nd ed., 1989.
- [32] C.-H. CHOU, *A necessary modification for groove tracking method*, Physica, B233 (1997), p. 130.
- [33] —, *Non-unique electron density profiles of liquid Mercury from a Smoothed Groove Tracking Method*, Chin. J. Phys., 36 (1998), p. 91.
- [34] —, *Complementarity of smoothing procedures for a Smoothed Groove-Tracking Method*, Chin. J. Phys., 37 (1999), p. 631.
- [35] —, *A scheme for Smoothed Groove Tracking*, Chin. J. Phys., 38 (2000), p. 182.
- [36] C.-H. CHOU, M. J. REGAN, P. S. PERSHAN, AND X.-L. ZHOU, *Model-independent reconstruction of smooth electron density profiles from reflectivity data of liquid surfaces*, Phys. Rev. E, 55 (1997), p. 7212.
- [37] W. L. CLINTON, *Phase determination in x-ray and neutron reflectivity using logarithmic dispersion relations*, Phys. Rev. B, 48 (1993), p. 1.
- [38] P. COMBETTES, *The convex feasibility problem in image recovery*, in Advances in Imaging and Electron physics, P. W. Hawkes, ed., vol. 95, Academic Press, London, 1996, p. 156.
- [39] R. A. CROWTHER, *A linear analysis of the non-crystallographic symmetry problem*, Acta Cryst., 22 (1967), p. 758.
- [40] —, *The use of non-crystallographic symmetry for phase determination*, Acta Cryst., B25 (1969), p. 2571.

-
- [41] C. DE BOOR, *A practical guide to splines*, Springer Verlag, New York, 1978.
- [42] W. H. DE JEU, J. D. SHINDLER, AND E. A. L. MOL, *The resolution function in diffuse x-ray reflectivity*, J. Appl. Cryst., 29 (1996), p. 511.
- [43] G. D. DE VILLIERS, B. MCNALLY, AND E. R. PIKE, *Positive solutions to linear inverse problems*, Inverse Problems, 15 (1999), p. 615.
- [44] M. DELLNITZ, O. SCHUETZE, AND Q. ZHENG, *Locating all the zeros of an analytic function in one complex variable*, J. of Comp. and Appl. Math., 138 (2002), p. 325.
- [45] R. DIETSCH, T. HOLZ, C.-F. MEYER, R. SCHOLZ, AND B. WEHNER, *High precision large area PLD of x-ray optical multilayers*, Appl. Surf. Sci., 127 (1998), p. 451.
- [46] R. DIETSCH, T. HOLZ, D. WEISSBACH, AND R. SCHOLZ, *Large area PLD of nanometer-multilayers*, Appl. Surf. Sci., 197 (2002), p. 169.
- [47] A. K. DOERR, *Untersuchung der strukturellen Eigenschaften dünner Benetzungsfilme*, PhD thesis, Christian-Albrecht-Universität Kiel, 1999.
- [48] A. K. DOERR, M. TOLAN, J.-P. SCHLOMKA, AND W. PRESS, *Evidence for density anomalies of liquids at the solid/liquid interface*, Europhys. Lett., 52 (2000), p. 330.
- [49] A. K. DOERR, M. TOLAN, T. SEYDEL, AND W. PRESS, *The interface structure of thin liquid hexane films*, Physica, B248 (1998), p. 263.
- [50] H. J. S. DORREN, *A novel approach to estimate the stability of one-dimensional quantum inverse scattering*. preprint available at <http://arXiv.org/abs/math-ph/9808008>, 1998.
- [51] H. J. S. DORREN, E. J. MUYZERT, AND R. K. SNIEDER, *The stability of one-dimensional inverse scattering*, Inverse Problems, 10 (1994), p. 865.
- [52] F. D. FADDEEV, *The inverse problem of quantum theory of scattering*, J. Math. Phys., 4 (1963), p. 72.
- [53] R. FENDT, M. SPRUNG, C. GUTT, O. H. SEECK, AND M. TOLAN, *X-ray reflectivity study of the influence of temperature fluctuations on the density profile of thin liquids*, Zeitschrift für Kristallographie, 219 (2004), p. 205.
- [54] I. D. FERANCHUK, S. I. FERANCHUK, L. KOMAROV, S. SYTOVA, AND A. ULYANENKOV, *Analytical ansatz for self-consistent calculations of x-ray transmission and reflection coefficients at graded interfaces*, Phys. Rev. B, 67 (2003), p. 235417.

-
- [55] A. C. FERRARI, A. LIBASSI, B. K. TANNER, V. STOLOJAN, J. YUAN, L. M. BROWN, S. E. RODIL, B. KLEINSORGE, AND J. ROBERTSON, *Density, sp^3 fraction, and cross-sectional structure of amorphous carbon films determined by x-ray reflectivity and electron-loss spectroscopy*, Phys. Rev. B, 62 (2000), p. 11089.
- [56] J. R. FIENUP AND C. C. WACKERMAN, *Phase-retrieval stagnation problems and solutions*, J. Opt. Soc. Am., A3 (1986), p. 1897.
- [57] I. M. GEL'FAND AND B. M. LEVITAN, *On the determination of a differential equation by its spectral function*, Izv. Akad. Nauk. SSR ser. Math., 15 (1951), p. 309.
- [58] R. GERCHBERG AND W. SAXTON, *A practical algorithm for the determination of phase from image and diffraction plane pictures*, Optik, 35 (1972), p. 237.
- [59] A. GIBAUD, G. VIGNAUD, AND S. K. SINHA, *The correction of geometrical factors in the analysis of x-ray reflectivity*, Acta Cryst., A49 (1993), p. 642.
- [60] D. E. GOLDBERG, *Genetic Algorithms in Search: Optimization and Machine Learning*, Addison-Wesley, Reading, MA, 1989.
- [61] G. H. GOLUB AND C. F. VAN LOAN, *Matrix Computations*, The John Hopkins University Press, 3rd ed., 1996.
- [62] J. GORDIS AND B. NETA, *An adaptive method for the numerical solution of Volterra integral equations*, in Recent Advances in Applied and Theoretical Mathematics, N. Mastorakis, ed., World Scientific and Engineering Society International Conference, Athenes, Greece, 2000, p. 1.
- [63] L. GRAVE DE PERALTA AND H. TAMKIN, *Improved Fourier method of thickness determination by x-ray reflectivity*, J. Appl. Phys., 93 (2003), p. 1974.
- [64] F. A. GRÜNBAUM, *Eigenvectors of a Toeplitz matrix: Discrete version of the prolate spheroidal wave functions*, SIAM J. Algebra Discr. Methods, 2 (1981), p. 136.
- [65] I. W. HAMLEY AND J. S. PEDERSEN, *Analysis of neutron and x-ray reflectivity data. I. Theory*, J. Appl. Cryst., 27 (1994), p. 29.
- [66] V. HOLÝ, J. KUBĚNA, I. OHLÍDAL, K. LISCHKA, AND W. POTZ, *X-ray reflection from rough layered systems*, Phys. Rev. B, 47 (1993), p. 15896.

- [67] N. E. HURT, *Phase Retrieval and Zero Crossings*, Mathematics and its application, Kluwer Academic Publishers, Dordrecht, Boston, London, 1989.
- [68] I. KAY, *The inverse scattering problem when the reflection coefficient is a rational function*, Comm. Pure and Applied Math., 13 (1960), p. 371.
- [69] K. KHARE AND N. GEORGE, *Sampling theory approach to prolate spheroidal wavefunctions*, J. Phys. A: Math. Gen., 36 (2003), p. 10011.
- [70] S. KIM, J. PEREPEZKO, Z. DONG, AND A. EDELSTEIN, *Interface reaction between Ni and amorphous SiC*, Journal of Electronic Materials, 33 (2005), p. 1064.
- [71] S. KIRKPATRICK, C. GELATT, AND M. VECCHI, *Optimization by simulated annealing*, Science, 220 (1983), p. 671.
- [72] M. K. KLIBANOV AND P. E. SACKS, *Use of partial knowledge of the potential in the phase problem of inverse scattering*, J. Comp. Phys., 112 (1994), p. 273.
- [73] M. K. KLIBANOV, P. E. SACKS, AND A. V. TIKHONRAROV, *The phase retrieval problem*, Inverse Problems, 11 (1995), p. 1.
- [74] M. V. KLIBANOV AND P. E. SACKS, *Phaseless inverse scattering and the phase problem in optics*, J. Math. Phys., 33 (1992), p. 3813.
- [75] I. V. KOZHEVNIKOV, *Physical analysis of the inverse problem of x-ray reflectometry*, Nuclear Instruments and Methods in Physics Research, A508 (2003), p. 519.
- [76] R. KRAWIETZ, B. WEHNER, D. MEYER, K. RICHTER, H. MAI, R. DIETSCH, S. HOPFE, R. SCHOLZ, AND W. POMPE, *Investigation of the thermal stability of Ni/C multilayers by x-ray methods*, Fresenius' Journal of Analytical Chemistry, 333 (1995), p. 246.
- [77] H. LANDAU AND H. POLLAK, *Prolate spheroidal wave functions, Fourier analysis and uncertainty II.*, Bell System Tech. J., 40 (1961), p. 65.
- [78] ———, *Prolate spheroidal wave functions, Fourier analysis and uncertainty III.*, Bell System Tech. J., 41 (1962), p. 1295.
- [79] B. Y. LEVIN, *Distribution of zeros of entire functions*, vol. 5 of Translation of Mathematical Monographs, Am. Math. Soc., 1964.
- [80] M. LI, *High resolution x-ray scattering investigation of II-VI Semiconductor Heterostructures*, PhD thesis, Julius-Maximilian Universität Würzburg, 1998.

-
- [81] M. LI, W. FASCHINGER, AND G. LANDWEHR, *Comment on "Uniqueness of the complex diffraction amplitude in x-ray Bragg diffraction"*, Phys. Rev. B, 59 (1999), p. 14781.
- [82] M. LI, M. MOELLER, AND G. LANDWEHR, *Fitting of x-ray or neutron specular reflectivity of multilayers by Fourier analysis*, J. Appl. Phys., 80 (1996), p. 2788.
- [83] M. LI, M. MOELLER, H. RESS, W. FASCHINGER, AND G. LANDWEHR, *The interpretation of x-ray rocking curves by the Fourier transform method*, J. Phys. D: Appl. Phys, 30 (1997), p. 3296.
- [84] R. LIPPERHEIDE, J. KASPER, AND H. LEEB, *Surface profiles from polarization measurements in neutron reflectometry*, Physica, B248 (1998), p. 366.
- [85] R. LIPPERHEIDE, G. REISS, H. LEEB, H. FIEDELDEY, AND S. A. SOFIANOS, *Solution of the inverse scattering problem in specular reflection*, Phys. Rev. B, 51 (1995), p. 11032.
- [86] S. LOGOTHETIDIS, *Sputtered amorphous carbon films: micro-structure, density, optical and mechanical properties*, International Journal of Modern Physics B, 14 (2000), p. 113.
- [87] S. LOGOTHETIDIS AND G. STERGIODIS, *Studies of density and surface roughness of ultrathin amorphous carbon films with regard to thickness with x-ray reflectometry and spectroscopic ellipsometry*, Appl. Phys. Lett., 71 (1997), p. 2463.
- [88] L. B. LUCY, *An iterative technique for the rectification of observed distributions*, Astron. J., 74 (1974), p. 745.
- [89] B. B. LUOKKALA, S. GAROFF, AND R. M. SLUTER, *Using x-ray reflectivity to determine the structure of surfactant monolayers*, Phys. Rev., E62 (2000), p. 2405.
- [90] C. F. MAJKRZAK AND N. F. BERK, *Exact determination of the phase in neutron reflectometry*, Phys. Rev. B, 52 (1995), p. 10827.
- [91] —, *Exact determination of the phase in neutron reflectometry by variation of the surrounding media*, Phys. Rev. B, 58 (1998), p. 15416.
- [92] C. F. MAJKRZAK, N. F. BERK, V. SILIN, AND C. W. MEUSE, *Experimental demonstration of phase determination in neutron reflectometry by variation of the surrounding media*, Physica, B283 (2000), p. 248.

-
- [93] L. MAKOWSKI, *The use of continuous diffraction data as a phase-constraint. I. One-dimensional theory*, J. Appl. Cryst., 14 (1981), p. 160.
- [94] D. MARQUARDT, *An algorithm for least squares estimation of nonlinear parameters*, J. Soc. Industr. Appl. Math., 11 (1963), p. 431.
- [95] C. MICHAELSEN, P. RICARDO, D. ANDERS, M. SCHUSTER, J. SCHILLING, AND H. GOEBEL, *Improved graded multilayer mirrors for XRD applications*, Adv. X-ray Anal., 42 (2000), p. 308.
- [96] M. O. MÖLLER, *Apparatus function of a five-crystal x-ray diffractometer with a four-reflection monochromator*, J. Appl. Cryst., 27 (1994), p. 369.
- [97] I. C. MOORE AND M. CADA, *Prolate Spheroidal Wave Functions, an Introduction to the Slepian Series and its Properties*, Applied and Computational Harmonic Analysis, 16 (2004), p. 208.
- [98] J. J. MORE, *The Levenberg Marquardt algorithm: Implementation and theory*, in Numerical Analysis, G. Watson, ed., vol. 630 of Lecture Notes in Mathematics, Springer-Verlag, Berlin, 1977, pp. 105–116.
- [99] A. Y. NIKULIN, *Uniqueness of the complex diffraction amplitude in x-ray Bragg diffraction*, Phys. Rev. B, 57 (1998), p. 11178.
- [100] A. Y. NIKULIN, A. W. STEVENSON, AND H. HASHIZUME, *Model-independent determination of the strain distribution for a $Si_{0.9}Ge_{0.1}/Si$ superlattice using x-ray diffractometry data*, Phys. Rev. B, 53 (1996), p. 8277.
- [101] H. M. NUSSENZWEIG, *Causality and Dispersion Relations*, Academic Press, New York, London, 1972.
- [102] R. E. A. C. PALEY AND N. WIENER, *Fourier Transforms in the Complex Domain*, Amer. Math. Soc., Providence, 1934.
- [103] A. PAPOULIS, *A new algorithm in spectral analysis and bandlimited extrapolation*, IEEE Trans. Circuits Syst., CAS-22 (1975), p. 735.
- [104] R. PAPROTH, *Untersuchung der Dichteprofile dünner flüssiger Filme mittels Röntgenstreuung*, diploma thesis, Christian-Albrecht-Universität Kiel, 1998.
- [105] L. G. PARRATT, *Surface studies of solids by total reflection of x-rays*, Phys. Rev., 95 (1954), p. 359.
- [106] A. L. PATTERSON, *Ambiguities in the x-ray analysis of crystal structures*, Phys. Rev., 65 (1944), p. 195.

-
- [107] J. S. PEDERSEN, *Model-independent determination of the surface scattering-length-density profile from specular reflectivity data*, J. Appl. Cryst., 25 (1992), p. 129.
- [108] J. S. PEDERSEN AND I. W. HAMLEY, *Analysis of neutron and x-ray reflectivity data. II. Constrained least-squares methods*, J. Appl. Cryst., 27 (1994), p. 36.
- [109] P. S. PERSHAN AND J. ALS-NIELSEN, *X-ray reflectivity from the surface of a liquid crystal: Surface structure and absolute value of critical fluctuations*, Phys. Rev. Lett., 52 (1984), p. 759.
- [110] P. POLOUČEK, U. PIETSCH, T. GEUE, C. SYMIETZ, AND G. BREZESINSKI, *X-ray reflectivity analysis of thin complex Langmuir-Blodgett films*, J. Phys. D: Appl. Phys., 34 (2001), p. 450.
- [111] W. PRANGE, *Struktur und Mischungsverhalten von binären Benetzungsfilmen*, PhD thesis, Christian-Albrecht-Universität Kiel, 2001.
- [112] W. PRANGE, T. KURBJUHN, M. TOLAN, AND W. PRESS, *The structure of hexane/perfluorohexane thin liquid films*, J. Phys. C: Condens. Matter, 13 (2001), p. 4957.
- [113] W. H. PRESS, S. A. TEUKOLSKY, W. T. VETTERING, AND B. P. FLANNERY, *Numerical Recipes in C*, Cambridge University Press, Cambridge, New York, 1997.
- [114] I. R. PRUDNIKOV, R. J. MATYI, AND R. D. DESLATTES, *Wavelet transform approach to the analysis of specular x-ray reflectivity curves*, J. Appl. Phys., 90 (2001), p. 3338.
- [115] G. REISS, *Zum inversen Streuproblem bei der Spiegelreflexion von Neutronen*, PhD thesis, Freie Universität Berlin, 1995.
- [116] —, *Inversion and the phase problem in specular reflection*, Phys. Rev. B, 53 (1996), p. 8157.
- [117] —, *Phase effects in neutron reflection by microemulsions and polymers*, Physica, B221 (1996), p. 533.
- [118] R. F. REMIS AND P. M. VAN DEN BERG, *On the equivalence of the Newton-Kantorovich and distorted Born methods*, Inverse Problems, 16 (2000), p. L1.
- [119] W. RICHARDSON, *Bayesian-based iterative method of image restoration*, J. Opt. Soc. of Am., 62 (1974), p. 55.

- [120] F. RIEUTORD, J. J. BENATTAR, R. RIVOIRA, Y. LEPÊTRE, C. BLOT, AND D. LUZET, *X-ray Phase Determination in Multilayers*, Acta Cryst., A45 (1989), p. 445.
- [121] G. ROSS, M. FIDDY, AND M. NIETO-VESPERINAS, *The inverse scattering problem in structural determinations*, in Inverse Scattering Problems in Optics, H. P. Baltes, ed., Springer-Verlag, Berlin, Heidelberg, New York, 1980, p. 15.
- [122] P. E. SACKS, *Reconstruction of steplike potentials*, Wave Motion, 18 (1993), p. 21.
- [123] M. K. SANYAL, J. K. BASU, A. DATTA, AND S. BANERJEE, *Determination of small fluctuations in electron density profiles of thin films: Layer formation in a polystyrene film*, Europhys. Lett., 36 (1996), p. 265.
- [124] M. K. SANYAL, S. HAZRA, J. K. BASU, AND A. DATTA, *Extraction of density profile for near perfect multilayers*, Phys. Rev. B, 58 (1998), p. R4258.
- [125] M. K. SANYAL, S. K. SINHA, A. GIBAUD, K. G. HUANG, B. L. CAVALHO, M. RAFAILOVICH, M. SOKOLOV, X. ZHAO, AND W. ZHAO, *Fourier reconstruction of density profiles of thin films using anomalous x-ray reflectivity*, Europhys. Lett., 21 (1993), p. 691.
- [126] M. SCHUSTER AND H. GOEBEL, *Application of graded multilayer optics in x-ray diffraction*, Adv. X-ray Anal., 39 (1997), p. 57.
- [127] O. H. SEECK, *Untersuchung des Wetting-Systems CCl_4 auf Si-SiO_2 mittels diffuser Röntgenstreuung*, diploma thesis, Christian-Albrecht-Universität Kiel, 1994.
- [128] O. H. SEECK, I. D. KAENDLER, M. TOLAN, K. SKIN, M. RAFAILOVICH, J. SOKOLOV, AND R. KOLB, *Analysis of x-ray reflectivity data from low contrast polymer bilayers using a Fourier method*, Appl. Phys. Lett., 76 (2000), p. 2713.
- [129] D. SENTANEC, A. N. SHALAGINOV, A. FERA, AND W. H. DE JEU, *On the instrumental resolution in x-ray reflectivity experiments*, J. Appl. Cryst., 33 (1999), p. 130.
- [130] N. SINGH, M. TIRRELL, AND F. S. BATES, *Application of Fourier-Synthesis Methods to the Analysis of Specular Reflectivity*, J. Appl. Cryst., 26 (1993), p. 650.
- [131] S. SINHA, E. SIROTA, S. GAROFF, AND H. STANLEY, *x-ray and neutron scattering from rough surfaces*, Phys. Rev. B, 38 (1988), p. 2297.

-
- [132] D. S. SIVIA, *Data Analysis: A Bayesian Tutorial*, Oxford University Press, 1996.
- [133] V. SKITA, M. FILIPKOWSKI, A. F. GARITO, AND J. K. BLASIE, *Profile structures of very thin multilayers by x-ray diffraction using direct and refinement methods of analysis*, Phys. Rev. B, 34 (1986), p. 5826.
- [134] D. SLEPIAN, *Some comments on Fourier analysis, uncertainty and modelling*, SIAM Review, 25 (1983), p. 379.
- [135] D. SLEPIAN AND H. POLLAK, *Prolate spheroidal wave functions, Fourier analysis and uncertainty I.*, Bell System Tech. J., 40 (1961), p. 43.
- [136] ———, *Prolate spheroidal wave functions, Fourier analysis and uncertainty IV. extension to many dimensions; generalized prolate spheroidal functions*, Bell System Tech. J., 43 (1964), p. 3009.
- [137] ———, *Prolate spheroidal wave functions, Fourier analysis and uncertainty V. the discrete case.*, Bell System Tech. J., 57 (1978), p. 1371.
- [138] E. SMIGIEL AND A. CORNET, *Characterization of a layer stack by wavelet analysis on x-ray reflectivity data*, J. Phys. D: Appl. Phys., 33 (2000), p. 1757.
- [139] E. SMIGIEL, A. KNOLL, N. BROLL, AND A. CORNET, *Determination of layer ordering using sliding-window Fourier transform of x-ray reflectivity data*, Modelling Simul. Mater. Sci. Eng., 6 (1998), p. 29.
- [140] J. L. STARCK AND E. PANTIN, *Deconvolution in astronomy: A review*, Publ. of the Astr. Soc. of the Pacific, 114 (2002), p. 1051.
- [141] O. STARYKOV AND K. SAKURAI, *Determination of interface roughness of Gd films deposited on Si surface using improved wavelet transform of X-ray reflectivity data*, Applied Surface Science, 244 (2005), p. 235.
- [142] R. STÖMMER, *X-ray scattering from silicon surfaces and thin oxides on silicon substrates*, PhD thesis, Universität Potsdam, 1999.
- [143] R. STÖMMER AND L. BRÜGEMANN, *D8 Discover Epitaxial Layer Investigation*, Analytical Application Note 358, Bruker-AXS GmbH.
- [144] J. STRAIN, *A fast Laplace transform based on Laguerre functions*, Mathematics of Computation, 58 (1992), p. 275.
- [145] J. STRÖR, R. JAEGER, J. FELDHAUS, S. BRENNAN, D. NORMAN, AND G. APAI, *EXAFS studies above the C,N,O and F K absorptions edges*, Applied Optics, 19 (1980), p. 3911.

-
- [146] I. M. TIDSWELL, B. M. OCKO, P. S. PERSHAN, S. WASSERMANN, G. M. WHITESIDES, AND J. D. AXE, *X-ray specular reflection studies of silicon coated by organic monolayers (alkylsiloxanes)*, Phys. Rev. B, 41 (1990), p. 1111.
- [147] A. N. TIKHONOV, *Solution of incorrectly formulated problems and regularization method*, Soviet math. Dokl., 4 (1963), p. 1053.
- [148] A. V. TIKHONRAROV, M. K. KLIBANOV, AND I. V. ZUEV, *Numerical study of the phaseless inverse scattering problem in thin-film optics*, Inverse Problems, 11 (1995), p. 251.
- [149] A. V. TIKHONRAVOV, *Amplitude-phase properties of the spectral coefficients of laminar media*, USSR Comp. Math. and Math. Phys., 25 (1985), p. 77.
- [150] —, *Some theoretical aspects of thin-film optics and their applications*, Appl. Opt., 32 (1993), p. 5417.
- [151] A. V. TIKHONRAVOV, P. W. BAUMEISTER, AND K. V. POPOV, *Phase properties of multilayers*, Appl. Opt., 36 (1997), p. 4382.
- [152] E. C. TITCHMARSH, *The zeros of certain classes of integral functions*, Proc. Lond. Math. Soc., 25 (1926), p. 283.
- [153] —, *The Theory of Functions*, Oxford University Press, London, New York, 2nd ed., 1939.
- [154] —, *Introduction to the Theory of Fourier Integrals*, Oxford University Press, London, New York, 2nd ed., 1948.
- [155] M. TOLAN, *X-Ray Scattering from Soft-Matter Thin Films*, vol. 148 of Springer Tracts in Modern Physics, Springer Verlag, 1999.
- [156] J. S. TOLL, *Causality and the dispersion relations: Logical foundations*, Phys. Rev., 104 (1956), p. 1760.
- [157] W. F. TRENCH, *An algorithm for the inversion of finite Toeplitz matrices*, J. SIAM, 12 (1964), p. 515.
- [158] A. ULYANENKOV, K. OMOTE, AND J. HARADA, *The Genetic Algorithm: Refinement of x-ray reflectivity data from multilayers and thin films*, Physica, B283 (2000), p. 237.
- [159] M. UNSER, *B-spline signal processing: Part I – Theory*, IEEE Transactions on Signal Processing, 41 (1993), p. 821.

-
- [160] —, *Sampling – 50 years after Shannon*, Proceedings of the IEEE, 88 (2000), p. 569.
- [161] A. VAN DER LEE, *Experimental feasibility of phaseless inverse scattering methods for specular reflectivity*, Euro. Phys. J. B, 13 (2000), p. 755.
- [162] —, *Practical aspects of inverse scattering methods applied to specular reflectivity data*, Physica, B283 (2000), p. 273.
- [163] —, *Critical comparison of recent analysis methods of x-ray and neutron reflectivity data*, Journal de Physique IV, 12 (2002), p. 255.
- [164] G. VIGNAUD, A. GIBAUD, G. GRUEBEL, S. JOLY, D. AUSSERRE, J. LEGRAND, AND Y. GALLOT, *Ordering of diblock PS–PBMA thin films: An x-ray reflectivity study*, Physica, B248 (1998), p. 250.
- [165] J. R. WEAVER, *Centrosymmetric (cross-symmetric) matrices, their basic properties, eigenvalues, and eigenvectors*, The American Mathematical Monthly, 92 (1985), p. 711.
- [166] R. WEBER, *Oberflächenempfindliche Röntgenstreuung an Polymer-Metall-Grenzflächen: Strukturelle Eigenschaften und thermisches Verhalten*, PhD thesis, Christian-Albrecht-Universität Kiel, 2002.
- [167] R. WEBER, K. M. ZIMMERMANN, M. TOLAN, R. WEBER, J. STETTNER, W. PRESS, O. H. SEECK, J. ERICHSEN, V. ZAPOROJTCHENKO, T. STRUNSKUS, AND F. FAUPEL, *X-ray reflectivity study on the surface and bulk glass transition of polystyrene*, Phys. Rev. E, 64 (2001), p. 61508.
- [168] H. XIAO, V. ROKHLIN, AND N. YARVIN, *Prolate spheroidal wavefunctions, quadrature and interpolation*, Inverse Problems, 17 (2001), p. 805.
- [169] C.-J. YU, A. G. RICHTER, A. DATTA, M. K. DURBIN, AND P. DUTTA, *Observation of molecular layering in thin liquid films using x-ray reflectivity*, Phys. Rev. Lett., 82 (1999), p. 2326.
- [170] C.-J. YU, A. G. RICHTER, J. KMETKO, S. W. DUGAN, A. DATTA, AND P. DUTTA, *Structure of interfacial liquids: X-ray scattering studies*, Phys. Rev. E, 82 (2001), p. 21205.
- [171] X.-L. ZHOU, *Quantitative analysis of the nonlinear relationship between neutron or x-ray reflectance and the scattering-length-density profile*, Phys. Rev. E, 52 (1995), p. 1938.
- [172] X.-L. ZHOU AND S. H. CHEN, *Model-independent method for the reconstruction of scattering-length-density profiles using neutron or x-ray reflectivity data*, Phys. Rev. E, 47 (1993), p. 3174.

-
- [173] X.-L. ZHOU, S. H. CHEN, AND G. P. FELCHER, *New analytical formula for neutron reflection from surface films*, The Journal of Physical Chemistry, 95 (1991), p. 9025.
- [174] ———, *Improved analytical formulas for x-ray and neutron reflection from surface films*, Phys. Rev. A, 46 (1992), p. 1839.
- [175] K. M. ZIMMERMANN, *Untersuchung der Grenzflächenstruktur von Metall-Polymer-Systemen mittels Röntgenstreuung im Bereich der Totalreflexion*, diploma thesis, Christian-Albrecht-Universität Kiel, 2000.
- [176] K. M. ZIMMERMANN, M. TOLAN, R. WEBER, J. STETTNER, A. K. DOERR, AND W. PRESS, *Phase determination of x-ray reflection coefficients*, Phys. Rev. B, 62 (2000), p. 10377.

Danksagung

Als erstes bedanke ich mich bei Herrn Prof. Dr. M. Tolan für die Vergabe des interessanten Themas und die von ihm gewährte Möglichkeit in der Industrie zu promovieren. Er hatte für meine Probleme stets ein offenes Ohr und hat durch seine permanente Diskussions- und Hilfsbereitschaft viel zum Gelingen dieser Arbeit beitragen. Auch danke ich ihm für die unbürokratisch organisierten Messzeiten an seinem Diffraktometer in Dortmund.

Als nächstes danke ich der Firma Bruker AXS für die finanzielle Unterstützung meiner Promotion und Lutz Brügemann sowie Heiko Ress für die firmeninterne Betreuung meiner Arbeit. Heikos Engagement in den letzten schweren Stunden dieser Arbeit verdient meine höchste Anerkennung.

Danny Weissbach, Thomas Holz und Rainer Dietsch von Fraunhofer IWS in Dresden haben durch hervorragend präparierte Proben dazu beigetragen, dass die im Rahmen dieser Arbeit präsentierten Reflektivitäten an Schönheit kaum zu überbieten sind.

Michael Jacob danke ich für die Einweisung die hohe Kunst des objekt-orientierten Programmierens und für zahllose Fahrtouren durchs Karlsruher Umland.

Olaf Bahr sei für die Einweisung in die hohe Kunst des Justierens von Bruker-Diffraktometern gedankt – und für seine Sprüche. Bei technischen Problemen stand er mir stets mit vollem Einsatz zur Seite.

Detlef Bahr hatte für meine Probleme stets ein offenes Ohr. Seine pragmatischen Lösungen waren mir eine grosse Hilfe.

Assunta Vigilante and Hugues Guerault danke ich für die schöne Zeit die ich in der Firma und auf Konferenzen mit ihnen verbringen durfte.

Alex Ulyanenko danke ich für anregende Diskussionen und das Korrekturlesen dieser Arbeit. Auch Michael Sprung und Christian Gutt sei für das Korrekturlesen meiner Arbeit gedankt.

Ich danke meinen Eltern dafür, dass sie mir meine Ausbildung ermöglicht haben und mir bei meinen Problemen stets mit Rat und Tat zur Seite standen.

Von ganzen Herzen bedanke ich mich bei Reinhard und Renate Schwärzler, die durch ihre Hilfsbereitschaft sehr dazu beigetragen haben, dass ich die vorliegende Arbeit beenden konnte. Nicola danke ich für ihre unendliche Geduld, Unterstützung und Liebe.

Abschliessend bedanke ich mich bei allen, die ich vergessen habe zu erwähnen und die ihren Beitrag zum Gelingen dieser Arbeit geleistet haben.

Lebenslauf

Klaus Martin Zimmermann

Liedolsheimer Ring 14

76148 Karlsruhe

Geburtsdatum	27.10.1970
Geburtsort	Kiel
Nationalität	Deutsch
1977–1981	Jahn-Schule, Grundschule in Kiel
1981–1988	Max-Planck-Gymnasium, Kiel
1988–1990	Internatsgymnasium Schloss Plön
Juni 1990	Allgemeine Hochschulreife
Juli 1990 – Sep. 1992	Ausbildung zum Offizier der Reserve
1992 – 1999	Diplomstudium der Physik
Apr. 1995	Vordiplom in Physik
Mai 1997 - Juli 1997	Studium der französischen Sprache an der Université Standhal/Grenoble
Aug 1997 - Sept 1998	Studium der Physik an der Université Joseph Fourier/Grenoble mit Abschluss <i>Maitrise en physique</i>
Jan./Febr. 1999	Mündliche Diplomprüfungen in Physik mit dem Nebenfach Chemie
März 1999 - Apr. 2000	Anfertigung der Diplomarbeit in der Arbeitsgruppe von Prof. Dr. W. Press Thema: <i>Untersuchung der Grenzflächenstruktur von Metall-Polymer-Systemen mittels Röntgenstreuung im Bereich der Totalreflexion</i>
Apr. 2000	Diplom in Physik
Aug. 2000 –	Anfertigung der vorliegenden Dissertation unter Betreuung von Prof. Dr. M. Tolan / Universität Dortmund

Eidesstattliche Versicherung

Hiermit versichere ich an Eides Statt, dass die vorliegende Dissertation - abgesehen von der Beratung durch meinen wissenschaftlichen Lehrer - nach Inhalt und Form meine eigene Arbeit ist. Sie hat weder ganz noch zum Teil an einer anderen Stelle im Rahmen eines Prüfungsverfahrens vorgelegen.

Karlsruhe, im Mai 2005

.....
(Klaus Martin Zimmermann)